

SINGLE CELL HIGH CONTENT TEXTURAL IMAGE ANALYSIS OF
DYNAMIC EPIGENETIC SIGNATURES AS A RESPONSE TO
DEFINED MICROENVIRONMENTAL PARAMETERS

By

JOSEPH JUNG-WOONG KIM

A Dissertation submitted to the
Graduate School - New Brunswick
Rutgers, The State University of New Jersey
In partial fulfillment of the requirements

For the degree of
Doctor of Philosophy
Graduate Program in Biomedical Engineering

Written under the direction of

Prabhas V. Moghe

And approved by

New Brunswick, New Jersey

January, 2015

ABSTRACT OF THE DISSERTATION

SINGLE CELL HIGH CONTENT TEXTURAL IMAGE ANALYSIS OF DYNAMIC EPIGENETIC SIGNATURES AS A RESPONSE TO DEFINED MICROENVIRONMENTAL PARAMETERS

By JOSEPH JUNG-WOONG KIM

Dissertation Director:

Prabhas V. Moghe

Currently, quantifiable investigations of the epigenome require cell lysis and are population based, prohibiting direct investigations of intact intranuclear structural organization and introducing noise into data obtained from inherently heterogeneous stem cell populations. To address this, we have developed and employed a single-cell high-content image informatics framework to capture organizational signatures of epigenetic signaling components from images of cellular nuclei obtained via superresolution nanoscopy. High dimensional quantitative texture descriptors of the organizational dynamics of key posttranslational modifications to core histone proteins were imaged in different human stem cell systems using time-gated stimulated emission depletion confocal nanoscopy. Influential texture descriptors were identified, validated at the nanoscale using immuno-gold electron microscopy, and organizational sub-classifiers were generated from this bioimage informatics data representing a range of “open” versus “closed” chromatin states. When applied to growth factor-induced lineage

differentiation of human mesenchymal stem cells, the organizational classifiers showed a clear evolution with temporal cell state, which was more sensitive than the conventional mass spectrometry-based quantitation of the relative abundance of these PTMs. When a range of stem cell phenotypes sharing common DNA sequences were imaged, clear sub-classifiers emerged correlating with the divergent phenotypes for undifferentiated, adipogenic, and osteogenic hMSCs, as well as for human foreskin fibroblasts, induced pluripotent stem cells, neural stem cells, and reprogrammed neurons. Thus, high content bioimage informatics reflective of chromatin organization yields a higher order organizational signature corresponding to an epigenetic “activity” state.

To elucidate the influence of biophysical factors on stem cell epigenetic states, these imaging-based organizational classifiers were tested on human mesenchymal stem cells exposed to physically constraining cues, and successfully predicted the early differentiation toward adipogenic hMSCs on hydrogel substrates with spatially graded mechanical stiffness, as well as osteogenic hMSCs on soft-lithographed, graded nanotopographies. In summary, in contrast to the traditional reductionist, population-level readouts in epigenomics, the approach outlined in this thesis offers a more integrated, single-cell, organizational index of emergent stem cell activity in response to defined environmental cues, and can be applied for the screening of discrete microenvironmental properties for the enhancement of stem cell behavioral control and facilitated integration in regenerative medicine applications.

ACKNOWLEDGEMENTS

The work presented in this thesis was highly collaborative and relied on the dedicated work and support from several professors, mentors, colleagues and students. Without their collective support, the completion of this dissertation would not have been possible, and as such, I am deeply indebted to the following people:

First and foremost, I owe the greatest amount of gratitude to my primary advisor, Dr. Prabhas Moghe, for guiding me throughout this PhD journey. Over the past several years, he has constantly challenged me to critically question my own ideas and never to lose hold of the “big picture” context of all of my efforts, and has groomed me to be the thoughtful and confident scientist I am today. He has afforded me numerous collaborative opportunities, seemingly endless financial support and superb mentorship. Throughout the rest of my scientific career, everything that I do and accomplish will be influenced, however subtly, by the countless things that Dr. Moghe has taught me, and thus I am forever indebted to him.

I am also sincerely thankful for my IGERT co-advisor, Dr. Michael Verzi, who has largely shaped my perspective of epigenetics in general, and has guided me through navigating its intricacies. From the first time I heard a talk Dr. Verzi gave at the NJ Stem Cell Research Symposium in 2011, I became utterly captivated by the influence of histone modification dynamics on transcriptional regulation, and I have been obsessed ever since. Dr. Verzi’s affable mentorship and Zen-like aura have always made working with him a very pleasant experience, and I strive to exude a similar quality in my own potential future mentor positions.

I have been very fortunate to have had the opportunity to work with Dr. Nathaniel Hwang at Seoul National University. From the day that we first met, Dr. Hwang has had the utmost faith in my ideas and abilities, and working with him has served to give an enormous boost to my confidence as a scientist. He has also provided me with much invaluable advice about a career in academia, and effective strategies for building a successful scientific career.

I owe a great amount of gratitude to all of the scientists that I have collaborated with and have contributed experimentally to much of the data presented throughout this dissertation. Dr. Rick Cohen, of the Rutgers Stem Cell Research Center, is a genius when it comes to genetic engineering, and was the principal scientist that developed the H3.1/Actin fluororeporter plasmid. Dr. Sanjay Chahar, of the Department of Genetics at Rutgers, has trained me on how to perform chromatin immunoprecipitation and process and interpret its results. Dr. Matthew Becker and Erin Childers, at the University of Akron, have provided the guidance for fabricating the PEGDM Young's Modulus continuous gradient hydrogels. Dr. Satish Viswananth, formerly of the Biomedical Engineering Department at Rutgers, and now at Case Western Reserve University, has provided guidance for much of the MATLAB-based computational image analysis techniques. Dr. Paul Shao, at Princeton University, has trained me on Immuno-electron microscopy, from sample preparation to image acquisition. Dr. Benjamin Garcia and Shichong Liu, at the University of Pennsylvania, have provided the mass spectroscopy based quantification of histone PTM abundance data. Dr. Marius Wernig, at Stanford University, has provided the plasmid vector for directly generating neuronal cells from other somatic phenotypes.

Dr. Aina Andrianarijaona, of the Department of Chemical Engineering at Rutgers, has trained me on performing western blots. And finally, Ashley Lee, at Seoul National University, has trained me on soft lithography techniques to fabricate nanotopographic substrates.

I am greatly indebted to my thesis committee and numerous professors that have provided me with their critical input, thoughtful advice and intellectual support: Dr. Nada Boustany, Dr. Anant Madabhushi, Dr. Lourdes Serrano, Dr. Ioannis Androulakis, Dr. Joachim Kohn, Dr. Vincenzo Pirrotta and Dr. Martin Yarmush. Your input has served to significantly shape this dissertation and I am sincerely grateful.

Being part of a larger, popular lab, such as Dr. Moghe's, inevitably attracts a constant influx of the brightest undergraduate students. I have been truly blessed with the opportunity to provide mentorship to a superb group of first-rate undergraduate students that have all contributed to much of the experimental efforts outlined in this thesis, as well as helped me to develop as a mentor: Anthony Kulesa, Kevin Ling, Elizabeth Silagi, Janice Jeschke and Mitchel Devita. I am grateful for all of the hard work you have all put in and have no doubt that you will all excel in your future professional endeavors.

I have had the opportunity to work in several labs prior to Dr. Moghe's, as an undergraduate and as a Masters student in Biological Sciences. I can easily say that working in Dr. Moghe's laboratory was, by far, the best laboratory I have ever worked in, and this is largely due to the great graduate students that comprise(d) it. I am grateful to you all for your assistance with numerous, various things, and I will forever cherish the more lighthearted times we shared together inside and outside of the lab. I am also

greatly indebted to the BME staff, Robin Yarborough, Larry Stromberg and Stratos Loukidis. The countless, vital coordinative and administrative tasks were only able to be fulfilled through your continuous arduous efforts.

Finally, I would like to thank all of my friends outside of the lab, who I have forged lasting relationships with long before I began this journey, and continue to support me today. And lastly, I'd like to sincerely thank my family, especially my parents. You have all been with me through thick and thin, and have provided the vital moral support I've needed to persevere through this difficult task. I love you all so much and am forever indebted to you. I only hope that one day I can provide for you a fraction of what you have provided for me.

DEDICATION

To my paternal grandparents, who are no longer with us: the Christian foundation that you have instilled in my parents has molded who they are, and subsequently who I am, and will continue to guide and motivate all of my future work in science to serve God and my fellow man.

And to my parents, who taught me to love learning.

Table of Contents

ABSTRACT OF THE DISSERTATION	II
ACKNOWLEDGEMENTS.....	IV
DEDICATION.....	VIII
LIST OF TABLES	XIV
LIST OF FIGURES	XV
CHAPTER 1. INTRODUCTION	1
1.1 Regenerative Medicine	1
1.1.1 Cell Replacement Therapy	2
1.1.2 Tissue Engineering	5
1.1.3 Current Challenges to Overcome in Regenerative Medicine	5
1.2 Epigenetic Control of Gene Transcription Regulation	7
1.2.1 DNA Methylation	9
1.2.2 Post Transcriptional Modifications to Histones	10
1.2.3 ATP-Dependent Chromatin Remodeling Complexes	12
1.2.4 Chromatin Structural Dynamics Navigate Cellular Differentiation	13
1.2.5 Environmental Influences to Chromatin Structure	17
1.2.6 Current Approaches to Interrogate the Epigenome	20
1.2.7 Current Approaches for Characterizing the Chromatin Structural Organization	23
1.3 Bioimage Informatics.....	27
1.3.1 Quantitative Morphometric Descriptors from High-Content Images	30
1.3.2 Haralick Texture Features	31
1.3.3 Quantitative Analysis of High-Content Descriptor Datasets	36
1.4 Hypothesis and Overview of Thesis Aims.....	39

CHAPTER 2. DEVELOPMENT AND CALIBRATION OF QUANTITATIVE TEXTURE DESCRIPTORS REFLECTIVE OF DYNAMIC CHROMATIN STRUCTURAL STATES	41
2.1 Introduction.....	41
2.2 Materials and Methods	45
2.2.1 Human Mesenchymal Stem Cell Culture	45
2.2.2 Lysine Methyltransferase Inhibition	47
2.2.3 Verification of KMTi Selectivity Using Western Blot	47
2.2.4 Immunocytochemistry of H3K4me3 and H3K27me3	49
2.2.5 Laser Scanning Confocal Microscopy	50
2.2.6 Immunoelectron Microscopy with Transmission Electron Microscope.....	50
2.2.7 Quantification of PTMs Using Mass Spectroscopy	52
2.2.8 Computational Methods of Calibration.....	52
2.3 Results	54
2.3.1 Efficacy and Specificity Verification of 3-Deazaneplanocin A	54
2.3.2 Combined Effect of KMT Inhibitors and Soluble Growth Factors on Differentiation	55
2.3.3 Calibration of Quantitative Texture Descriptors Using KMT Inhibitors	59
2.3.4 Immunoelectron Microscopic Quantification of H3K4K27me3 manifestation	61
2.3.5 Mass Spectrometric Quantification of PTM Relative Abundance	63
2.4 Discussion	67
2.5 Conclusion	69
2.6 Supplementary Data.....	70
CHAPTER 3. HIGH CONTENT TEXTURAL IMAGE ANALYSIS OF THE DYNAMICS OF POST TRANSLATIONAL MODIFICATIONS TO HISTONES IN DIFFERENTIATING STEM CELLS.....	72
3.1 Introduction	72
3.2 Materials and Methods.....	75
3.2.1 HFF-1 Cell Culture and Reprogramming.....	75
3.2.2 Lineage Marker Staining Differentiation Assays	76

3.2.3 Förster Resonance Energy Transfer	77
3.2.4 Chromatin Immunoprecipitation	78
3.2.5 Quantitative Real Time Polymerase Chain Reaction.....	79
3.2.6 Immunocytochemistry of Heterochromatin Protein 1 alpha and H3K9me3...	80
3.3 Results	82
3.3.1 Histological Evaluation of Osteogenic and Adipogenic Differentiation	82
3.3.2 Biomarker verification of iPSCs, NSCs and iNs	83
3.3.3 Förster Resonance Transfer Analysis of H3K4K27me3 Bivalency	84
3.3.4 Chromatin Immunoprecipitation of H3K4K27me3	87
3.3.5 Four Dimensional Spatiotemporal Analysis of H3K4K27me3 Dynamics in hMSCs	88
3.3.6 Texture Image Analysis of H3K4K27me3 in HFF-1 derived differentiating iPSCs	91
3.3.7 Dynamics of HP1 α and H3K9me3 as a response to differentiation cues.....	89
3.4 Discussion	96
3.5 Conclusion	101
3.6 Supplementary Data.....	102
CHAPTER 4. MECHANICAL, CHEMICAL AND TOPOGRAPHICAL INFLUENCES ON CHROMATIN ORGANIZATIONAL DYNAMICS AND DIFFERENTIATION.	103
4.1 Introduction.....	103
4.2 Materials and Methods	105
4.2.1 PEGDM Continuous Young's Modulus Gradient Hydrogel Fabrication	105
4.2.2 Polyurethane Acrylate Topographic Pattern Substrate Fabrication	106
4.2.3 k-means Cluster Analysis	107
4.3 Results	108
4.3.1 hMSC Differentiation as a Response to Young's Modulus Gradient.....	108
4.3.2 Texture Image Analysis of H3K4K27me3 Dynamics in hMSCs on PEGDM Substrate	109
4.3.3 Combined Effect of KMTi and Young's Modulus on Differentiation	111
4.3.4 hMSC Differentiation as a Response to Nanotopography	113

4.3.5 Texture Image Analysis of H3K4K27me3 Dynamics in hMSCs on PUA Substrate	115
4.3.6 Combined Effect of KMTi and Nanotopography on Differentiation	118
4.4 Discussion	122
4.5 Conclusion	125
4.6 Supplementary Data.....	126

CHAPTER 5. MUTUAL INFLUENCE OF CYTOSKELETAL MORPHOLOGY AND INTRANUCLEAR ORGANIZATION THROUGHOUT CELLULAR DEVELOPMENT

.....	129
5.1 Introduction	129
5.2 Materials and Methods.....	133
5.2.1 Lentiviral Plasmid Construction.....	133
5.2.2 Lentivirus Production and Harvest	138
5.2.3 Cell Transduction and Selection	139
5.2.4 Live-cell microscopy	140
5.2.5 Quantitative Assessment of Cell Body and Nucleus Relationship	140
5.3 Results	142
5.3.1 Texture Image Analysis of Actin, Integrin β -1 and PTMs as a Response to Chemical Cues.....	142
5.3.2 Texture Image Analysis of Actin, Integrin β -1 and PTMs as a Response to Biophysical Cues	147
5.3.3 Live Image Analysis of H3B and Actin in Response to Chemical Cues	150
5.4 Discussion	161
5.5 Conclusion	163

CHAPTER 6. DISSERTATION SUMMARY AND FUTURE DIRECTIONS

6.1 Dissertation Summary	164
6.2 Future Directions	169
6.2.1 Fabrication of Bioactive Scaffolds for Directed Cell Differentiation	170
6.2.2 Epigenetic Drug Development for Cancer Therapy	171

6.2.3 Epigenetic Modifications to Induce Pluripotent Stem States	171
6.2.4 Mapping Material-Responsive PTM Landscapes Using Mass Spectrometry	173
6.2.5 Quantitative Analysis of Chromatin Structural Dynamics Using Fluorescence Correlation Spectroscopy	174
6.3 Closing Remarks	177
CHAPTER 7. REFERENCES	178

List of Tables

Table 1.1 Haralick Texture Descriptors	34
Table 3.1 Sequences of primers used in chromatin immunoprecipitation assays.....	80
Table 5.1 Final sequence of pSin-EF2-LA-tGFP-T2A-Histone H3.1-mRFP-IRES-Puro plasmid.....	135

List of Figures

Figure 1.1 Regenerative medicine strategies	4
Figure 1.2 Nucleosome crystal structure	8
Figure 1.3 Dynamic chromatin structural states schematic	9
Figure 1.4 Combinatorial complexities of posttranslational modifications to histones. .	11
Figure 1.5 ATP-dependent chromatin remodeling complexes.....	12
Figure 1.6 Epigenetic mechanisms involved in pluripotency / differentiation.	16
Figure 1.7 Mechanical properties influence cellular development.....	18
Figure 1.8 Chromatin immunoprecipitation schematic.....	21
Figure 1.9 Mass spectrometric quantification of PTMs schematic.	22
Figure 1.10 X-ray crystallography progress.	24
Figure 1.11 Chromatin Conformation Capture.....	26
Figure 1.12 Bioimage Informatics schematic.....	29
Figure 1.13 Grey Level Co-occurrence Matrices.	32
Figure 1.14 Weka decision tree example.....	38
Figure 2.1 H3K4K27me3 dynamics schematic	43
Figure 2.2 High-content imaging schematic	44
Figure 2.3 Immunoblots of DZNep effects.....	55
Figure 2.4 Combined effect of 3-Deazaneplanocin A and differentiation induction	56
Figure 2.5 Combined effect of Deoxymethylthioadenosine and differentiation induction	58
Figure 2.6 Immunolabeled H3K4K27me3 response to KMTi dose	59
Figure 2.7 Heat map of KMTi dose response.....	60
Figure 2.8 Immuno-electron microscopic investigation of H3K4K27me3 distribution	62
Figure 2.9 Mass spectrometric quantification of H3K4K27me3.....	64
Figure 2.10 PTM quantification landscape in response to chemical cues.....	65

Figure 2.11 Quantitative correlation between confocal and electron microscopy	68
Supplementary Figure S2.1 Lineage marker staining in developing hMSCs.....	70
Supplementary Figure S2.2 Parsing index zone of undifferentiated stem cells.....	71
Figure 3.1 Clinical trials of hMSCs classified by disease type	73
Figure 3.2 Lineage marker quantification of differentiating hMSCs	82
Figure 3.3 Biomarker verification of iPSCs, NSCs and iNs.....	84
Figure 3.4 FRET schematic	85
Figure 3.5 FRET efficiency quantification between H3K4me3 and H3K27me3.....	87
Figure 3.6 Chromatin immunoprecipitation of H3K4K27me3 in differentiating hMSCs & iPSCs	88
Figure 3.7 Four dimensional spatiotemporal image analysis of H3K4K27me3 in differentiating hMSCs	90
Figure 3.8 High content image analysis of H3K4K27me3 in differentiating hMSCs & iPSCs	92
Figure 3.9 H3K9me3 recruits HP1- α	94
Figure 3.10 High content image analysis of H3K9me3 in differentiating hMSCs	95
Figure 3.11 Intensity quantification analysis of differentiating hMSCs	97
Figure 3.12 High content image analysis of Hoechst in differentiating hMSCs & iPSCs ..	98
Figure 3.13 Nucleoli image analysis in differentiating hMSCs.....	99
Figure 3.14 Decision Tree analysis of descriptors of H3K4K27me3	100
Supplementary Figure S3.1 High content image analysis of HP1 α in iPSCs & mouse embryonic spinal cord neurons	102
Supplementary Figure S3.2 Agarose gel electrophoresis of sonicated hMSC DNA	102
Figure 4.1 Schematic of computer controlled syringe pump device used for PEGDM continuous gradient hydrogel fabrication	106
Figure 4.2 Atomic force microscopy images of PUA topography patterned substrate..	107
Figure 4.3 Lineage staining quantification of hMSCs cultured on PEGDM hydrogels....	108
Figure 4.4 High content image analysis of H3K4K27me3 in hMSCs cultured on PEGDM continuous gradient hydrogels	110

Figure 4.5 Combined effect of KMTi's and PEGDM hydrogels of varied stiffness.....	112
Figure 4.6 Lineage staining quantification of hMSCs cultured on PUA nanogrooves	114
Figure 4.7 High content image analysis of H3K4K27me3 in hMSCs cultured on PUA topography patterned substrate	116
Figure 4.8 Heat map of normalized texture descriptor values of H3K4K27me3 in hMSCs cultured on PUA nanogrooves	117
Figure 4.9 Lineage staining quantification of combined effect of varied nanotopography and KMTi treatment on early hMSC development.....	120
Figure 4.10 Lineage staining quantification of combined effect of varied nanotopography and KMTi treatment on late hMSC development	121
Supplementary Figure S4.1 Textural image analysis of nuclear mitotic apparatus in hMSCs exposed to different ECM and bleomycin treatment.....	126
Supplementary Figure S4.2 Morphological analysis of actin organization in hMSCs cultured on titanium nanopillars of varying height	127
Supplementary Figure S4.3 High content image analysis of H3K4K27me3 in hMSCs cultured on varying degrees of PEG concentration	128
Supplementary Figure S4.4 Weka decision tree data mining of H3K4K27me3 texture descriptors of hMSCs cultured on varying degrees of PEG concentration.....	128
Figure 5.1 Schematic of major players involved in transduction of microenvironmental stimuli to the cytoskeleton and nucleus.....	131
Figure 5.2 LifeAct-tGFP-T2A-Histone H3.1-RFP-IRES-Puro plasmid design	135
Figure 5.3 Quad-immunolabeling of hMSCs exposed to soluble growth factors and KMTi's.....	143
Figure 5.4 Heat maps of relationship between intranuclear texture descriptors and morphometric geometrical descriptors in hMSCs exposed to combinations of chemical cues	144
Figure 5.5 Quad-immunolabeling of hMSCs cultured on PEGDM hydrogels of varying stiffness in combination with KMTi treatment.....	148
Figure 5.6 Heat maps of relationship between intranuclear texture descriptors and morphometric geometrical descriptors in hMSCs cultured on PEGDM hydrogels with KMTis.....	149
Figure 5.7 Time-lapse image panel of hMSCs exposed to adipogenic growth factors...	151

Figure 5.8 Time-lapse image panel of undifferentiated hMSCs	152
Figure 5.9 Time-lapse image panel of hMSCs exposed to osteogenic growth factors...	153
Figure 5.10 Time-lapse image panel of hMSCs exposed to adipogenic growth factors and 3-Deazaneplanocin A	154
Figure 5.11 Time-lapse image panel of undifferentiated hMSCs exposed to 3-Deazaneplanocin A	155
Figure 5.12 Time-lapse image panel of hMSCs exposed to osteogenic growth factors and 3-Deazaneplanocin A	156
Figure 5.13 Time-lapse image panel of hMSCs exposed to adipogenic growth factors and Deoxymethylthioadenosine.....	157
Figure 5.14 Time-lapse image panel of undifferentiated hMSCs exposed to Deoxymethylthioadenosine.....	158
Figure 5.15 Time-lapse image panel of hMSCs exposed to osteogenic growth factors and Deoxymethylthioadenosine.....	159
Figure 5.16 Principal component analysis of H3.1 texture descriptors across time	160
Figure 6.1 Model for relationship between PTM organization, quantitative texture descriptors and gene transcription regulation	168
Figure 6.2 Fluorescence correlation spectroscopy schematic.....	176

CHAPTER 1: INTRODUCTION

1.1 Regenerative Medicine

The acceleration of research on stem cells has revolutionized clinical strategies for treating damaged tissues/organs and cellular degeneration. In the United States, the first research projects investigating human embryonic stem cells (hESCs) were funded by the NIH over a decade ago [1, 2]. Since then, significant interest and investment has been poured into the use of stem cells in regenerative medicine, with over 2,000 research reports being published in peer reviewed scientific journals every year [3]. Since 2008, the NIH has continually supported the field of regenerative medicine with approximately \$1.5 billion allocated to research involving human stem cells [4]. This federal funding, coupled with state funding, has continued to increase over the past several years, along with increasing public support due to the realization of the potential of stem cell therapy to treat a wide range of debilitating diseases [4]. This paved the way for the NIH's establishment of the *Center for Regenerative Medicine* in 2010, which is dedicated to accelerating the pace of stem cell therapy, as well as overcoming the many scientific and political hurdles to its ultimate clinical translation. Outside of the US, the worldwide market value for regenerative medicine in 2010 was estimated to be in excess of \$500 billion [5]. Thus, it is quite clear that both intellectual and financial investment into regenerative medicine using stem cells is quite large, and steadily rising, as it harbors massive potential to vastly revolutionize cell replacement strategies and tissue engineering of the future.

1.1.1 Cell Replacement Therapy

The foundational principle of cell replacement therapy lies in the restoration of the normal function of tissues/organs by replacing damaged, dying, or diseased cells with fresh, functional ones [6]. There are numerous degenerative diseases that are caused by the loss of functional cells due to disease (both acquired and genetic), injury and aging. Perhaps the most promising potential solution for treating such diseases is employing cell replacement therapy after generating desired cell phenotypes through the directed differentiation of stem cells. In the US, many clinical trials using both pluripotent and multipotent stem cells for cell replacement therapy are actively being conducted to treat a wide variety of degenerative diseases [7].

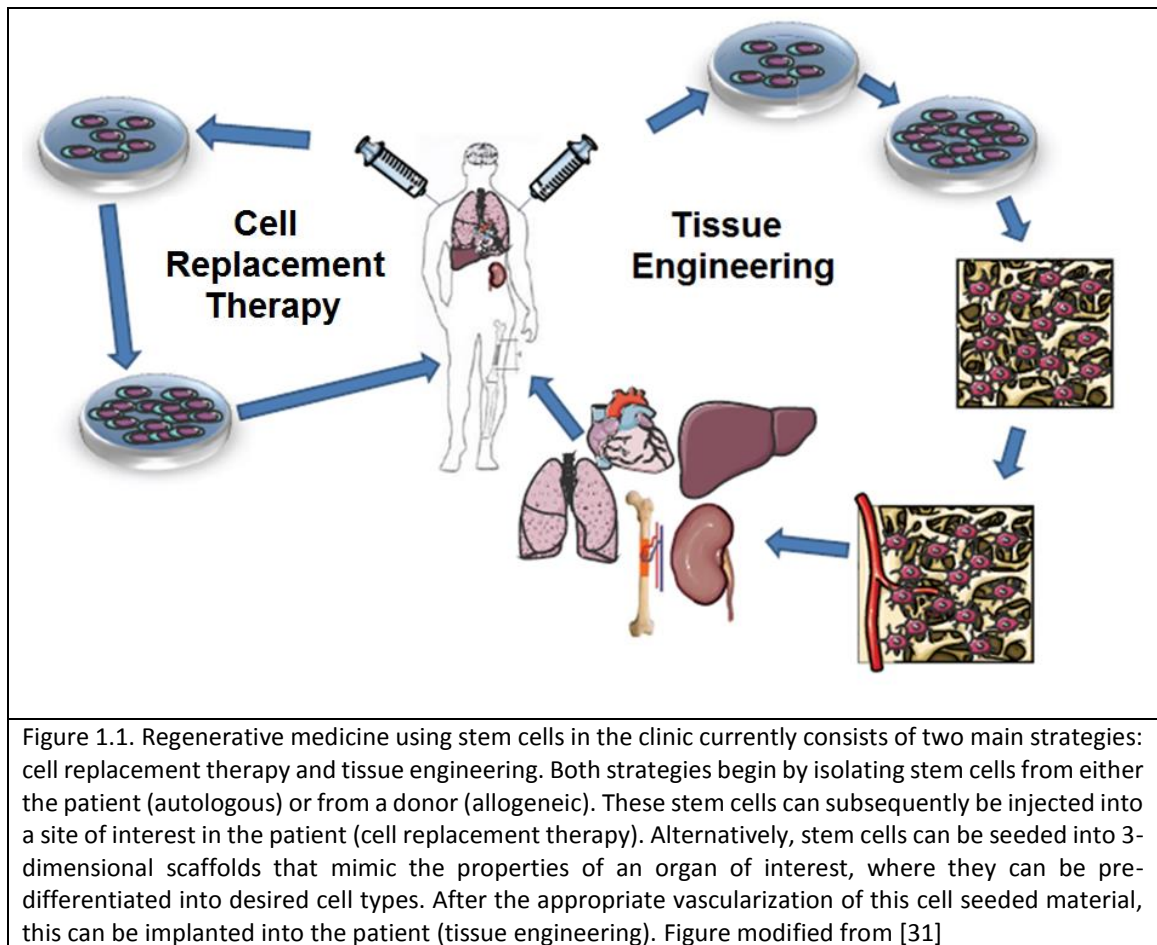
Pluripotent hESCs have been differentiated into retinal pigment epithelium cells and subsequently have been injected into patients with Stargardt's Macular Dystrophy [8]. hESCs have also been used to derive oligodendrocyte precursor cells to inject into patients suffering from traumatic spinal cord injury [9]. However, despite the numerous advantages of hESCs, they will always maintain a politically controversial profile due to ethical concerns regarding their source. Furthermore, they will always be allogeneic to any patient receiving cell replacement therapy using hESCs, thus immunological rejection will always remain an issue.

A less controversial and potentially autologous source of pluripotent stem cells are induced pluripotent stem cells (iPSCs). These are generated from somatic cells and "reprogrammed" into a pluripotent state by transfecting them with a viral vector which causes the upregulated expression of a set of key developmental genes [10]. The practical

logistics involved in the clinical translation of iPSCs involves obtaining a skin biopsy (or similarly easily obtainable cell sample) from a patient with a degenerative disease, reprogramming the patient's cells to a pluripotent state and subsequently directing the differentiation of these cells towards the desired cell phenotype *in vitro*, and injecting these differentiated autologous cells into the degenerated tissue/organ to facilitate normal function. The realization of this approach will have a large impact on modern medicine and greatly facilitate the progression of personalized medicine. However, the current methods of iPSC generation using viral vectors limits their use to *in vitro* settings, for drug/material screening or disease modeling in basic science research.

Thus, due to these current limitations of human pluripotent stem cells, multipotent adult stem cells are much more commonly used in the clinic. The bone marrow is a particularly abundant source for self-renewing stem cells, harboring hematopoietic, endothelial and mesenchymal stem cells [11]. Both hematopoietic and endothelial stem cells are quite limited in their differentiation ability, with the former shown to give rise to all blood cell types [12], and the latter shown to differentiate into endothelial cells [13]. Mesenchymal stem cells, on the other hand, have been reported to give rise to a large range of different cell phenotypes, by having the ability to transdifferentiate into cells of ectodermal [14, 15] and endodermal [16, 17] lineages, in addition to its native mesoderm [18, 19]. Thus, human mesenchymal stem cells (hMSCs) are a particularly attractive source of cells to use in cell replacement therapy, as they avoid many of the issues that accompany using pluripotent stem cells while maintaining a wide range of differentiation ability. Furthermore, their inherent ability to migrate

chemotactically to tissues exhibiting inflammation and injury enables their direct injection into the damaged tissue or into the blood circulation [20]. Moreover, the beneficial effects of cell replacement therapy using hMSCs have already been demonstrated in humans in several clinical cases [7, 21-30]. Thus, it is quite clear that cell replacement therapy has enormous potential to treat a variety of diseases and injuries, and the efficacy and safety of future cell replacement therapy treatments is largely dependent on continually increasing an acute comprehension of the behavior of different stem cells.



1.1.2 Tissue Engineering

Of the many diseases and injuries that regenerative medicine seeks to treat, many cannot be addressed with merely cell replacement therapy. Oftentimes, entire debilitating tissues and organs need to be completely removed and replaced with new tissues/organs. This can be accomplished when functional organs are donated to be transplanted into the patient, but the demand for such organs often greatly outweighs their supply.

To address this imbalance, scientists have worked towards engineering artificial tissues and organs *in vitro* for their ultimate transplantation into patients *in vivo*. Since the conception of the field of tissue engineering [6], scientists have strived to engineer tissues and organs from virtually every part of the human body over the past few decades. Some more prevalent examples include the development of an engineered liver [32], kidney [33], pancreas [34], cornea [35], heart components [36-39], blood vessels [40, 41], bone tissue [42, 43], cartilage [44] and tendons [45], amongst many other tissues and organs. Despite the abundant progress made in the generation of functional neo-tissues, their clinical translation is often impeded due to several limitations.

1.1.3 Current Challenges to Overcome in Regenerative Medicine

Regenerative medicine holds promise to treat a wide range of degenerative diseases and injuries in the future, and virtually eliminate many of the problems which arise from such diseases/injuries. However, prior to its practical and effective clinical realization, several critical challenges to the field must be addressed. First and perhaps

foremost, the safety of any regenerative medical procedure must be ensured. This entails the employment of xeno-free culture conditions, the removal of any residual pluripotent stem cells remaining after directed differentiation to prevent tumor formation, and the appropriate immunomodulation of transplanted cells, as well as the patient, in allogeneic clinical settings [46].

Aside from these safety considerations, reliable cell sourcing is quite important since all cells used in regenerative medicine are the building blocks for successful regeneration. As previously mentioned, different stem cells have varied differentiation and self-renewal capacities. For regenerative medical applications involving autologous cells, their thorough characterization and purification is vital for successful integration, and this must be closely monitored on a case-by-case basis. However, not all degenerating tissues harbor a readily available source for primary cell expansion, which may prompt allogeneic cell therapy as a more viable option [47]. In these cases, a movement toward the creation of universal donor cells that would not be immunologically rejected would be particularly advantageous [48]. One particularly clever study used F(ab')₂ antibody fragments to effectively mask the histocompatibility proteins on the surface of donor cells and prevent their immunorejection upon their transplantation [49]. Regardless of the source, all cells used for regenerative medical treatments in clinical settings require a meticulously comprehensive characterization.

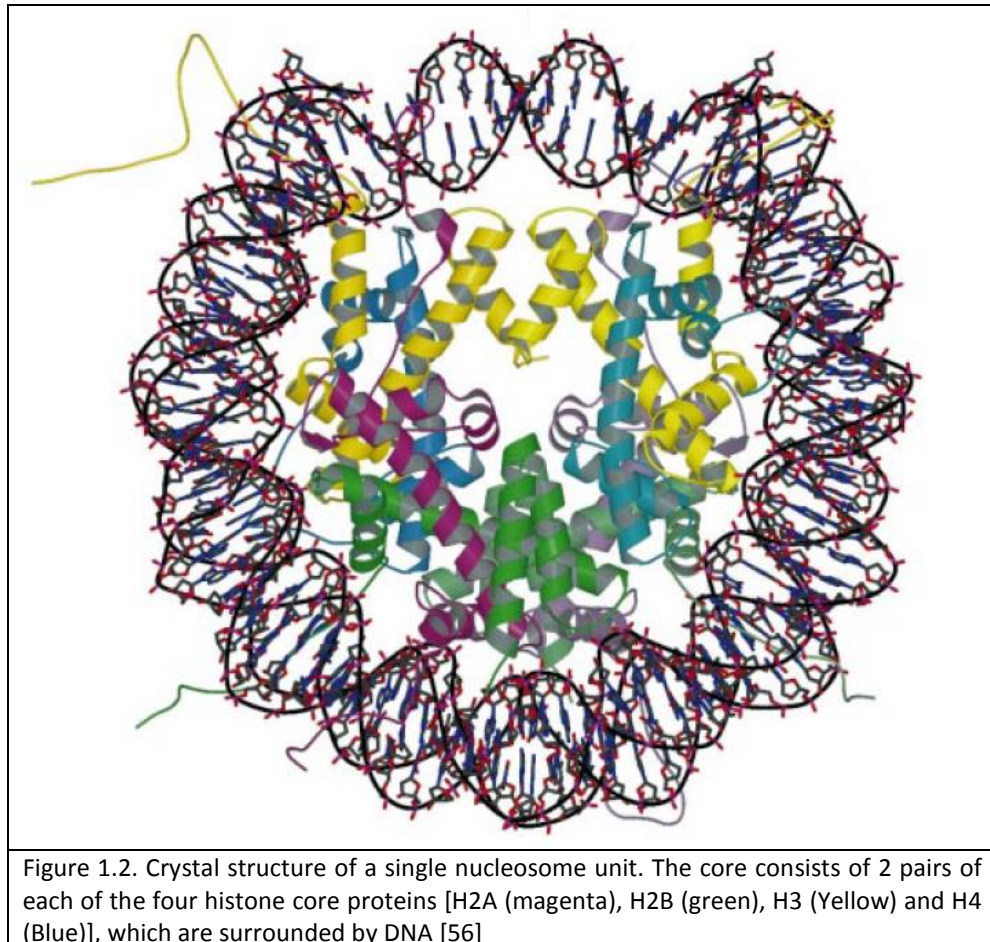
This detailed characterization is also crucial for efficiently controlling the behavior of stem cells, whether it is for maintaining their self-renewal and facilitating their expansion or efficiently directing their differentiation [50]. It is well established that

different gene transcription patterns, particularly involving transcription factors, are a hallmark of establishing a phenotypic identity in stem cells. However, correlating gene expression changes to environmental stimuli merely sheds some light on the downstream changes that occur in response to varied stimuli (i.e. growth factors, drugs/small molecules, materials). The underlying "cause" of these gene transcription change "effects" is believed to be epigenetic modifications that are constantly occurring in chromatin. These modifications are at the root of orchestrating the precise gene expression patterns necessary for the normal development, or maintenance of self-renewal, of stem cells. Thus, a rather large gap currently exists in our ability to have precise control over stem cell behavior; we have correlated many environmental changes to important developmental gene transcription changes, but the causative epigenetic modifications driving these gene transcription changes are still largely obscure. Therefore, it is important to work towards bridging this gap by increasing our comprehension of the dynamic epigenome in response to different environmental stimuli.

1.2 Epigenetic Control of Gene Transcription Regulation

In eukaryotic organisms, the precise spatiotemporal orchestration of gene activation and silencing from a common primary DNA sequence is largely governed by chemical modifications to chromatin, which yield dynamic chromatin structures which regulate accessibility to specific parts of their DNA [51-53]. These modifications are referred to as epigenetic, to the extent that they regulate patterns of gene transcription without actually altering the primary DNA sequence itself [54, 55]. The key to

understanding how epigenetic modifications control gene transcription patterns lies in understanding how chromatin is structured, and how changes to this structure is accomplished to cause downstream changes in gene transcription.

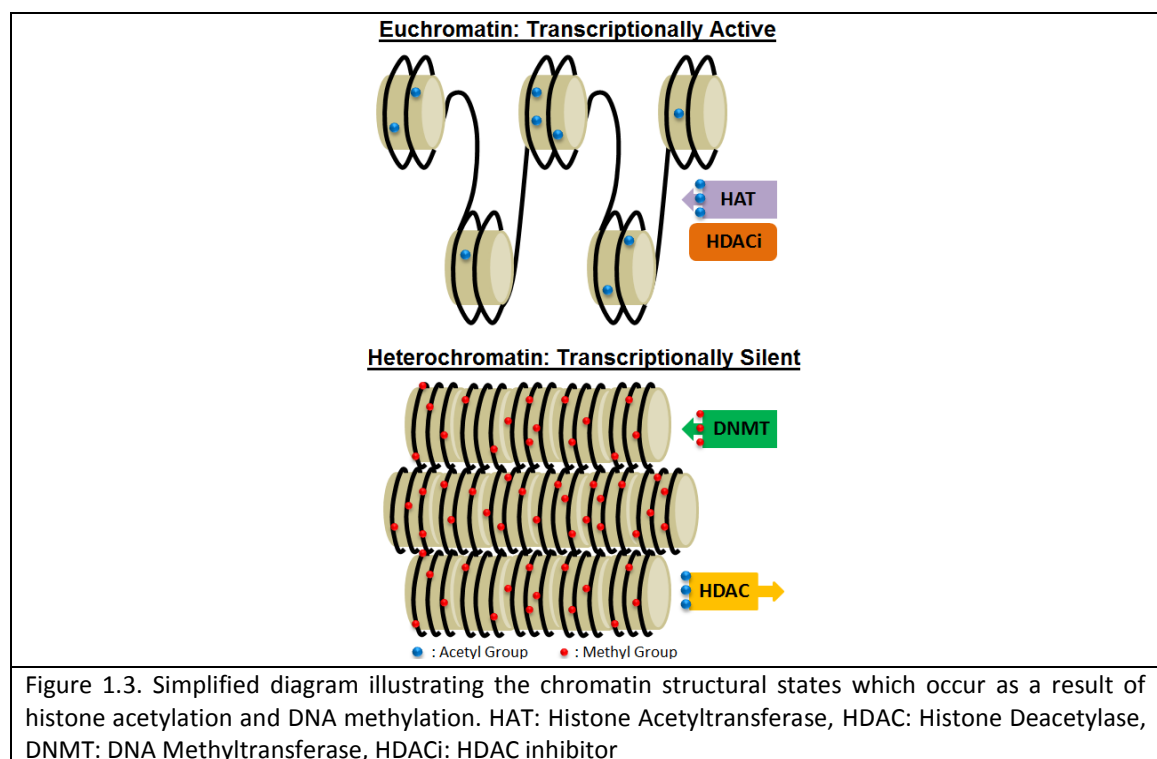


The basic repeat unit of chromatin is the nucleosome, which is comprised of approximately 147 nucleotide base pairs of DNA wound around a histone octamer which consists of two copies of each of the four core histones (H2A, H2B, H3, H4) [57-59](**Figure 1.1**). The charge based interaction between histones and their surrounding DNA allows for chromatin remodeling to different gene transcriptional states [60-62]. The dynamics of these chromatin structures are governed in three main ways: DNA methylation, post

translational modifications (PTMs) to core histones and the activity of chromatin remodeling complexes.

1.2.1 DNA Methylation

When the DNA strand itself is methylated, this causes structural changes to chromatin conformation and subsequently gene transcription activity [63, 64]. Briefly, DNA methyltransferases (DNMTs) catalyze the transfer of methyl groups from S-adenosyl-methionine to the C-5 position of cytosines on DNA [65]. This methylation occurs in regions of DNA which contain a high frequency of cytosine nucleotides adjacent to guanine nucleotides,



known as CpG islands [64]. Global hypomethylation in CpG-devoid regions has been shown to promote an “open” chromatin conformation, called euchromatin [66]. Conversely, CpG-island hypermethylation at the promoters of key developmental genes

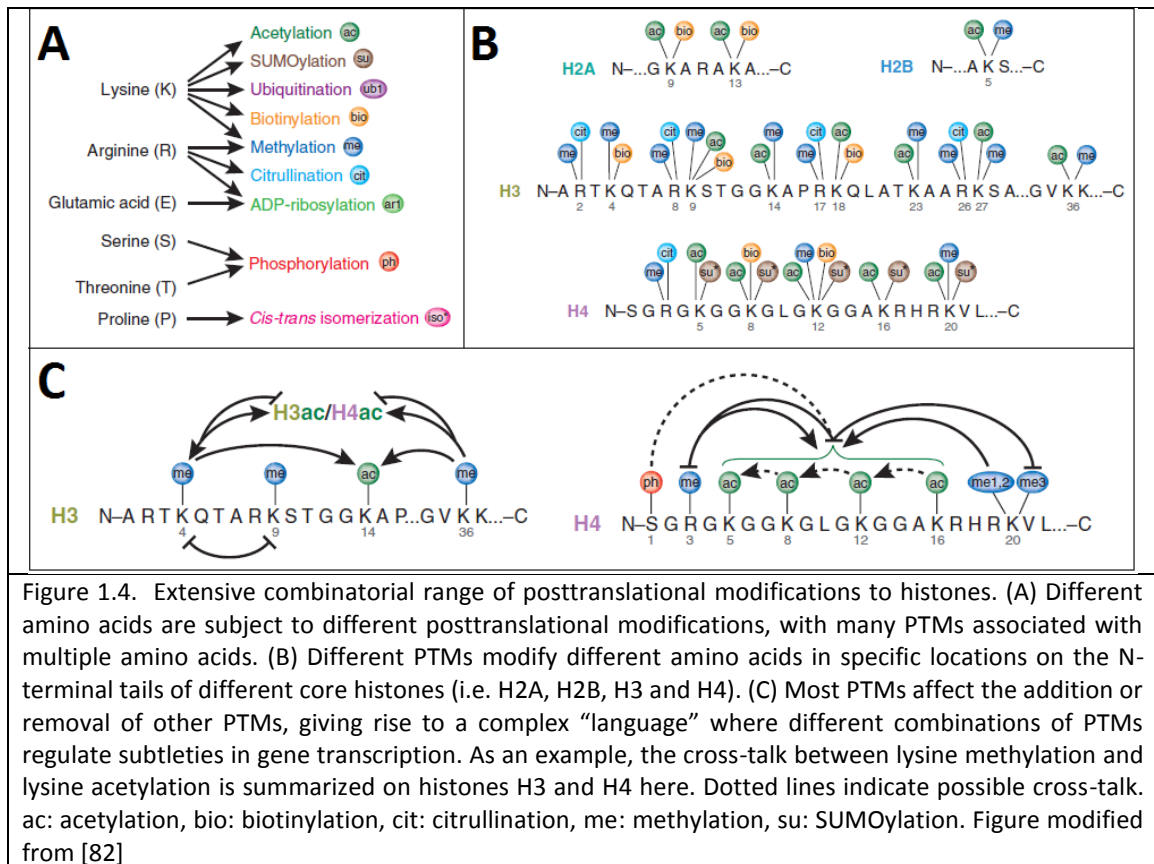
results in a “closed” chromatin conformation, called heterochromatin, and a subsequent silencing of these genes [67, 68]. Since DNA methylation causes changes to the charge of DNA, which impacts the interaction between DNA and the histone core, this methylation is eventually manifested in structural changes to chromatin [69, 70].

1.2.2 Posttranslational Modifications to Histones

Compared to DNA methylation, posttranslational modifications (PTMs) to the core histone proteins are much more complex. Aside from methylation, there are many other chemical modifications that occur to different amino acid residues on histones, including acetylation [71], phosphorylation [72], ubiquitylation [73], sumoylation [74] and biotinylation [75, 76], amongst others [77, 78]. Different combinations of PTMs occur on select amino acid residues in each of the four core histones which make up the core of the nucleosome, all of which combinatorially contribute to different subtle structural changes which influence the accessibility of the surrounding DNA to transcriptional machinery [79]. The finding that certain PTMs influence the addition or removal of other specific PTMs has led to the hypothesis of a “histone code,” where complex combinations of PTMs translate to specific combinations of gene activation or silencing [80] (**Figure 1.4**).

This rich PTM language enables a large range of dynamic chromatin structures largely by causing subtle changes to the charge interaction between DNA and the histone core. PTMs to histones can reduce their positive charge, causing a reduction in the force of attraction between the core histones and their surrounding negatively charged DNA phosphate backbone. This results in the loosening of the DNA around the histones

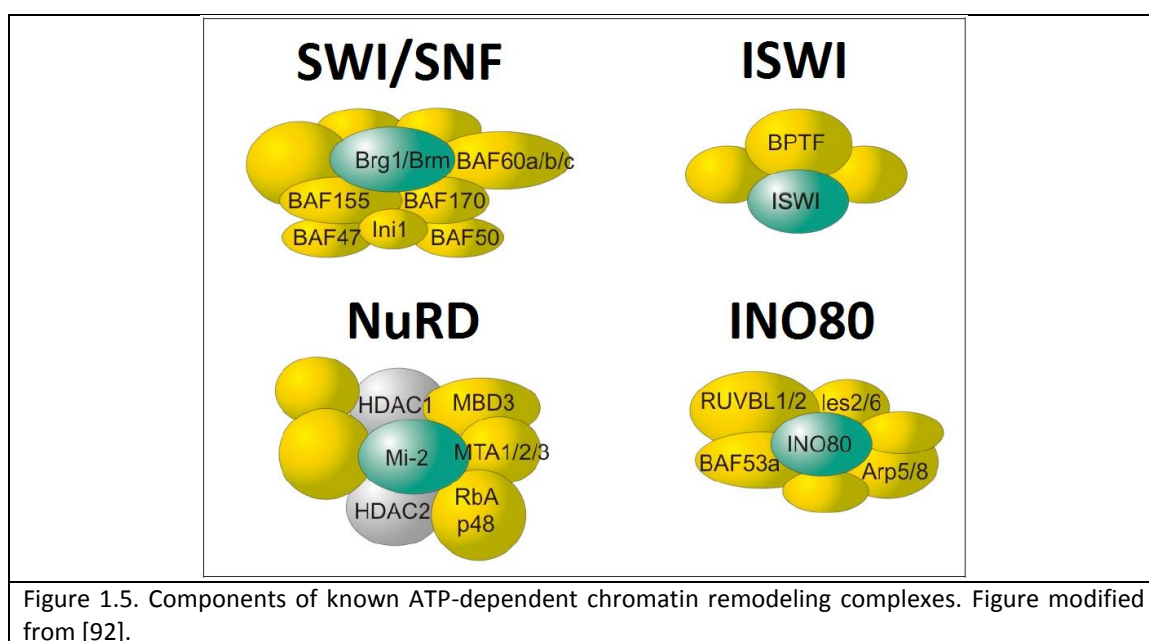
towards euchromatin, which is more accessible to transcriptional machinery and assumes a transcriptionally active state. In contrast, PTMs can also restore or increase the positive charge of the core histones, which promotes a strong attraction with the negatively charged DNA, resulting in a closed heterochromatin structure, which is less accessible to transcriptional machinery and therefore assumes a transcriptionally silent state [60, 81] (Figure 1.2).



1.2.3 ATP-Dependent Chromatin Remodeling Complexes

In addition to covalent modifications to amino acid residues on core histones, nucleosome structure is actively altered by specialized multi-protein complexes referred to as chromatin remodelers [83, 84]. These complexes are able to non-covalently

manipulate chromatin structure by mobilizing and expelling histones to regulate access to the DNA [85]. All identified chromatin remodeling complexes are powered by ATP hydrolysis, as they contain a catalytic ATPase subunit which is similar to known DNA-translocating motor proteins, which implicates DNA translocation to be a part of their mechanism of action [86]. To date, five families of chromatin remodeling complexes have been identified and classified based on their protein composition and functional roles: SWI/SNF [87], ISWI [88, 89], NuRD [90] and INO80 [91] (**Figure 1.5**).



Each of these complexes have been shown to participate in a wide range of biological activities, including DNA elongation [93], double strand break repair [94], cellular development and differentiation [95], transcriptional activation [96] and tumor suppression [97], amongst many other roles [98-103]. Thus, in combination with posttranslational modifications to histones and DNA methylation, chromatin remodeling contributes to directing the dynamic nucleosome which specifies and regulates desired patterns of gene transcription for the navigation of cellular behaviors.

1.2.4 Chromatin Structural Dynamics Navigate Cellular Differentiation

It is clear that epigenetic modifications which produce dynamic chromatin structures are at the heart of gene transcription regulation. One theory posits that this chromatin structure may be part of a heritable epigenetic memory that influences the promotion or silencing of key developmental genes in descendant cells [104-106]. Indeed, evidence has been found for the residual retention of DNA methylation signatures from somatic cell types of different germ lineage origins reprogrammed to a pluripotent state [105]. The notion that various epigenetic marks are inherited as naïve stem cells develop and differentiate down specific lineages suggests that these very marks are vital for their proper development. In support of this theory, several studies have investigated and reported on the link between chromatin structural dynamics and cellular differentiation [107-112].

Embryonic stem cells have been demonstrated to undergo both global and gene-specific remodeling of chromatin structure in order to cease self-renewal and initiate differentiation [113]. For example, key regulator genes for the neural induction of ESCs exhibit high levels of the PTMs H3K9ac and H3K4ac at their promoter regions [114]. Once ESCs commit to a germ lineage, their histones are further posttranslationally modified to direct them towards specific cell subtypes, as histone deacetylation was reported to be critical for the timing of myelin-forming oligodendrocyte differentiation from ESCs [115]. EZH2, a critical component of the polycomb repressor complex and the enzyme responsible for the trimethylation of lysine 27 on histone 3, was shown to be

downregulated as ESCs stop proliferating and begin to differentiate [116]. During hematopoiesis, hematopoietic progenitor cells have been reported to exhibit specific patterns of hyperacetylation and methylation on histone 3 which trigger the activation of human globin promoters during their development [117]. In the development of the heart, distinct epigenetic patterns were found to be correlated with stage-specific expression of genes associated with heart development and cardiac function [118]. Furthermore, aberrant patterns of histone lysine methylation have been linked to perturbed development in ESCs [119], further confirming the vital role of appropriate epigenetic modifications for normal development.

Not only is chromatin remodeling important for the appropriate directed differentiation of stem cells, but it is also critical for the maintenance of their stemness. One study reports that a component of the NuRD chromatin remodeling complex was found to be required for the maintenance of pluripotency in ESCs [120]. The acetylation patterns on histones was also found to be critical for proper proliferation and stemness maintenance, with a decrease in global acetylation and an increased activity of the histone deacetylases 1&2 (HDAC1&2) leading to increased proliferation and pluripotency maintenance [121]. The trithorax group protein, Ash2l, was reported to contribute embryonic stem cell stemness maintenance via the trimethylation of specific locations on histone 3 lysine tails, which is generally a trait of gene activation and open chromatin structure [122]. However, the language of the “histone code” is not as simple as the presence/absence of activating marks leading to one behavioral outcome, and the presence/absence of silencing marks leading to an opposing outcome. Some recent investigations into the role of lysine-

specific demethylase 1 (LSD1) have shown its role in navigating embryonic stem cell development via the demethylation of lysine tail residues on histone 3 [123, 124]. And aside from these specific examples, there have been a plethora of other studies investigating different histone modifications, chromatin remodeling factors and DNA methylation regulation that influence this balance between self-renewal and differentiation in pluripotent stem cells [125-134].

Thus, it is quite clear that the epigenome plays a vital, complex role in navigating cellular behavior throughout development. Therefore, there are tremendous insights that can be gained from not only investigating how this epigenetic plasticity drives cellular differentiation, but also from understanding how the immediate microenvironment of a naive stem cell influences this epigenome, and subsequently the resultant gene transcription patterns and behavior of the cell.

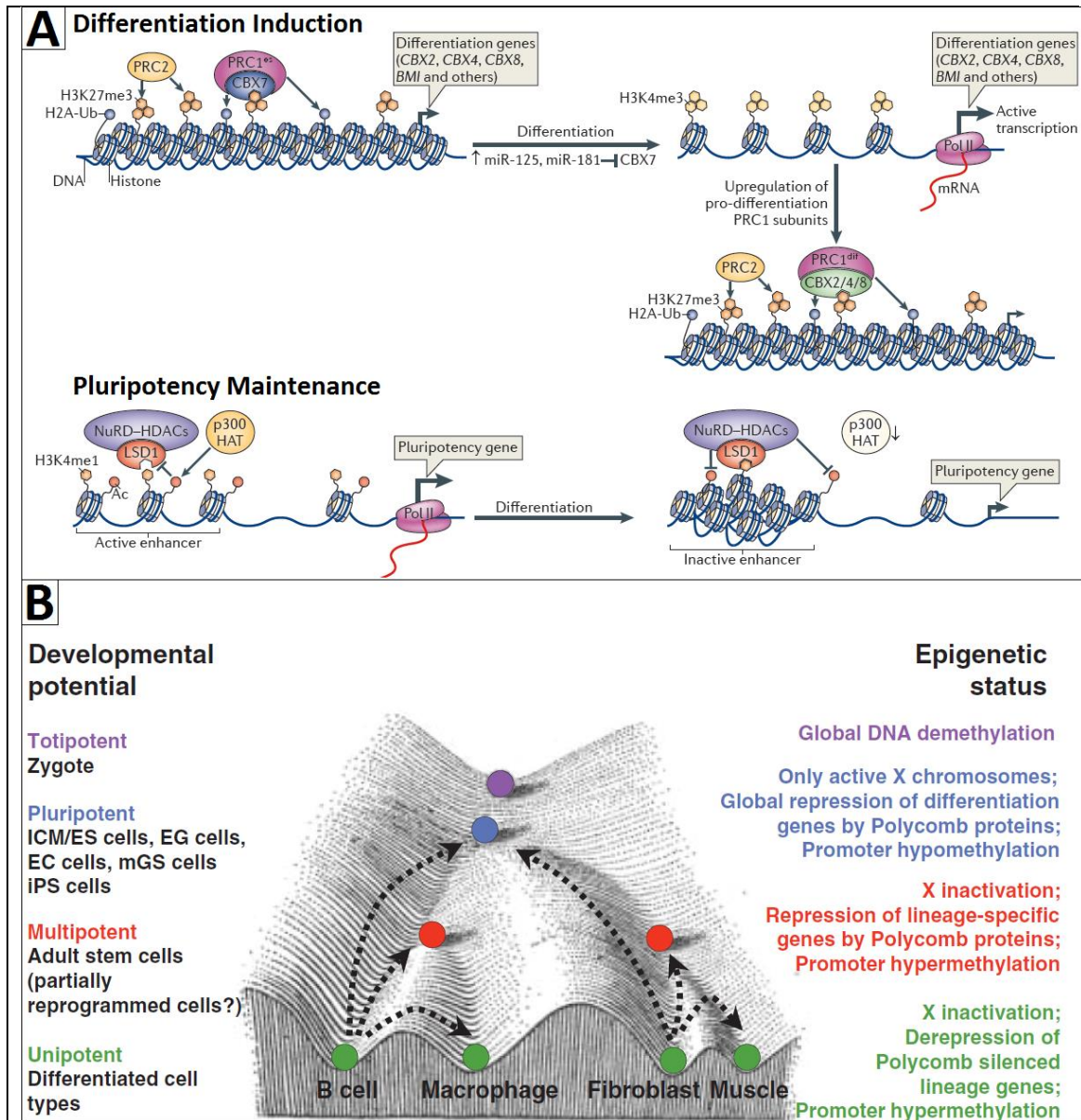


Figure 1.6. Epigenetic mechanisms are at the root of navigating the balance between pluripotency and differentiation. (A) Schematic of some key PTMs and protein complexes that regulate chromatin structure and subsequent gene transcription. Polycomb repressive complexes (PRC) auto-regulates differentiation associated CBX proteins and represses developmental regulators. Desired genes for a specific lineage are largely turned on via H3K4me3 activation, while other undesired genes are largely turned off via PRCs and H3K27me3. On the other hand, pluripotency is largely maintained via Lys-specific demethylase 1 (LSD1) and NuRD chromatin remodeling complex, which work together to demethylate H3K4 and inactivate enhancers of undesired differentiation genes. Figure modified from [131]. (B) Waddington's epigenetic landscape schematic relating cell phenotypes at different developmental stages (left) and their respective epigenetic states (right). Cell phenotypes have not only been found to transdifferentiate (i.e. from one phenotype to another (green circles)), but have also been shown to reprogram to a less committed developmental state, even to the point of pluripotency (blue circle). Figure from [135]

1.2.5 Environmental Influences to Chromatin Structure

It is well established that there are ideal physical and chemical properties of a cell's substrate that are optimal for maintaining its health and functionality. From a broad perspective, every tissue and organ in all mammalian organisms rely on this fact. There are a wide range of different attributes of these substrates that contribute to influencing cellular behavior, and they can be grouped in a general sense into mechanical, topographical and chemical properties.

It is evident from nature that there is quite a large range of mechanical properties found in different tissues, each of which is optimal for its respective maintenance and function. As an example, osteoclasts and osteoblasts maintain proper bone functionality only in the rigid environment in which bone thrives [136, 137]. Similarly, neurons and glia develop and maintain functionality in the softer, highly elastic environment of the brain [138-140]. This differential development and functionality is possible since cells have the ability to monitor and respond to the stiffness of its microenvironment via sensors that are studded throughout the cell body. This causes changes to protein signaling cascades throughout the cell body, which directly affect cytoskeletal organization and indirectly affect gene transcription patterns. These facts inspired the work of many scientists to investigate the quantifiable properties of substrates of varying matrix elasticity and correlate this with specific lineage specification patterns in stem cells [138, 141]. One group investigated a variable Young's modulus hydrogel system and found that softer gels of 0.1-0.5 kPa yielded neurons, whereas stiffer gels of 1-10 kPa yielded glial cultures from adult neural stem cells [142].

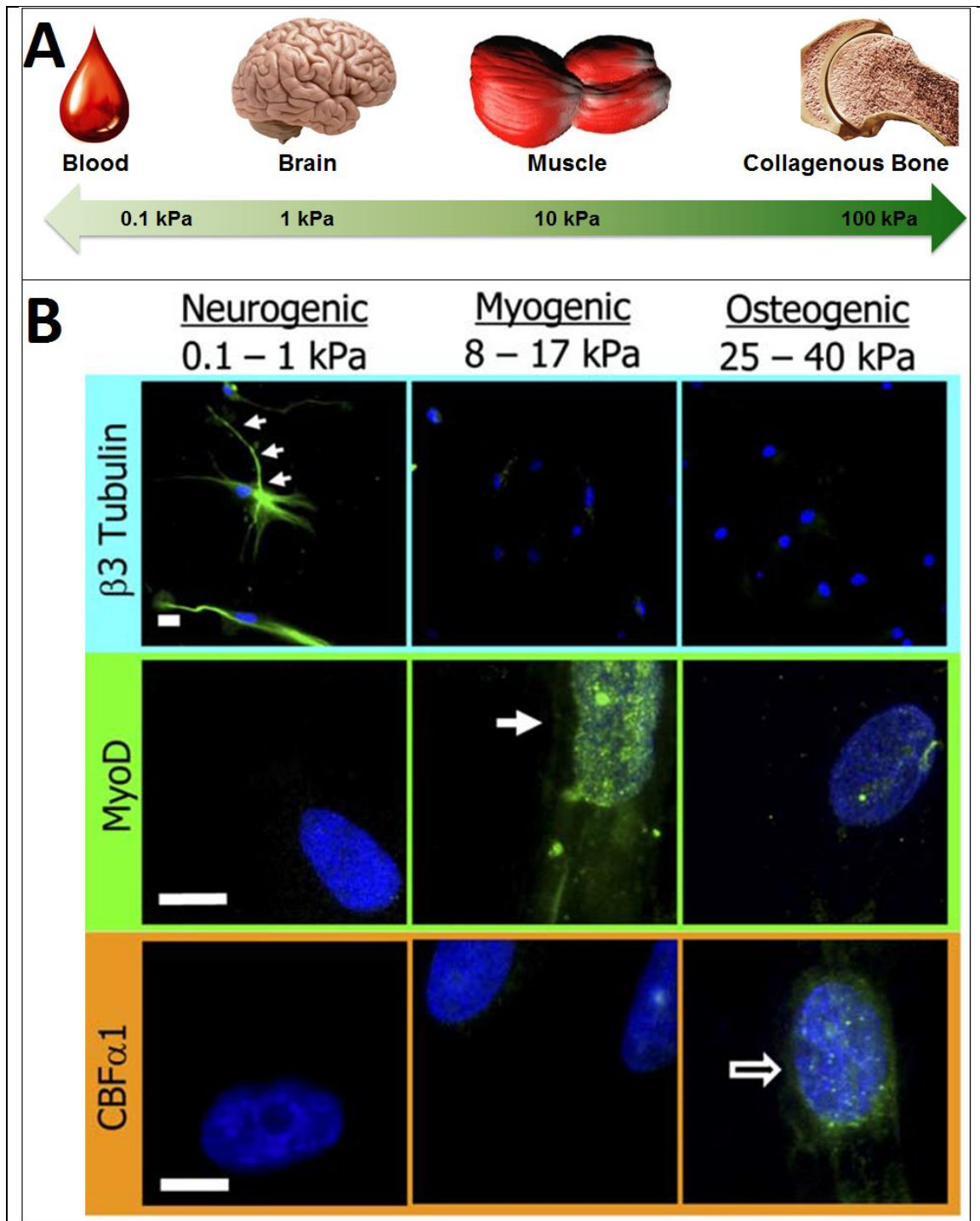


Figure 1.7. Mechanical properties largely influence stem cell differentiation. (A) There is a large range of mechanical properties in the environments occupied by the many different functionally distinct cellular phenotypes, ranging from fractions to hundreds of kPa's. (B) Matrix elasticity alone influenced naïve MSCs to differentiate towards neurogenic (0.1-1 kPa), myogenic (8-17 kPa) and osteogenic (25-40 kPa) lineages, as assessed by immunofluorescence of their corresponding biomarkers [138].

Another group reported that matrix elasticity provides mechanical cues that are vital for angiogenesis [143]. And aside from these examples, there have been countless other reports on the critical link between the mechanical properties of a cell's microenvironment and its subsequent behavior [144-153].

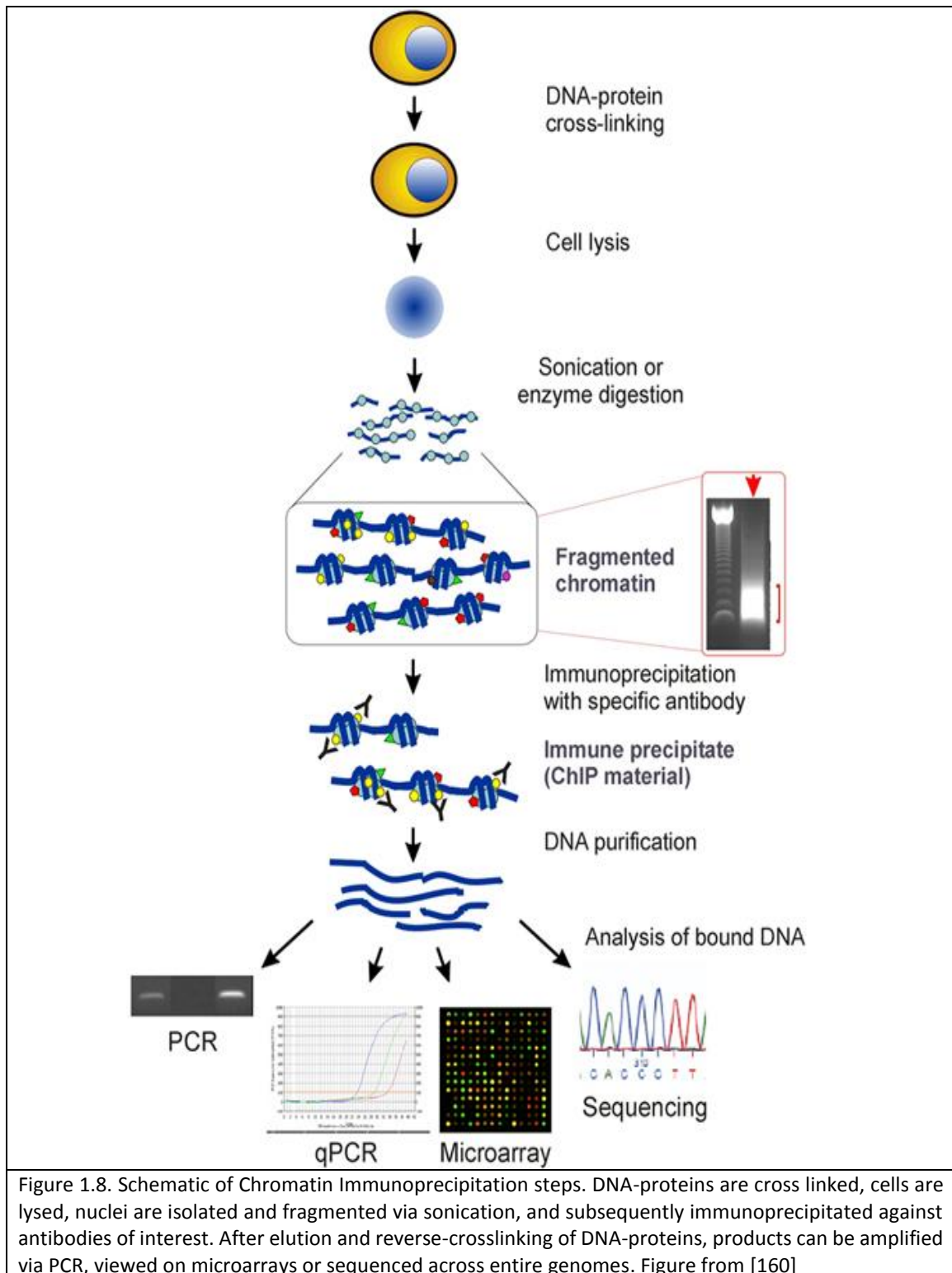
Beside mechanical stiffness properties, the geometric / topographic attributes of a stem cell's microenvironment also largely influence its development. Many studies have investigated geometric/topographic properties of different biocompatible materials and how they impact cellular behavior. The range of different materials and devices fabricated for this purpose is wide, from magnetic microposts used to measure traction forces and focal adhesions [154], to titanium nanopillars of varying heights and patterns [155], to distinct patterns and shapes carved from PDMS slabs [156], to slide-size chips containing over 2,000 different mathematical algorithm guided random surface features produced on poly(lactic acid) [157]. However, a common aspect of most of these studies is the type of data that is acquired; a quantitative assessment of how cells respond to these different materials is usually made by probing a "downstream" reporter, whether it is protein/gene expression changes, cell viability and proliferation, metabolomics, or other downstream effects. All of these consequential changes in cell behavior are ultimately orchestrated by specific instructions indicating which combinations of genes are activated or silenced spatially and temporally, which is largely regulated and directed by epigenetic mechanisms. Thus, an increased understanding of how specific epigenetic marks orchestrate desired gene transcription programs can allow for an unprecedented degree of control over cellular behavior.

1.2.6 Current Approaches to Interrogate the Epigenome

Currently, there are two main biochemical approaches to interrogating the complexities of the epigenome: (1) Gene expression quantification associated with specific chromatin modifiers using chromatin immunoprecipitation (ChIP) [158], (2) PTM identification and distribution assessment based on mass/charge separation using mass spectrometry [159]. While each of these powerful techniques provide extensive data relevant to characterizing the epigenome, they are usually conducted independent of each other and thus are each lacking critical pieces to the puzzle of demystifying epigenetic gene regulation.

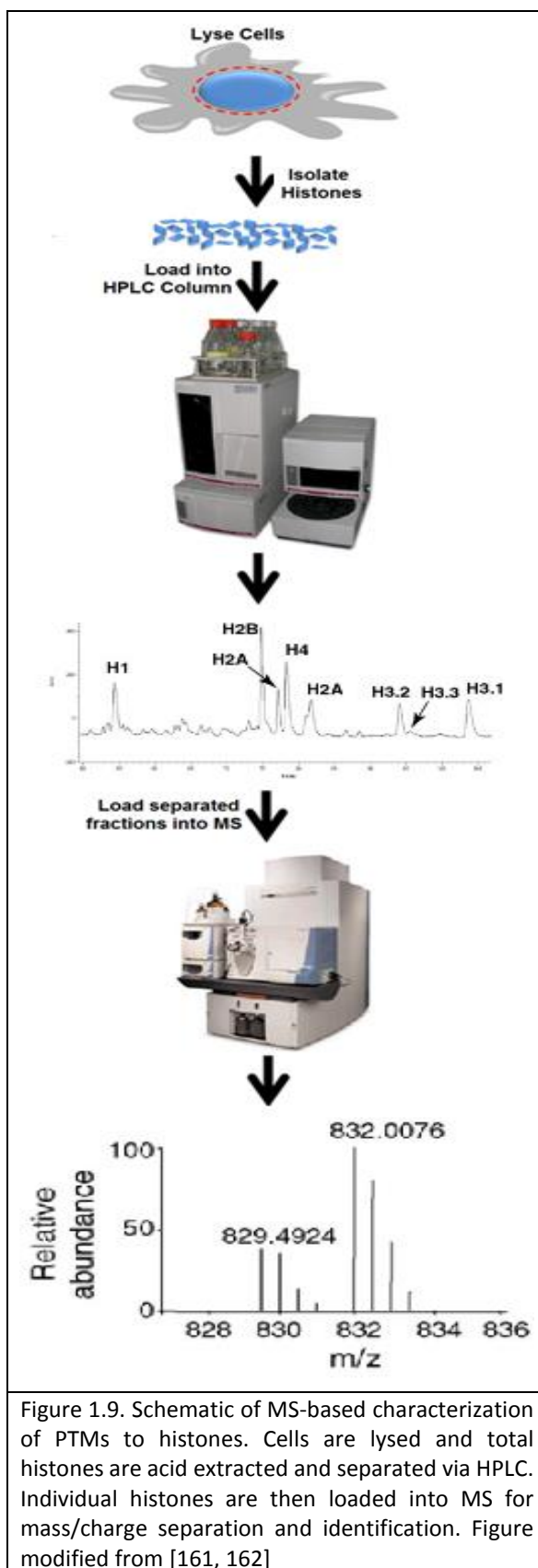
The principle of chromatin immunoprecipitation is based on determining the relative amounts of DNA/protein interactions. This is accomplished by isolating chromatin from cells or tissues, fragmenting this DNA into manageable size lengths suitable for the application of interest (i.e. 200-500 bp for qRT-PCR amplification and smaller fragments for deep sequencing), and then immunoprecipitating these DNA fragments against antibodies of interest (**Figure 1.3**). The integrity of any data that is produced from ChIP relies heavily on the quality of the antibodies used. In general, most antibodies that are commercially available are not suitable for ChIP applications, as most antibodies targeting PTMs to chromatin are produced specifically for ChIP, and are thus categorized as “ChIP-grade.” [163] An additional concern is epitope occlusion, which is the ability of certain unwanted PTMs to block the intended recognition of a PTM by a site-specific antibody, and this may cloud ChIP data particularly on histones highly decorated with PTMs [162].

Despite these concerns, ChIP, and assays based on ChIP, are currently the only ways to quantify gene expression levels associated with specific PTMs. When ChIP



is coupled to genomic sequencing (ChIP-seq), one is able to quantitatively investigate the relative expression of genes associated with a PTM at a remarkably high resolution across entire genomes [164].

On the other hand, mass spectrometric approaches to interrogating the epigenome are unbiased and avoid any issues that arise from using antibodies. This approach first involves isolating chromatin, acid extracting whole histones, separating histone fractions on a High Performance Liquid Chromatography (HPLC) column, and subsequently separating and identifying PTMs decorated on these histone fractions based on their m/z ratio [161] (**Figure 1.4**). This technique has been successfully used to discover several novel PTMs that have since been strongly tied to regulating the transcription of



certain genes [162, 165, 166]. In addition, this approach has revealed the combinatorial nature of PTMs, where certain PTMs only occur in the presence of others [167]. However, certain PTMs are extremely similar in mass, which makes their accurate separation and identification difficult without highly sensitive and precise state-of-the-art instruments. For example, the difference between an acetylation and a tri-methylation is merely 36 millidaltons [168], which can be quite difficult to discern using less sensitive mass spectrometers. Furthermore, mapping PTMs from isolated histones provides no direct information regarding the genes that these PTMs regulate.

Perhaps the greatest drawback of both of these methods is the fact that both require the lysis and destruction of a relatively large number of cells. Since chromatin is rapidly dynamic in real time, much of its' structural subtleties may be lost upon lysis. Moreover, due to the heterogeneous nature of undifferentiated stem cell populations, these population based approaches produce data that is inevitably cluttered with artefacts. Thus, the need for and potential benefits from epigenetic investigations is warranted and has the potential to address many previously unanswered questions regarding the subtleties of epigenetically induced stem cell development.

1.2.7 Current Approaches for Characterizing Chromatin Structural Organization

Due to the large spatial organizational implications of chromatin structural influences on transcriptional regulation and gene expression, there has been much investment and interest in the development and employment of methods to increase our

collective comprehension of nuclear architecture. There have been numerous investigations to this end, employing a wide range of non-optical, charge-based imaging techniques to resolve specially prepared subcellular structures, , fluorescent labeling methodologies to localize specific DNA sequences, and biochemical approaches to probe long range DNA interactions coupled with state-of-the-art DNA sequencing techniques. Some of the more prominent efforts to date will be summarized here.

Over the past century, the resolution of structural biology details at the atomistic and molecular level has been mainly accomplished using x-ray crystallography. Continual improvements in resolution since its conception one hundred years ago has led to increased details in the structural interactions and subtle details in configuration of numerous DNA-protein interactions that have provided countless insights for the structural basis for transcriptional control (Figure 1.10). Following the discovery and resolution of how DNA is wrapped around core histone proteins to form the core nucleosome particle at 7 angstroms in 1984 [170], this ignited a somewhat exponential

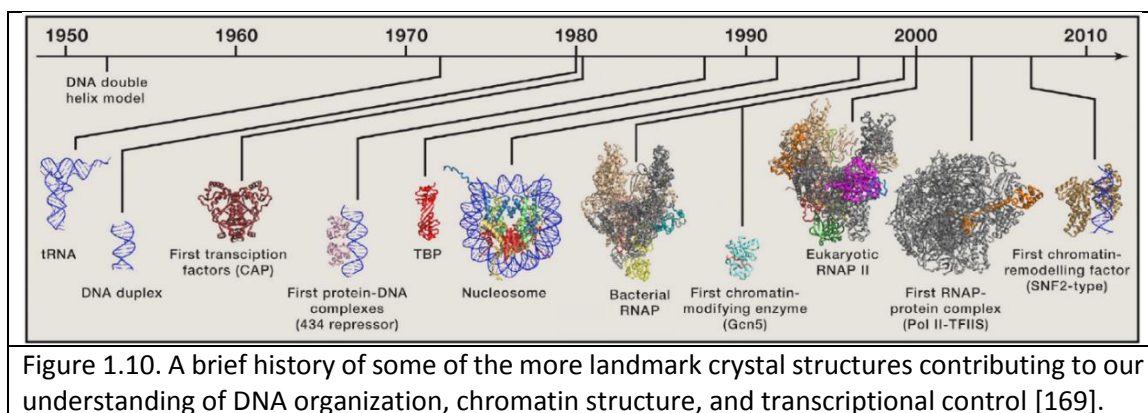


Figure 1.10. A brief history of some of the more landmark crystal structures contributing to our understanding of DNA organization, chromatin structure, and transcriptional control [169].

progress for unraveling the structural perspective of gene transcription, with a more detailed 2.8 angstrom resolution achieved in 1997 [57], and interactions between nucleosomes to compose chromatin in 2005 [171]. Electron microscopic investigations complemented these structural investigations, speculating on the arrangement of chromatin fibers and these implications for transcriptional control [172, 173]. In summary, these non-optical, high-resolution imaging techniques have proved invaluable for the advancement of our comprehension of DNA organization and transcriptional control. However, these techniques always require the destruction and careful preparation of subcellular components for analysis, thus making these approaches impractical as quick, simple tests to assay cellular responses to multiple adjustable parameters of controlled environments.

Developments in optical microscopic techniques to map the loci of chromosome territories has been accomplished via 3D Fluorescence *in situ* hybridization (FISH). These studies suggest that higher-order arrangements of chromatin may be phenotype specific, and are certainly reflective of where a cell is in respect to its cell cycle [174]. Further speculation into these results indicates that gene rich chromosomes largely occupy the periphery of a nucleus, whereas gene rich chromosomes condense in the interior of the nucleus, which has implications for transcriptional regulation through the spatial organization of chromosomes.

A much more rigorous biochemical approach for understanding DNA:DNA and/or DNA:protein interactions is a technique called chromatin conformation capture. Based

upon the specificity of the data required (i.e. gene quantification via PCR or sequencing), a few varieties of the basic core technique have been developed (Figure 1.11). The

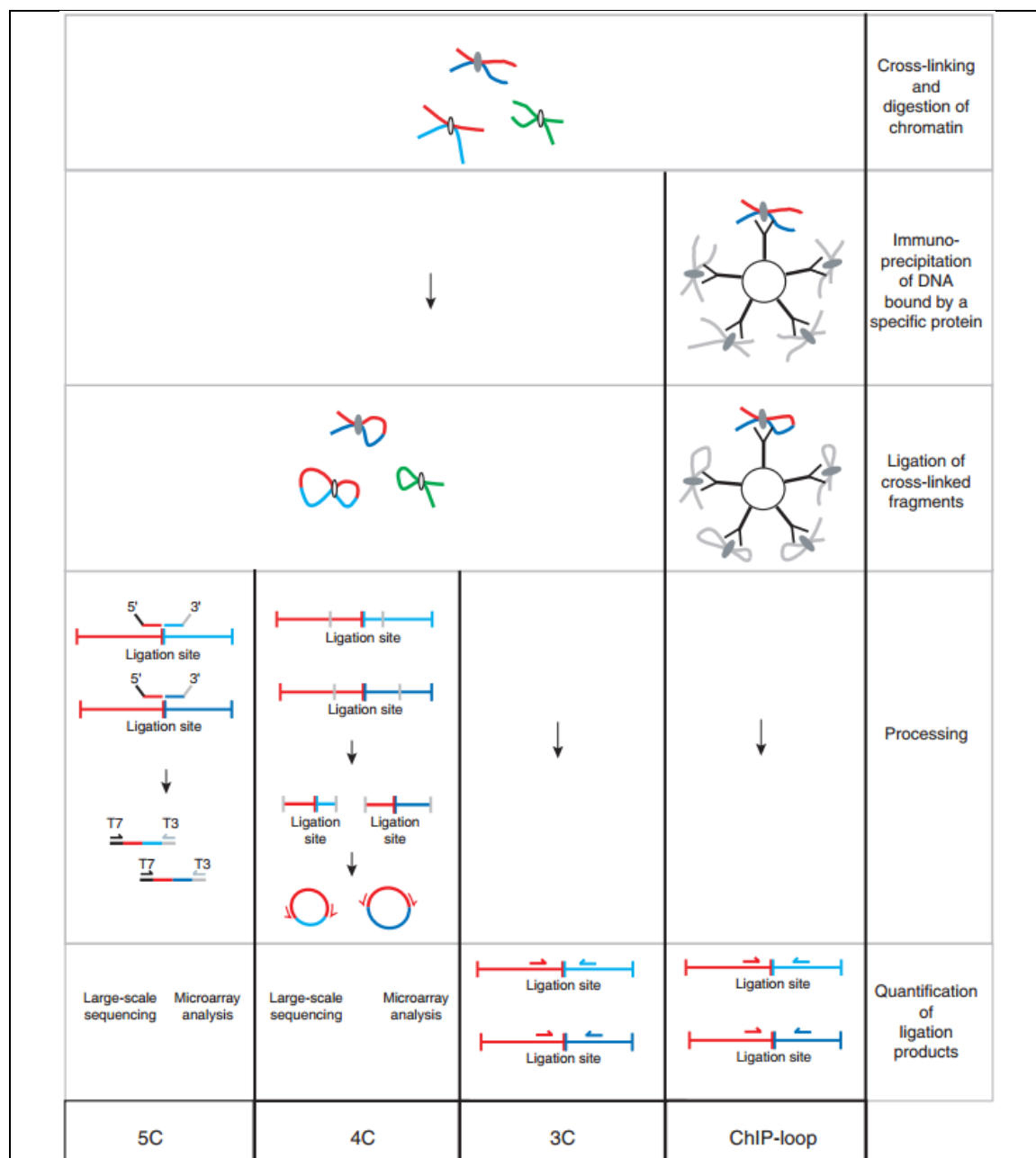


Figure 1.11. Chromatin conformation capture and its varieties. DNA interactions are fixed via formaldehyde treatment, and restriction enzymes digest the DNA to be cut at specific sequences. Ligation is subsequently performed under conditions that favor ligation events to occur between cross-linked DNA fragments. This can then be amplified (3C), processed further with secondary restriction enzymes and ligated again to form circles (4C) or amplified with T3 and T7 primers (5C), after which they can be sequenced. In ChIP-loop, fragments bound by a protein of interest are enriched with antibody beads, and then eluted off and amplified via PCR.

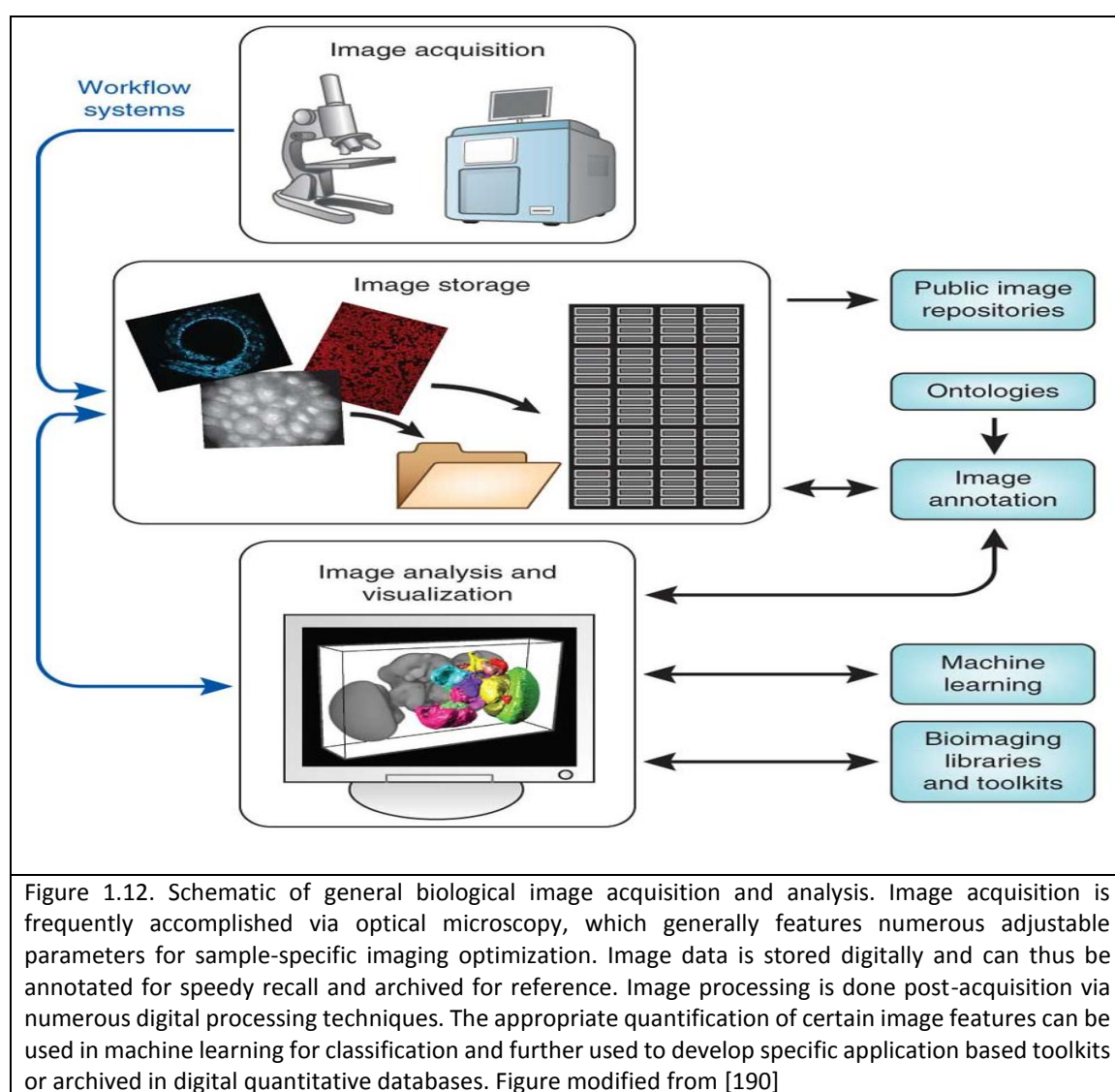
commonality between these variants, and hence the reason they all fit under the same umbrella term, is a formaldehyde based fixation approach to interrogate inter-DNA interactions via a clever approach employing restriction enzymes and ligation of cut DNA ends. This results in a quantitative assessment of where, and relatively how much, two DNA sequences may interact with each other, or when combined with ChIP, how interacting DNA sequences interact with a protein. Although this approach does not provide any direct structural perspectives on chromatin structure *per se*, it does provide precise quantifications of interacting DNA parts that can be amplified for comparative analysis, or even sequenced and mapped to reference genomes. Taken together, all of the aforementioned efforts to characterize chromatin organizational structure to date have proven to be effective at providing important insights to the spatial organizational control of gene transcription, but are each limited in both scope and degree, and may be impractical as cellular assays to screen a larger number of conditions in high-throughput applications.

1.3 Bioimage Informatics

For centuries now, optical microscopy has provided innumerable and invaluable insights into the complexities of microbiology, which are unable to be viewed by the naked eye. With the advent of super-resolution confocal microscopy, we are no longer limited by the diffraction barrier of light, thanks to several clever methods of improving spatial resolution [175-178]. This has revolutionized our approaches, and expanded the

possibilities, for resolving and investigating structures at the nanoscale, which were previously unresolvable. The combination of high resolution imaging and quantitative modeling has spawned an emerging field, called “Bioimage Informatics,” which is focused on extracting and interpreting quantitative molecular information about cellular and tissue biology and organization from image data [179-181]. Continued progress and investment in this field has inspired researchers to develop several open-source [182, 183] and commercially available image analysis software tools. [184]. Most general image analysis software packages, whether open source or commercial, include several common features that are widely applicable to many different types of biological images. Image feature extraction and selection is a rather basic element of image analysis, as it allows the user to filter pixels/voxels based on specific properties, such as morphological, geometrical and statistical data [185]. Image segmentation is also vital, as it allows the user to pinpoint and focus in on pixels/voxels that are relevant to the research at hand [186]. Image registration allows one to fuse multiple images into a common coordinate system so that you can compare or integrate image data obtained from either different conditions or measurements [187]. Image annotation associates images with metadata, so they are able to be efficiently organized, searched and retrieved [188]. Because of the large volumes of some biological image data, particularly three dimensional image z-stacks obtained from confocal imaging or time-lapse image data monitoring phenomena over long periods of time, automated annotation is critical for the timely retrieval and access of such data. Finally, pattern clustering and classification methodologies are increasingly becoming integrated into image analysis software packages, which allow the

user to detect common patterns in multiple images and use this information to appropriately characterize and classify different objects of interest [189]. This quantitative characterization approach allows one to investigate subtle structural features that may not be immediately evident upon visualization by eye. This technique has been the foundation for several studies that accurately characterized and classified different cell phenotypes based on the immunolabeled expression of specific proteins [191-193].



1.3.1 Quantitative Morphometric Descriptors from High-Content Images

The interdependent nature of structure and function is evident in all living biological organisms. From the micro- (i.e. cellular organelles) to the macro-scale (i.e. whole organs), organisms exemplify, at each level, how structure is vital for the proper function of numerous biological phenomena. Several approaches have sought to extract quantitative information from high resolution images of intracellular organization and use this data to characterize subtleties in the structures of various cytoskeletal proteins in the context of differentiation [191, 193, 194]. The underlying concept of these approaches is fairly straightforward: cells grown in culture or tissues from animal models are immunolabeled for relevant proteins of interest and imaged at high-resolution. After image processing (techniques mentioned in previous section 1.3), quantitative descriptors, which reflect different properties of identified ROIs, are obtained. These can subsequently be used to characterize and classify different cell types, or used as probes to forecast cell behavior when exposed to different environmental stimuli. Early generation descriptor packages included metrics relevant to larger geometric features, such as area, perimeter, diameter and roundness, which were able to forecast, as early as 72 hours, the differentiation tendencies of hMSCs towards adipogenic and osteogenic lineages based on their cytoskeletal organization [191]. These descriptors are quite useful for detecting gross geometrical features for distinguishing and classifying cell body morphology, but when used in the context of nanoscale chromatin structural differences, they were unable to detect differences sufficient for accurate classification. Thus, in order

to apply this approach to more subtle features of protein expression relevant to nanoscale features, the mathematical algorithms that generate quantitative descriptor values must meaningfully reflect these structural complexities. This can be achieved using algorithms based on sliding windows that capture how neighboring pixels relate to one another.

1.3.2 Haralick Texture Features

Even with the advances in optical microscopy with super-resolution instruments achieving nanoscale resolutions [195], we are still only able to resolve a single nucleosome unit to, at best, a single pixel. Therefore, it is not meaningful to focus on single nucleosome units using optical microscopy, but instead, to look for meaningful patterns of the many nucleosome units which are contained in the nucleus, particularly euchromatin to heterochromatin ratios. In order to approach this nanoscale characterization, it is vital to employ quantitative algorithms which are based on sliding windows that move across each and every pixel in an ROI, and assign values based on the relationship between a pixel and its neighboring pixels. This can be achieved by computing angular nearest-neighbor grey-tone spatial-dependence matrices (i.e. grey level co-occurrence matrices), which form the foundation for Haralick textural features [196].

Nearest-neighbor pixels are spatially distinguished based on their angular relationship to the pixel of interest; for example, a single pixel has a total of eight surrounding nearest neighbors, with the two pixels to the immediate left and right of a

pixel as 0° nearest neighbors, whereas the pixels to the immediate top and bottom are designated as 90° , and the two sets of pixels on the corners are 45° and 135° (**Figure 1.13**). Haralick texture features take these angular relationships into account and compute values based on pixel intensities and the distances between different intensities [196].

After the generation of such grey-tone spatial dependence matrices from high resolution images, we can begin to compute textural features based on the following equations (Table 1.1).

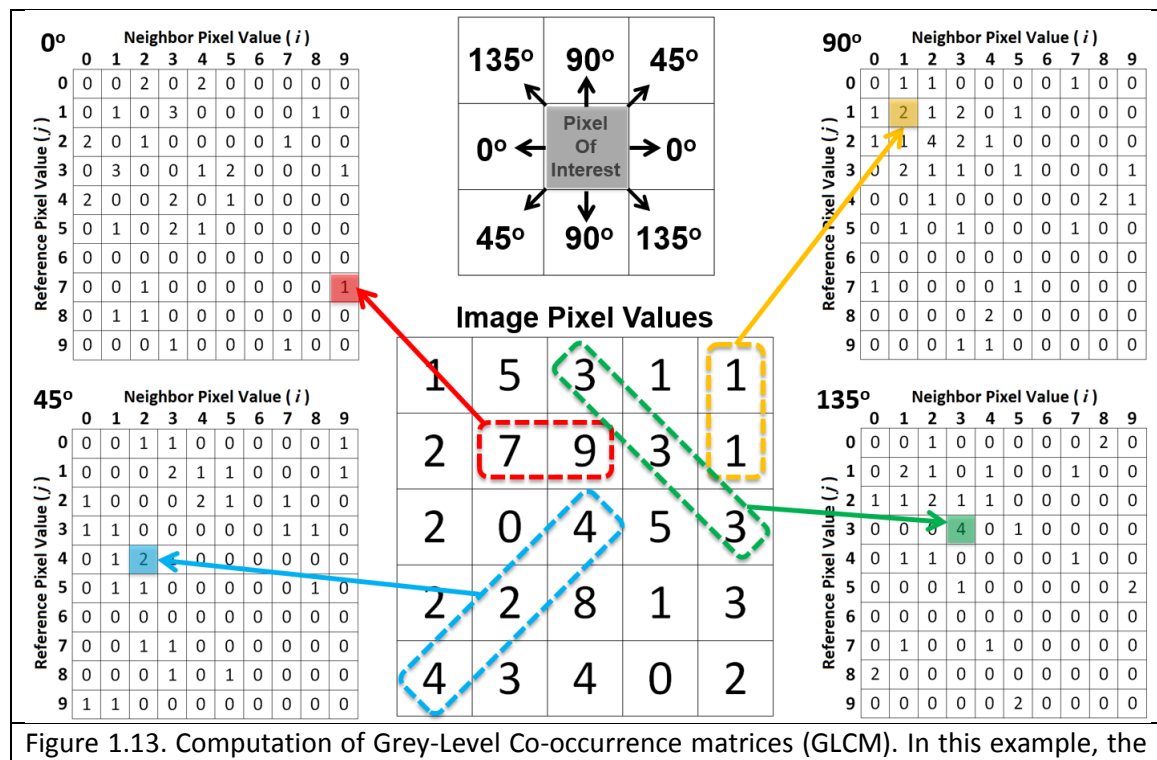


Figure 1.13. Computation of Grey-Level Co-occurrence matrices (GLCM). In this example, the image pixel values are used to form GLCMs based on the frequency and angle where two numbers co-occur (several examples are shown). These GLCMs then form the basis for the computation of Haralick texture features. For simplicities sake, in this example, the ROI is only a 5x5 area (25 pixels), and the pixel range is only from 0-9, but for the high-content analysis of nuclei performed in this thesis, the ROI is much larger (a few million), and the pixel range is from 0-255.

Each of these thirteen features is computed for two different distance measures of spatial dependence matrices (1 & 2), and three additional higher moment statistical values (standard deviation, kurtosis and skew), for a total of $13 \times 2 \times 4 = 104$ descriptors. Once these large quantitative data sets are obtained, they can be further mined and analyzed with a number of data analysis approaches, including dimensionality reduction analysis, data mining for feature selection and extraction, identification of relative influence of each descriptor relative to one another based on the formation of principal components by identifying the coefficients to the eigenvectors along each principal component, and k-means cluster analysis to identify the mean spatial proximity centroid of a group of nuclei.

Descriptor	Equation	Intuitive Description	H3K4K27me3 Organization
Entropy	$\sum_{i,j} P_{i,j} \log P_{i,j}$	Measure of randomness of GLCM values High entropy: large variations in GLCM values extracted from an image Low entropy: increasingly homogenous GLCM values	Orderly patterns of H3K4K27me3 that tend to repeat throughout the nuclear space will yield lower entropy values, whereas greater disorder and variation yield higher entropy values.
Energy	$\sum_{i,j} P_{i,j}^2$	Measure of homogeneity of GLCM values High energy: increasingly uniform distribution of GLCM values from a ROI Low energy: increasingly heterogeneous GLCM values	Repeating patterns of pixel values and general uniformity throughout the nucleus yield higher energy values, whereas lack of uniformity yields lower energy values
Inertia	$\sum_i \sum_j (i - j)^2 (P_{i,j})$	Measure of variations present in local regions of contrast High inertia: higher spatial frequencies corresponding to large differences in a contiguous set of pixels Low inertia: lower spatial frequencies	Greater contrast in small ROIs throughout the nucleus will yield high inertia values, whereas a lack of contrast in such ROIs will yield lower inertia values. Thus, high differences between inertia values of H3K4me3 and H3K27me3 indicate a shift in balance towards one mark over the other and a lack of bivalency, whereas smaller differences reflect increasing bivalency
Inverse Difference Moment	$\sum_{i,j} \frac{P_{i,j}}{1 + (i - j)^2}$	Measure of local regions of homogeneity High IDM: Higher presence of locally uniform windows in GLC matrix Low IDM: Higher presence of locally heterogeneous windows in GLC matrix	Similar to energy, IDM is a reflection of the presence or absence of uniformity, but it is sensitive to smaller regions throughout the nucleus. Thus, "clusters" of uniformity of H3K4K27me3 will yield high IDM values, whereas a lack of uniformity in even small ROIs throughout the nucleus will yield low IDM values
Correlation	$\sum_{i,j} \frac{(ij)p(i,j) - \mu_x \mu_y}{\sigma_x \sigma_y}$	Measure of gray-level linear dependency High Correlation: scale of local texture is larger than the distance Low Correlation: scale of local texture is smaller than the distance	Increased presence of linear patterns of H3K4K27me3 yield higher correlation values, whereas lack of image linearity yield lower correlation values
Information Measure of Correlation 1	$\frac{entropy + \sum_i \sum_j p(i,j) \log\{p_x(i)p_y(j)\}}{\max(entropy_x, entropy_y)}$	Measure of gray level linear dependency with respect to directional entropy. Roughly inversely varies with correlation, but provides a more "natural" measure of correlation due to its invariance under logarithmic transformation High IMC1: Greater presence of heterogeneous GLCM values in linear directions Low IMC1: Uniformity of GLCM values in linear directions	Lack of linearity of H3K4K27me3 expression yields higher values of IMC1, whereas repeating patterns in linear directions yield low values.
Information Measure of Correlation 2	$\sqrt{1 - \exp \left[-2.0 \left[- \sum_i \sum_j P_x(i) P_y(j) \log\{P_x(i) P_y(j)\} \right] \right]}$	Measure of gray level linear dependency with respect to randomness of spatial dependency. Roughly directly varies with correlation, but provides a more "natural" measure of correlation due to its invariance under logarithmic transformation. High IMC1: Higher presence of repeating patterns in linear directions. Low IMC2: Lack of uniformity or repeating patterns in linear directions	Consistent patterns or overall uniformity of H3K4K27me3 expression in local linear directions yield higher IMC2 values, whereas low IMC2 values indicate lack of local linearity

Sum Average	$\sum_{i=2}^{2N_g} iP_{x+y}(i)$	Measure of GLCM distribution relationship to mean intensity accumulations High sum average: indicative of higher presence of punctate regions of high intensity Low sum average: lack of presence of such punctate regions	The accumulation of H3K4me3 and/or H3K27me3 to smaller ROIs leads to the appearance of brighter "spots" studded throughout the nucleus, which yields higher sum average values. This can also be an indication of increased bivalency. Low sum average values indicate a lack of such "spots" in more uniform H3K4K27me3 distribution, or a lack of accumulation to common areas, which can be reflective of the overall absence of bivalency.
Sum Entropy	$-\sum_{i=2}^{2N_g} P_{x+y}(i) \log\{P_{x+y}(i)\}$	Measure of GLCM relationship to distribution of intensity with respect to entropy High and low values correspond similarly to entropy values	Orderly patterns of H3K4K27me3 that tend to repeat throughout the nuclear space yield lower sum entropy values, whereas greater disorder and variation yield higher sum entropy values.
Sum Variance	$\sum_{i=2}^{2N_g} (i - \text{Sum Entropy})^2 P_{x+y}(i)$	Measure of GLCM relationship to distribution of intensity with respect to variance High sum variance: greater standard deviation of sum average Low sum variance: low standard deviation of sum average	Greater variation of H3K4K27me3 accumulated spot size yields higher sum variance values, whereas similar accumulated spot sizes and less variation yield lower sum variance values.
Difference Average	$\sum_{i=0}^{N_g-1} iP_{x-y}(i)$	Measure of GLCM relationship to mean intensity differences Inversely varies with sum average	Roughly inversely varies with sum average. Increased bivalency yields lower difference average values, whereas a lack of bivalency yields higher difference average values.
Difference Entropy	$\sum_{i=0}^{N_g-1} P_{x-y}(i) \log\{P_{x-y}(i)\}$	Measure of GLCM relationship to intensity differences with respect to entropy Inversely varies with sum entropy	Roughly inversely varies with sum entropy. Increased disorder/variation in H3K4K27me3 expression yield lower difference entropy values, whereas increased uniformity/repeating patterns yield higher difference entropy values.
Difference Variance	$\sum_{i=0}^{N_g-1} (i - \text{Sum Entropy})^2 P_{x-y}(i)$	Measure of GLCM relationship to intensity differences with respect to variance Inversely varies with sum variance	Roughly inversely varies with sum variance. Uniform distribution of spot sizes yield higher difference variance values, whereas a wider distribution yield lower difference variance values.

Table 1.1. Mathematical definitions of each Haralick texture descriptor, with accompanying intuitive description and potential insight regarding H3K4K27me3 organization.

$P(i,j)$ = (i,j) th entry in the normalized gray-tone spatial dependence matrix. $P_x(i)$ = i th entry in marginal-probability matrix obtained by summing the rows of $P(i,j)$. N_g = number of distinct gray levels in quantized image. μ_x & μ_y = means of P_x & P_y .

σ_x & σ_y = standard deviations of P_x & P_y . P_{x+y} = probability of co-occurrence matrix coordinates summing to $x+y$.

1.3.3 Quantitative Analysis of High-Content Descriptor Datasets

In order to meaningfully comprehend quantitative datasets of high-dimensionality, it is necessary to analyze these datasets to determine patterns and correlations that are buried within them. Since data points in multivariate datasets are usually not uniformly distributed, correlations often exist among certain variables that stretch the data along different directions in the variable space. These correlations often arise due to similarities in response of certain parameters (i.e. descriptors) to a given stimulus, which causes a kind of redundancy among groups of descriptors. The identification and exploitation of such correlated descriptors allows for the visualization, and subsequent quantitative analysis, of high-dimension datasets in a three dimensional space. A commonly used method for dimensionality reduction of large datasets is principal component analysis (PCA) [197, 198], which is a multivariate analytical approach which analyzes multiple variables by consolidating them into single entities. Mathematically, PCA is based on the linear transformation of sets of correlated variables in large datasets into a new set of uncorrelated variables, which form the principal components. The greatest amount of variability found in the original large dataset forms the basis for each principal component in a new coordinate system. Each principal component is mathematically computed by determining the eigenvectors of the covariance matrix of the dataset, where eigenvectors with the largest eigenvalues correspond to the direction of greatest variations. This process is accomplished without a loss of information and could potentially identify new variables with greater meaning [199].

Once large datasets are dimensionally reduced into a three dimensional space, they can be further characterized by employing k-means clustering, which is a learning algorithm that groups data points of relative similarity into clusters [200]. The centroid for each cluster can subsequently be determined, where larger distances between cluster centroids correspond to decreasing similarity between clusters (i.e. conditions), and thus more easily classified, and smaller distances correspond to increasing similarity between clusters (i.e. conditions), which are less easily classified from each other, but may represent organizational similarities. This can be an effective approach for determining scalar values (based on cluster centroid values) of large datasets, such as populations of cell types [201]. These scalars can be subsequently used to compare the similarity, or dissimilarity, of datasets acquired from different conditions, such as cells exposed to different environmental conditions. One useful application of this approach is for screening the response of cells exposed to different materials or drugs.

It is also advantageous to apply data mining techniques to large datasets of high dimensionality, in order to determine parameters (i.e. descriptors) that are most influential in the classification of different conditions, or filter out those parameters that do not correlate with accurate classification and could be considered noise. An effective way to accomplish this data mining is by employing decision trees, which are predictive models that reveal the minimum number of parameters necessary to correctly classify different conditions. The visual outcome of decision tree data mining is a “tree” with several “nodes,” where each node represents a key parameter that contributes to the ability to accurately classify the data. All of the different conditions in the original dataset

are located at the bottom of each “branch” of the tree, and can be traced back through each node to reveal the parameters, and their range of values, that are necessary for accurate classification [202] (**Figure 1.10**).

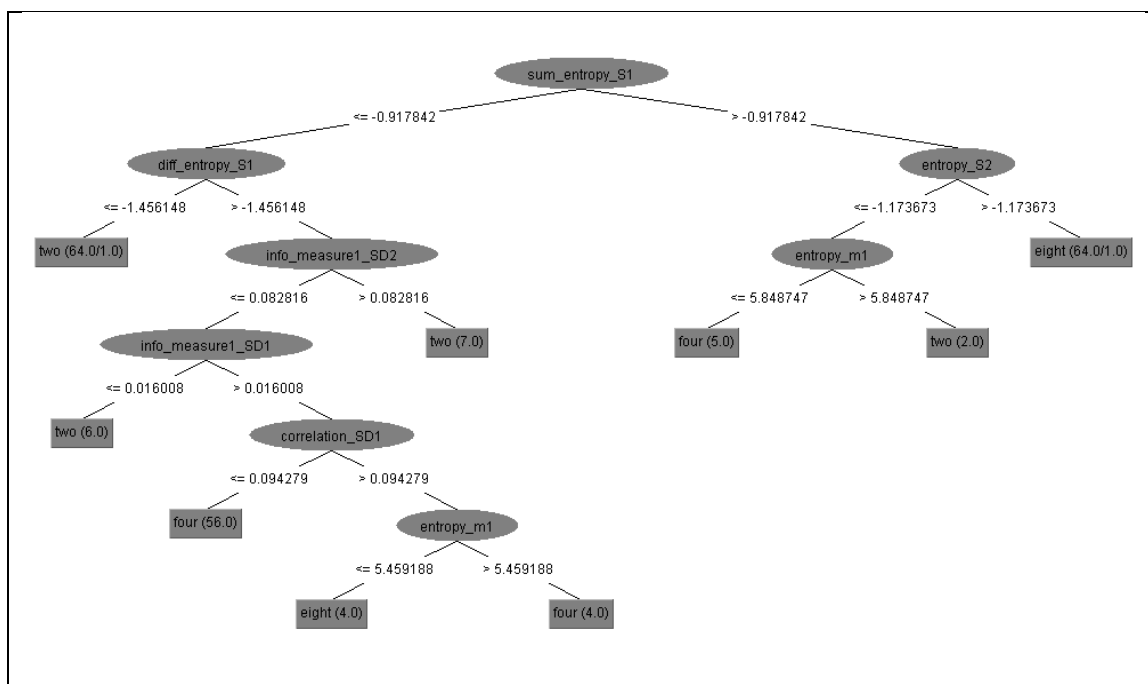


Figure 1.10. Example of a decision tree created using the J48 algorithm of the Weka data mining package. Starting from the top node (sum entropy), different condition groups (i.e. two, four and eight) can be classified from each other by going down each node of the tree until a condition is reached. Based on this example, a minimum of two descriptors (i.e. sum entropy and entropy) are needed to accurately classify some “eight” conditions, whereas a maximum of six descriptors are needed to accurately classify some “four” conditions.

Thus, there are a number of techniques to analyze large datasets of quantitative descriptors from high resolution images, all of which are useful for characterizing and classifying different conditions. Although there is much insight that can be gained from high content descriptor datasets, simpler insights can also be gained from less mathematically complex image analysis, such as Forster Resonance Energy Transfer.

1.4 Dissertation Hypothesis, Aims and Overview

This dissertation was largely inspired by the current state of regenerative medicine and the need for increasingly rigorous and comprehensive approaches for characterizing cellular phenotypic states as a response to defined microenvironmental properties. There are two main objectives of this dissertation:

- 1) Increase the cognizance of the general scientific community of the importance of epigenetic modifications for orchestrating chromatin structural dynamics and subsequent gene transcriptional regulation for altered cell behavioral states.
- 2) Accelerate the pace of biomaterial / drug discovery in the context of stem cell differentiation via the spatiotemporal organizational analysis of intranuclear biomarkers relevant to chromatin structural dynamics.

In this thesis, the realization of these objectives depended on the successful development and employment of an image analytical tool that quantifies subtle intranuclear organizational differences of relevant post translational modifications to histones. The main hypothesis is that it is not merely the relative presence / absence of different PTMs to histones that offer insights into a cell's epigenetic / gene transcriptional state, but the spatiotemporal organization of these marks also provides critical information, which can be captured via optical microscopy and quantitatively characterized, for the improved comprehension of the structure-function relationships of nuclear architecture and cellular behavior. This hypothesis was tested on developing stem cells exposed to a variety of controlled chemical, mechanical and topographical stimuli using a number of biochemical and bioinformatics assays. The data acquired from these assays contributed

to an overall story that was organized into this dissertation as such: The development and calibration of this image based textural analytical tool is outlined in chapter 2. This tool was subsequently applied to analyze the intranuclear organizational response of select PTMs in two developing human stem cell systems to defined chemical stimuli, and these results are presented in chapter 3. Chapter 4 explores the response of PTM organizational dynamics to defined mechanical and topographical stimuli of biomaterial substrates. Finally, in chapter 5, the dynamic response of a histone 3 fraction to various chemical stimuli was monitored in living cells, and the intranuclear and cytoskeletal organizational dynamics were related to each other.

Thus, the specific aims of this thesis were twofold:

- 1) To develop high-content quantitative techniques to analyze high-resolution images of differentiating stem cell nuclei to characterize and classify stem cells and their phenotypic derivatives based on epigenetic signatures reflective their chromatin structural state.
- 2) To identify microenvironment responsive quantitative organizational features of epigenetic states to investigate the influence of defined physicochemical properties of biomaterials to induce lineage-specific epigenetic states, for the facilitation of directed stem cell differentiation.

CHAPTER 2: DEVELOPMENT AND CALIBRATION OF QUANTITATIVE TEXTURE DESCRIPTORS REFLECTIVE OF DYNAMIC CHROMATIN STRUCTURAL STATES

2.1 Introduction

The abundance of functionally distinct cell phenotypes which make up a single organism are all derived from the controlled regulation of gene transcription from a common primary DNA sequence. The precise spatiotemporal orchestration of gene activation and silencing is largely modulated by dynamic chromatin structures which regulate the accessibility to specific parts of their DNA. These structural dynamics are highly influenced by post-translational modifications (PTMs) to core histones, where complex combinations of PTMs regulate gene activation or silencing [80]. Some PTMs, and the enzymes that manifest them, have been linked with cellular differentiation towards specific phenotypes [203-207], as well as cellular reprogramming to a pluripotent state [107, 208]. Thus, these studies, along with numerous others, indicate that this “epigenetic language” is at the core of regulating specific patterns of gene transcription.

Since PTMs are events which often occur upstream of, and thus heavily influence, gene transcription regulation, they have been extensively investigated using a number of biochemical assays. Current methods of investigating the complexities of the epigenome are mostly population based, which involve the lysis of large numbers of cells to isolate a sufficient amount of chromatin for immunoprecipitation or proteomic interrogation via mass spectrometry, both of which destroy any potential structural insight from dynamic chromatin architectures. We therefore developed an optical image based technique that

does not require lysing cells and fractionating histones nor isolating DNA, and can thus provide insights into how the structural organization of chromatin correlates with gene expression.

The rationale for the development of this methodology is grounded in the fact that living cell organization can serve as probes of long-term cell functions, as the organization, distribution and overall expression of specific cellular proteins provide a wealth of information on the state of the cell. Recently, quantitative morphometric image analysis of early cytoskeletal organization was used to successfully predict osteogenic differentiation in developing mesenchymal stem cells [191]. These geometric features were effective in characterizing subtleties in cell body organizational dynamics in response to chemical cues. However, due to several practical/technical limitations, the effectiveness of this technique is largely compromised when cells are cultured in three-dimensional biomaterials, due to over-confluency and/or artefacts arising from the geometric properties of the material forcing changes to the shape of the cell body, which are independent of, and thus not reflective of, gene transcription program changes. To address this, we have since focused on developing quantitative descriptor sets that are relevant to intra-nuclear organizational patterns that reflect cell behavioral state using Haralick texture based algorithms [196]. These features are quickly computable and easily automatable, which allows for the fusion of high-throughput and high-content image analysis capabilities.

Due to the abundance of studies reporting on the highly influential nature of histone PTMs on the epigenome and subsequent regulation of gene transcription, and

the relative specificity and availability of antibodies against PTMs for ChIP applications, we chose to investigate the potential of extracting high-content images from nuclei immunolabeled for PTMs. Among the numerous PTMs that have been linked to gene transcription regulation, perhaps the most widely investigated in stem cells have been the co-occurring trimethylation of lysine residues 4 and 27 on histone 3 (H3K4K27me3) [209, 210]. The manifestation of this bivalent mark is carried out by a group of lysine methyltransferases (KMTs) that specifically target lysine 4 (hSET1A/B & MLL1-5) [211] and lysine 27 residues (EZH2) [212]. As these bivalent marks have been shown to be associated with important transcription factor genes at low levels, one theory posits that their co-occurrence may serve to silence developmental genes but keep them poised for activation [210]. Genes with bivalent marks can be subsequently activated or silenced by a group of lysine demethylases (KDMs) by catalyzing the removal of methyl

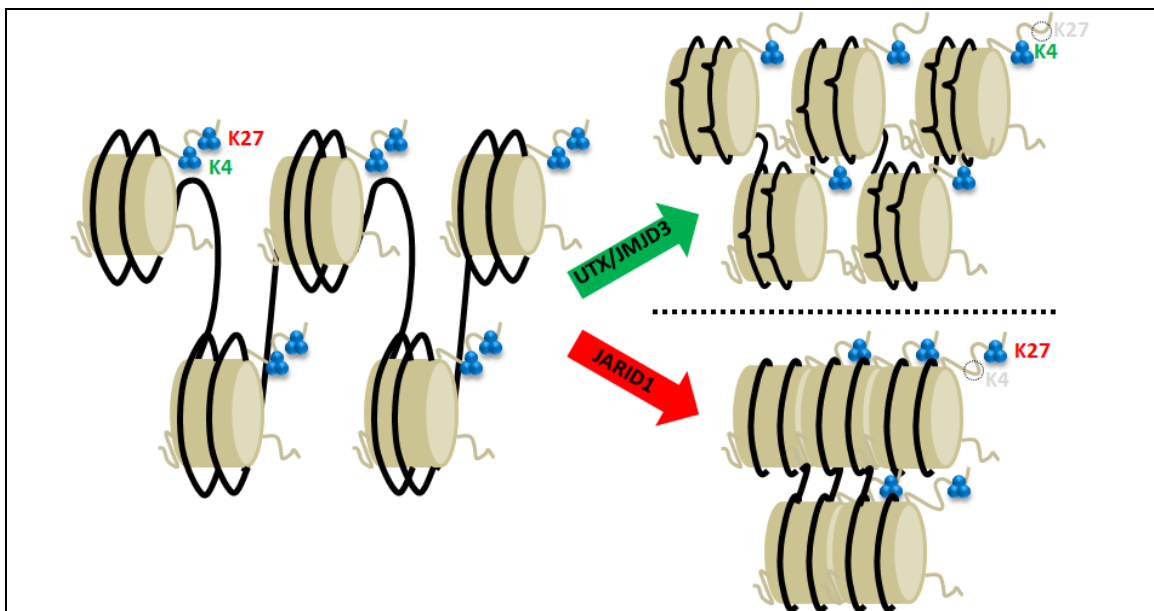
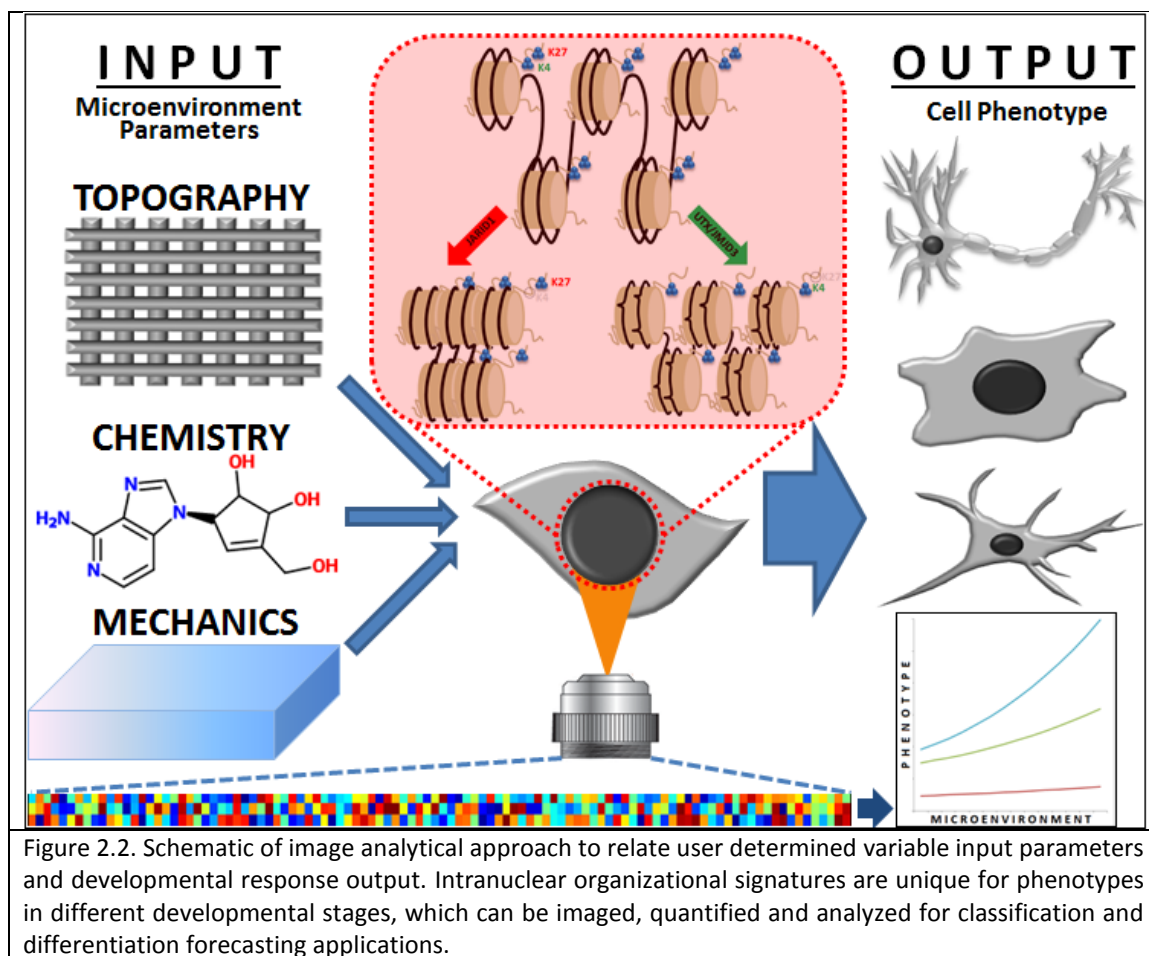


Figure 2.1. The presence of both H3K4me3 and H3K27me3 serves to keep DNA primed for activation. H3K27me3 is removed by the lysine demethylases UTX and JMD3, which causes desired genes to be “open” for transcription with the presence of H3K4me3. The removal of H3K4me3 by JARID1 causes DNA to tighten around the core histones, as the singular presence of H3K27me3 serves to silence genes.

groups from either lysine 27 (UTX & JMJD3) [213] contributing to a chromatin structure that promotes active gene transcription, or lysine 4 (JARID1) [214] for gene silencing (Figure 2.1).



In this chapter, we investigate the quantitative patterns and trends of thirteen core Haralick texture algorithms computed from H3K4me3 and H3K27me3 immunocytochemical expression in hMSCs in response to varying degrees of specific lysine methyltransferase inhibition. Subsequently, we exploit these quantitative responses to train a support vector machine to ultimately classify cellular phenotypic

state as a function of H3K4me3 and H3K27me3 expression. The development and calibration of this textural image analytical tool serves as a foundation for the investigation of the dynamic response of H3K4me3 and H3K27me3 to chemical, mechanical and topographical cues, which are summarized in chapters 3 and 4.

2.2 Materials and Methods

2.2.1 Human Mesenchymal Stem Cell Culture

hMSCs were obtained from the bone marrow of three different donors (22 year old male, 37 year old female and 47 year old female) by drawing a bone marrow aspirate and separating mononuclear cells via density centrifugation. These cells were subsequently plated, expanded and frozen in α -MEM (Life Technologies, Grand Island, NY, USA) containing 4 mM L-glutamine (Invitrogen, Carlsbad, CA, USA), 30% Fetal Bovine Serum (Life Technologies) and 5% Dimethyl Sulfoxide (Sigma-Aldrich, St. Louis, MO, USA). Frozen vials of hMSCs were received, thawed and cultured in α -MEM containing 10% FBS and 0.5% Penicillin/Streptomycin (Invitrogen) in a water-jacketed incubator kept at 37°C and 5% CO₂. Basal culture media was changed every 72 hours until cells reached 70% confluency, at which point they were passaged into fresh flasks or dishes at a seeding density of 5,000 cell/cm².

Adipogenic hMSCs were generated by supplementing the basal culture media with soluble growth factors that promote adipogenic differentiation. Two media formulations were involved: Adipogenic induction media (AIM) and adipogenic maintenance media

(AMM). AIM consisted of basal culture media supplemented with 1 μ M Dexamethasone (Sigma-Aldrich), 50 μ M Indomethacin (Sigma-Aldrich), 10 μ g/ml Insulin (Sigma-Aldrich) and 100 μ M 3-Isobutyl-1-methyl-xanthine (Sigma-Aldrich). AMM consisted of basal culture media supplemented with 10 μ g/ml Insulin. Adipogenic hMSCs were generated over a two week culture period, with differentiation beginning when hMSCs reached ~100% confluency, at which point the basal culture media was replaced with AIM and incubated for 72 hours. Next, AIM was replaced with AMM and incubated for 48 hours. AMM was then replaced with AIM for another 72 hours, then replaced with AMM for another 48 hours. AIM and AMM was alternated as such for two weeks.

Osteogenic hMSCs were generated by supplementing the basal culture media with 0.5 mM L-Ascorbic Acid-2-Phosphate (Sigma-Aldrich), 20 mM β -glycerol phosphate (Sigma-Aldrich) and 0.2 μ M Dexamethasone. Differentiation induction began 24 hours after plating undifferentiated hMSCs at a seeding density of 3,000 cell/cm², by replacing the basal culture media with osteogenic media, which was subsequently replaced every 72 hours over a two week period.

Cell cycle synchronization of all cell types was achieved using an early S-phase block by applying Thymidine (Sigma-Aldrich) in two cycles to allow cells to progress synchronously through the G2 and mitotic phase. Briefly, at about 30% confluency, each respective culture media was supplemented with 2 mM Thymidine and applied for 18 hours. Then the Thymidine was removed and replaced with normal culture media for 9 hours to release the cells from the S-phase block, after which 2 mM Thymidine was reintroduced to the cells for 17 hours. Cells were subsequently washed in PBS and

incubated back in their normal culture media, where they were allowed to grow until ready for analysis.

2.2.2 Lysine Methyltransferase Inhibition

hMSCs were treated with lysine methyltransferase inhibitors (KMTi) to forcibly assume a chromatin structural state that is either more open or more closed. Cells were treated with 1, 5 and 10 μ M of 3-Deazaneplanocin A (DZNep) (Cayman Chemical, Ann Arbor, Michigan, USA) for 72 hours to selectively inhibit the enzymatic activity of EZH2 [215], which is a KMT that targets lysine residue 27 on histone 3. 1, 2 and 4 mM of 5'-Deoxy-5'-(methylthio)adenosine (MTA) (Sigma-Aldrich) was introduced to cells for 24 hours to inhibit the MLL family of enzymes, which catalyze the trimethylation of lysine residue 4 on histone 3 [216, 217]. After drug treatment, cells were either fixed in 4% Paraformaldehyde (Electron Microscopy Sciences, Hatfield, PA, USA) and prepared for immunocytochemical labeling, or lysed for protein analysis using Western Blot.

2.2.3 Verification of KMTi Selectivity and Efficacy Using Western Blot

The inhibitory efficacy of the KMTi's was determined via immunoblot analysis. Following KMTi treatment, cells were lysed on ice using RIPA lysis buffer (Thermo Scientific, Waltham, MA, USA) and harvested via scraping. Raw cell lysates were clarified via centrifugation at 15000 RPM, 4°C for 15 minutes. Supernatant was subsequently collected and flash frozen in liquid nitrogen until ready for analysis. Protein quantification

was determined using the BCA protein assay (Thermo Scientific) by following the manufacturer's instructions.

After quantification, samples were heated on a heating block preheated to 95 °C for 10 minutes. Samples were subsequently diluted in the appropriate amount of RIPA buffer to load the same amount of protein (15 µg) into each well, and 5 µl of loading dye was added to each sample. An electrophoresis unit (Bio-Rad, Hercules, CA, USA) was assembled with a 7.5% polyacrylamide gel (Bio-Rad) immersed in 1X SDS Running Buffer consisting of 25 mM Tris (Bio-Rad), 192 mM glycine (Fisher Scientific, Pittsburgh, PA, USA) and 0.1% Sodium dodecyl sulfate (Sigma-Aldrich). After each well was loaded with protein and dye, the electrophoresis unit was allowed to run for 1 hour at 140 V. Next, a gel holder cassette was assembled with two sponges, four filter papers (Whatman plc, Maidstone, Kent, UK), nitrocellulose paper (Bio-Rad) and the gel. This cassette was placed into a transfer tank (Bio-Rad) and filled with 1X Transfer Buffer consisting of Tris/Glycine Buffer (Bio-Rad) supplemented with 20% Methanol (Sigma-Aldrich) and allowed to run for 2 hours at 300 mA at 4 °C while stirring. The membrane blot was subsequently removed and placed in Blocking Buffer consisting of 5% nonfat milk in 1X TBS-T for 1 hour at room temperature with gentle rocking. Membranes were then cut according to a reference protein ladder (Fisher Scientific) and then incubated in the primary antibodies H3K4me3 (Abcam, Cambridge, MA, USA), H3K27me3 (Abcam) and the control GAPDH (Santa Cruz Biotechnology, Dallas, TX, USA) diluted in a blocking solution (5% Bovine Serum Albumin in TBS-T) overnight at 4 °C on a rocker. The following day, membranes were washed with TBS-T for 10 minutes, four times. Then the membranes were incubated in HRP-conjugated

secondary antibodies (Santa Cruz Biotechnology) diluted in a blocking solution (5% BSA in TBS-T) for 2 hours at room temperature, on a rocker. The membrane was then washed with TBS-T for 10 minutes, four times. After washing, the HRP detection solution, Luminata Forte Western HRP Substrate (Millipore, Billerica, MA, USA), was added for 5 minutes. Finally, the membranes were developed with autoradiography film (Denville Scientific, South Plainfield, NJ, USA) in a dark room using a Kodak X-Omat 2000A Processor (Kodak, Rochester, NY, USA).

2.2.4 Immunocytochemistry of H3K4me3 and H3K27me3

Cells cultured on glass coverslips were fixed in 4% Paraformaldehyde (Electron Microscopy Sciences) for 20 minutes at room temperature, then washed for 5 minutes with PBS w/o Ca^{2+} or Mg^{2+} (Lonza) three times. Next, they were permeabilized in a solution of 0.1% Triton X-100 (Sigma-Aldrich) in PBS for 10 minutes under gentle agitation, after which they were blocked with 8% Normal Goat Serum (Cell Signaling Technology, Danvers, MA, USA) for 1 hour. The primary antibodies H3K4me3 (cat. no. ab8580, Abcam) and H3K27me3 (cat. no. ab6002, Abcam) were diluted in 8% Normal Goat Serum solution at a 1:500 ratio and incubated at room temperature for 1 hour under gentle agitation. After incubation, cells were washed in PBS for 30 minutes at room temperature, three times. Secondary antibodies were diluted in 8% normal serum solution at a 1:1000 ratio and incubated at room temperature under gentle agitation for 2 hours, while protected from light. Secondary antibody solution was subsequently washed in PBS for 45 minutes, four times. After 3 total hours of washing, coverslips were inverted and mounted onto

glass slides with ProLong Gold antifade mounting media (Life Technologies) and sealed along their perimeter with nail polish.

2.2.5 Laser Scanning Confocal Imaging

Immunocytochemically labeled samples were imaged using a Leica TCS SP8 confocal laser scanning microscope equipped with a time-gated stimulated emission depletion laser (G-STED) (Leica Microsystems). AlexaFluor 488 was visualized using a supercontinuum white light laser source set to 492 nanometer wavelength excitation and emission was detected using a hybrid detector (HyD) set to a range of 505 to 550 nanometers. AlexaFluor 594 was visualized with 592 nanometer wavelength excitation, and emission was detected with a HyD set to a range of 600 to 655 nanometers. The objective used for all high content image acquisition was a 100x Oil Immersion Objective with a numerical aperture of 1.44. Three dimensional z-stacks were taken with a pinhole of 0.75 airy units at a zoom of 5X to yield an XY physical dimension of 23.25 x 23.25 μm at a resolution of 1024 x 1024 pixels. Z-depth varied between 5-15 μm for different nuclei, and the optical section thickness remained constant at 0.5 μm . Z-stacks were subsequently projected onto a 2D plane using an average projection. The scanning speed was kept constant at 400 Hz.

2.2.6 Immunoelectron Microscopy with Transmission Electron Microscope

Nuclei from cultured cells were isolated using the Nuclei EZ Prep Kit (Sigma-Aldrich) by following the manufacturer's instructions. Nuclear pellets were fixed in 4% paraformaldehyde (Electron Microscopy Sciences) and 0.25% glutaraldehyde (Electron

Microscopy Sciences) in PBS for 1 hour at room temperature. Fixative was subsequently removed and rinsed in dH₂O before dehydration in a concentration series of ethanol (50%, 70%, 85%, 95%, 100%, for 10 minutes each). 100% ethanol was removed and replaced with a solution consisting of 50% ethanol and 50% LR White resin (Electron Microscopy Sciences) for 1 hour. This solution was subsequently removed and the pellet was incubated in 1 ml of 100% LR White resin at 60°C overnight. After polymerization, 75 nm sections were cut using a Leica EM UC6 ultramicrotome and subsequently transferred onto formvar-carbon copper grids. Residual aldehydes were deactivated via incubation in 0.1M glycine for 15 minutes. Sections were then permeabilized in 0.1% Triton-X100 in PBS for 5 minutes, and then blocked with 5% normal donkey serum (Abcam) for 1 hour at room temperature. After blocking, sections were incubated in primary antibodies for H3K4me3 (cat. no. ab8580, Abcam) and H3K27me3 (cat. no. ab6002, Abcam) at a 1:20 dilution ratio for 2 hours at room temperature. Sections were then washed in 5% normal donkey serum three times for 5 minutes each wash. Sections were subsequently incubated in secondary Aurion immunogold antibodies sized at 6 and 10 nm (Electron Microscopy Sciences) at a 1:30 dilution ratio for 2 hours at room temperature. Sections were then washed in PBS four times for 5 minutes each wash, and then post-fixed in 2.5% glutaraldehyde for 20 minutes. Sections were then washed in dH₂O three times for 5 minutes each wash, and then stained with 2% uranyl acetate for 30 minutes followed by lead citrate for 30 seconds. Immunolabeled sections were subsequently imaged using a Zeiss LEO 912 transmission electron microscope.

2.2.7 Quantification of PTMs Using Mass Spectrometry

Histones were acid extracted as previously described [218]. Total histones were subjected to chemical derivatization using propionic anhydride and digested with trypsin for 6 hours at 37°C at 10:1 substrate to enzyme ratio. The digested peptides were treated with an additional round of propionylation and desalted using C18 extracted mini disk (Empore 3M, MN, USA). Approximately 1µg of each sample was loaded via an autosampler (EASY-nLC, Thermo Fisher Scientific Inc) onto a homemade 75µm reversed phase analytical column packed with C18-AQ resin (3µm particle sizes, 120 Å pore size). Peptides were chromatographically resolved using a 66-min 2-98% solvent B gradient (solvent A = 0.1% formic acid, solvent B = 100% acetonitrile) at a flow rate of 300nL/min. The electrosprayed peptides were detected by Orbitrap Elite mass spectrometer (Thermo Fisher Scientific Inc) with a resolution of 60,000 for full MS spectrum followed by MS/MS spectra obtained in the ion trap. The relative abundance of each modification, expressed as a percentage on a histone peptide sequence, was quantified by analyzing its MS and MS/MS spectra via an in-house software, EpiProfile.

2.2.8 Computational Methods of Calibration

Images were processed for analysis using background subtraction and object segmentation, to clearly isolate nuclear signals from any potential noise, using Image Pro 7.0 (Media Cybernetics, Rockville, MD, USA). 42 Morphological descriptors included in the Image Pro software package were obtained for comparative purposes. 104 Haralick texture descriptors were acquired using a custom MATLAB script (Mathworks, Natick, MA, USA) written to compute different features based on gray level co-occurrence matrices (GLCM). Thirteen total mathematically defined texture features (Table 1.1) were computed for four different biomarker values: H3K4me3, H3K27me3, H3K4me3 +

H3K27me3 and H3K4me3 – H3K27me3. These were based on GLCMs of two varieties: the first combination was based on measurements made from spatial distances of one pixel, and the second combination was based on spatial distances of two pixels. Thus, a total of $13 \times 4 \times 2 = 104$ different quantitative textural values were computed for each nucleus.

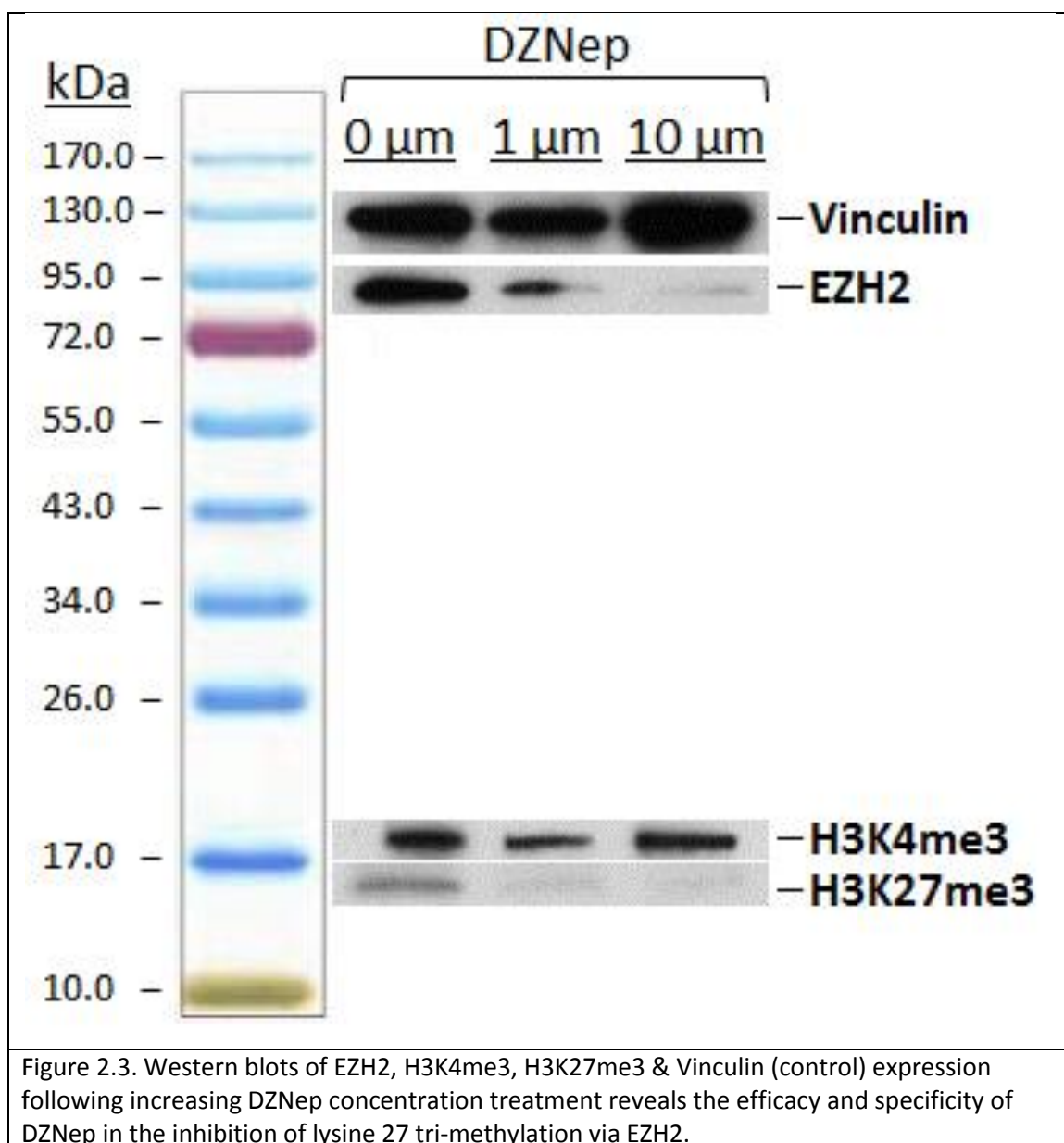
Haralick texture descriptors of KMTi treated cells were obtained and compared with those of untreated cells via Student's T-TEST using Microsoft Excel 2010, and p-values were subsequently plotted onto a Heat Map using MATLAB (Mathworks). Normalized values of raw descriptor values were standardized according to mean and standard deviation using Microsoft Excel 2010, and also plotted as Heat Maps using MATLAB. Descriptor sets of cells treated with the highest concentrations of each respective drug (DZNep - 10 μ M, MTA 4 mM) were used to train a support vector machine, which was subsequently used in all experimental PCA classifications and analyses. All PCA classifications were conducted using the Multivariate Data Analysis package, which is part of MATLAB's Statistics Toolbox (Mathworks). Subsequent K-means cluster analysis was performed using the Cluster Analysis package, which is part of the same toolbox. The phenotype parsing index was computed from texture descriptor datasets extracted from confocal images by averaging the three values of the XYZ coordinates of centroids determined from k-means cluster analysis. The open chromatin index was determined from IEM micrographs by subtracting the ratio of H3K27me3 positive marks to H3K4me3 positive marks in heterochromatic regions from the ratio of H3K4me3 positive marks to H3K27me3 positive marks in euchromatic regions.

2.3 Results

2.3.1 Efficacy and Specificity Verification of KMT Inhibitors

Direct perturbations of activating and silencing PTMs to histones are reflective of diametric chromatin structural states that give rise to opposing gene transcriptional states. We achieved large shifts in the balance between the bivalent PTMs H3K4me3 and H3K27me3 via the pharmaceutical inhibition of specific lysine methyltransferases (KMTs). Low, medium and high concentrations of the KMT inhibitors (KMTi) 3-Deazaneplanocin A (DZNep) and 5'-Deoxy-5'-(methylthio)adenosine (MTA) were introduced to cell cycle synchronized hMSCs to selectively inhibit the activity of the KMT encoding genes, EZH2 and MLL, respectively, and their inhibitory efficacy was determined by immunoblots (**Figure 2.3**).

It is qualitatively clear that as the concentration of DZNep increases, the presence of EZH2 and H3K27me3 decreases, whereas the vinculin control and H3K4me3 remain unaffected, which indicates the specificity of DZNep to inhibit the activity of EZH2 and decrease tri-methylation of lysine residue 27 on histone 3.



2.3.2 Combined Effect of KMT Inhibitors and Soluble Growth Factors on Differentiation

Next, we investigated the developmental response of mesenchymal stem cells to KMT inhibition combined with exposure to soluble chemical growth factors. The hypothesis is that perturbation of normal levels of activating or silencing PTMs may influence the development of

differentiating stem cells by either accelerating or decelerating the transcription of gene programs vital for proper development. We began by investigating the combined influence of the inhibition of EZH2 (Lysine 27 methyltransferase) with 10 μ M 3-Deazaneplanocin A (DZNep) and exposure to adipogenic (Insulin, 3-Isobutyl-1-methylxanthine) and osteogenic (Ascorbic Acid, Glycerophosphate) soluble growth

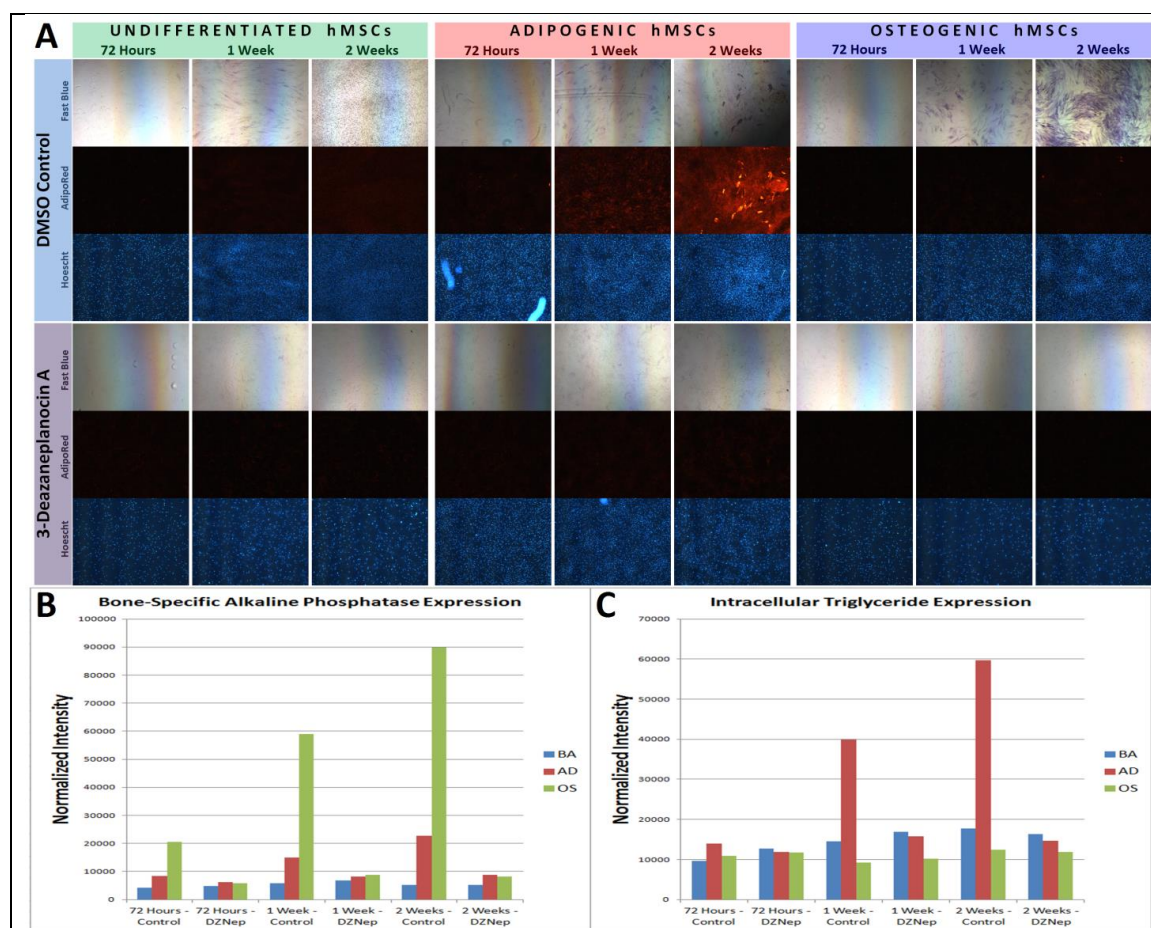


Figure 2.4. Combined effect of 3-Deazaneplanocin A (DZNep) and soluble differentiation induction chemicals on adipogenic and osteogenic differentiation. (A) hMSCs were induced to differentiate towards adipogenic and osteogenic lineages, as well as maintained in basal media to prevent differentiation, in 10 μ M DZNep and 0.5% DMSO control, and fixed at 3 time points and subsequently stained for bone-specific alkaline phosphatase (Fast Blue) and intracellular triglycerides (AdipoRed). (B) Quantification of lineage markers normalized to cell count demonstrates that DZNep prevents both differentiation and proliferation.

factors. After exposure, hMSCs were subsequently fixed along three time points (72 hours, 1 week, 2 weeks) and stained for adipogenic and osteogenic lineage markers. Interestingly, hMSCs exposed to DZNep displayed a lack of both intracellular triglyceride formation and bone-specific alkaline phosphatase expression across the entire treatment time period. Furthermore, DZNep treated hMSCs seem to stop proliferating, with similar cell numbers at 1 week and 2 weeks of culture. Control hMSCs continue to proliferate, with continued increase in cell count across all time points. Control hMSCs also display characteristic adipogenic and osteogenic lineage markers when exposed to their respective soluble differentiation-induction growth factors (**Figure 2.4**). Thus, it is clear that the inhibition of lysine 27 trimethylation results in decreased cell division and differentiation induction.

Next, we investigated the combined effect of the inhibition of lysine 4 trimethylation with 1 mM 5'-Deoxy-5'-methylthioadenosine (MTA) and exposure to adipogenic and osteogenic inducing soluble growth factors. The same approach was performed, staining fixed cells at early, mid and late time points. Interestingly, administration of MTA increased the production of triglyceride formation compared to the control, with higher intensity quantifications at every time point. Moreover, MTA exposure seemed to halt the differentiation of osteogenic hMSCs, with close to baseline levels of bone-specific alkaline phosphatase expressed at the late time point of hMSCs exposed to both MTA and osteogenic inducing soluble growth factors (**Figure 2.5**).

The halt in proliferation ability seen with DZNep exposure is less pronounced, if at all so, with MTA exposure. These results indicate that MTA is a facilitator of adipogenic

differentiation, which is quite the opposite of what was reported in the past by Musri et al [219]. Thus, our findings indicate that MTA has the potential to greatly increase the rate of adipogenic differentiation when combined with other adipogenically inducing microenvironmental cues.

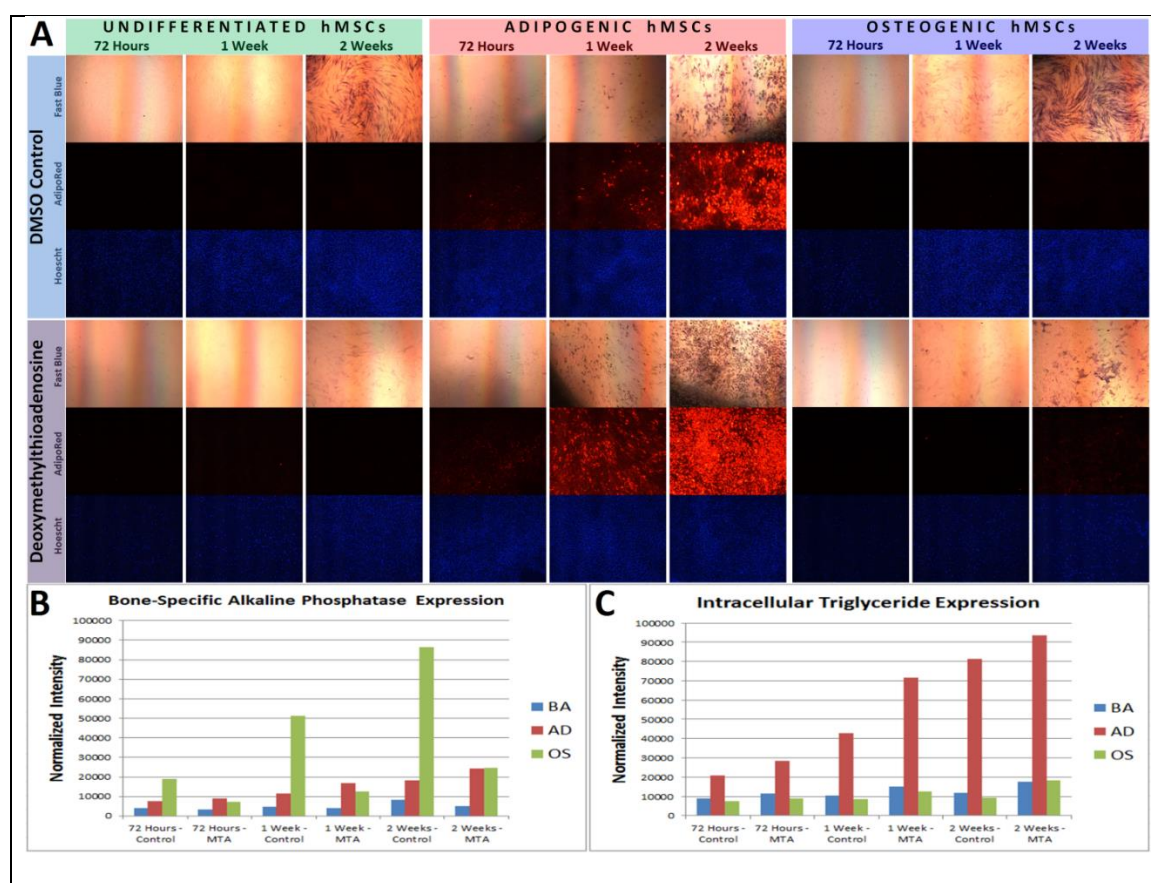
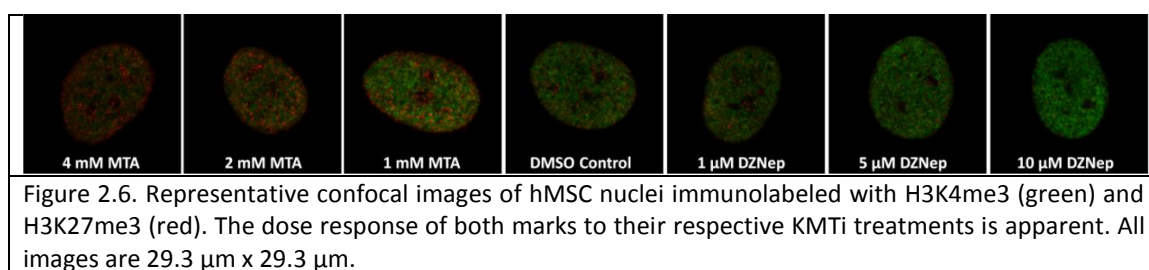


Figure 2.5. Combined effect of Deoxymethylthioadenosine (MTA) and soluble differentiation induction factors on adipogenic and osteogenic differentiation. (A) hMSCs were induced to differentiate towards adipogenic and osteogenic lineages, as well as maintained in basal media to prevent differentiation, in 1 mM MTA and a 0.1% DMSO control, and fixed at 3 time points and subsequently stained for bone-specific alkaline phosphatase (Fast Blue) and intracellular triglycerides (AdipoRed). (B) Quantification of lineage markers normalized to cell count reveals that MTA selectively facilitates adipogenic differentiation and prevents osteogenic differentiation.

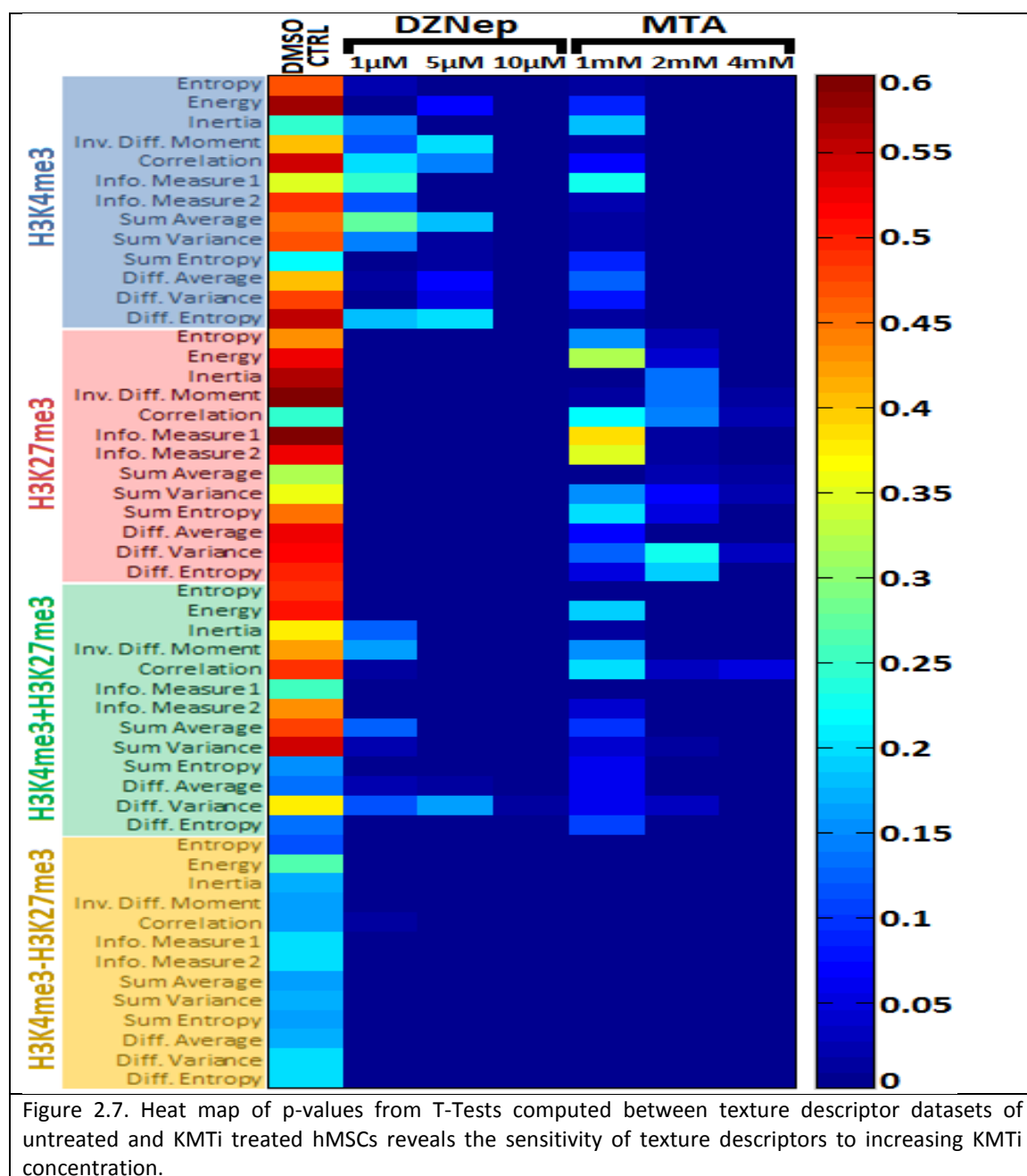
2.3.3 Calibration of Quantitative Descriptors Using KMT Inhibitors

The nuclei of KMTi treated vs. non-treated cells were imaged at high resolution and used to generate training datasets of descriptors reflective of relatively "open" vs. "closed" chromatin structure states. After 72 hours of treatment with DZNep or 24 hours of treatment with MTA, cells were fixed and co-immunolabeled for H3K4me3 and H3K27me3. High content images of nuclei were acquired with a time-gated stimulated emission depletion (G-STED) laser scanning confocal microscope, and quantitative texture descriptors were subsequently extracted from these images (**Figure 2.6**). A total of 104 quantitative texture descriptors were acquired for each single nucleus, and a minimum of 50 nuclei were imaged per condition. These large descriptor datasets were dimensionally reduced using principal component analysis (PCA), which enabled the visualization of descriptor vectors of single cells in a three dimensional space. A "phenotype parsing index" value was computed from the coefficients of the eigenvectors used to linearly transform each of the three principal components.



Statistical T-Test analysis was performed on the descriptor sets of KMTi treated cells vs. a DMSO vehicle control, and these p-values were plotted onto heat maps (**Figure 2.7**). Even at the lowest concentrations of KMTi treatment (i.e. 1 μM DZNep and 1 mM MTA), the majority of texture descriptors were shown to be quite different from the

DMSO control, with only a handful of descriptors with a p-value over 0.15 (i.e. correlation and information of correlations 1&2). The highest concentrations of KMTi



exposure (i.e. 10 μM DZNep & 4 mM MTA) yield the most different organizational patterns of H3K4K27me3 expression from the untreated control, with virtually every

descriptor displaying a p-value of less than 0.05. Thus, descriptor sets of nuclei exposed to the highest KMTi concentrations (10 μ M for DZNep, 4 mM for MTA) were used to train a support vector machine classifier to distinguish these two opposing structural signatures, which we subsequently applied to our test sets of non-treated differentiating cells.

2.3.4 Immunoelectron Microscopic Quantification of PTM Manifestation

The image analytical approaches we are employing involve use of optical microscopy, which is commonly limited by the Abbe diffraction limit, which is dictated by the numerical aperture of the objective lens and the excitation wavelength, as outlined in the following equation:

$$d = \frac{\lambda}{2n \sin\theta}$$

where d = diffraction limit distance, λ = excitation wavelength and $n \sin\theta$ = numerical aperture.

Therefore, even with objective lenses of very high numerical aperture (i.e. 1.6) and shorter excitation wavelengths (i.e. 400 nm), we would still be limited to roughly 400 nm / 3.2 = 125 nm, which is quite large when considering the size of a nucleosome (~ 80-110 angstroms, 8-11 nm) [59, 220]. Therefore, in an effort to overcome these resolution limits and more accurately capture the organization of individual nucleosomes, we used a time-gated stimulated emission depletion laser to deplete surrounding fluorescent signals emanating from any particular point and improve our resolving power to approximately 25 nm [176, 221]. Although this is between 5-10 fold of an improvement over

conventional optical microscopy, we still cannot claim that we are able to resolve individual nucleosomes.

Thus, in order to verify that the distinct organizational intranuclear patterns of H3K4K27me3 on individual nucleosomes that we are capturing via optical microscopy are indeed occurring at the nanoscale, we employed immunoelectron microscopic imaging of H3K4K27me3 antibodies conjugated to gold nanoparticles to localize where these marks are occurring with regards to heterochromatic and euchromatic regions of the nucleus. (Figure 2.8).

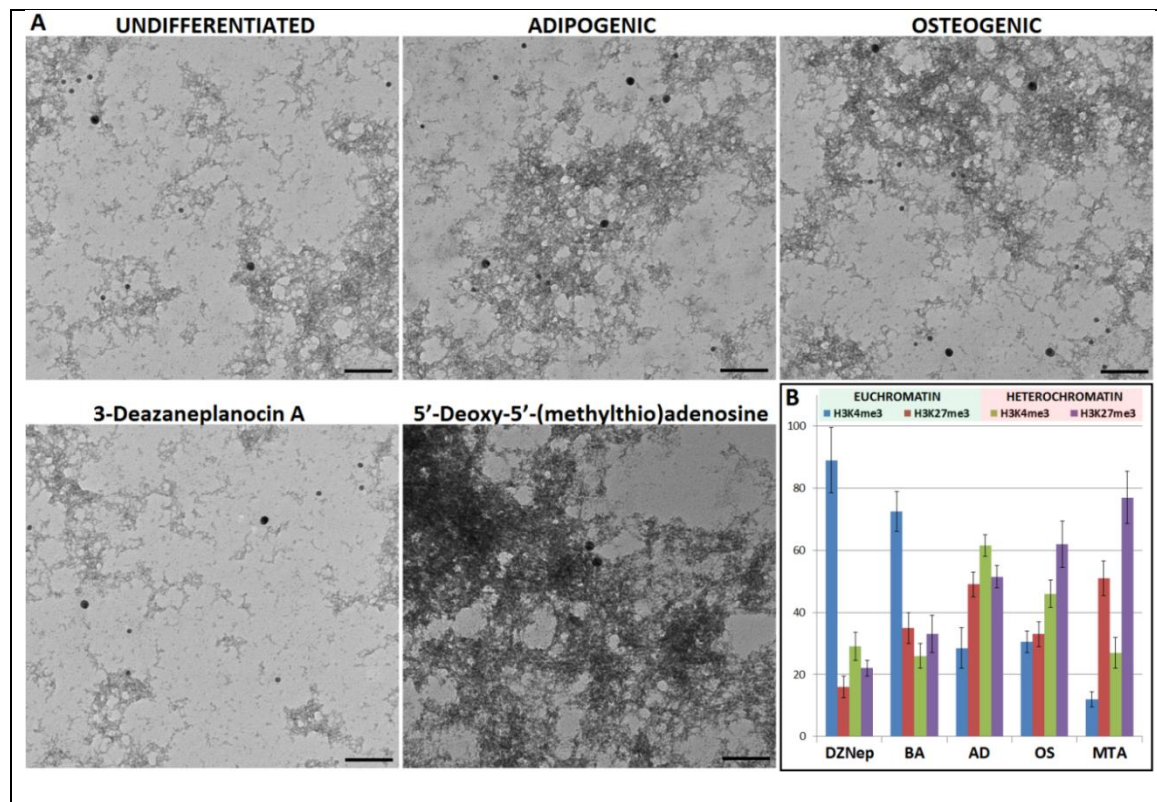


Figure 2.8. Immunoelectron micrograph quantification of H3K4me3 and H3K27me3 marks reveals distinct distribution of both marks in euchromatic and heterochromatic areas as a response to chemical cues. (A) TEM micrographs were taken at 40000X magnification of hMSCs exposed to 5 different conditions of soluble chemical cues: undifferentiated, adipogenic inducing, osteogenic inducing, 10 μ M DZNep and 4 mM MTA. H3K4me3 was conjugated to 12 nm diameter gold beads, and H3K27me3 was conjugated to 18 nm beads. Scale bar = 100 nm. (B) The presence of the gene activating mark, H3K4me3, is highest in hMSCs exposed to DZNep and undifferentiated hMSCs in euchromatin and lowest in heterochromatin, whereas the gene silencing mark, H3K27me3, is relatively more prevalent in both post-mitotic phenotypes in heterochromatin and highest in MTA treated cells.

This enabled us to quantify individual PTMs and further categorize whether these marks are manifested in euchromatic or heterochromatic regions. After counting the marks in approximately 30 micrographs per condition, we were able to clearly see that these PTMs are indeed localizing to different parts of the nucleus, depending on the condensation of chromatin and the phenotypic state of the cell. In general, the activating mark, H3K4me3, is highest in euchromatic regions in undifferentiated hMSCs, whereas the silencing mark, H3K27me3, is higher in differentiating hMSCs in heterochromatic regions. Furthermore, there are significant differences between the relative presence of H3K27me3 in adipogenically vs. osteogenically induced hMSCs in both euchromatic and heterochromatic areas, with higher H3K27me3 presence in euchromatin in adipogenic hMSCs and higher H3K27me3 in heterochromatin in osteogenic hMSCs (**Figure 2.8B**), indicating that these differences may also have an effect on the regulating distinct gene transcription programs that ultimately give rise to different phenotypic identities.

2.3.4 Mass Spectrometric Quantification of PTM Relative Abundance

The current “gold standard” approach to assessing global levels of PTM distribution in histone fractions is via proteomic interrogation using mass spectroscopy. Briefly, this involves the extraction of chromatin from large populations of cells, separating this total chromatin by histone fractions (i.e. H1, H2A, H2B, H3.1, H3.2, H3.3 etc.) using high-performance liquid chromatography (HPLC), and then analyzing these fractions via mass spectroscopy to identify individual PTMs based on their m/z ratio. We applied this approach to our developmental hMSC system to assess the relative abundance of H3K4me3 and H3K27me3 in different phenotypes (**Figure 2.9**). Intriguingly,

there were not any significant differences between H3K4me3 or H3K27me3 levels between all three phenotypes. Since it has been widely reported that these marks are heavily involved in the developmental fate of naïve stem cells [209, 210, 222-225], these MS findings imply that perhaps it is not the overall relative levels of H3K4K27me3, but differences in their activity, that cause markedly different gene transcription programs to occur. This hypothesis was tested using chromatin immunoprecipitation, with the results summarized in section 3.3.4.

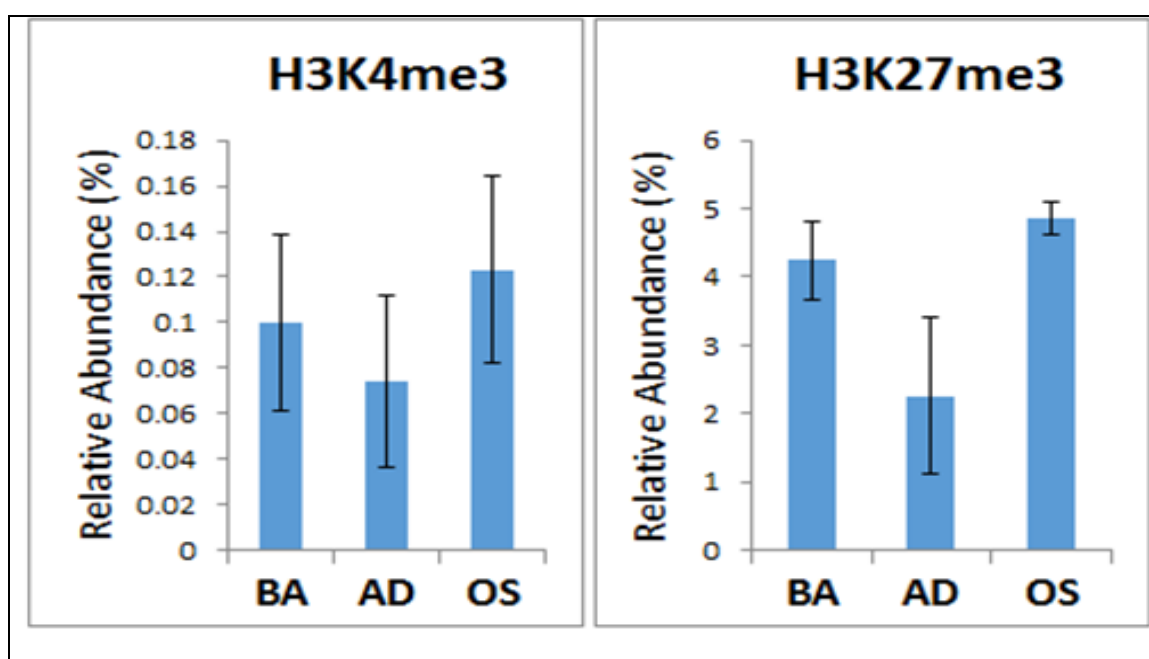


Figure 2.9. Mass spectrometric quantification of H3K4me3 and H3K27me3 reveals their relative abundances are not significantly altered in response to soluble growth factors and differentiation. Lack of statistical significant differences determined by one-way ANOVA (K4me3: $F(4,10)=0.537235$, $p=0.712008$; K27me3: $F(4,10)=1.188573$, $p=0.373457$)

Aside from these two marks, several other PTMs were simultaneously detected and their relative abundances were quantified (**Figure 2.10**). There are many different marks quantified, and many observations and speculations to be made.

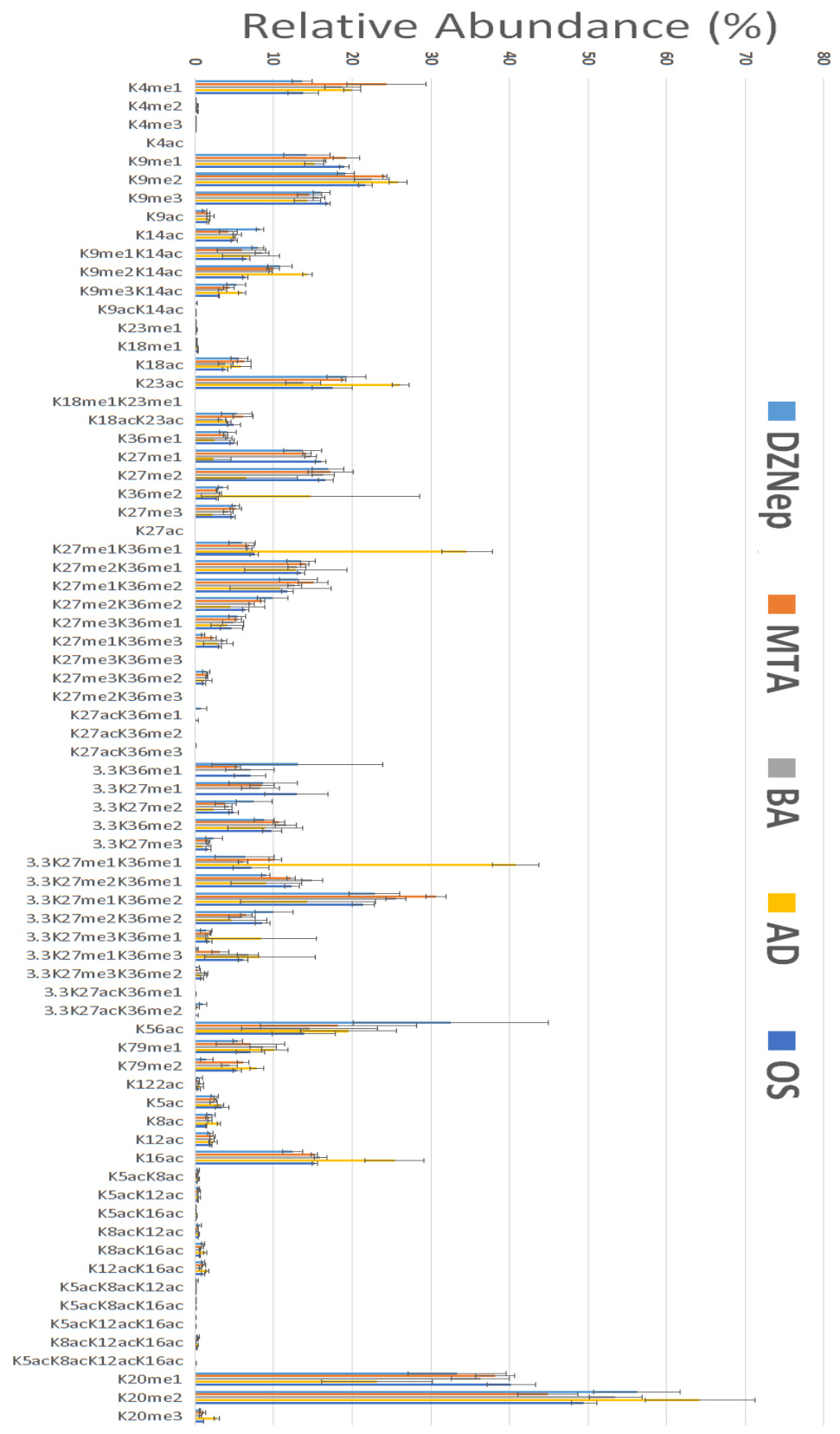


Figure 2.10. Proteomic interrogation of histone PTM levels using mass spectrometry. A total of 73 unique PTMs were identified and detected based on their m/z ratio. There were a total of three different hMSC donor lines (i.e. n=3) used to generate each cell phenotype. Certain marks were significantly enriched after exposure to different chemical cues, whereas most marks displayed a lack of significant difference, suggesting the abundance in PTM levels may be secondary to other potential factors (i.e. spatiotemporal organization) that may be important to developmental gene transcription regulation.

H4K16ac is notably highest in adipogenically differentiated hMSCs, which may be due to decreased LSD1 activity, as LSD1 has been reported to be involved in the maintenance of pluripotency, and decreased LSD1 activity has been linked to increased H4K16ac [226]. Other PTMs that exhibit higher levels in adipogenic hMSCs include K23ac, K36me2, K27me1K36me1 (both fractions) and 3.3K27me3K36me1. 3.3K27me1 is the only PTM that is highest in osteogenic hMSCs, and there seem to be no marks that are significantly highest in undifferentiated hMSCs.

In terms of the effect of KMTi's on PTM levels, it may be advantageous to note which marks are similarly effected by a particular KMTi and a soluble growth factor treatment condition. For example, the marks K9me3K14ac, K18ac and 3.3K27me2K36me1 are most similar in DZNep treated and adipogenic hMSCs, which may suggest that DZNep is acting to achieve similar PTM levels as adipogenic induction treatment using soluble growth factors. The most number of similar PTMs between KMTi and differentiation condition occur between MTA treatment and osteogenic hMSCs, which exhibit similar levels of the following PTMs: K9me1, K27me2, K27me3, K27me1K36me1, K27me1K36me1, K27me2K36me1, 3.3K27me2K36me1, K79me1, K79me2, K16ac and K20me1. MTA treatment yields similar PTM levels to adipogenic hMSCs for K9me2, K9me3, K18ac and K56ac. Thus, global PTM quantifications using MS may lead to insights of how certain specific KMTi's affect other PTMs that they are not advertised to target. Narrowing in on those KMTi's that achieve similar PTM levels as a cell phenotype of interest may facilitate the discovery of KMTi's that promote the development or maintenance of that cell type. However, it is important to note that this

type of analysis requires the lysis of large populations of cells, which inevitably clouds data with artefacts originating from inherently heterogeneous stem cell populations.

2.4 Discussion

The overall goal of the work presented in this chapter was to develop quantitative methodologies that capture the dynamics of H3K4K27me3 manifestation as a response to lysine methyltransferase inhibition. The driving hypothesis and motivation for this goal was rooted in the idea that characterizing the localization of relevant PTMs throughout a nucleus can be reflective of how individual nucleosome units are organized and distributed, which can in turn provide insights into the influence of these organizational dynamics on gene transcription regulation. Although single nucleosome units are currently unresolvable via optical microscopy, patterns in their spatial organization within a nucleus can be interrogated, characterized and meaningfully related to their consequential downstream gene transcriptional changes. Thus, using high resolution confocal images, we computed a group of Haralick texture features that were able to quantify unique “H3K4K27me3 signatures” in response to different chemical cues. We related these micro-scale quantifications to nano-scale quantifications of H3K4K27me3 manifestation from TEM micrographs, which revealed a positive correlation between the phenotype parsing index computed from LSCM and open chromatin index computed from TEM (**Figure 2.11**). Thus, the organizational “signatures” detected with optical microscopy were shown to correlate with the differential manifestation of H3K4K27me3 at the nano-scale, verifying the integrity of our approach.

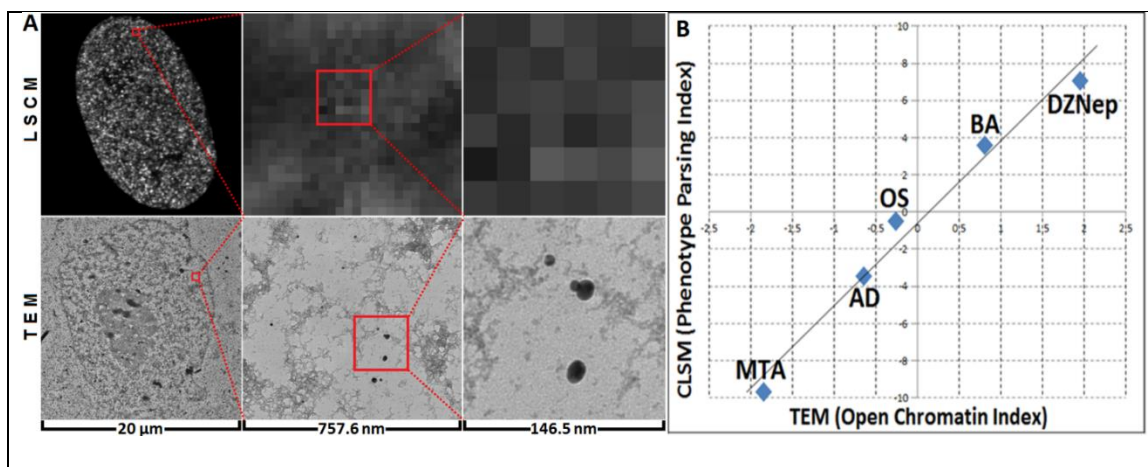


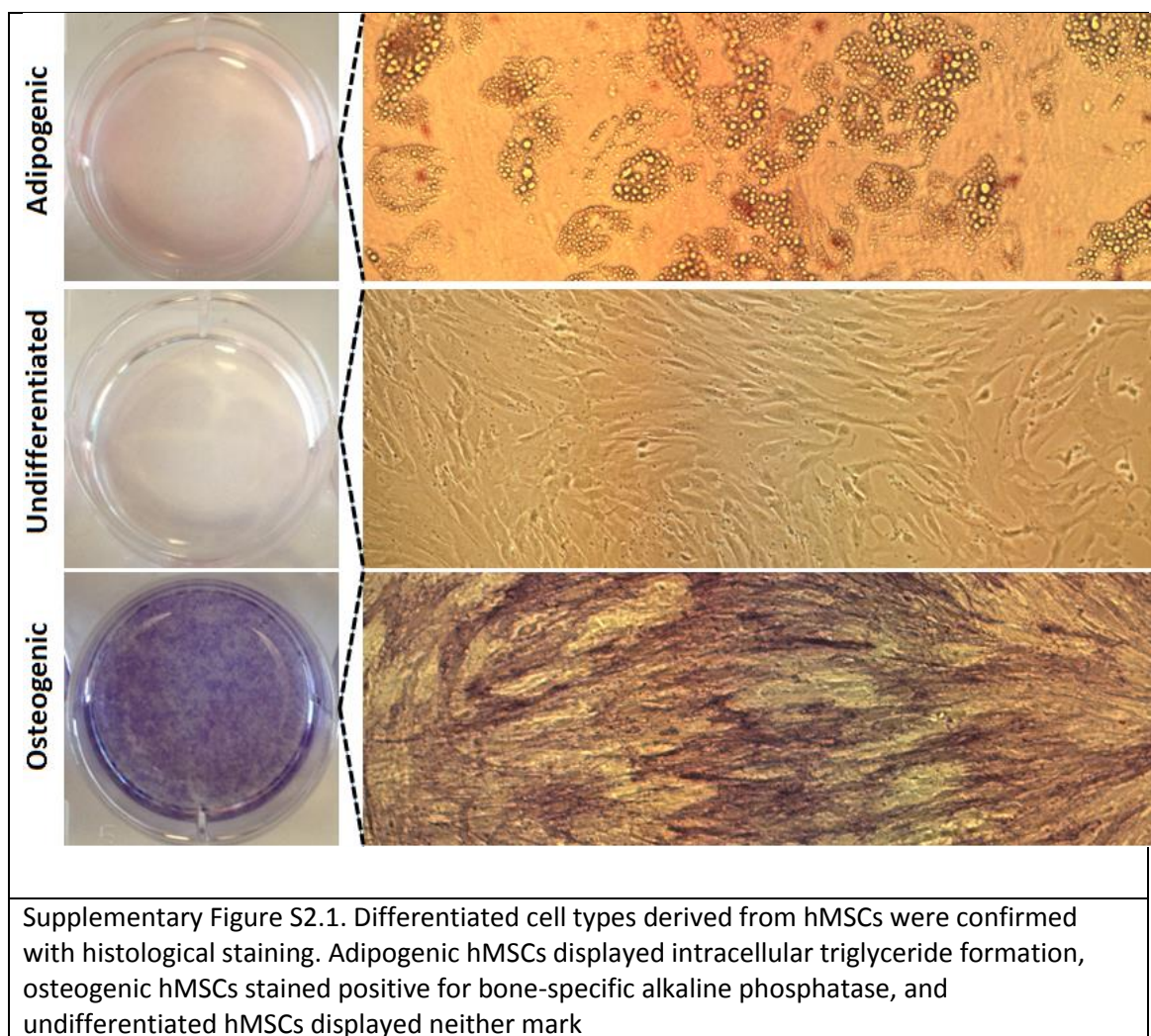
Figure 2.11. Correlation between H3K4K27me3 manifestation as assessed by LCSM and TEM. (A) Size scale relationship between high-content confocal images acquired with LCSM and electron micrographs obtained with TEM. Quantifications obtained from these images correspond to the dynamics of the gene transcription regulating bivalent mark H3K4K27me3. (C) Correlation between LCSM and TEM quantitative datasets. A positive correlation between the “open chromatin index” from TEM micrographs and “phenotype parsing index” from LCSM images is apparent, with negative values of both indices corresponding to relatively closed chromatin states in post-mitotic cells and positive values of both indices corresponding to relatively open chromatin in undifferentiated stem cells. DZNep and MTA treated cells correspond to their positive and negative extremes, respectively.

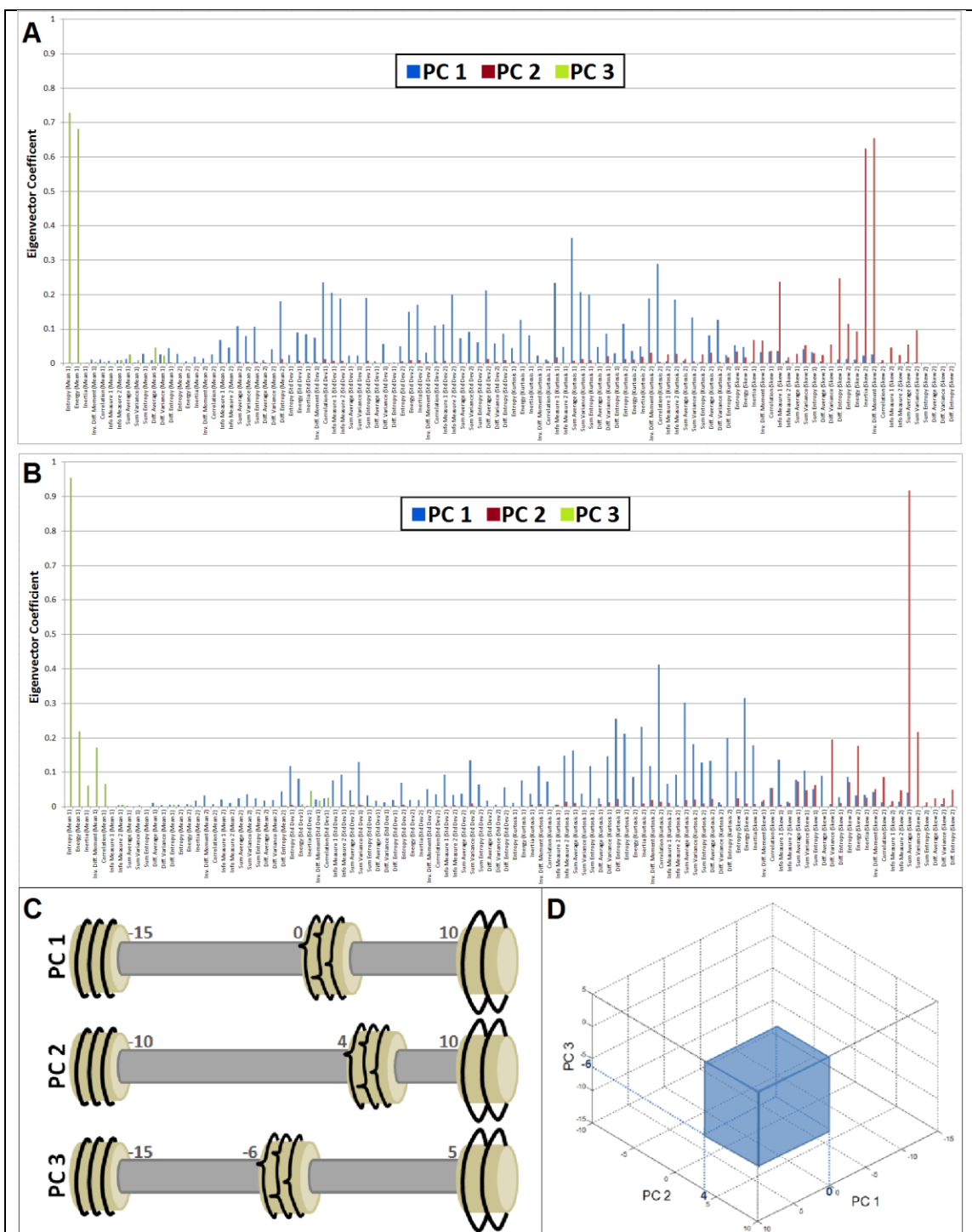
One particularly attractive aspect of this image analytical tool is its ability to extract such epigenetic relevant quantitative information from single cells. The bulk of contemporary biochemical assays used to investigate the epigenome (i.e. chromatin immunoprecipitation, DNA sequencing, mass spectroscopic quantification of PTMs) are population based. Due to the heterogeneous nature of naïve stem cell populations, the generation of noise and/or artefacts is an inevitable byproduct from such assays. This noise is substantially minimized via this single-cell approach, as any extreme outliers are immediately apparent following descriptor acquisition.

2.5 Conclusion

This texture based image analytical approach to quantifying organizational signatures of functionally relevant biomarker manifestation was developed for the detection of distinct organizations of post translational modifications to core histones in response to different, defined chemical environments. Lysine methyltransferase inhibitors were employed to achieve increasingly “closed” chromatin structures reflective of gene transcription silencing with Deoxymethylthioadenosine (MTA) or increasingly “open” chromatin structures reflective of gene transcription activation with 3-Deazaneplanocin A. After verification of selectivity and efficacy, these KMTi’s were used to calibrate graded changes to the H3K4me3 / H3K27me3 balance, and related to the expression of H3K4K27me3 in hMSCs exposed to adipogenic and osteogenic inducing soluble growth factors. Finally, the micro-scale detections made with confocal microscopy were related to nano-scale quantifications of H3K4K27me3 manifestation in relation to euchromatic and heterochromatic areas, illustrating the ability to detect similar quantitative trends using both instruments. This image analytical tool was subsequently employed to analyze developing stem cells (chapter 3) and hMSCs exposed to different mechanical and topographical cues (chapter 4).

2.6 Supplementary Data





Supplementary Figure S2.2. Parsing Index Zone of undifferentiated stem cells in PCA plots. The eigenvector coefficients comprising each principal component were plotted for the PCA plots of developing hMSCs (A) and iPSCs (B), with many similarities between both systems. The proximity of undifferentiated hMSCs and iPSCs enabled the establishment of a parsing index zone, occupying a space between 0 and 10 on principal component 1, 4 and 10 on principal component 2, and -6 and 5 on principal component 3 (C). This can be visually represented as a 10 x 6 x 11 three-dimensional cuboid in a PCA plot (D).

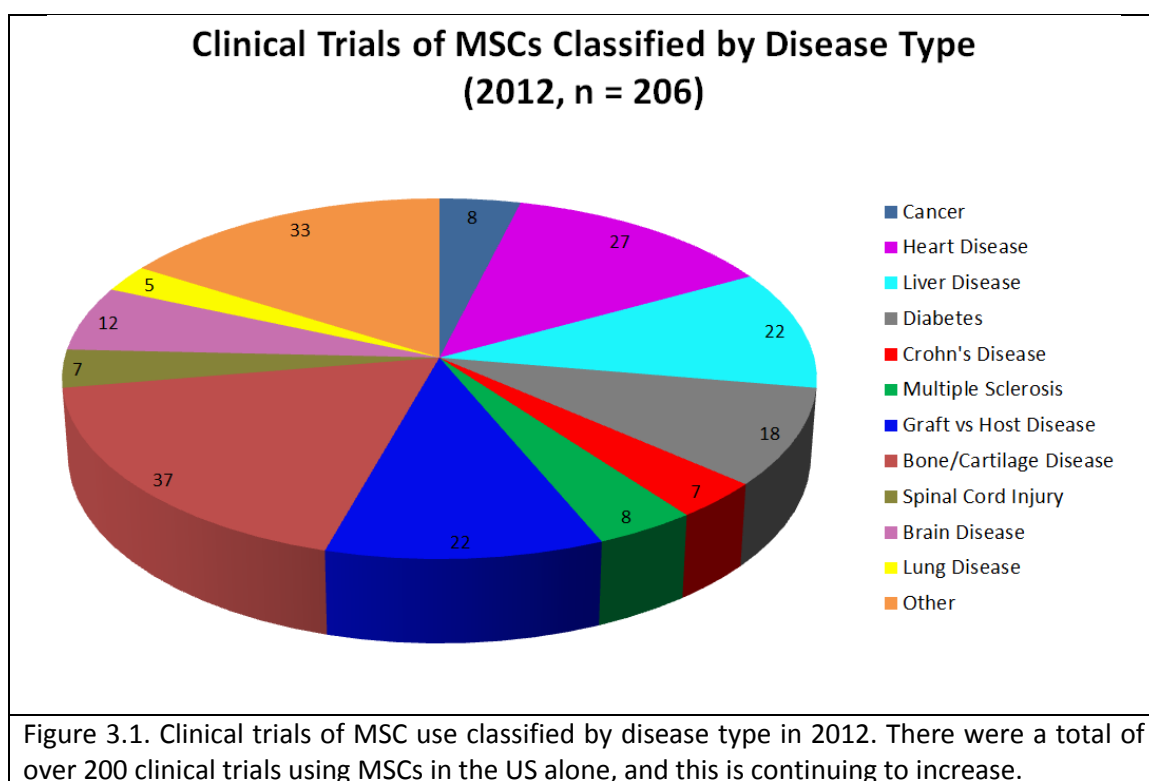
CHAPTER 3: HIGH CONTENT TEXTURAL IMAGE ANALYSIS OF THE DYNAMICS OF POST TRANSLATIONAL MODIFICATIONS TO HISTONES IN DIFFERENTIATING STEM CELLS

3.1 Introduction

Modern clinical advancements have greatly benefited from the incorporation of stem cell use in a variety of medical treatments. The large majority of these treatments fall under the umbrella of regenerative medicine, which generally aims to restore the normal function of a physiological entity by replacing damaged, diseased or dying cells or tissues with viable, functional ones. In the human body, there are over 200 distinct cellular phenotypes that maintain unique identities rooted in their morphology and function [227], which are governed by specific gene transcription programs that orchestrate the expression of different proteins in space and time, which in turn are largely orchestrated by epigenetic mechanisms. Thus, the future progress of stem cell use in regenerative medicine relies on the increased comprehension of how specific cellular differentiation programs are executed to most efficiently produce the many different differentiated cell types needed to treat a wide range of disease or damage that occurs throughout the entire human body.

The generation of specialized cell phenotypes can come from a handful of different stem cell sources. Adult stem cells are perhaps the most promising source of undifferentiated cells in the clinic, as they are found throughout the body continuously throughout development [228]. The rapid rise in use of adult stem cells in the clinic has

given rise to the formulation of guidelines and standards for their isolation, processing, testing, storage and distribution [229]. The most common and most widely investigated source for adult stem cells is the bone marrow, where mesenchymal stem cells are found [230, 231]. Due to their advantages in differentiation ability, rapid *in vitro* proliferation for expansion, and ability to produce anti-inflammatory molecules [232, 233], their use in the clinic is continuing to rise for a variety of applications (**Figure 3.1**).



Although these cells have been rather comprehensively characterized in terms of their general function [231, 234], morphology [191, 235] and unique expression of certain cell surface protein markers [236], their epigenetic identity has largely been overlooked, with only a handful of investigations that have been reported to date [237-239]. Therefore, we chose to focus on some of the intranuclear epigenetic dynamics in

developing hMSCs to establish correlations with downstream gene transcriptional changes that result in their differentiation towards adipocytes and osteocytes. Elucidating such correlations has the potential to greatly increase the efficacy and efficiency of directed stem cell differentiation via the manipulation of specific epigenetic mechanisms, which always lie upstream of, and therefore influence, gene transcription regulation.

Another exciting stem cell developmental system is composed of formerly somatic cell types virally reprogrammed to a pluripotent state, which are known as induced pluripotent stem cells (iPSCs) [10]. The theoretical advantage of iPSCs is that they can be patient specific, in that a cell sample from a patient can be used to generate fully pluripotent stem cells capable of differentiating into virtually any cell type in the human body. However, due to their method of generation (i.e. lentiviral transfection), their incorporation into regular clinical use is limited due to safety concerns [240], although alternative ways of using iPSCs in the clinic have been gaining steam lately [241, 242]. Nonetheless, the scope of their use in basic science research and drug/material screening is seemingly limitless [243]. Thus, in addition to hMSCs, we investigated the organizational dynamics of several influential PTMs as a response to cellular reprogramming to pluripotency and neural differentiation.

The ultimate goal of this work to is expedite the generation of specific differentiated phenotypes from stem cells partly through the controlled regulation of epigenetic processes. After establishing quantitative chromatin structure signature identities of various developed phenotypes, we can begin to relate these to cells exposed to different, defined microenvironmental factors.

3.2 Materials and Methods

3.2.1 HFF-1 Cell Sourcing, Reprogramming and Directed Differentiation

Human foreskin fibroblasts (HFF-1) were obtained from the Rutgers University Cell and DNA Repository (RUCDR) and cultured in DMEM (Life Technologies) supplemented with 2 mM L-glutamine, 10% FBS, 1% Non-essential amino acids (Life Technologies) and 1% Penicillin/Streptomycin. Induced pluripotent stem cells (iPSCs) were generated from HFF-1s by retroviral transfection with OCT4, SOX2, Klf4 and c-Myc, as previously reported [10]. After selection and purification, iPSCs were cultured on Matrigel (BD Biosciences, San Jose, CA, USA) treated culture dishes in the defined medium mTeSR-1 (Stem Cell Technologies, Vancouver, CA), and this media was changed every 24 hours.

Neural stem cells (NSCs) were generated from iPSCs by replacing their mTeSR culture media with an N2 conversion medium which consists of 50% DMEM/F12 (Life Technologies), 50% Neurobasal Media (Life Technologies), 2 mM L-glutamine, 0.5X N2 Supplement (Life Technologies), 0.5X B27 Supplement w/o Vitamin A (Life Technologies), 1% Penicillin/Streptomycin and 20 ng/ml basic fibroblast growth factor (Sigma-Aldrich) and this media was replaced every 24 hours. After 2 weeks of neuronal induction, media was changed to neural differentiation media, which consists of Neurobasal media supplemented with 1X B27 Supplement w/o Vitamin A, 1% Penicillin/Streptomycin, and 10 ng/ml brain derived neurotrophic factor (PeproTech, Rocky Hill, NJ, USA).

Induced neuronal cells (iNs) were generated from both iPSCs and HFF-1s via retroviral transfection, as described previously [244]. Briefly, iPSCs or HFF-1s were transfected in a growth medium containing 8 ug/ml polybrene with rtTA plus Brn2, Ascl1,

Myt1l and NeuroD1. After 24 hours of transfection, media was replaced with growth media supplemented with 2 ug/ml doxycycline (Sigma-Aldrich). After an additional 24 hours, media was replaced with N2 conversion media for a period of 6 days, and then replaced with neural differentiation media.

3.2.2 Lineage Marker Staining Differentiation Assays

The successful generation of adipogenic and osteogenic cells was assessed using staining assays for intracellular triglyceride droplet formation and bone-specific alkaline phosphatase activity, respectively. Briefly, intracellular triglyceride droplets were stained with AdipoRed assay reagent (Lonza, Allendale, NJ, USA) by following the manufacturer's directions. Positively stained adipogenic hMSCs were imaged using a Nikon Eclipse TE2000-S fluorescence microscope (Nikon Instruments, Melville, NY, USA) under a G-2A longpass emission filter covering 510-560 nm. Bone-specific alkaline phosphatase activity was detected using the fast blue rapid release alkaline phosphatase kit (Sigma-Aldrich) and following the manufacturer's directions. Positively stained osteogenic hMSCs were imaged with the same microscope under bright field. Cells were also labeled with Hoechst 33342 (Life Technologies) via incubation in a 0.01 mg/ml solution for 10 minutes. All quantifications were made by measuring the Density / Intensity Sum values using Image Pro Plus 7.0 (Media Cybernetics, Rockville, MD, USA), and then normalizing to cell number by dividing by Hoechst positive nuclei.

3.2.3 Förster Resonance Energy Transfer

Förster Resonance Energy Transfer (FRET) experiments were performed using the FRET Sensitized Emission Wizard bundled with the Leica Confocal Software version 2.61 build 1537 (Leica Microsystems, Buffalo Grove, IL, USA). First, the experimental conditions were set by defining laser power, photomultiplier tube detection range, and electronic gain and offset values for the donor and acceptor fluorophores. Next, calibration images were acquired from samples labeled with only the donor fluorophore and only the acceptor fluorophore, using the defined parameters that were set. Regions of interest (ROI) were defined by outlining areas of the image where ~100% of the ROI was occupied with donor signal, and background subtraction was performed. Finally, FRET samples were imaged and FRET efficiencies were computed based on the following equation:

$$Fe = \frac{B - A * b - C * (c - a * b)}{C}$$

Where A = Donor intensity, B = FRET intensity, C = Acceptor intensity, and a, b and c are the calibration factors determined from the donor alone and acceptor alone reference images, which are defined as: $b = B/A$, $c = B/C$, and $a = A/C$.

3.2.4 Chromatin Immunoprecipitation

To prepare for a single ChIP experiment, cells were expanded in culture to a minimum total of 1×10^6 to yield a sufficient amount of purified chromatin. After expansion, cells were fixed in 1% formaldehyde in DMEM (Life Technologies) for 10 minutes at 37 °C, with gentle agitation every 2-3 minutes. Plates were then quickly

washed in 1X PBS, two times, and cells were harvested via scraping in 1X PBS containing 1X Protease inhibitor (G-Biosciences, St. Louis, MO, USA) and collected in DNA Lobind tubes (Eppendorf, Hauppauge, NY, USA). Tubes were centrifuged at 600xG at 4 °C for 5 minutes, then supernatant was removed and cell material was resuspended in 300 µl of lysis buffer (10 mM EDTA, 50 mM Tris, 1X Protease Inhibitor and 1% SDS in DI H₂O). At this point, samples could be flash frozen in liquid nitrogen and stored at -80 °C for future use. Sonication conditions were empirically determined for each cell type to yield chromatin fragments of 200-500 base pairs, and DNA fragment size was determined via electrophoresis on a 1% agarose gel run at 85 V for 1 hour. Reverse crosslinking of DNA and protein was achieved via heating at 65 °C for 6 hours.

Magnetic Protein G Dynal beads (Life Technologies) were transferred to DNA Lobind tubes which were placed on a magnetic rack (New England BioLabs, Ipswich, MA, USA) to separate beads from their solution. This solution was removed and replaced with 500 µl of 5% BSA in PBS and placed on a rotator for 15 minutes at 4 °C. Antibodies targeting proteins of interest were diluted in 5% BSA and incubated on a rotator for a minimum of 4 hours, or overnight, at 4 °C. After antibodies bound, the beads were washed in 5% BSA for 30 minutes, followed by a quick rinse.

Immunoprecipitation was achieved by diluting chromatin samples in dilution buffer (1X Protease Inhibitor, 20 mM Tris, 150 mM NaCl, 2 mM EDTA, 1% Triton in DI H₂O) at a 1:7 ratio. Diluted chromatin was added to beads with bound antibody and allowed to incubate on a rotator at 4 °C overnight. The following day, DNA bound beads were washed in RIPA buffer for 5 minutes, five times, followed by a quick rinse in TE buffer. TE was

removed and beads were suspended in a buffer consisting of 1% SDS and 10% NaHCO₃. DNA was subsequently eluted off the beads and reverse-crosslinked from protein via heating at 65 °C for a minimum of 6 hours. After reverse-crosslinking, DNA was purified using the QIA quick PCR purification kit (Qiagen, Hilden, Germany, EU), by following the manufacturer's instructions. DNA yield was quantified using the Quant-iT PicoGreen Assay (Life Technologies) by following the manufacturer's instructions.

3.2.5 Quantitative Real Time Polymerase Chain Reaction

DNA oligonucleotide sequences were designed to target slightly upstream of the promoter region of the genes of interest (**Table 3.1**). These sequences were obtained from Integrated DNA Technologies (Coralville, IA, USA) as 25 nmole lyophilized powders, and resuspended in 250 µl of dH₂O to yield 100 µM stock concentrations.

Following ChIP DNA quantification via the Quant-iT PicoGreen assay, 1.5 ng of DNA was obtained via diluting ChIP DNA in the appropriate amount of dH₂O. A single well in a 384-well PCR plate contained a target/condition combination which consisted of 6 µl of diluted DNA (1.5 ng total), 4 µl of diluted primer (both forward and reverse), and 10 µl of 2X SYBR Green PCR Mastermix (Life Technologies). Genes were amplified on a ABI Prism 7900HT Sequence Detection System (Applied Biosystems, Foster City, CA, USA) with a thermal profile consisting of 40 cycles of the following: 50°C for 2 minutes, 95°C for 10 minutes, 60 °C for 1 minute, 95 °C for 15 seconds, 60 °C for 15 seconds and finally 95 °C for 15 seconds.

Gene	Primer Sequence
------	-----------------

OCT4	Fwd: 5'-GAGCAGAAGGATTGCTTTGG-3' Rev: 5'-AAAACCGGGAGACACAACCTG-3'
NANOG	Fwd: 5'-AAAGTTTTATCCCATTCCTG-3' Rev: 5'-TTAATCCCGTCTACCACTCT-3'
LIN28	Fwd: 5'-TGTTTCTGATTGGCCAGCGC-3' Rev: 5'-GTCTCTGACACCTCTGGGGT-3'
PAX6	Fwd: 5'-CCTTCACTTGACCGCTCAAG-3' Rev: 5'-ACCCACTAATCACTCCGCAACA-3'
TUBB3	Fwd: 5'-CCCTCCGAGCTCTGATCC-3' Rev: 5'-CTGAGCTTTTGCCGGTTTT-3'
NESTIN	Fwd: 5'-TACCTCTCTCGGATGTGTTG-3' Rev: 5'-AGCGACTGAGAGTCGGGAGTG-3'
BGLAP	Fwd: 5'-CGC TCTCAGGGGCAGACACT-3' Rev: 5'-GCACCCTCCAGCATCCAGTA-3'
RUNX2	Fwd: 5'-CCACCCGGCCGAAGTGGTCC -3' Rev: 5'-CCTCGTCCGCTCCGGCCCCACA -3'
PPAR- γ	Fwd: 5'-TATTCAGCCTGCAGTCTCATTTGG-3' Rev: 5'-CCAGAGTCCGGAGTTTTGGAGTT-3'
LPL	Fwd: 5'-GAGATTTCTCTGTATGGCACC -3' Rev: 5'-CTGCAAATGAGACACTTTCTC -3'

Table 3.1. Forward and Reverse primer sequences targeting the promoter regions of POU5F1, NANOG, NESTIN, PAX6, BMP2, RUNX2, PPARG, RHOA used in Chromatin Immunoprecipitation assays.

3.2.6 Immunocytochemistry of Heterochromatin Protein 1 alpha and H3K9me3

Cells were fixed in 4% Paraformaldehyde (Electron Microscopy Sciences) for 20 minutes at room temperature, then washed for 5 minutes with PBS w/o Ca²⁺ or Mg²⁺ (Lonza) three times. Next, they were permeabilized in a solution of 0.1% Triton X-100 (Sigma-Aldrich) in PBS for 10 minutes under gentle agitation, after which they were blocked with 10% Bovine Serum Albumin (BSA) (Sigma-Aldrich) for 1 hour. The primary antibodies HP1-alpha (cat. no. ab77256, Abcam) and H3K9me3 (cat. no. ab8898, Abcam) were diluted in 10% BSA solution at a 1:500 ratio and incubated at room temperature for

1 hour under gentle agitation. After incubation, cells were washed in PBS for 30 minutes at room temperature, three times. Secondary antibodies were diluted in 10% BSA at a 1:1000 ratio and incubated at room temperature under gentle agitation for 2 hours, while protected from light. Secondary antibody solution was subsequently washed in PBS for 45 minutes, four times. After 3 total hours of washing, coverslips were mounted onto glass slides with ProLong Gold antifade mounting media (Life Technologies) and sealed along the perimeter with nail polish.

3.3 Results

3.3.1 Histological Evaluation of Osteogenic and Adipogenic Differentiation

hMSCs were cultured in three media formulations: basal, adipogenic inducing and osteogenic inducing, the recipes of which were previously described in section 2.2.1. hMSCs were fixed along 9 time points post differentiation induction initiation, and subsequently stained for intracellular triglyceride formation and bone-specific alkaline

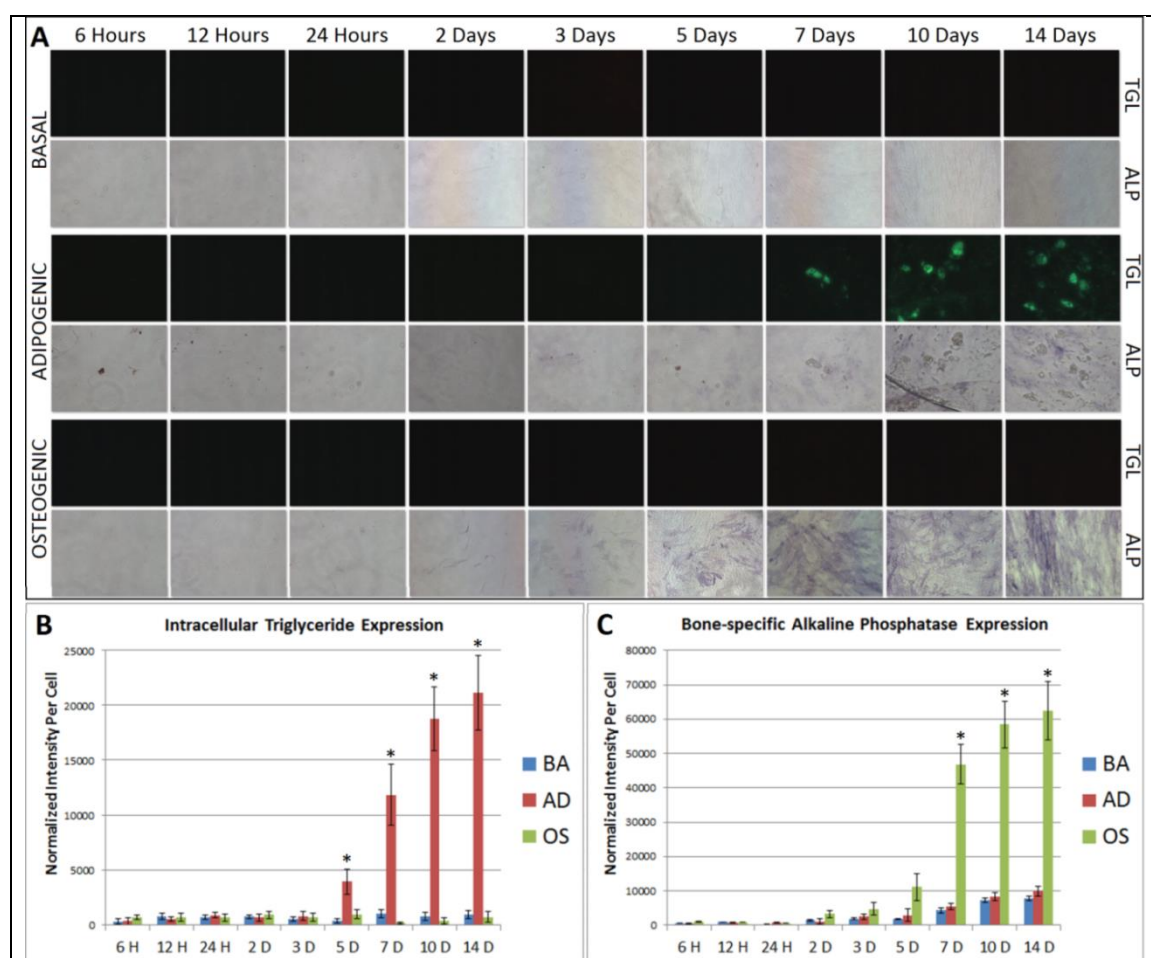


Figure 3.2. Lineage staining quantification of hMSCs induced to differentiate towards adipogenic and osteogenic lineages was performed by staining for intracellular triglyceride (TGL) accumulation and bone-specific alkaline phosphate (ALP) expression, respectively (A). Distinguishable expression of these markers occurred after 7 days for ALP (B) and 5 days for TGL (C), with steady increased expression thereafter. Statistical significance was evaluated by One-way ANOVA with Tukey post hoc test. * $p < 0.05$

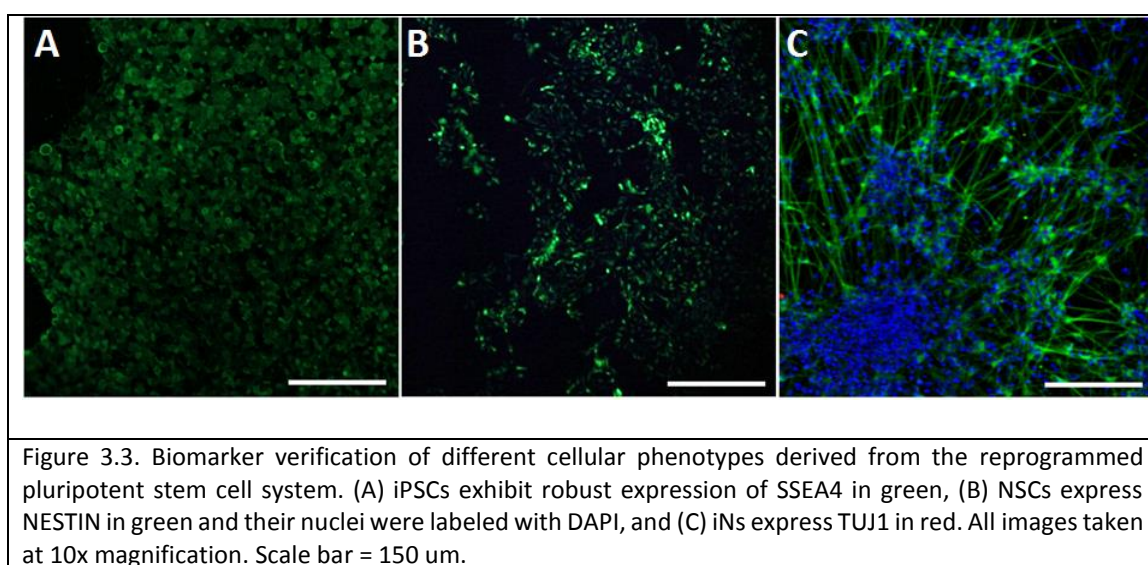
phosphatase expression (**Figure 3.2A**). Intensities of the stains were quantified and normalized to cell count, as assessed by DAPI labeling (**Figure 3.2B&C**).

It is clear that the media formulations used gave rise to the correct cell phenotypes, with a continuous increase in each lineage stain with time. Significant differences in

intracellular triglyceride expression did not occur until 5 days post-induction, whereas significant differences in bone-specific alkaline phosphatase expression took 7 days post-induction. hMSCs cultured in basal media maintained low levels of both stains throughout the 2 week period.

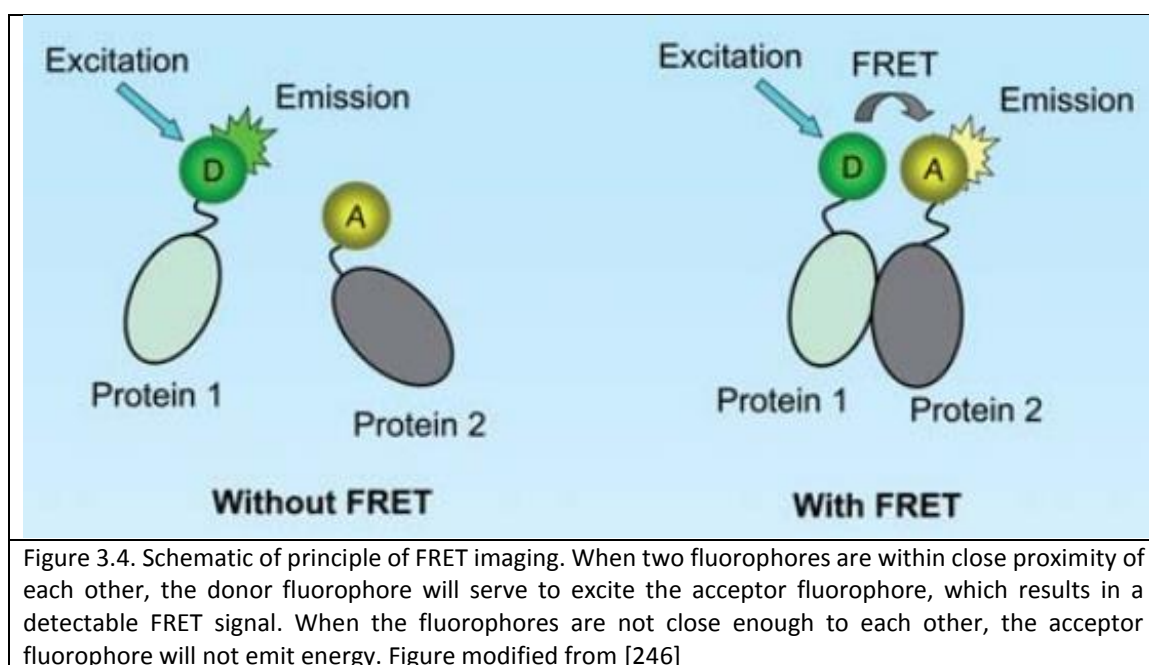
3.3.2 Biomarker Verification of iPSCs, NSCs and iNs

The successful cellular reprogramming of HFF-1's to iPSCs and subsequent induced differentiation of iPSCs to NSCs and iNs was verified using immunological labeling of biomarkers unique to each cellular phenotype. Briefly, HFF-1's were transfected with a lentivirus consisting of OCT4, SOX2, Klf4 and c-myc to yield iPSCs. iPSCs were differentiated to NSCs with a media cocktail consisting of B27 supplement and brain derived neurotrophic factor (BDNF). iNs were generated from iPSCs via retroviral transduction with the factors Brn2, Ascl1 and Myt1. Each cell phenotype was subsequently fixed and immunolabeled for biomarkers unique to each respective cell type (**Figure 3.3**)



3.3.3 Forster Resonance Transfer Analysis of H3K4K27me3 Bivalency

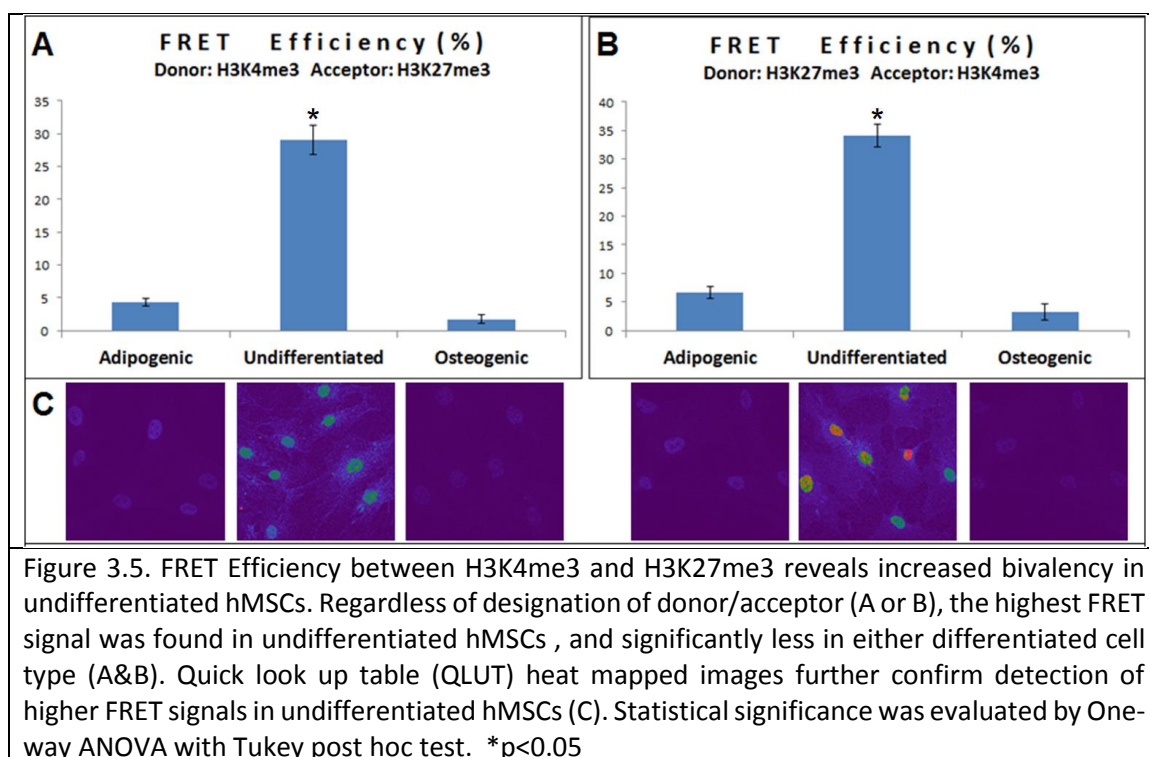
The quantitative measurement of relative co-localization can be determined using Forster resonance energy transfer (FRET). The principle of FRET is based on the energy transfer between two fluorophores which are in close proximity of each other. These two fluorophores are conjugated to two proteins of interest, where the lower wavelength energy emitting fluorophore is designated as the donor, and the higher as the acceptor. The donor is excited with a laser at a specific excitation wavelength, and the energy emitted is transferred to the acceptor fluorophore through a dipole-dipole coupling mechanism. The acceptor fluorophore is then able to emit some energy, and this energy is captured and quantified (**Figure 3.4**). A common quantitative expression of relative FRET signal is FRET efficiency, which is the proportion of donor fluorophores that have transferred energy to acceptor fluorophores [245]. This value increases as the distance between the donor and acceptor fluorophores decreases, and has a value of zero if the donor and acceptor fluorophores are further than approximately 10 nm from each other. Thus, FRET imaging is an efficient and accurate method to determine fluorophore proximity and protein-protein interaction in cells.



In the context of the epigenome, there are numerous modifications to chromatin that are categorized as bivalent, which indicates two marks with opposing effects on gene transcription (i.e. activation & repression) that occur in the same area (i.e. on the same nucleosome unit) [209, 210]. An effective way to assay for global levels of bivalency in nuclei is through the quantification of the FRET efficiency that occurs between two fluorescently labeled candidate bivalent marks. This can be accomplished by either transfecting cells with fluorescent fusion proteins tagged to bivalent marks of interest [247], or immunocytochemically labeling cells after fixation. For opposing bivalent modifications, this FRET approach can be used to quantify relative levels of gene activating vs. silencing marks as stem cells develop, and can also be applied to screen larger libraries of drugs/materials using high-throughput platforms. While FRET can be a tool for assaying for bivalency in different contexts, it is limited to a kind of end-point

reporter value, and minimally addresses the dynamics of chromatin modifications in real time.

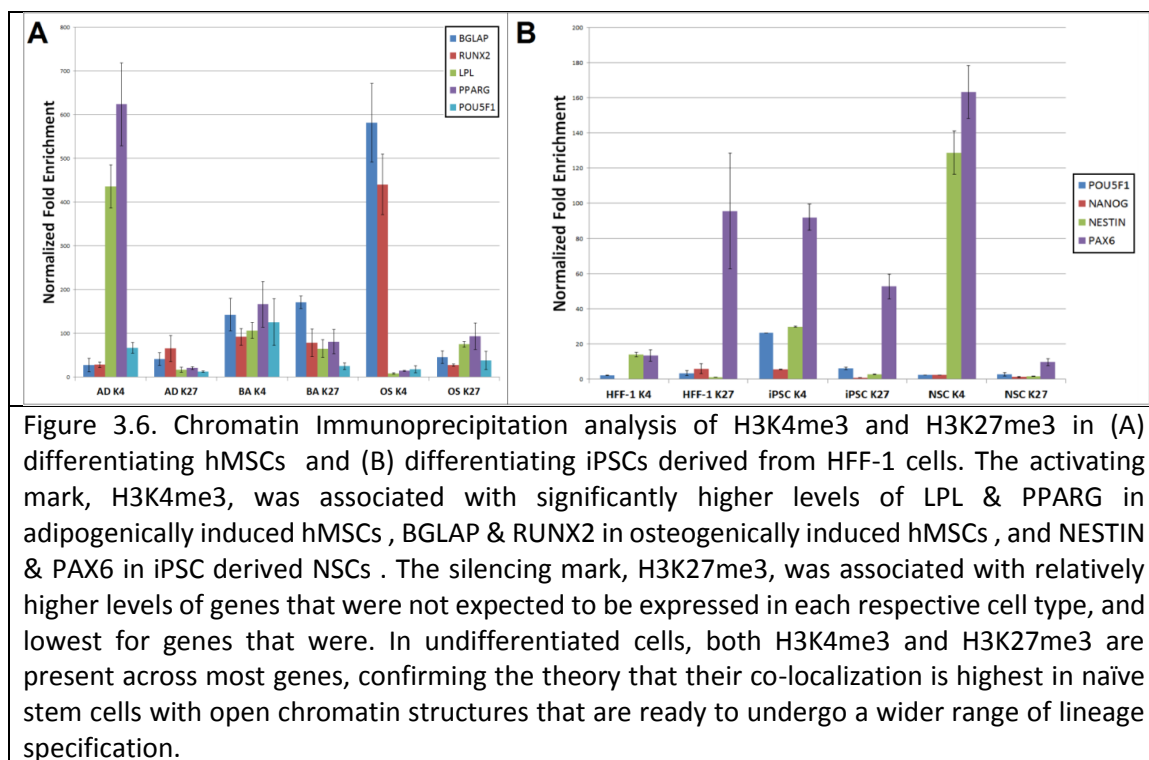
Thus, in order to determine the proximal bivalency and balance shifts of H3K4K27me3 in differentiating hMSCs, we employed Förster resonance energy transfer (FRET) imaging. A high H3K27me3 : H3K4me3 ratio is indicative of a closed chromatin structure that silences genes in terminally differentiated cells, whereas a high H3K4me3 : H3K27me3 ratio reflects an open chromatin structure which activates genes in naïve cells actively undergoing lineage specification [209]. Similar H3K4me3 and H3K27me3 expression levels reflect the presence of bivalency, where developmental genes are largely silenced, but are simultaneously primed for activation (**Figure 2.1**). This was quantitatively validated by determining the FRET efficiency in undifferentiated, osteogenic and adipogenic hMSCs labeled with H3K4K27me3. Regardless of which PTM acted as the donor fluorophore, the highest FRET efficiency occurred in undifferentiated hMSCs, indicating a higher presence of bivalency between the two marks, and significantly lower FRET signals in either differentiated cell type (**Figure 3.5**).



3.3.4 Chromatin Immunoprecipitation of H3K4K27me3

The role of these selected PTMs in regulating key developmental genes during differentiation was confirmed using chromatin immunoprecipitation (ChIP). The same antibodies used for immunocytochemical labeling were used to immunoprecipitate crosslinked DNA:protein fragments of 200-1000 kilobases. Cut DNA fragments were achieved via sonication, and length was assessed by agarose gel electrophoresis (**Supplementary figure S3.2**). These ChIP'd fragments were then used in the amplification of key developmental genes relevant to osteogenic, adipogenic and neural differentiation via qRT-PCR. It is clear that the activating mark H3K4me3 plays a crucial role in promoting the transcription of the correct developmental genes relevant to each cell type, whereas the silencing mark H3K27me3 serves to prevent the transcription of unwanted genes

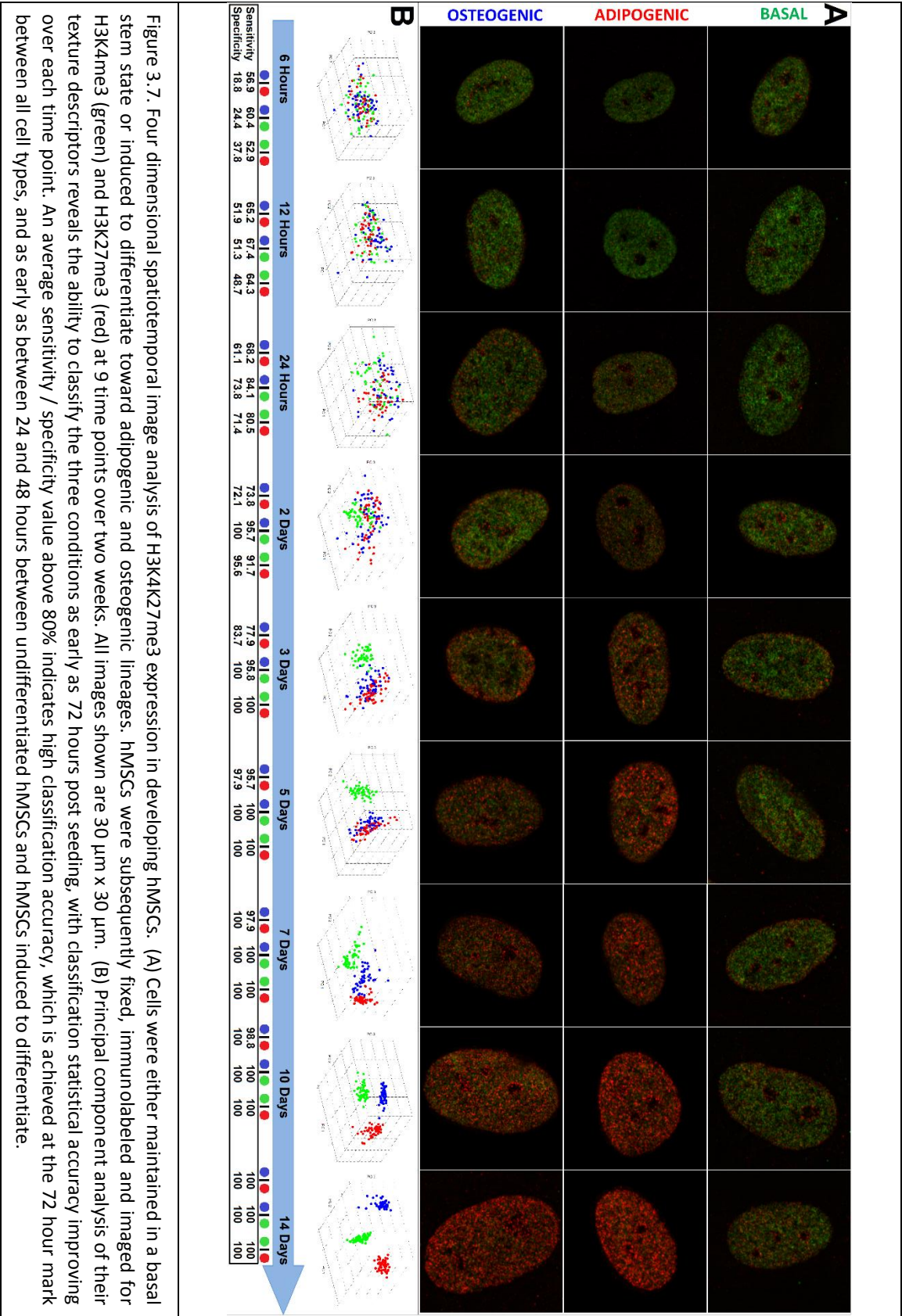
(Figure 3.6). In undifferentiated cells, both H3K4me3 and H3K27me3 are present across most genes, confirming the theory that their colocalization is highest in naïve stem cells with open chromatin structures which are ready to undergo a wider range of lineage specification.



3.3.5 Four Dimensional Spatiotemporal Analysis of H3K4K27me3 Dynamics in hMSCs

After calibrating quantitative texture descriptors according to controlled states of H3K4K27me3 manifestation, we investigated the potential ability to detect early distinctions in H3K4K27me3 prior to the onset of downstream gene transcription changes. hMSCs were cultured on glass coverslips and differentiated towards adipogenic and osteogenic lineages by including the appropriate soluble growth factors in their growth

media, as previously described [191]. They were subsequently fixed in 4% paraformaldehyde along 9 time points over a 2 week period (6 and 12 hours, 1, 2, 3, 5, 7, 10 and 14 days). These cells were subsequently immunolabeled for H3K4K27me3, imaged and analyzed (**Figure 3.7**). A shift in balance towards a higher H3K27me3:H3K4me3 ratio as hMSCs are induced to differentiate towards adipogenic or osteogenic lineages is qualitatively apparent, compared to the basal control (**Figure 3.7A**). However, distinctions between H3K4K27me3 expression in adipogenically and osteogenically induced hMSCs are not apparent by eye. Thus, in an effort to detect potential differences in phenotypically distinct H3K4K27me3 organization, Haralick texture image analysis was employed. 104 quantitative textural descriptors were acquired for each cell and subsequently classified by reducing these large descriptor dataset to 3 dimensions using principal component analysis. After applying PCA analysis to descriptor sets acquired from each time point, it was revealed that these three cell types were able to be classified from each other as early as 72 hours (**Figure 3.7B**), 2-4 days prior to the significantly distinguishing onset of any functional markers (**Figures 3.2**). Classification statistics also improved over each time point, and k-means cluster analysis revealed that the centroids of each cell type cluster also increased in three-dimensional spatial distance from each other over each time point. Perfect classification (i.e. 100% sensitivity & specificity) was achieved after 2 weeks, therefore the coordinates of centroids of cell phenotypes differentiated for 2 weeks were referenced in subsequent biomaterial screening experiments.



3.3.5 Texture Image Analysis of H3K4K27me3 in HFF-1 Derived Differentiating iPSCs

High resolution confocal images were acquired from cells that were immunocytochemically labeled using the same ChIP-grade antibodies used in the ChIP assay (**Figure 3.8A**). Based on the expression of H3K4K27me3, different functionally distinct phenotypes were clearly classified from each other with 100% statistical accuracy (i.e. 100% specificity and sensitivity) (**Figure 3.8B**). Furthermore, cells that have been transfected with a lentivirus (i.e. iPSCs, NSCs and iNs) are clearly distinguished from HFF-1s, suggesting that the H3K4K27me3 expression of these cells corresponds to the phenotypic alteration of these cells (**Figure 3.8B**). These results indicate the ability of our texture analytical approach to capture differences in organizational patterns of H3K4K27me3 in different cell phenotypes other than hMSCs.

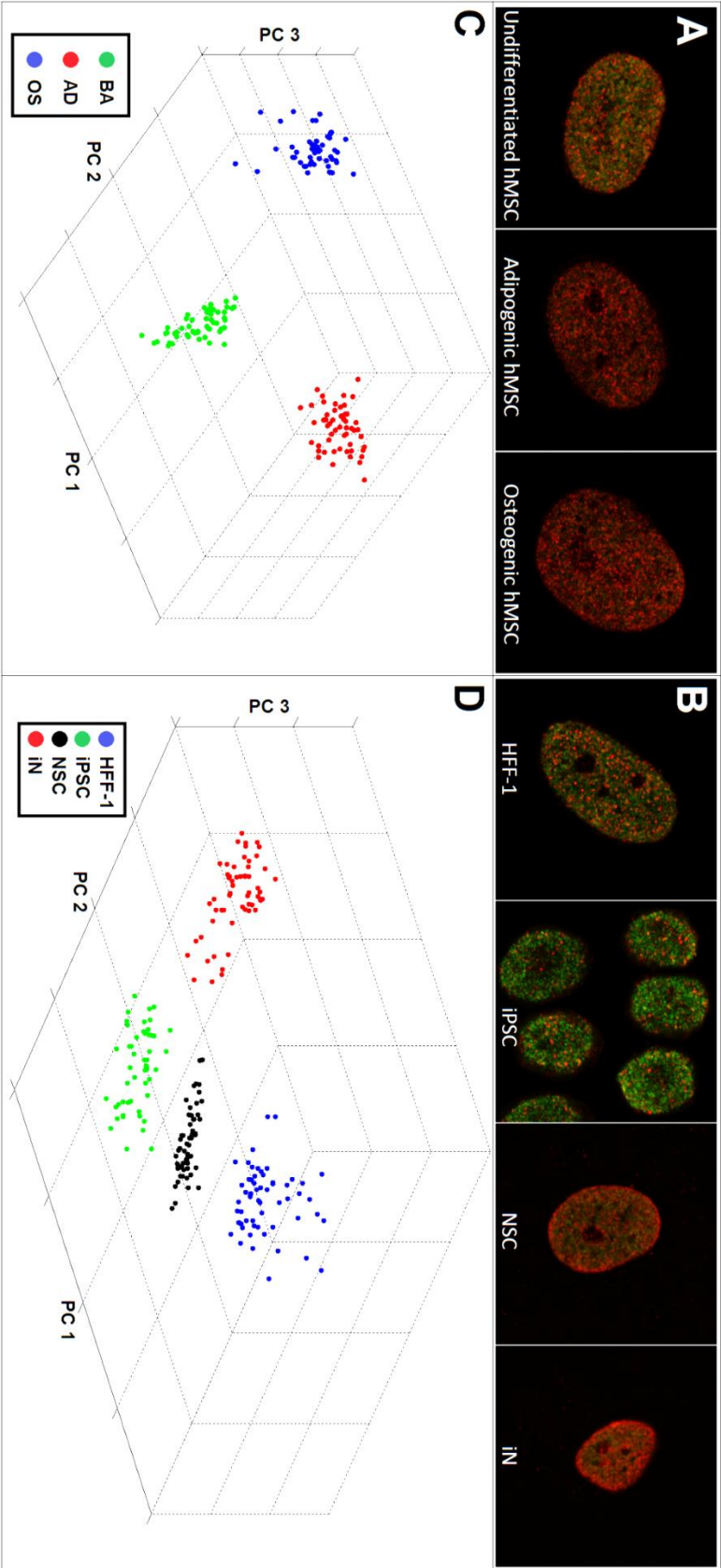
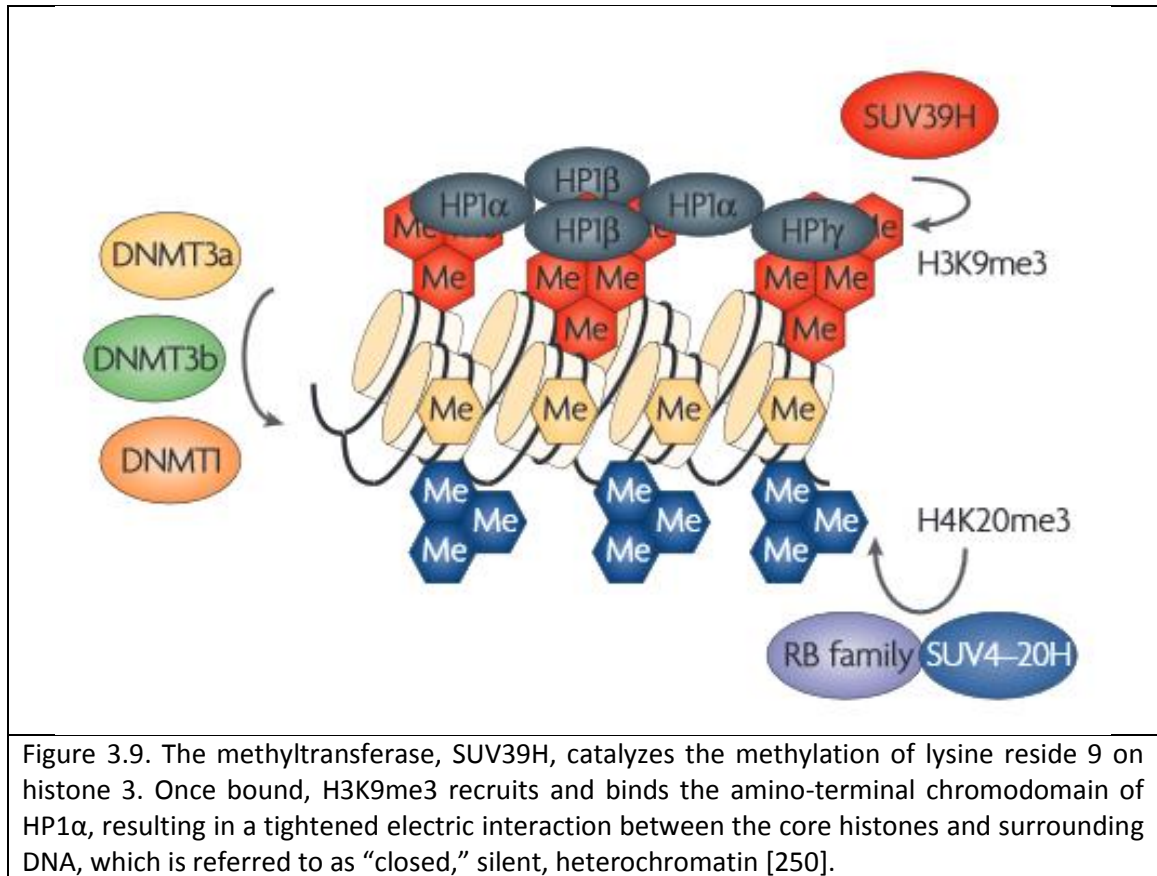


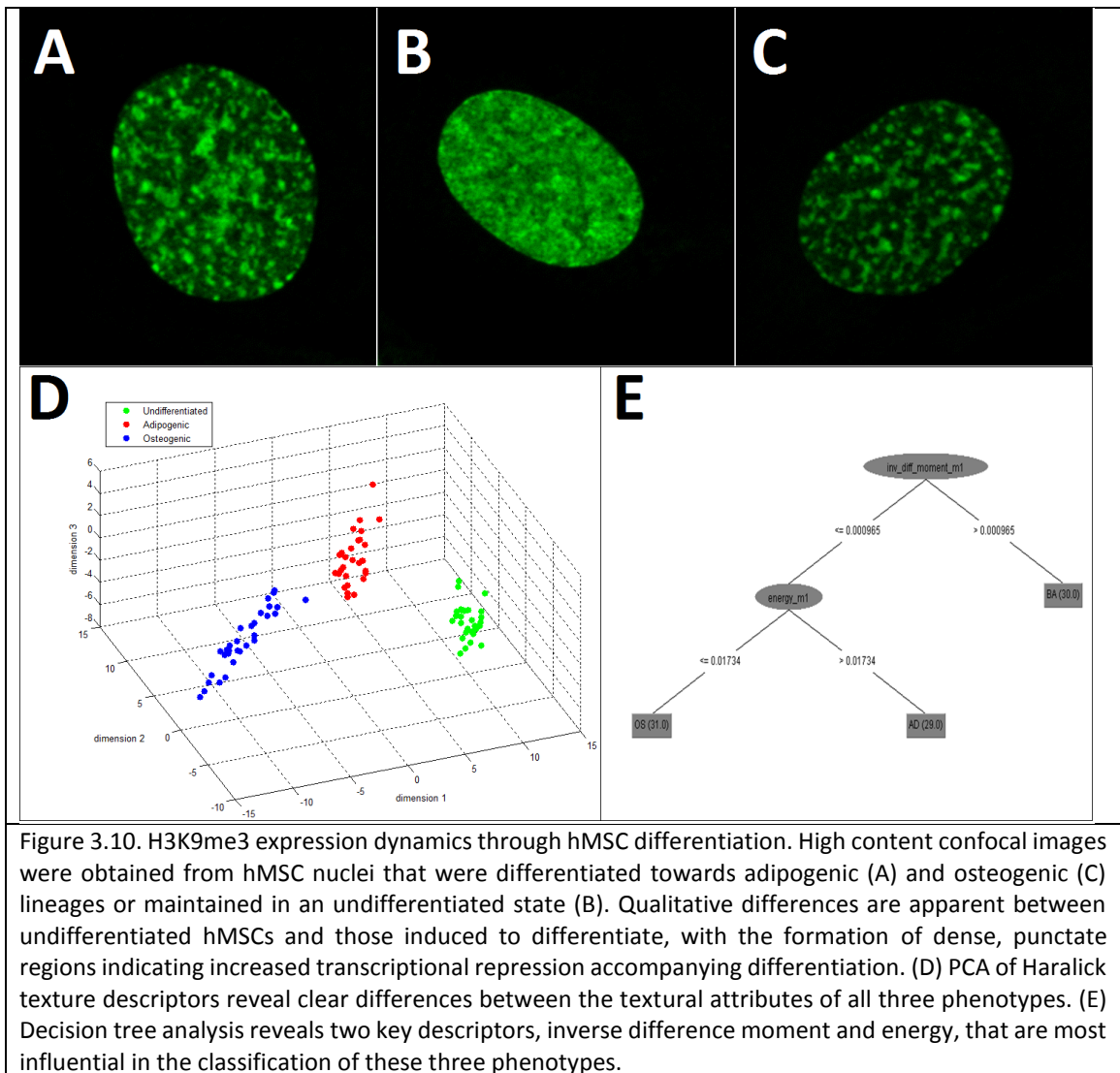
Figure 3.8. H3K4K27me3 is dynamically regulated and differentially expressed throughout stem cell differentiation. (A&B) High content LSCM G-STED images and corresponding quantitative texture descriptors of cells immunolabeled for H3K4me3 (green) and H3K27me3 (red) were acquired and subsequently analyzed via principal component analysis (C&D), which reveals the ability to clearly classify each different cellular phenotype from each other based on H3K4K27me3 textural expression with 100% sensitivity and specificity. All images are 30 x 30 μm .

3.3.6 Dynamics of HP1 α and H3K9me3 as a Response to Differentiation Cues

The ever dynamic and functionally relevant balance between heterochromatic versus euchromatic regions largely influences a cell's gene transcriptional state and subsequent development and function. Although the formation of specific chromatin structural states is orchestrated by numerous different PTMs, chromatin remodeling complexes and DNA methylation states, there are certain players that play a much larger role in directly facilitating chromatin condensation and heterochromatin formation. Of these, two more widely investigated marks are H3K9me3 and Heterochromatin protein 1 alpha (HP1 α). These two marks work in concert to facilitate transcriptional repression, as the trimethylation of lysine residue 9 on histone 3 recruits and binds the amino-terminal chromodomain of HP1 α [248-250]. Once HP1 α is bound to the nucleosome, resultant chromatin condensation and heterochromatin formation contributes to the silencing of genes in its immediate vicinity [251] (**Figure 3.9**). Thus, there is a clear cooperative impact of these two marks on gene silencing and subsequent cellular differentiation.



We investigated the potential for these marks to reflect different perspectival aspects of epigenetic state and chromatin structural organization. Similarly to H3K4K27me3, we immunolabeled differentiating hMSCs with H3K9me3 ChIP-grade antibodies, acquired high content images and quantified and analyzed their textural properties. Interestingly, the heterochromatic areas were visually much more apparent and condensed appearing in both differentiating cell type, whereas less apparent, and more diffuse in undifferentiated hMSCs (**Figure 3.9A-C**).



Principal component analysis reveals a clear ability to distinguish between the three cellular phenotypes, with either differentiated cell type closer in proximity to each other when compared to the undifferentiated hMSCs (**Figure 3.10D**). Data mining analysis of the most influential descriptors (highest eigenvector coefficients) to the formation of the principal components reveals two key descriptors, Inverse Difference Moment and Energy, both of which are descriptors of levels of homogeneity within an ROI. Based on these data mining results, it seems that osteogenic cells display the least amount of

homogeneity, indicating a more random nature of their punctate, heterochromatic regions. Adipogenic cells are less disordered, and undifferentiated cells clearly exhibit the greatest degree of homogeneity in the distribution of H3K9me3.

3.4 Discussion

The main objective of this chapter was to quantitatively capture unique organizational patterns of transcriptionally relevant epigenetic marks in stem cells developing towards different functional phenotypes. Since the epigenetic events that orchestrate the activation / silencing of specific genes occur upstream of transcription, we hypothesized that capturing such dynamic differences in PTM manifestation early in development may be predictive of how a stem cell is going to differentiate. We found this to indeed be the case in developing hMSCs, with unique H3K4K27me3 expression signatures able to be detected as early as 48-72 hours after induction initiation. Qualitative observations of H3K4K27me3 expression temporal dynamics in differentiating hMSCs reveal that the intensity of H3K27me3 increases as hMSCs commit to a particular lineage (**Figure 3.7**). Therefore, we explored intensity based descriptors of H3K4K27me3 as potential characterizers of cell fate. However, it was quickly revealed that intensity alone may provide some insight into whether or not a cell is beginning to differentiate, but is not sufficient for distinguishing differently differentiated phenotypes (**Figure 3.11**).

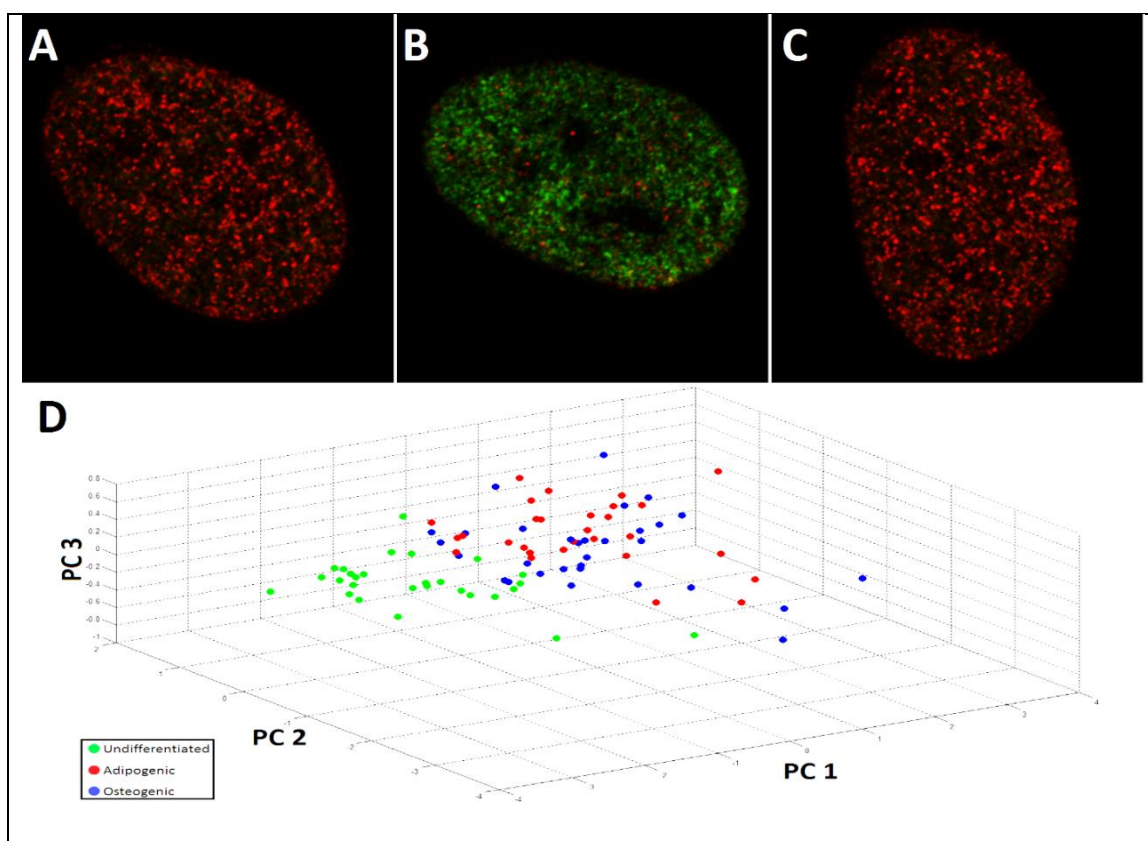
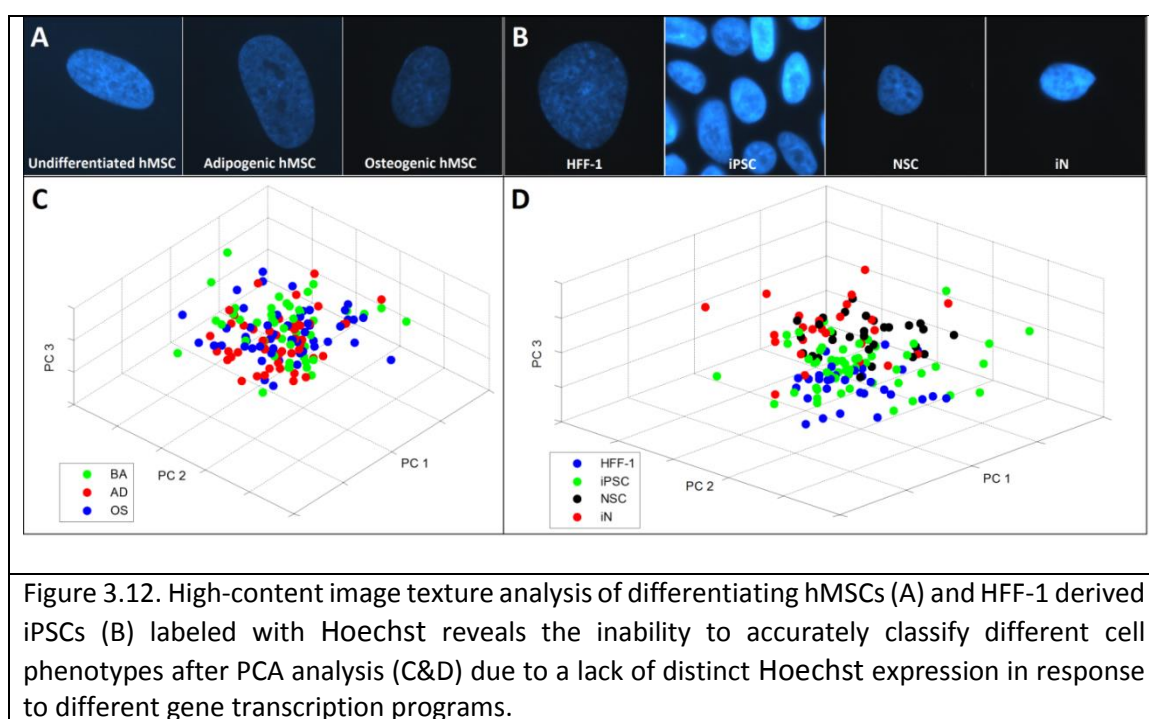


Figure 3.11. Intensity quantifications alone are not sufficient to accurately characterize and classify different cell phenotypes. Adipogenic (A), Osteogenic (C) and undifferentiated hMSCs (B) were labeled with H3K4me3 and H3K27me3 and intensity descriptors (mean, sum, standard deviation) were obtained. (D) PCA plot of these descriptors reveal their inability to accurately detect and classify differences in H3K4K27me3 expression between osteogenic and adipogenic hMSCs. Undifferentiated hMSCs were able to be distinguished from either differentiating cell type based on intensity, but with far less accuracy when compared to texture descriptors.

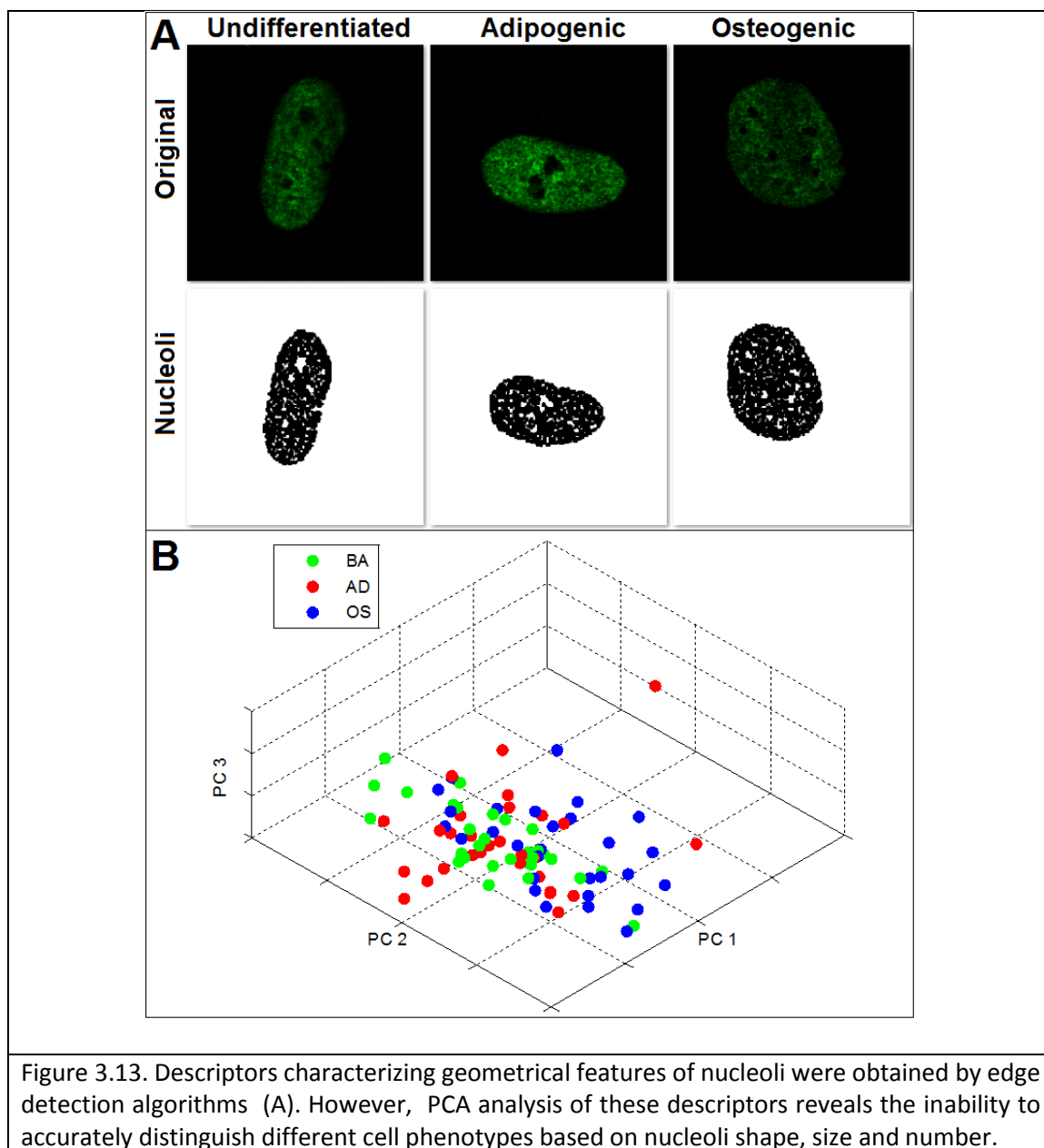
We further investigated the potential of other nuclear markers and features that are not as directly relevant to cellular differentiation to characterize and classify different cell phenotypes. After labeling different cell phenotypes with the common nuclear fluorescent stains 4',6-diamidino-2-phenylindole (DAPI) and Hoechst 33342, we obtained their Haralick texture descriptors and employed PCA. Since these dyes are known to ubiquitously bind to all nucleic acids, quantifications of their texture was not found to be unique to different cellular phenotypes (**Figure 3.12**). These findings further emphasize

the importance of the correlative expression of specific proteins to cellular behavior for meaningful image analysis. Although this study was limited to an investigation of methylation of Histone 3 and heterochromatin formation, there are a host of other nuclear markers whose textural organization could potentially provide meaningful insight into the behavioral state of a cell. The investigation of more PTMs and other relevant nuclear proteins using this approach has the potential to provide an increasingly comprehensive characterization of a cell's gene transcriptional state.



Another feature that was explored was the size, shape and number of nucleoli in differentiating cells. However, upon analysis of these features, it became clear that they were not sufficient for distinguishing different cell types from each other (**Figure 3.13**). This is most likely due to the fact that all cells analyzed were cell-cycle synchronized, and

it has been reported that nucleoli patterns and growth dynamics change according to where cells are along in their cell cycle [211].



We also investigated the potential of other mathematically rigorous algorithms for characterizing phenotype-specific nuclear features, including 52 grey features, 192

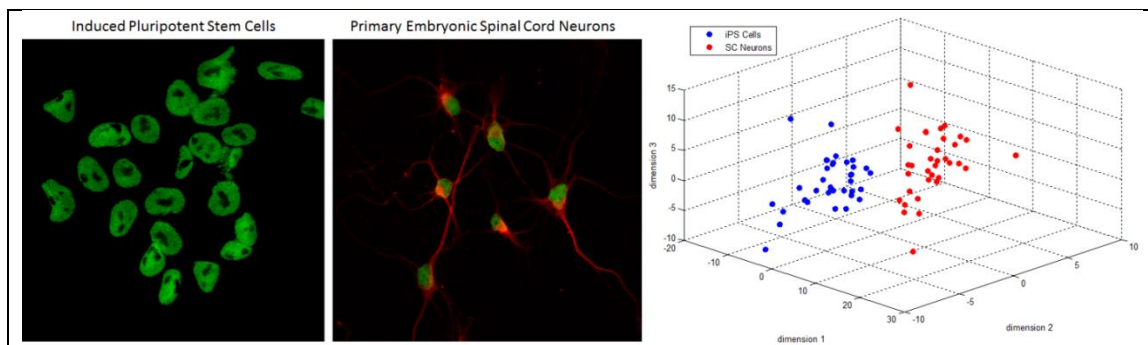
Figure 3.14. J48 Decision tree of a total of 396 descriptors (52 grey features, 192 Gabor filter features, 104 Haralick texture features and 48 Haar wavelet features) of H3K4K27me3 expression in adipogenic, osteogenic and undifferentiated hMSCs. Out of the 396 total descriptors, the decision tree identified a total of 32 nodes, and out of the 32 nodes, 31 of them were Haralick texture descriptors, clearly indicating their relevance over the other features.

Gabor filter features and 48 Haar wavelet features. After combining all of these features with the 104 Haralick texture features, we analyzed this entire dataset of 396 features with WEKA decision tree (**Figure 3.14**). This classification tree identified a total of 32 nodes, of which 31 were Haralick texture features, which indicates their relatively higher sensitivity to capturing phenotype-specific features of H3K4K27me3 organization.

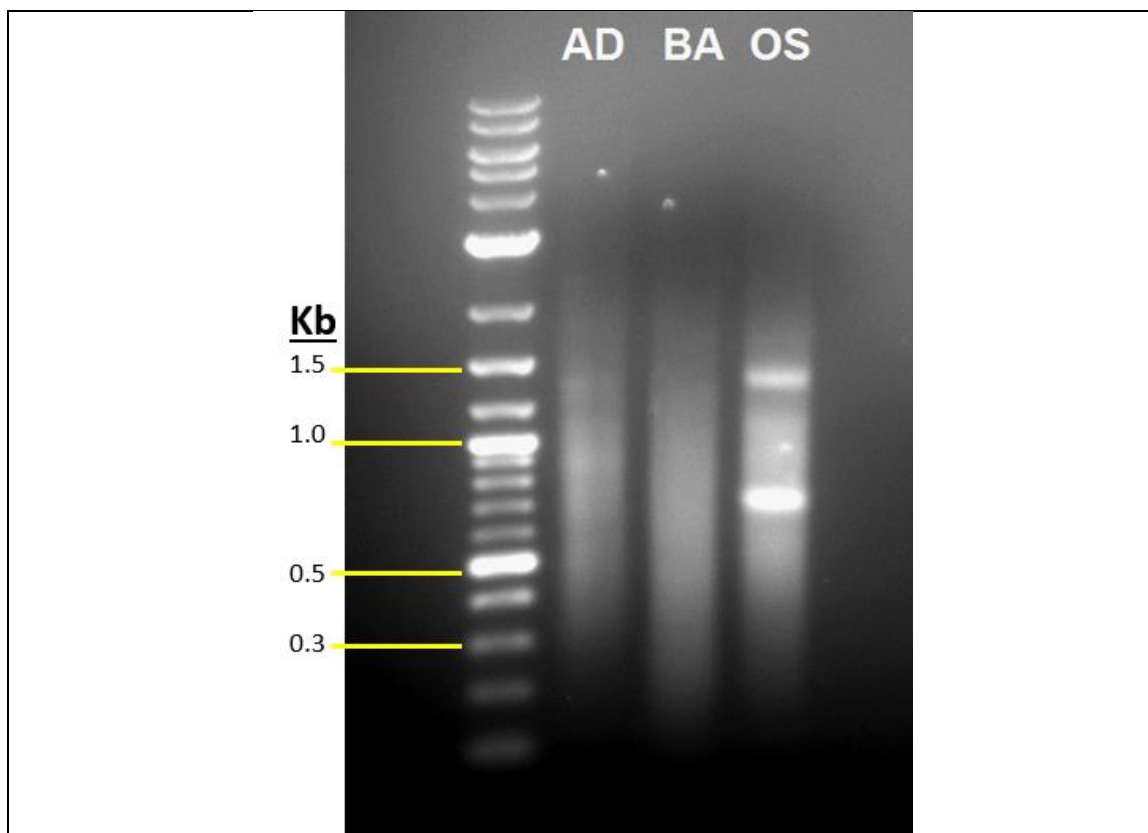
3.5 Conclusion

In summary, this high-content textural image analytical tool provides a unique perspective on chromatin structural dynamics and their influence on gene transcription regulation. It is relatively easy to perform and substantially reduces the time and costs required for more comprehensive methods of interrogating the epigenome, thus making it a good place to begin investigations, as well as supplement data, on the structural dynamics of chromatin as a response to epigenetic modifications. With the incorporation of additional PTM organizational data, and other developmental stem cell systems, this type of bioimage information can potentially be archived and referenced for future drug and biomaterial property screening. Initial explorations of applying this tool to cells cultured on two well-defined material systems is summarized in the next chapter.

3.6 Supplementary Figures



Supplementary Figure S3.1. HP1 α expression in two different phenotypes: Induced pluripotent stem cells and mouse embryonic spinal cord neurons. Expression of this heterochromatin marker is starkly different in pluripotent cells compared to in differentiated neural cells.



Supplementary Figure S3.2. Agarose gel electrophoresis of sonicated DNA from three mesenchymal stem cell based phenotypes (AD: adipogenic, OS: osteogenic, BA: undifferentiated). The DNA length range for all three types is from 200-1500 bp, with the bulk of the fragments in the range of 500-1000 bp.

CHAPTER 4: MECHANICAL, CHEMICAL AND TOPOGRAPHICAL INFLUENCES ON CHROMATIN ORGANIZATIONAL DYNAMICS AND DIFFERENTIATION

4.1 Introduction

The design of effective biomaterials for tissue engineering requires a comprehensive understanding of the microenvironment of the tissue/organ of interest. The varying nanoscale structures contained in different tissue-types provide specific physical cues to the cells comprising it in order to guide their proper growth, survival and functionality [252]. This regulation of cellular behavior is further coordinated by intracellular and extracellular protein signaling pathways that respond to and actively manipulate both physical and chemical parameters [253-256]. A vital element to proper tissue development and maintenance is the organization and composition of the extracellular matrix (ECM), which serves as a naturally produced scaffolding for different cellular phenotypes [257]. Not only does the protein abundant ECM provide vital cues to cells to guide cellular behavior, but cells provide feedback to their ECM by actively interacting with and remodeling their surrounding matrix [258, 259]. In fact, many cell phenotypes grown *in vitro* do not mimic the behavioral properties of their *in vivo* counterparts without the prerequisite of at least an ECM-like environment, and some cell types cannot begin to even survive without it [260]. Thus, it is clear that successful biomaterial design relies on the careful construction and provision of specific microenvironmental elements that mimic *in vivo* tissues and are optimal for cell survival and functionality.

Studies in the field of tissue engineering to date have been permeated with investigations on how cells are affected by defined perturbations to physical and chemical properties of their immediate microenvironment. There is a quite large, diverse range of substrates that have been studied, with materials that vary rigidity [261-263], topography [157, 264-266], geometry [156, 267, 268], growth factor incorporation [269-271], electrical properties [272], sheer stress [273-275] and quite many others [276-279]. The overtly distinct responses of cells to different materials are perhaps not surprising, and these responses have been detected and thoroughly studied via analyzing differences in protein and gene expression. However, it is critical to note that all of these cell behavioral changes, which are a result of these differences in protein and gene expression, are orchestrated and enforced by epigenetic mechanisms. This is precisely how so many morphologically and functionally distinct cell phenotypes are achieved despite their possession of a common DNA backbone. Thus, these epigenetic modifications are at the core of navigating all cellular development. Although the current paradigm for controlling cellular behavior is rooted in manipulating secondary downstream mechanisms of gene and protein expression, the increased comprehension of dynamic epigenetic landscapes has the potential to provide a much greater degree of cell behavioral control. In fact, one can argue that the changes to gene and protein expression that are observed from changes to a cell's microenvironment are really a result of upstream epigenetic responses to the environment.

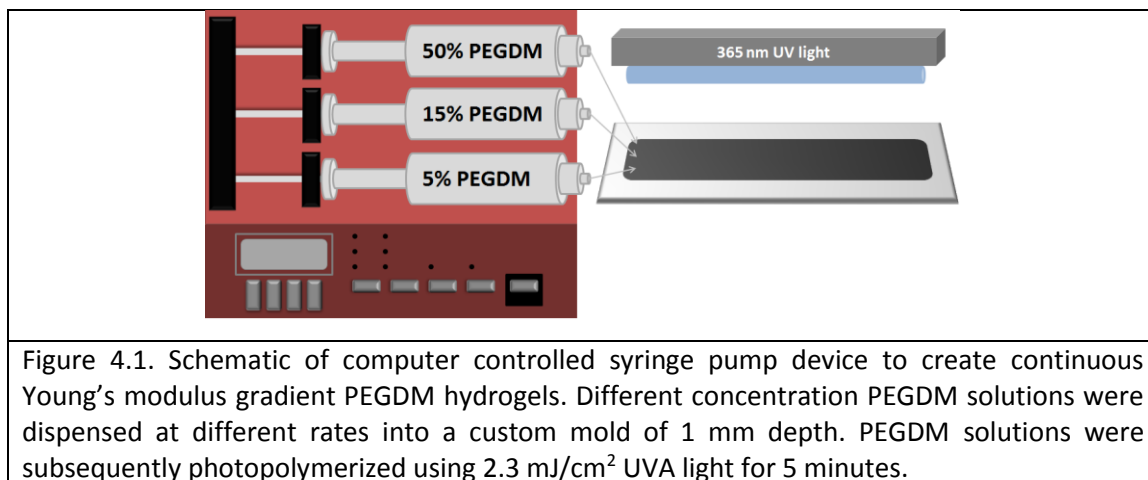
Thus, in order to achieve optimal control over cellular behavior, it is necessary to understand and exploit the links between the physicochemical properties of the

microenvironment, the transcriptionally related modifications that occur in the nucleus, and the resultant cellular behavior. To this end, we investigated the segregated influence of defined mechanical, topographical and chemical properties of biocompatible materials and epigenetic drugs on cellular development by systematically varying substrate stiffness, nanotopography, and histone-3 N-terminal tail methylation. We subsequently investigated their individual and combinatorial influence on H3K4K27me3 organizational expression and related this to differentiation patterns of hMSCs. The ultimate goal of such studies is to facilitate the identification of ideal combinations of biomaterial properties that drive hMSCs towards specific cell fates.

4.2 Materials and Methods

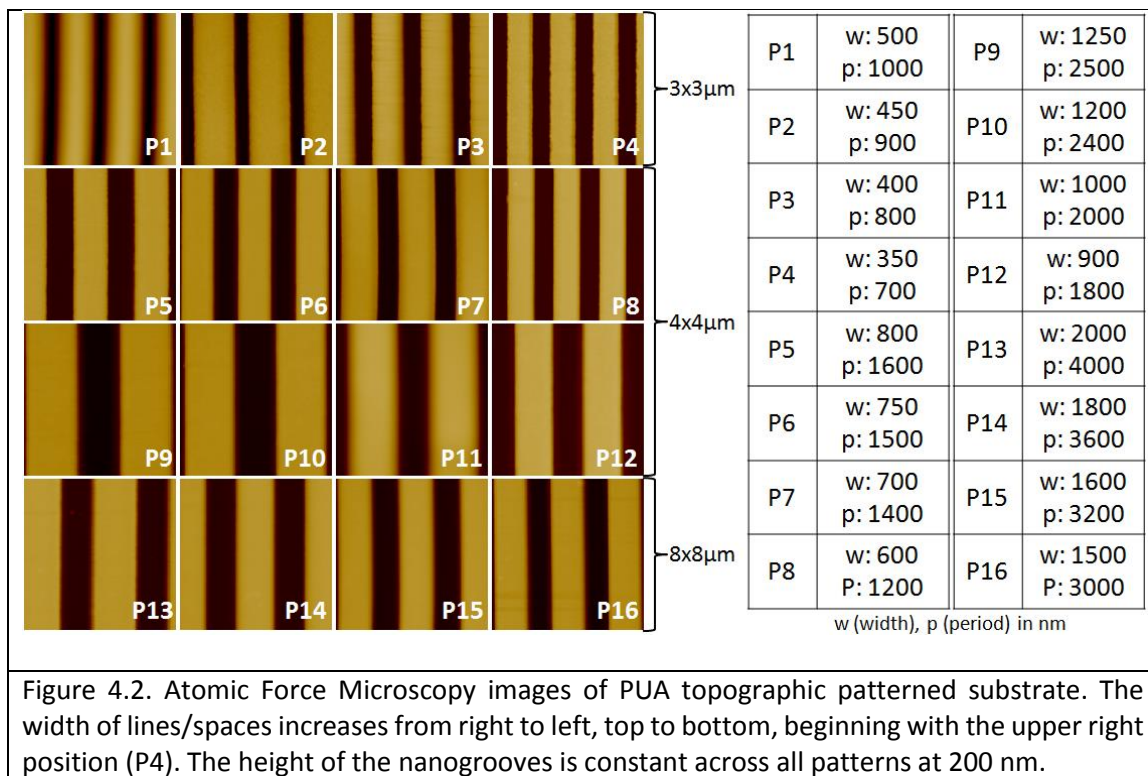
4.2.1 PEGDM Continuous Young's Modulus Gradient Hydrogel Fabrication

Continuous Young's modulus gradient PEGDM hydrogels were fabricated using this computer controlled, multi-syringe pump device. PEGDM solutions of three different concentrations (5%, 15% and 50%) were dissolved in Opti-MEM media (Life Technologies) containing 0.1% Irgacure 2959 (Ciba Specialty Chemicals, Basel, Switzerland). The computer controlled, multi-syringe system was used to dispense 15% and 50% PEGDM solutions into a custom mold (**Figure 4.1**). These solutions were dispensed in an inverse ramp manner, ranging from 55 ml/hr down to 0 ml/hr over 90 seconds. The 5% PEGDM solution was dispensed at a constant rate of 10 ml/hr. The PEGDM hydrogels were subsequently photopolymerized by exposure to 2.3 mJ/cm² UVA light for a period of 5 minutes, then submerged in Opti-MEM medium for storage [280].



4.2.2 Fabrication of Polyurethane Acrylate Topographically Patterned Substrate

Controlled topographical patterns of 16 varying line width and space were fabricated from poly urethane acrylate (PUA) resin (Minuta Technologies, Gyeonggi-Do, South Korea) containing 10% (v/v) acrylic acid. Using a soft-lithography technique, 20 μ l of the PUA/acrylic acid mixture was dropped onto a polystyrene slide (Thermo Scientific) and polydimethylsiloxane (PDMS) stamps with defined line and space patterns were subsequently pressed onto the PUA/acrylic acid droplet. This construct was subjected to UV light (3 mW/cm²) for 10 minutes, after which the stamp was removed. The resultant patterned substrate was cured for an additional 6 hours under UV light and then washed with warm 2-propanol (Fisher Scientific) for 3 hours, and then thoroughly rinsed in dH₂O prior to cell culture. Measurements of nanogroove widths and spacings were confirmed using atomic force microscopy (**Figure 4.2**).



4.2.3 k-Means Cluster Analysis

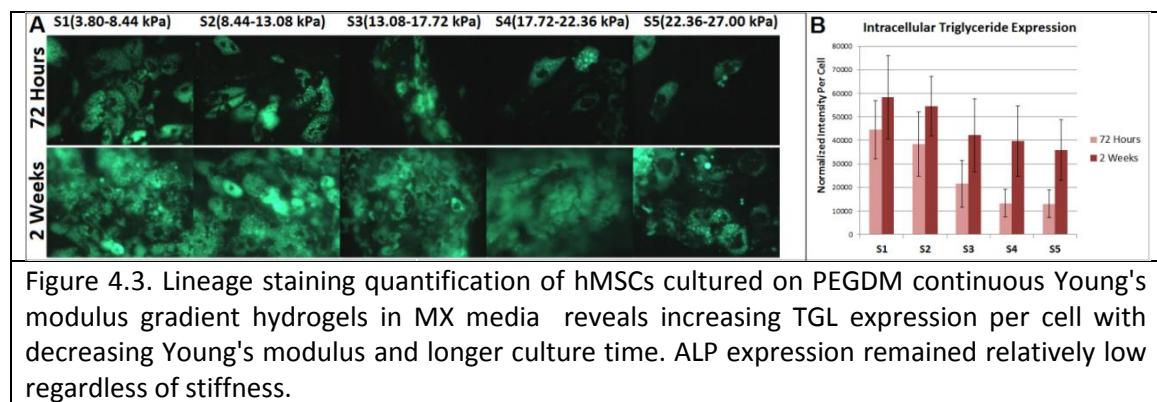
In order to relate the three dimensional PCA spatial identities of predifferentiated hMSCs to those cultured on different biomaterial substrates, we employed k-means cluster analysis. The main algorithm employed was provided as part of MATLAB'S Cluster Analysis package, which is part of MATLAB'S Statistics toolbox (Mathworks). The three dimensional spatial coordinates of the centroids of clusters of hMSCs cultured in different defined conditions were determined and plotted in relation to those of predifferentiated hMSCs. Distances between centroids were calculated using the distance formula, where closer proximity indicated greater similarity in H3K4K27me3 organizational expression.

4.3 Results

4.3.1 hMSC Differentiation as a Response to Young's Modulus Gradient

hMSCs were cultured on a PEGDM continuous modulus gradient hydrogel ranging in stiffness from 3.8 to 27 kilopascals (kPa) with a uniform topographical profile and a constant concentration of the RGD peptide. Cells were cultured in a 50:50 cocktail of osteogenic:adipogenic induction media and fixed at early (72 hours) and late (2 weeks) time points. The PEGDM substrate was subdivided into five equal sized regions, and hMSCs were stained for intracellular triglycerides, bone-specific alkaline phosphatase and DAPI, as previously described in section 3.2.2.

On the PEGDM stiffness gradient hydrogel, hMSCs that were cultured on the least stiff section of the hydrogel (3.8-8.44 kPa) exhibited the greatest amount of intracellular triglyceride formation per cell at both the early (72 hours) and late (2 weeks) time points. hMSCs expressed baseline levels of bone-specific alkaline phosphatase on all parts of the hydrogel at both time points, indicating that this substrate is not conducive to osteogenic differentiation (**Figure 4.3**).



4.3.2 Texture Image Analysis of H3K4K27me3 Dynamics in hMSCs on PEGDM Substrate

In parallel to differentiation staining, hMSCs were cultured on the PEGDM substrate in preparation for immunocytochemical analysis. Cells were fixed at early and late time points, immunolabeled for H3K4K27me3 and imaged (**Figure 4.4**). Texture descriptor datasets were extracted from a minimum of 30 nuclei cultured on each of the five subdivided regions. K-means cluster analysis was subsequently performed to determine the centroids of the descriptor sets of cells from each region, and these centroids were subsequently plotted to compare to the centroids of pre-differentiated hMSCs (**Figure 4.4C**). Centroids of cells cultured on the softest region of the gel (S1) were closest in proximity to the centroid of pre-differentiated adipocytes, even at the early timepoint (72 hours), which also correlated with the highest levels of intracellular triglyceride staining (**Figure 4.3**). Centroids of hMSCs cultured on increasingly stiffer regions of the gel were shown to migrate further from the centroid of adipogenic hMSCs, with more pronounced differences at the early time point (**Figure 4.4B**). Interestingly, no centroids seem to be in close proximity of the osteogenic hMSC centroid, suggesting that this substrate is not effective for ultimately generating osteocytes, which agrees with the lack of bone-specific alkaline phosphatase expression. All texture descriptor values were averaged for each hydrogel section and normalized, and subsequently plotted onto a heat-map to identify potential trends and compare with descriptors of pre-differentiated phenotypes. Aside from a consistent lack of trend with the of texture

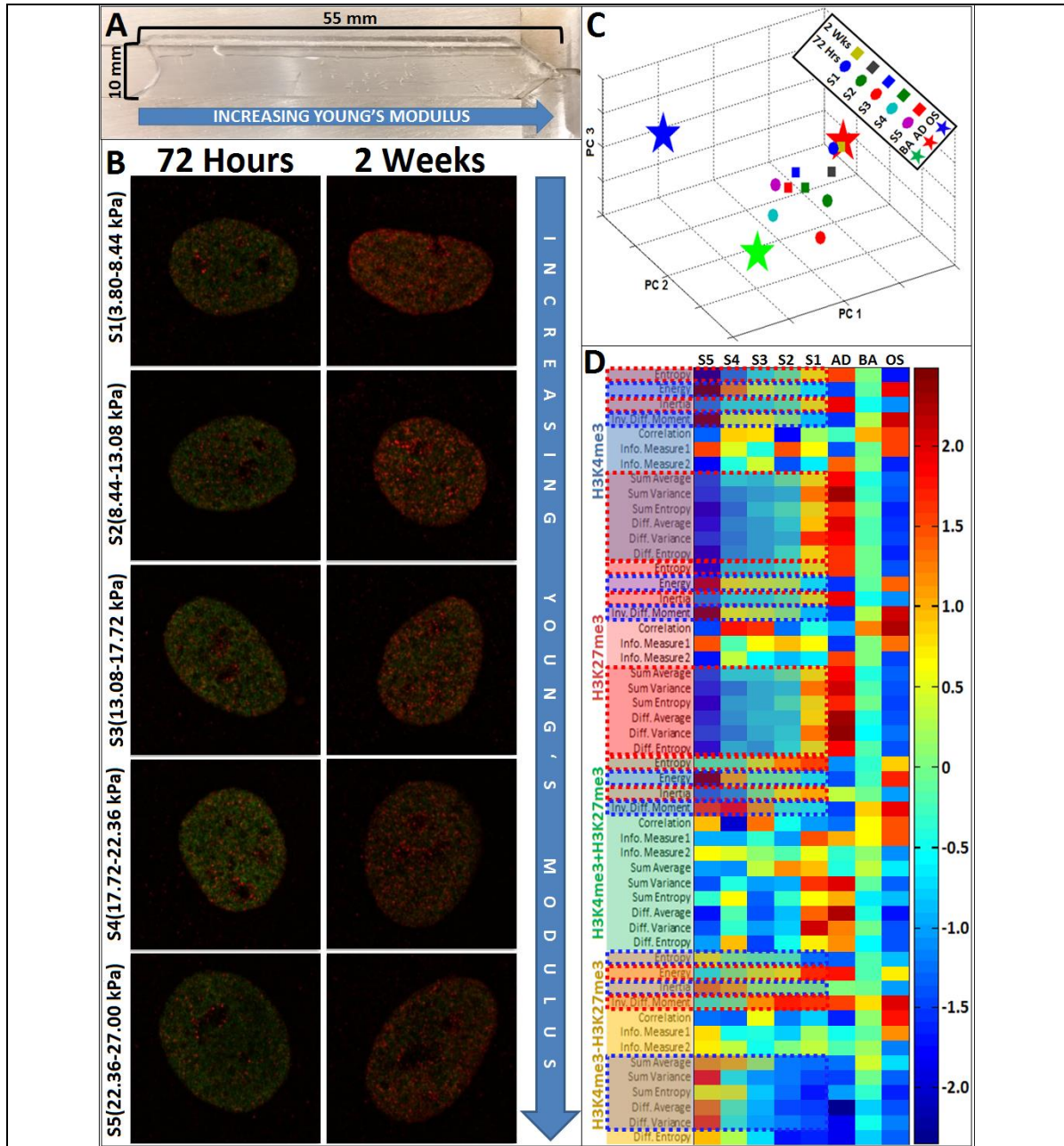


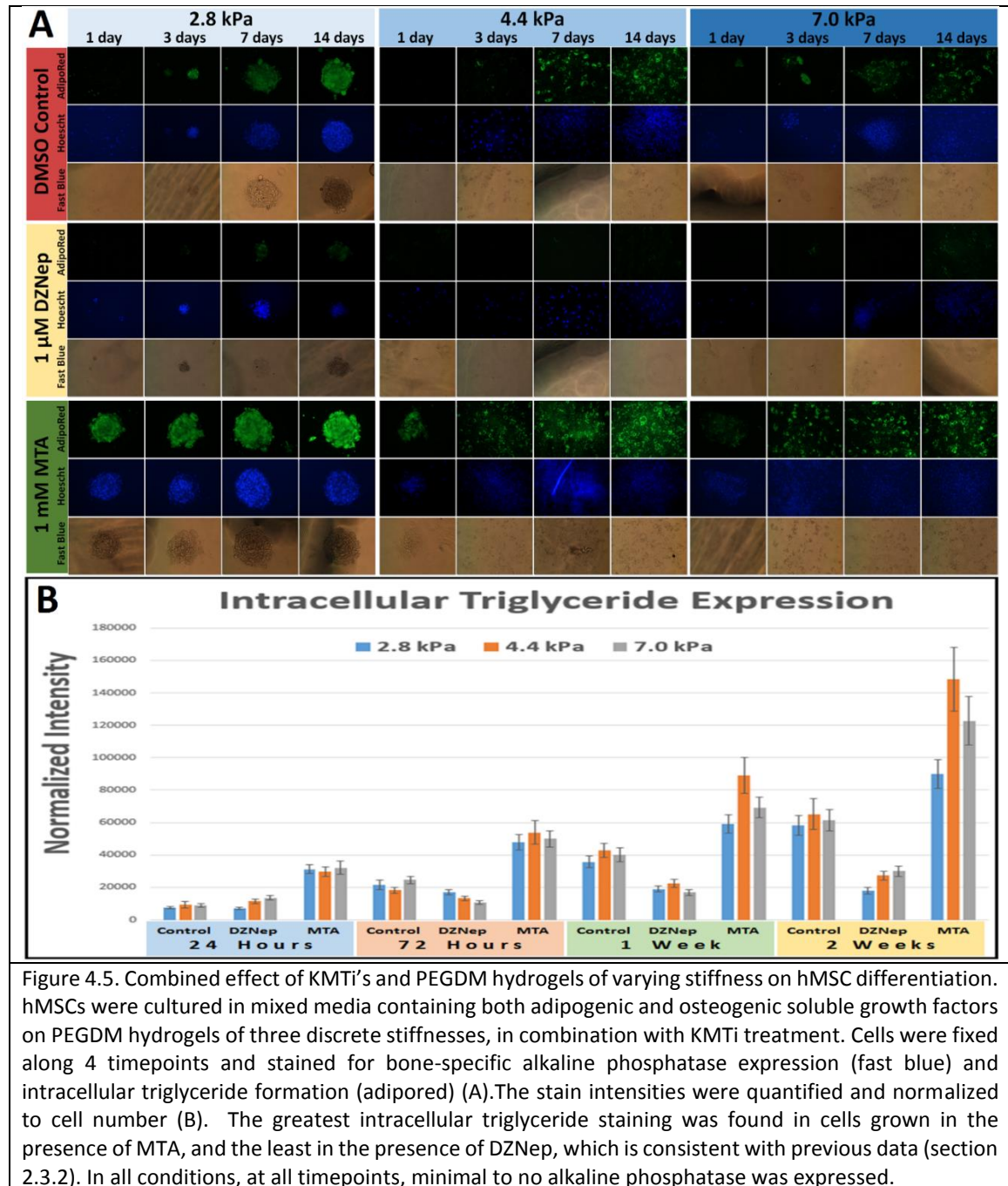
Figure 4.4. H3K4K27me expression is responsive to minute changes in Young's modulus. (A) PEGDM continuous Young's modulus gradient hydrogels were fabricated by varying the dispensing rates of different PEGDM concentration solutions into a custom mold, yielding a final hydrogel "strip" measuring ~10 mm in width and ~55 mm in length. (B) hMSCs cultured on PEGDM continuous Young's modulus gradient hydrogels were fixed and immunolabeled for H3K4me3 (green) and H3K27me3 (red) at early (72 hours) and late (2 weeks) timepoints along the entire length of the hydrogel, which ranged in Young's modulus from 3.8 to 27 kPa. (C) Haralick texture descriptors were acquired and analyzed via Principal component analysis followed by k-means cluster analysis to determine centroids of clusters of cells cultured for a specified time and position on the gradient. Centroids of cells grown on the softest part of the gel (S1) were closest in proximity to the centroid of pre-differentiated adipogenic cells, indicating their similarity of H3K4K27me3 expression and subsequent lineage commitment. (D) Heat-map of normalized texture descriptor values reveals increasing (outlined in red) and decreasing (outlined in blue) trends that vary with decreasing hydrogel stiffness.

descriptors exhibit an increasing/decreasing trend that varies with correlation descriptors, the majority decreasing PEGDM hydrogel stiffness (**Figure 4.4D**). Furthermore, the normalized descriptors of hMSCs cultured on the softest part of the gel (S1) approach values that are closest to those of per-differentiated adipogenic hMSCs. Due to the agreement with histological lineage marker staining assays (**Figure 4.3**), these results indicate that the textural profile of H3K4K27me3 expression during hMSC development could be leveraged for screening defined mechanical properties of biomaterials.

4.3.3 Combined Effect of KMTi and Young's Modulus on Differentiation

After identifying the optimal range of stiffness that promotes the highest rate of adipogenic differentiation (i.e. 3.8 – 8.4 kPa), we investigated several discrete stiffness hydrogels spaced within this range for studies on the combined effect of substrate Young's Modulus and lysine methyltransferase inhibition on hMSC development. Based on differentiation studies performed on hMSCs treated with KMTi's and differentiation inducing soluble growth factors (refer to results in section 2.3.2), we hypothesized that methylthioadenosine (MTA) may facilitate adipogenesis in hMSCs cultured on adipogenically inducing soft PEGDM hydrogels. Three discrete stiffness PEGDM hydrogels of 2.8, 4.4 and 7.0 kPa were fabricated from PEGDM solutions of 10, 25 and 50%, respectively. hMSCs were cultured on top of these hydrogels in culture media containing a 50/50 mixture of both adipogenic and osteogenic growth factors, combined with 1 μ M DZNep, 1 mM MTA and a DMSO control. Cells were fixed along 4 timepoints (1, 3, 7 and

14 days), and subsequently labeled for intracellular triglyceride formation and bone-specific alkaline phosphatase expression (**Figure 4.5**).



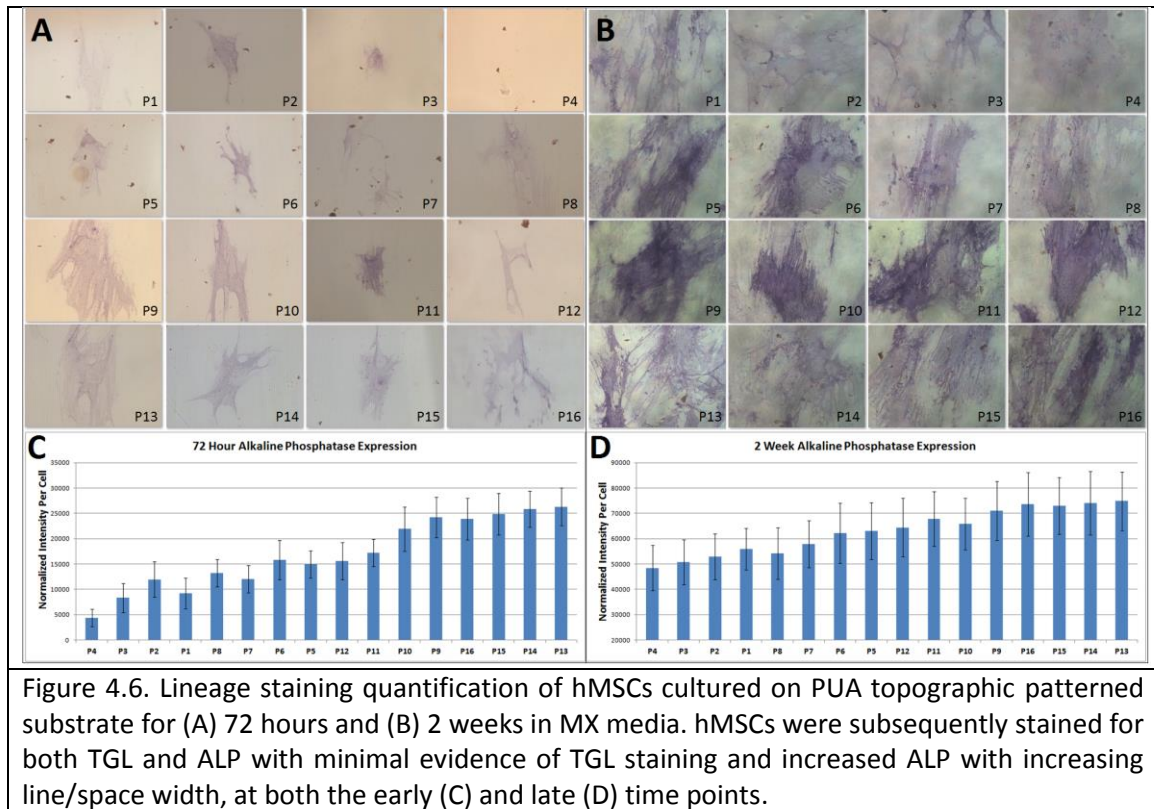
Not surprisingly, little to no alkaline phosphatase was expressed on any of the hydrogels, at all timepoints, without regard to media treatment condition. Adipogenic

differentiation, however, was prominent in most conditions, with higher levels of intracellular triglyceride formation per cell in cells cultured with 1mM MTA. On the softest hydrogels (2.8 kPa), cells tended to aggregate and form colonies, whereas they exhibited normal distribution and spreading on the other two stiffnesses (4.8 and 7.0 kPa). The greatest triglyceride expression was achieved in cells cultured on 4.4 kPa hydrogels with MTA, which displayed higher expression by one week compared to the control at two weeks (**Figure 4.5B**). At all three stiffness values, cells treated with MTA exhibited more intracellular triglyceride expression at just 72 hours when compared with the control at 1 week. These results strongly indicate that MTA is quite effective at expediting the rate of adipogenic differentiation in hMSCs, and this effect is compounded when hMSCs are cultured on soft, adipogenically inducing substrates.

4.3.4 hMSC Differentiation as a Response to Nanotopography

We next investigated the effect of topography on chromatin structural dynamics and downstream differentiation. Surface topography can influence mesenchymal stem cell development through the orchestration of a wide range of interconnected signaling pathways throughout the cytoskeleton, which ultimately converge on the nucleus to influence gene transcription regulation. Topographical effects are manifested in cytoskeletal dynamics mediated by focal adhesions [281], which influence wnt signaling to mobilize β -catenin into the nucleus where it functions as a scaffold to link various signaling proteins to specific chromatin remodeling complexes, as well as to recruit protein complexes that mediate H3K4 methylation [282-284]. Thus, to investigate the

potential topographical effects on hMSC development, we employed a substrate consisting of 16 different defined topographical patterns that was fabricated via the soft lithography of polyurethane acrylate (PUA). These patterns consist of systematically varied line/space widths, ranging from 350 nm to 2000 nm (Figure 4.2).



hMSCs were cultured on this PUA topographic substrate in a similar manner to those that were grown on the PEGDM hydrogel, in a 50:50 cocktail of osteogenic and adipogenic induction media, after which they were fixed at early and late time points. hMSCs began to express bone-specific alkaline phosphatase after 72 hours, with gradual slight increases in expression with increasing line/space width distances (Figure 4.6 A&C). After 2 weeks, we observe an overall increase in bone-specific alkaline phosphatase

throughout the substrate, and again see gradual slight increases with increasing line/space width, with the greatest expression on the widest portion of the substrate (i.e. P13 – 2000 nm) (**Figure 4.6B&D**). Cells did not express any intracellular triglyceride accumulation when cultured on this substrate at neither early nor late timepoints, suggesting the mechanical/topographical properties of this substrate overcome the adipogenic chemical soluble cues that were presented simultaneously.

4.3.5 Texture Image Analysis of H3K4K27me3 Dynamics in hMSCs on PUA Substrate

High-content images were acquired and analyzed, and texture descriptor sets were computed and dimensionally reduced via PCA into the same three dimensional space as those of pre-differentiated hMSCs. K-means cluster analysis was performed to determine the centroids of cells cultured on each of the 16 patterns, and these centroids were plotted in relation to those of pre-differentiated hMSCs (**Figure 4.7**). Interestingly, the centroids from cells cultured on increasingly wider line/space widths grew closer towards the centroid of pre-differentiated osteogenic hMSCs, even at the early time point (**Figure 4.7C**), but much more pronounced at the late time point (**Figure 4.7D**). Heat-maps of normalized descriptor values on each topographical pattern reveal correlating trends with widening line/space patterns, with values approaching those of pre-differentiated osteogenic hMSCs on the widest patterns. (**Figure 4.7D**). Moreover, the correlation texture descriptors perfectly correlate to nano-scale variations in line/width spacing, which was not previously seen. This may indicate a manifestation of H3K4K27me3 that is

sensitive to linear patterns when cultured on this substrate. These findings agree with the late time point bone-specific alkaline phosphatase staining data, which was performed in parallel (**Figure 4.6**). Furthermore, no centroids of hMSCs

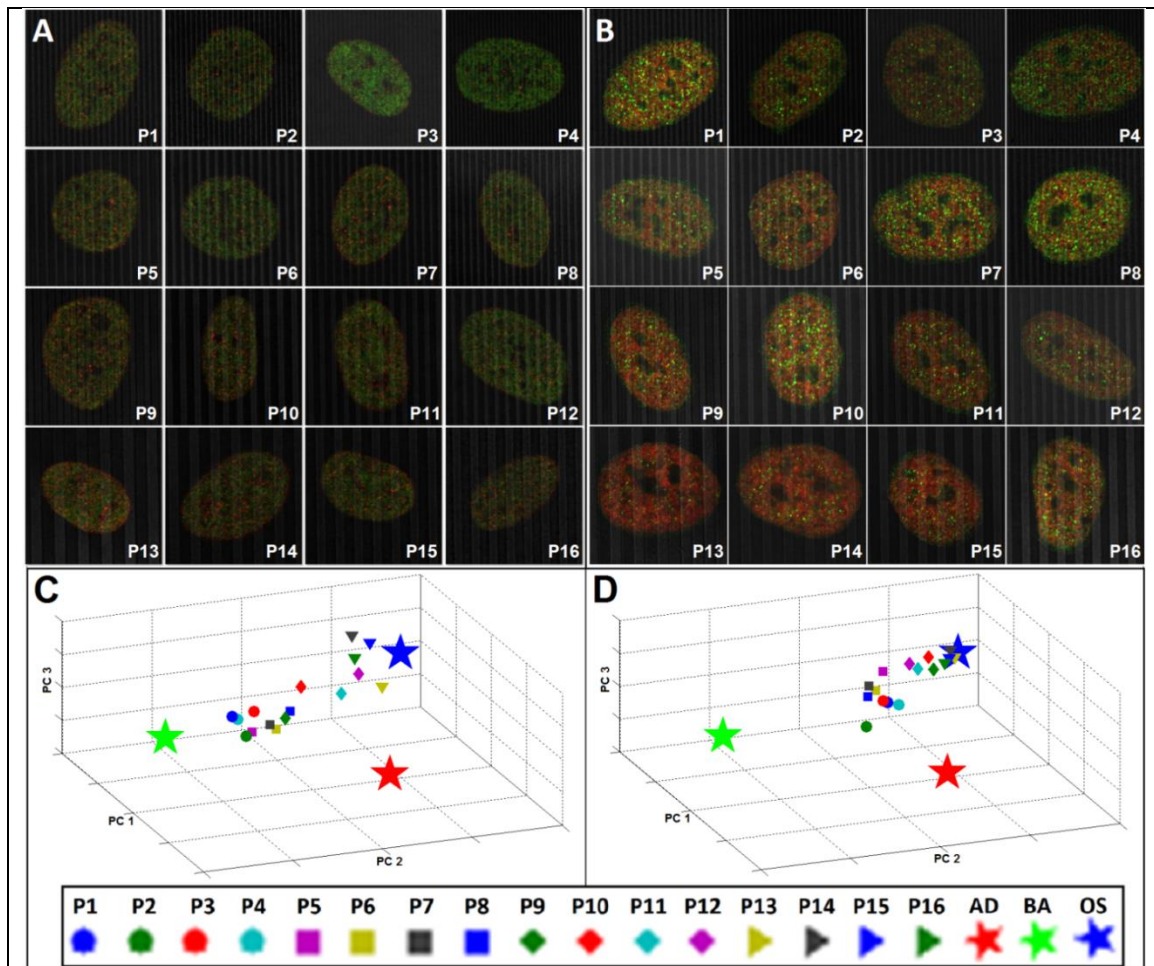
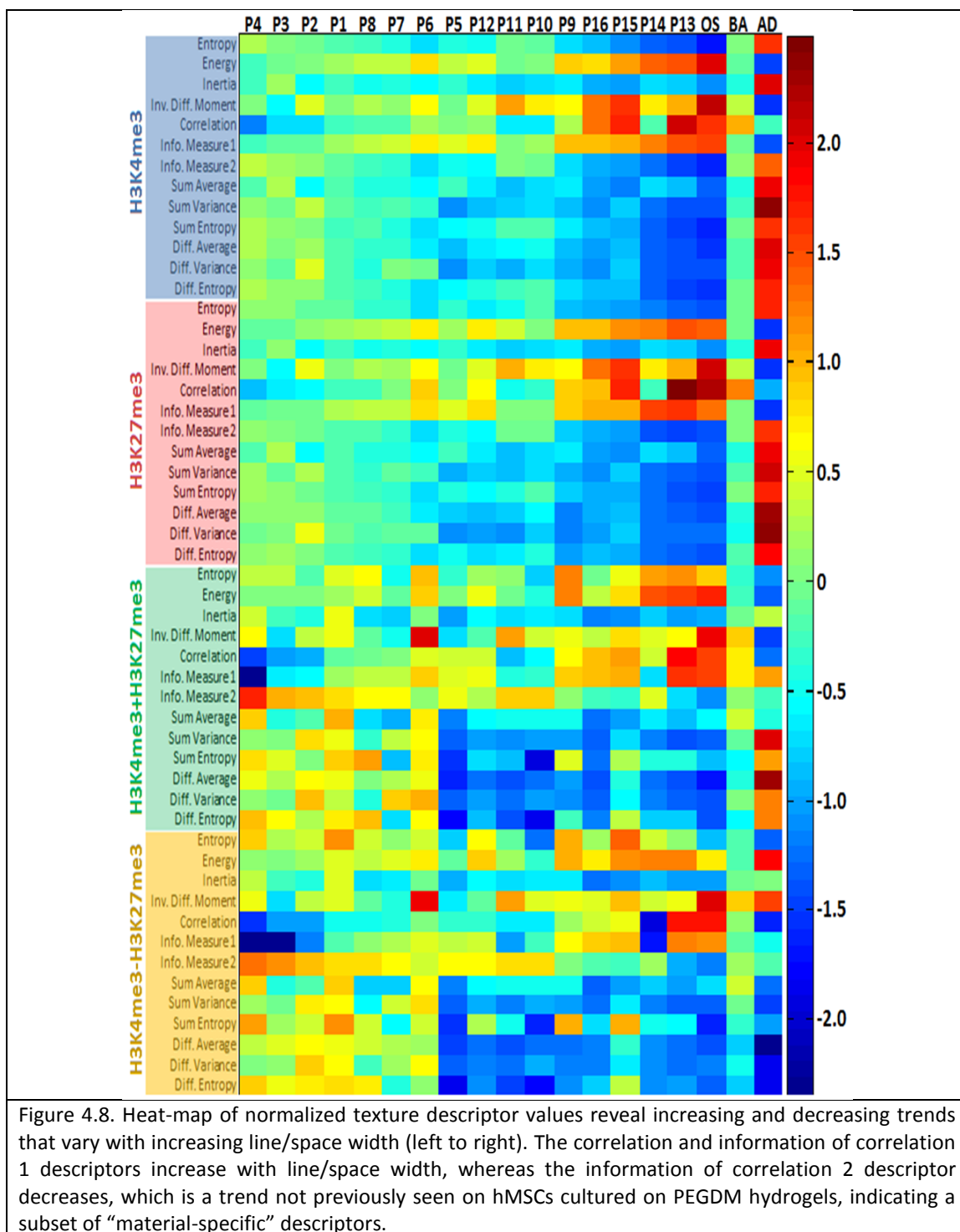


Figure 4.7. H3K4K27me3 expression is responsive to varied topographic line/space patterns. (A&B) LSCM G-STED images of hMSCs cultured on PUA topographic line/space patterns labeled for H3K4me3 (green) and H3K27me3 (red) reveal a shift in balance from H3K4me3 to H3K27me3 as line/space widths widen that can be qualitatively observed after 2 weeks (B), but less apparent earlier after 72 hours (A). (C&D) K-means cluster analysis reveals that centroids of hMSCs seeded on the widest line/space patterns (triangles) are closest in proximity to osteogenically differentiated hMSCs after 72 hours (C) and migrate closer after 2 weeks (D), whereas centroids of hMSCs cultured on the narrowest line/space patterns (circles) are closest in proximity to undifferentiated hMSCs after 72 hours (C), but gradually migrate closer towards osteogenic after 2 weeks (D).



grown on these nano-grooves were in close proximity with that of adipogenically pre-differentiated hMSCs, indicating that their H3K4K27me3 signatures are quite different.

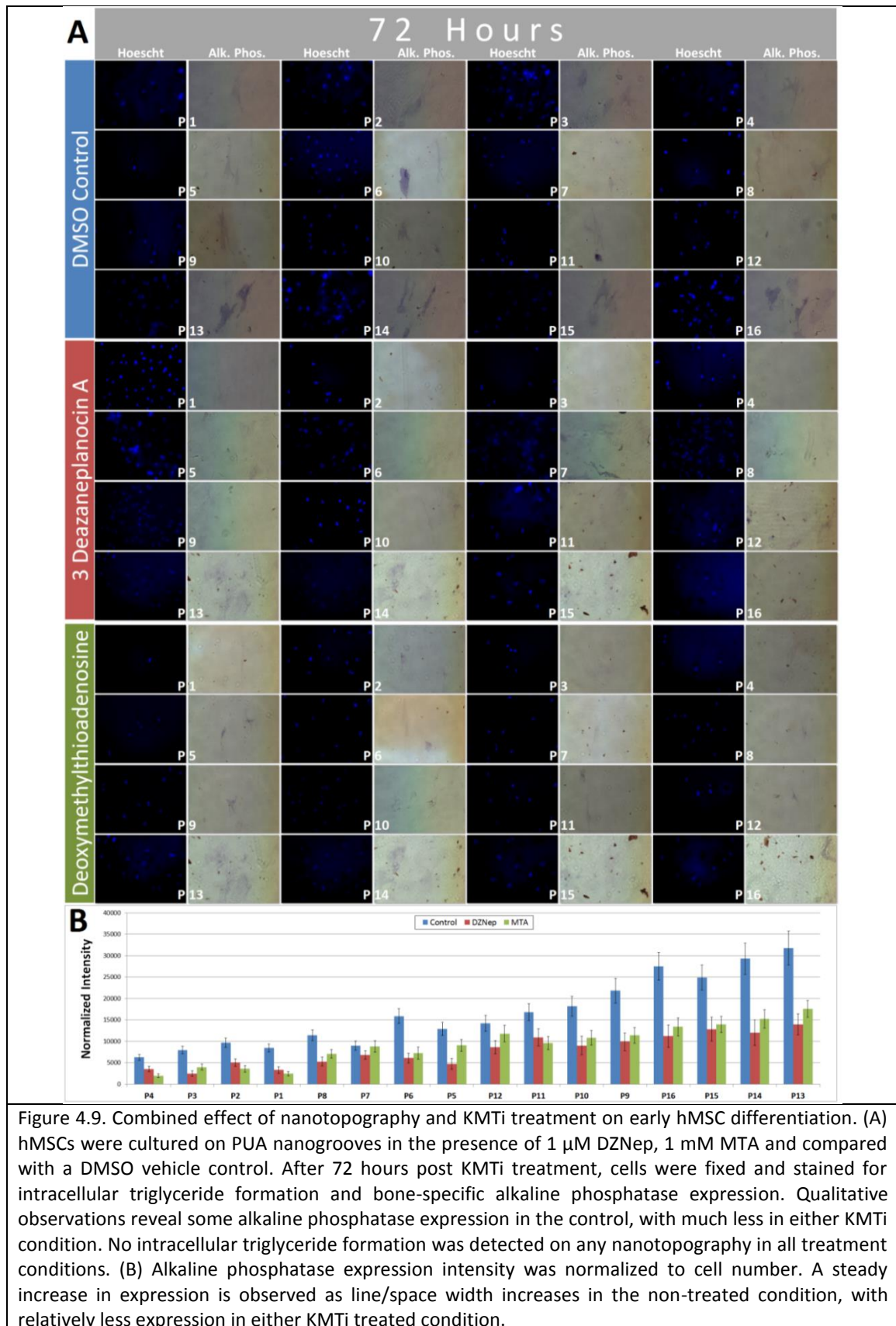
This also agrees with the lack of intracellular tri-glyceride staining and fat-globule formation from hMSCs cultured on this substrate (**Figure 4.6**), as well as a lack of similarity with the normalized descriptor values (**Figure 4.8**). Thus, these results indicate that the organizational expression of H3K4K27me3 can be probed to accurately screen topographical properties of biocompatible substrates for insights on cellular development for applications in regenerative medicine.

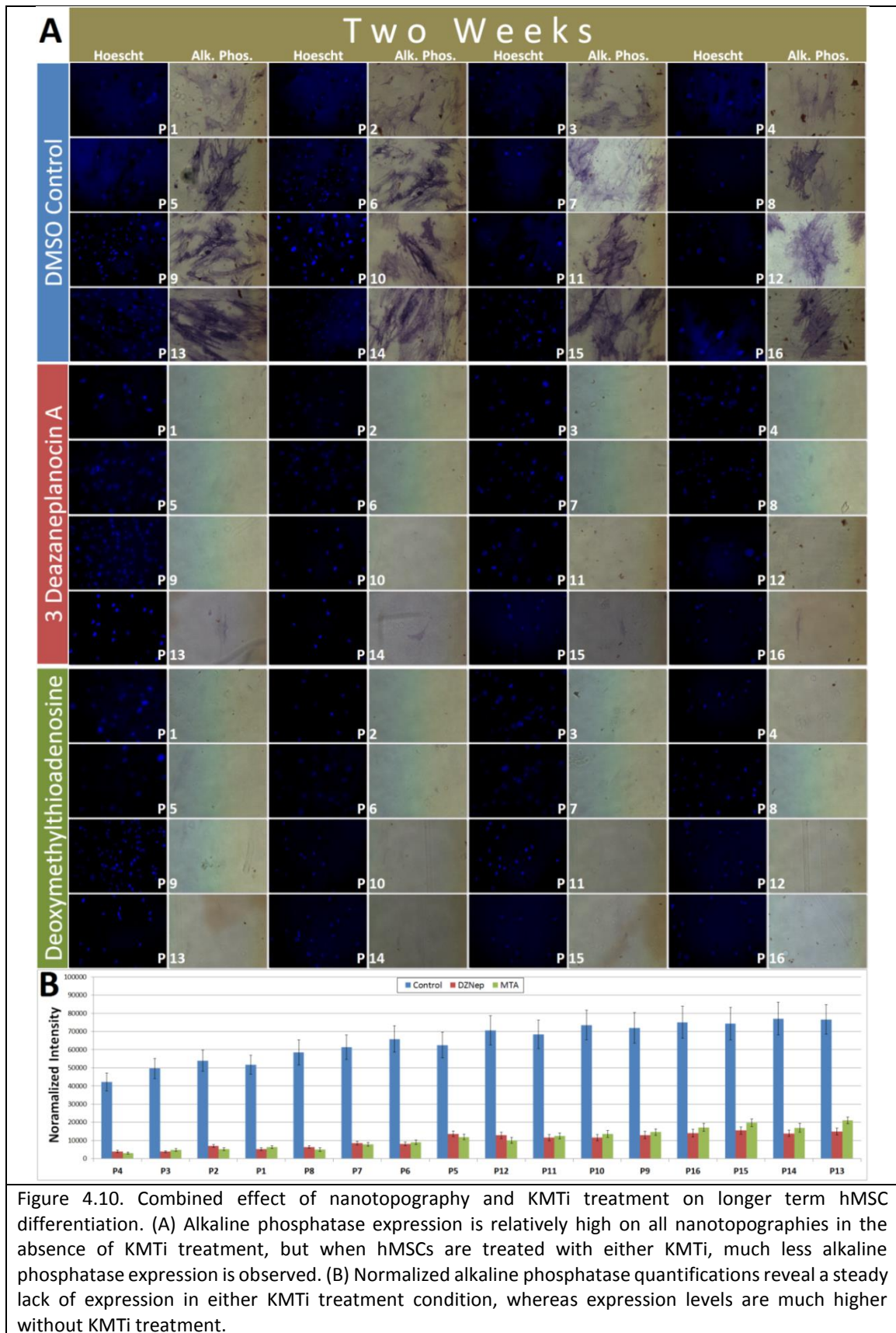
4.3.6 Combined Effect of KMTi and Nanotopography on Differentiation

Previous investigations on the effect of lysine methyltransferase inhibitors on hMSC differentiation revealed that both 3-Deazaneplanocin A and deoxymethylthioadenosine seem to curb osteogenic differentiation, with the latter producing a preference for adipogenic differentiation. Since the PUA nanotopographic substrate facilitates osteogenic differentiation, with greater bone-specific alkaline phosphatase expression seen on wider line/space widths (i.e. 2000 nm), we were interested in investigating whether these osteogenic inducing effects can overcome the opposing effects of the lysine methyltransferase inhibitors (i.e. are the topographical properties of a cell's microenvironment more influential to its development than chemical perturbations to its normal PTM distribution?). We approached this question by investigating the combined effect of nanotopography and lysine methyltransferase inhibition on hMSC differentiation.

hMSCs were cultured on PUA nanotopographic substrates in the presence of 1 μ M DZNep and 1 mM MTA, along with a DMSO control, all with the presence of both

adipogenic and osteogenic soluble growth factors (i.e. 50:50 mixed media). Cells were fixed after 72 hours and 2 weeks post KMTi treatment, and subsequently labeled for intracellular triglyceride formation, bone-specific alkaline phosphatase expression and nuclei were counterstained with Hoechst. All lineage marker intensities were quantified and normalized to cell number (Figure 4.9).





The effect of both KMTi's on preventing osteogenic differentiation can be seen early on, after only 72 hours. On every nanotopographic pattern, there is less bone-specific alkaline phosphatase expression in either treatment condition when compared to the DMSO vehicle control. Moreover, as bone-specific alkaline phosphatase expression increases with increasing line/space width in the control, we observe a slight increase in expression in both KMTi treatment conditions as well, but the effect is not nearly as dramatic (**Figure 4.10B**).

After two weeks post KMTi treatment, alkaline phosphatase expression is dramatically increased, as expected. However, hMSCs treated with either KMTi never seem to recover from their early prevention of osteogenic differentiation, despite the continual replenishment of osteogenic growth factors over two weeks (**Figure 4.10**). In both the early and late timepoints, minimal to no intracellular triglyceride expression is observed. These results indicate that major perturbations to histone modifications result in irreversible changes to cellular differentiation. Furthermore, these perturbations seem to overcome nanotopographical influences that normally promote osteogenic differentiation.

4.4 Discussion

The future success of tissue engineering relies on the harmonious amalgamation of purified cell phenotypes of interest and biomaterials that optimally support their viable thriving and function. Investigating the continuous reciprocal communication between a

cell and its immediate microenvironment provides us with an increasingly comprehensive understanding of the signaling pathways orchestrating different behavioral outcomes, while simultaneously presenting a considerable challenge in isolating and attributing these effects to their primary influences. A substantial amount of time and money has been invested into exploring the countless signaling molecules implicated in the control of cellular behavior, but comparatively fewer efforts have been made towards understanding the epigenetic mechanisms that are at the root of orchestrating these signaling pathways. Here, we have begun efforts to make connections between how dynamic epigenetic marks respond to defined physical attributes of biomaterials.

The investigations on the combined effect of lysine methyltransferase inhibition and material properties on hMSC development provide some intriguing insights into the nature of stem cell development and lineage commitment. For simplicities sake, the two material systems that were investigated can be referred to as “adipogenically inducing hydrogels” and “osteogenically inducing nanogrooves.” Without further perturbation (i.e. DMSO vehicle control), adipogenically inducing hydrogels robustly direct undifferentiated hMSCs to form intracellular triglycerides quite early post seeding. Quite remarkably, the administration of DZNep seems to prevent the transcription of key adipogenic genes that contribute to intracellular triglyceride formation, which suggests that blocking the appropriate gene silencing mediated by lysine 27 tri-methylation hijacks the normal gene transcription programs that would navigate adipogenic differentiation (i.e. genes unnecessary for adipogenic differentiation that are normally silenced by H3K27me3 are not deactivated and subsequently interfere with normal adipogenic development).

Treatment with MTA expedites this adipogenic development, as seen in studies in 2D (section 2.3.2), and this effect is enhanced when hMSCs are cultured on adipogenically inducing soft substrates.

KMTi treatment on hMSCs cultured on osteogenically inducing nanogrooves results in a lack of osteogenic differentiation. This is doubly intriguing as DZNep and MTA target opposing enzymes in the context of gene activation vs. silencing, so one would hypothesize that treatment with these molecules would result in opposite effects. However, since these KMTi's are mainly involved in perturbing H3K4K27me3 manifestation, one may speculate that the osteogenic gene programs necessary for proper osteogenic differentiation may be more highly regulated by PTMs other than H3K4K27me3.

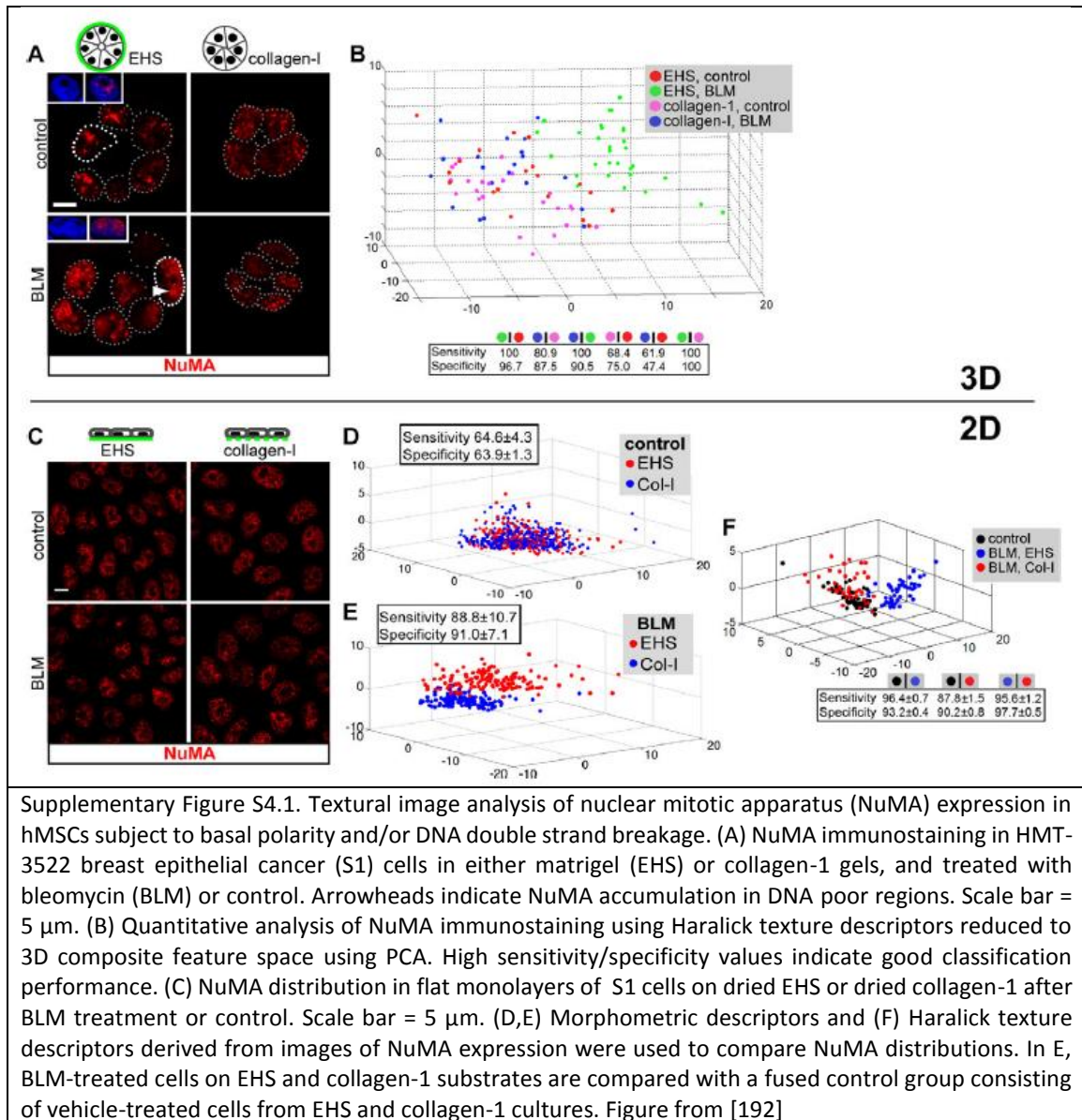
The most insightful and practically useful result of this chapter is the ability to directly compare the organizational signature of H3K4K27me3 of cells cultured on different materials with those that were pre-differentiated. We demonstrate that k-means cluster analysis of hMSCs grown on two different material systems yield very different H3K4K27me3 organizational patterns that are accurately predictive of their ultimate lineage commitment. This could be elucidated at an early time point (72 hours) prior to the manifestation of significantly distinguishable downstream lineage markers (i.e. intracellular triglyceride and alkaline phosphatase expression). Thus, in a similar manner, this approach can be applied to screen other defined microenvironmental properties that could potentially give rise to a phenotype of interest. With the accumulation of such data on a wider range of relevant nuclear markers in different stem

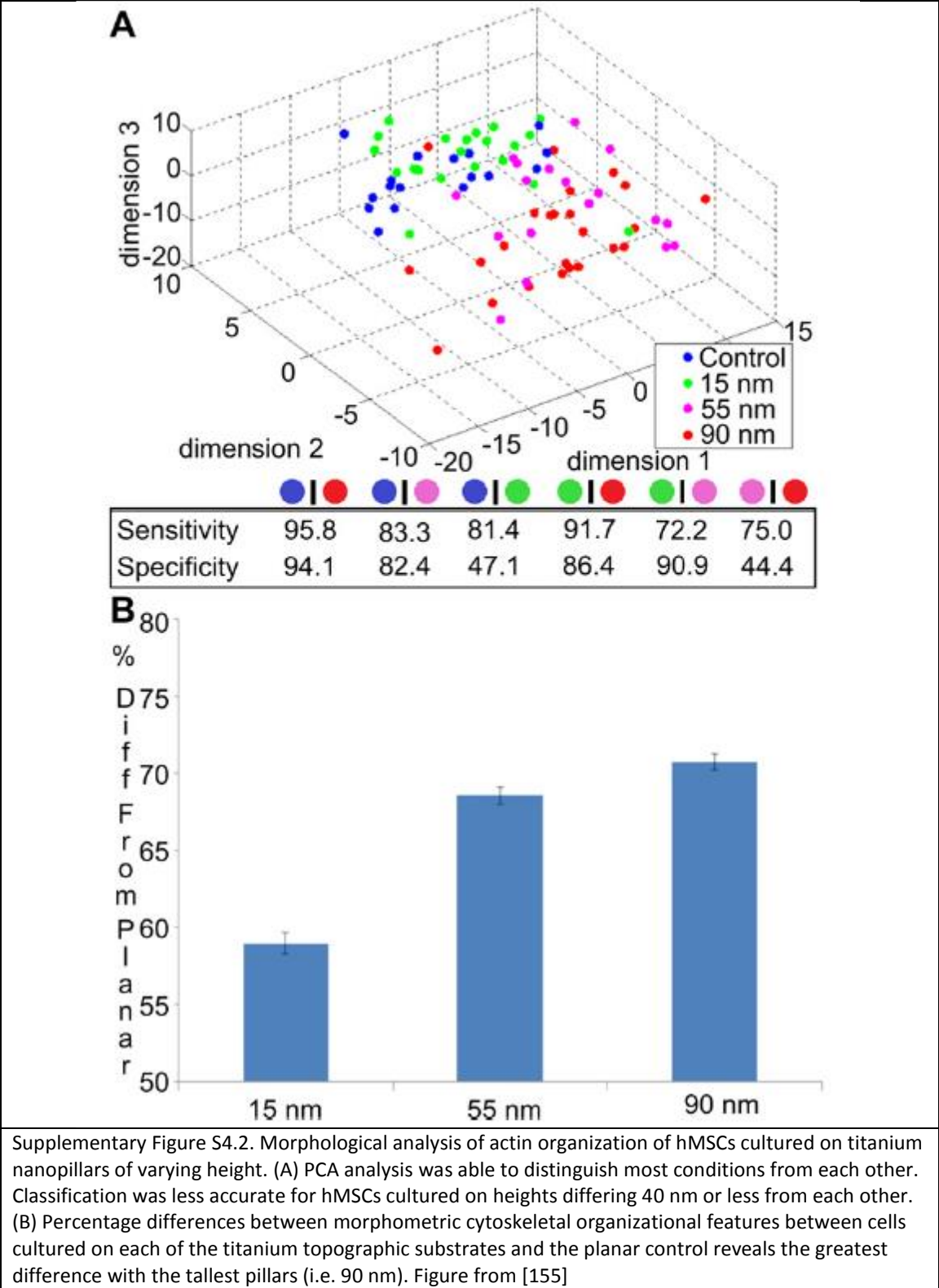
cell systems that yield a variety of different cellular phenotypes, this type of data could potentially be archived and referenced for future screenings of different defined chemical, mechanical and topographical properties to optimally facilitate desired cellular behaviors.

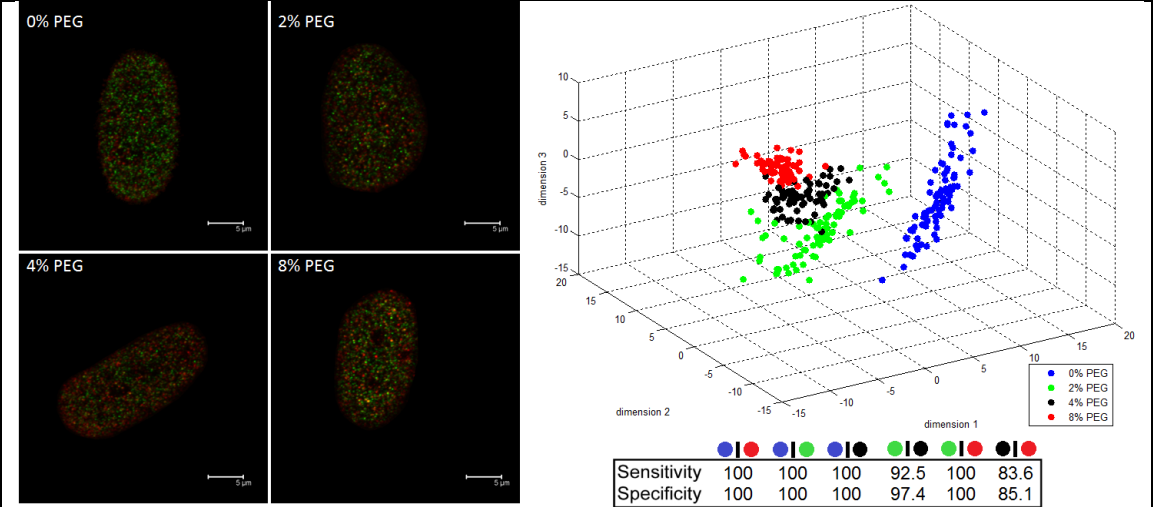
4.5 Conclusion

In this chapter, we investigated the efficacy of textural analysis of PTM organization as a reporter and accurate predictor of stem cell development in two mechanically and topographically defined material systems. This mode of analysis was able to relate the organizational patterns of H3K4K27me3 in hMSCs cultured on different materials to those of pre-differentiated phenotypes to accurately predict hMSC differentiation prior to the onset of classical downstream lineage markers. With the incorporation of additional PTM organizational data, and other developmental stem cell systems, this type of bioimage information can potentially be archived and referenced for future drug and biomaterial property screening. Thus, the increased comprehension of how the dynamic epigenome responds to environmental perturbations to regulate gene transcription programs may greatly facilitate the pace of tissue engineering's ultimate incorporation into clinical practice.

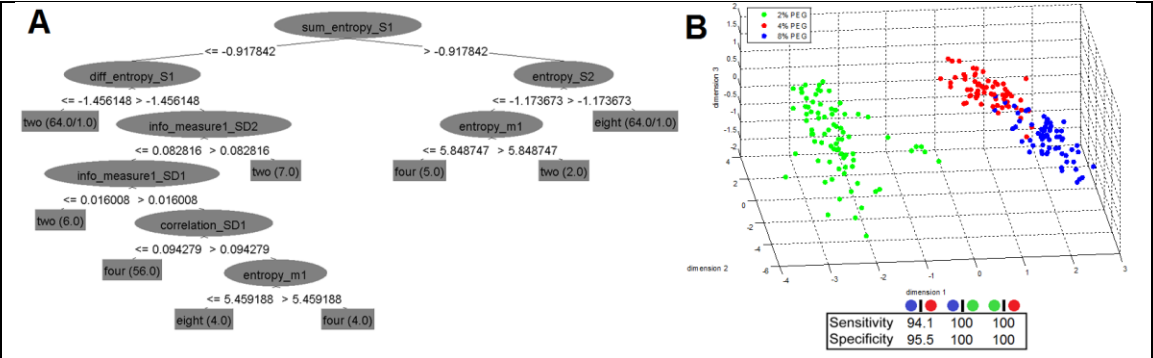
4.6 Supplementary Figures







Supplementary Figure S4.3. High content image analysis of hMSCs cultured on varying degrees of PEG incorporated in pDTEc. Cells were labeled for H3K4me3 (green) and H3K27me3 (red) on (A) 0% PEG, (B) 2% PEG, (C) 4% PEG and (D) 8% PEG. (E) PCA analysis of texture descriptors reveals that the expression of H3K4K27me3 is responsive to PEG content.



Supplementary Figure S4.4. Data mining of H3K4K27me3 texture descriptors of hMSCs cultured on varying degrees of PEG concentration. (A) Decision tree analysis reveals the most influential descriptors for accurate classification, most of which are related to entropy. (B) Isolation of these descriptors yields improved PCA classification results

CHAPTER 5: MUTUAL INFLUENCE OF CYTOSKELETAL MORPHOLOGY AND INTRANUCLEAR ORGANIZATION DYNAMICS THROUGHOUT CELLULAR DEVELOPMENT

5.1 Introduction

Proper cellular development relies on the continuous, reciprocal communication between the cell body and nucleus. Signals transduced across the plasma membrane into the cell body ultimately influence the spatiotemporal regulation of signals communicated across the nuclear membrane, which cause direct changes to chromatin structure and gene transcription patterns [285]. These intranuclear changes are communicated back out to the cell body and can cause the cytoskeleton to trigger desired morphological changes for specific cellular functions [286]. We can consider this constant feedback communication between the cell body and nucleus as occurring in two main signaling directions, which for simplicities sake we can designate as “outside-in” and “inside-out” signaling.

Outside-in signaling begins at the interface between a cell and its immediate environment where signals are transmitted through the body of the cell and ultimately to the nucleus. At the interface, cells can actively sense the physical and chemical properties of its surroundings via integrins, which are transmembrane receptors mediating the link between extracellular adhesion sites and intracellular signal transduction pathways [287, 288]. Mechanical stretching of the cell surface can also be detected by stretch activated ion receptors, which respond by allowing or preventing the flow of specific ions (mainly Ca^{2+}) [289, 290]. Other mechanosensors along the surface of cells include G-protein

coupled receptors [291] and growth factor receptors [292], although these two receptor types are more directly influenced by chemical cues. All of these mechanosensors collectively coordinate and regulate signals that are transmitted through the cell body and relayed to the nuclear envelope via nesprins [293], which directly interact with Klarsicht/ANC-1/Syne Homology (KASH) domains and Sad1p/UNC-84 (SUN) domains to relay these signals across the nuclear membrane [294, 295]. In this manner, signals from a cell's microenvironment are communicated into the nucleus to trigger the causative post translational modifications to histones, which influence chromatin structural dynamics and subsequent gene transcription [296, 297]. These consequential nuclear changes are communicated back out to the cell body, which result in morphological changes to the cytoskeleton and the expression of specific proteins that regulate intracellular signaling as well as external secretions of the cell. Thus, this signaling which originates from the nucleus and triggers changes to a cell's behavior, and ultimately influences how it interacts with its environment, can be considered as inside-out signaling (Figure 5.1).

Thus, the mutually reciprocal relationship between a cell's body and nucleus is vital to a cell's viability and function. Structural insights provided by both cytoskeletal and intranuclear organization can be leveraged to characterize, and even forecast, cell phenotypic states. Therefore, in an effort to establish quantitative correlations between cytoskeletal and intranuclear organization, we analyzed the morphometric organization of actin and integrin β -1 and related this to the textural intranuclear organization of several PTMs.

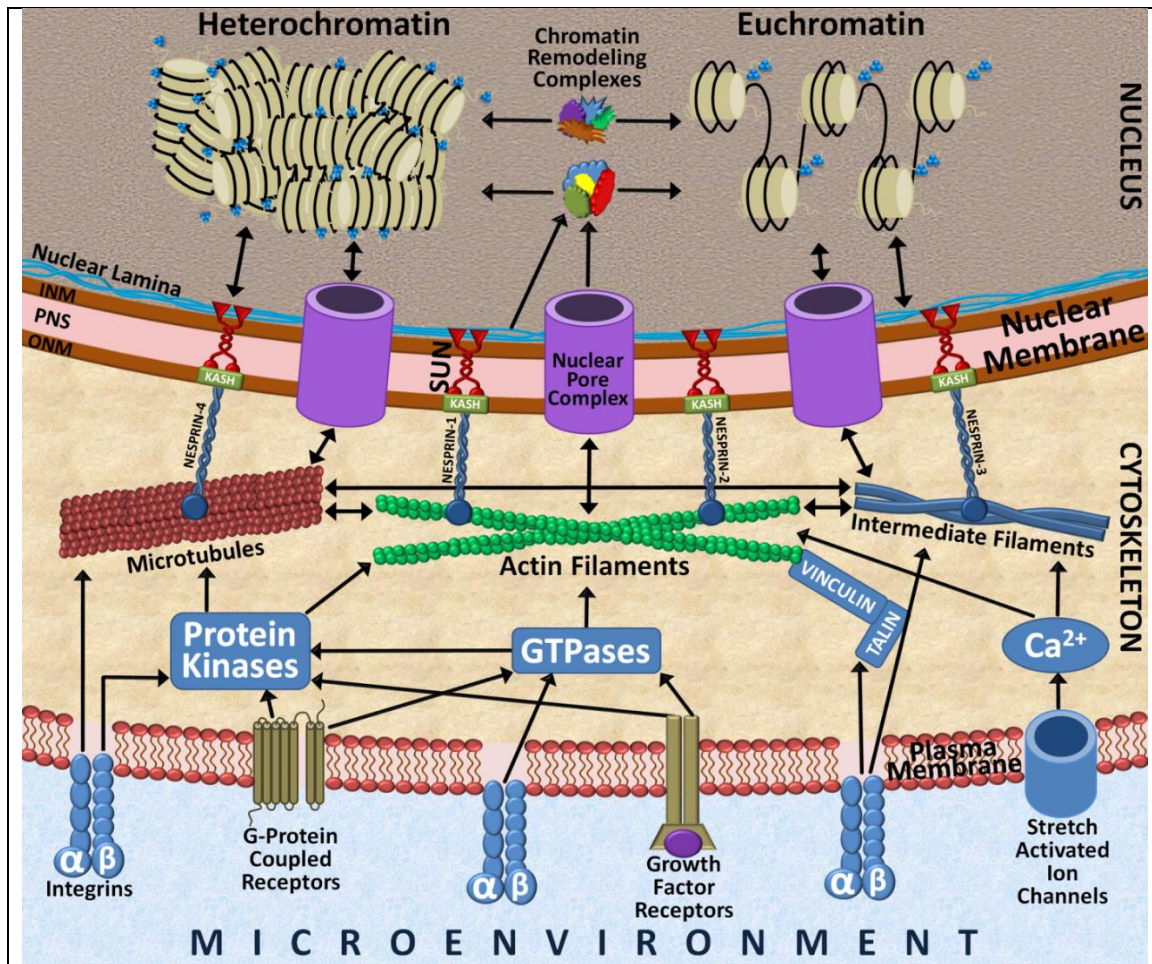


Figure 5.1. Schematic of major players involved in the transduction of microenvironmental stimuli to the cytoskeleton and nucleus. Chemical factors are largely communicated across the cell membrane via g-protein coupled receptors and growth factor receptors, which trigger numerous GTPases and protein kinases to influence complex signal transduction networks that cause distinct changes to the cytoskeleton. Mechanical and topographical factors are largely sensed via integrins and stretch activated ion-channels, which can directly or indirectly alter cytoskeleton organization and function. These changes to the cytoskeleton are communicated across the nuclear membrane via the LINC-complex, which consists of nesprins anchored to KASH domains that are largely localized to the outer nuclear membrane (ONM), which interact directly with SUN domains across the perinuclear space (PNS) and ultimately across the inner nuclear membrane (INM). The interactions between the LINC-complex and the nuclear lamina cause direct changes to chromatin organizational dynamics, largely via post translational modifications to core histones. ATP-powered chromatin remodeling complexes are prevalent within the nucleus, which cause direct changes to chromatin organization. Nuclear pore complexes are studded throughout the nuclear membrane, which allow for the exchange of many small molecules and proteins across. Chromatin organizational changes regulate gene transcription, which is mediated by RNA export across these nuclear pores and can ultimately cause changes to cytoskeletal organization.

Although this analytical approach can serve as an effective assay to probe cellular behavior, it ultimately requires the fixation of cells. Aside from the obvious disadvantage of the inability to keep cells alive post-analysis, fixing cells at an arbitrary point in time does not allow one to monitor the organizational dynamics in a single cell as it develops.

In particular, chromatin structural organization is highly dynamic, which enables the expansive, yet extremely precise, orchestration of DNA accessibility and transcriptional activation or repression in space and time. Former conceptualizations of rather static chromatin architectures [298] (i.e. 30 nm nucleosome fiber model [299] and beads on a string model [300]) are now obsolete, as newer imaging technologies and biochemical approaches have provided evidence for the existence of structural dynamics which actively occur along nucleosome fibers [301-304]. Since these subtle structural changes are continually occurring at the local level (i.e. along single nucleosomes and within fractions of seconds [304]), appropriate imaging acquisition and analytical techniques should be employed to capture such fleeting changes. Thus, in an effort to capture these dynamics in real time in response to controlled microenvironmental conditions, we constructed a lentiviral plasmid that dually expresses fluororeporters for Histone H3B and cytoskeletal actin, and transduced hMSCs to monitor their real time response to KMTi's and differentiation cues in real-time.

5.2 Materials and Methods

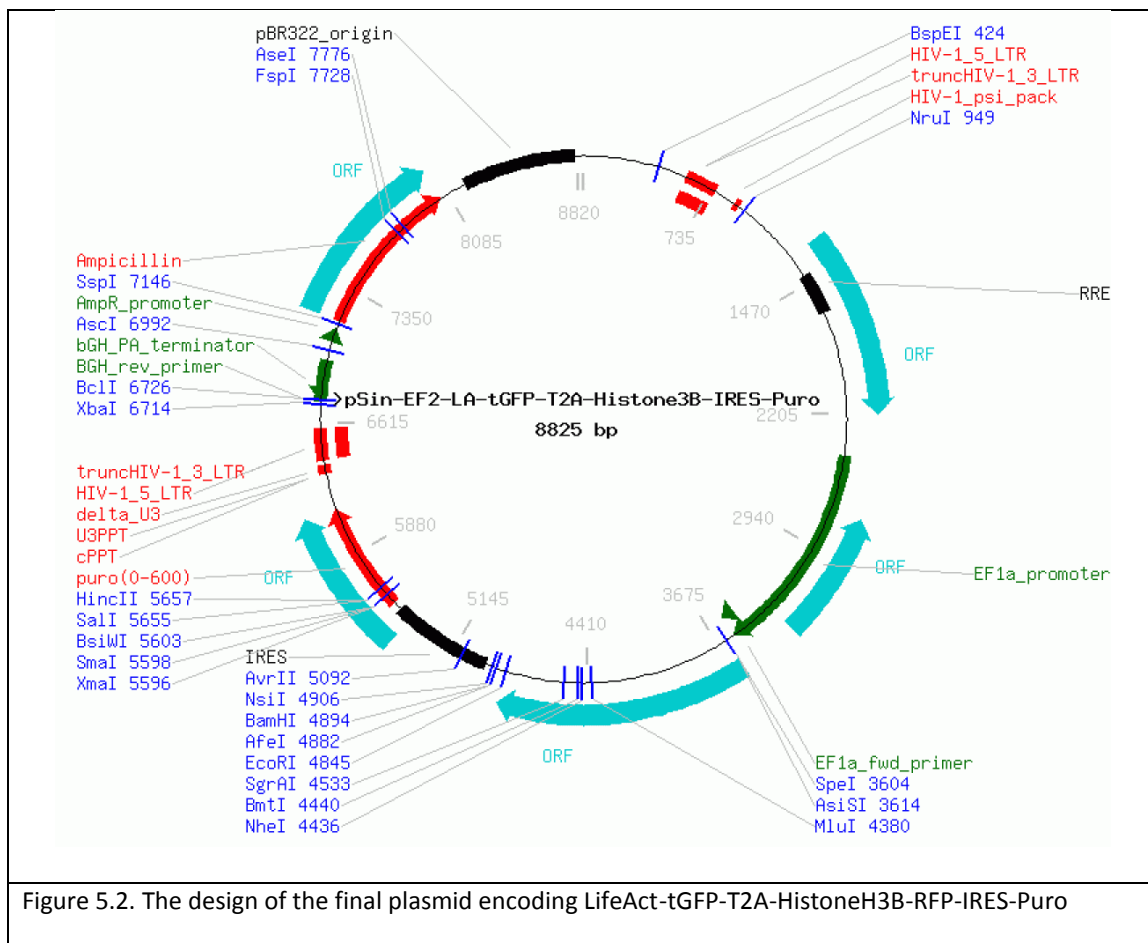
5.2.1 Lentiviral Plasmid Construction

The vector backbone pSIN-Glis1-IP was first cut with the restriction enzymes SpeI/MluI (Thermo Scientific / Fermentas) by combining 44 μ l of H₂O, 42 μ l of the vector DNA, 10 μ l of 10x BamHI restriction enzyme buffer, 2 μ l of SpeI and 2 μ l of MluI and incubated overnight. The following day, this mixture was treated with alkaline phosphatase for 10 minutes at 37°C to prevent self-ligation, and then mixed with 40 μ l of 6 X loading dye and resolved on a 0.7% TBE gel containing GelStar (Lonza) to purify the backbone from the insert. The digested DNA was visualized using a blue transilluminator and the top band was cut from the gel and subsequently purified using a Gel extraction kit (Qiagen). Bands were approximately 2 grams, which were spread between 2 columns and eluted. The overall yield was about 80 μ l total at 63 ng/ μ l, for a total of approximately 5040 ng which represents ~50% yield.

Next, DNA inserts were cloned by proof-reading PCR using PfuUltra II Hotstart PCR Master Mix (Agilent Technologies, Santa Clara, CA), or if GC rich using Herculase II (Agilent Technologies). Each PCR reaction was cleaned using the EZNA Cycle Pure Kit (Omega Bio-Tek, Norcross, GA) and subsequently quantified using Nano Drop. PCR products were then digested with enzymes to prepare for cloning: T2A-H3B was digested with MluI / EcoRI in EcoRI buffer, RFP in EcoRI/BamHI in EcoRI buffer, and LifeAct-tGFP in SpeI/MluI in BamHI buffer. Each PCR product was digested for 4 hours, then run through EZNA Cycle Pure columns, eluted with elution buffer, quantitated and set aside for ligation reactions.

Triple ligations of LifeAct-tGFP and T2A-H3B into pSIN-IRES-Puro cut with SpeI/EcoRI were performed at room temperature for 60 minutes. Next, ligation products were transformed into STBL3 bacteria and screened for successful ligation using PCR. Briefly, STBL3 were defrosted on ice, mixed with ligation products in a round bottom polystyrene tube, incubated for 30 minutes on ice, placed in 42°C water bath for 2 minutes for heat shock, then placed back on ice for 1 minute. Cold LB media was added and tube was agitated on a shaker at 37°C for 1 hour. 2 ml was then transferred into a microcentrifuge tube and centrifuged at 8000 RPM for 1 minute. Supernatant up to 100 μ l was discarded and pellet was resuspended in remaining LB buffer. This was spread on a pre-warmed LB/Agar plate supplemented with carbenicillin and allowed to incubate overnight.

Bacterial colonies were then screened via PCR using a pSIN primer with a Lifeact-tGFP-R primer, and plasmid DNA was isolated and purified using the EZNA plasmid mini kit II (Omega Bio-tek). Clones were subsequently sequenced to verify accuracy against a reference sequence.



```

cggaccgcccactgccattacctgtggtttcatttactctaaacctgtgattcctctgaattattttcat
tttaaagaaattgtatttgttaaataatgtactacaaaccttagtagttggaagggttaattcactcccaa
gaagacaagatatccttgatctgtggatctaccacacacaaggctacttccctgattagcagaactacac
accagggccaggggtcagatatccactgacctttggatggtgctacaagctagtaccagttgagccagat
aaggtagaagaggccaataaaggagagaaacaccagcttggtacacctgtgagcctgcatgggatggatg
accgggagagagaagtgttagagtggaggtttgacagccgcttagcatttcatcacgtggcccgagagct
gcatccggagtacttcaagaactgctgatatcgagcttgctacaagggaactttccgctggggactttcca
gggaggcgtggcctgggagggtggtgagtggtgagccctcagatcctgcatataagcagctgcttttt
gcctgtactgggtctctctggttagaccagatctgagcctgggagctctctggctaactaggaaccac
tgcttaagcctcaataaagcttgcttgagtgttcaagtagtggtgcccgtctgttgtgtgactctgg
taactagagatccctcagacccttttagtcagtggtgaaaatctctagcagtgggcgccgaacagggact
tgaaagcgaaagggaaccagaggagctctctcgacgcaggactcggcttgctgaagcgcgacggcaag
aggcgagggggcgcgactggtgagtagcgcacaaatatttgactagcggaggctagaaggagagagatggg
tgcgagagcgtcagtattaagcgggggagaattagatcgcatgggaaaaaattcgggttaaggccagggg
gaaagaaaaaataataaattaaaacatatagtagtggaagcaggagctagaacgattcgcagttaatcc
tggcctgttagaaacatcagaaggctgtagacaaatactgggacagctacaaccatcccttcagacagga
tcagaagaacttagatcattatataatacagtagcaacctctattgtgtgcatcaaaggatagagataa
aagacaccaaggaagcttttagacaagatagaggaagagcaaaacaaaagtaagaccaccgcacagcaagc
ggccgctgatcttcagacctggaggaggagatctgagggacaattggagaagtgaattataataataa
agtagtaaaaattgaaccattaggagtagcaccaccaaaggcaagagaagagtggtgagagagaaaaa
agagcagtggggaataggagctttgttccttgggttcttgggagcagcaggaagcactatgggagcagcgt
caatgacgctgacggtacaggccagacaattattgtctggtatagtcagcagcagagaacaatttgctgag

```

ggctattgagggcgcaacagcatctgttgcaactcacagctctggggcatcaagcagctccaggcaagaatc
 ctggctgtggaaagatacctaaggatcaacagctcctggggatttgggggtgctctggaaaactcattt
 gcaccactgctgtgccttgggaatgctagttggagtaataaatctctggaacagatttgggaatcacacgac
 ctggatggagtgaggacagagaaaattaacaattacacaagcttaatacactccttaattgaagaatcgcaa
 aaccagcaagaaaagaatgaacaagaattattggaattagataaatgggcaagtttgtggaattggttta
 acataacaaattggctgtggtatataaaattattcataatgatagtaggaggcttggttaggtttaagaat
 agtttttgcgtgacttttctatagtgaatagagtttaggcagggatattcaccattatcgtttcagacccac
 ctcccaacccccgaggggacccgacagggcccgaaggaatagaagaagaaggtggagagagagacagagaca
 gatccattcgattagtgaacggatctcgacggatctgccacaaatggcagattcatccacaatttttaa
 agaaagggggggattgggggggtacagtgacaggggaaagaatagtagacataatagcaacagacatacaaa
 ctaaagaattacaaaaacaaattacaaaaattcaaaatttttcgggtttattacagggacagcagagatcc
 actttggctgataagctttgcaaagatggataaagttttaaacagagaggaatctttgcagctaattggac
 ctcttaggtcttgaaaggagtgggaattggctccgggtgccgtcagtgggcagagcgcacatcgcccaca
 gtccccgagaagttggggggaggggtcggaattgaaccgggtgcctagagaaggtggcggggttaaact
 gggaaagtgatgtcggtactggctccgcctttttcccgaggggtgggggagaaccgtatataagtgcagt
 agtcgccgtgaacgttctttttcgcaacgggtttgcccgcagaacacaggttaagtgcgtgtgtggttcc
 cgcgggcctggcctctttacgggttatggcccttgctgccttgaattacttccacctggctgcagtacg
 tgattcttgatcccgagcttcgggttggaagtgggtgggagagttcgaggccttgcgcttaaggagcccc
 ttgcctcgtgcttgagttgaggcctggcctggggcgctggggcgccgcgtgcgaatctggtggcacctt
 cgcgctgtctcgctgctttcgataagtctctagccattttaaatttttgatgacctgctgcgacgcttt
 ttttctggcaagatagtcttgtaaatgcggggccaagatctgcacactgggtatttcgggtttttggggccgc
 gggcgggcagcggggcccggtgcgtcccagcgcacatgttcggcgaggcggggcctgcgagcgcggccaccg
 agaatcgagcgggggtagtctcaagctggcggcctgctctggtgcctggcctcgcgccgcgtgtatcg
 ccccgccctggcgggcaaggctggcccggctggcaccagttgcgtgagcggaaagatggccgcttcccgg
 ccctgctgcaggagctcaaaatggaggacgcggcgctcgggagagcgggagggtgagtcacccacacaa
 aggaaaagggcctttccgtcctcagcgcgtcgttcatgtgactccacggagtaccggggcgccgtcca
ggcacctcgattagttctcgagcttttggagtacgtcgtcttttaggttggggggaggggttttatgcat
 ggagtttccccacactgagtgggtggagactgaagttagg**ccagcttggcaattgatgta**attctccttg
 gaatttgccttttttgagtttggatcttgggtcattctcaagcctcagacagtggttcaaagtttttttc
 ttccatttcaggtgtcgtgagg
 aattgatccttcga
ACTAGT
GCGATCGC
 Acc **ATG GGT GTG GCC GAT CTG ATT AAG AAG TTC GAA TCA ATT AGT AAG GAA**
GAG GGT GGA TCA GGT
 GAG AGC GAC GAG AGC GGC CTG CCC GCC ATG GAG ATC GAG TGC CGC ATC ACC
 GGC ACC CTG AAC GGC GTG GAG TTC GAG CTG GTG GGC GGC GGA GAG GGC ACC
 CCC GAG CAG GGC CGC ATG ACC AAC AAG ATG AAG AGC ACC AAA GGC GCC CTG
 ACC TTC AGC CCC TAC CTG CTG AGC CAC GTG ATG GGC TAC GGC TTC TAC CAC
 TTC GGC ACC TAC CCC AGC GGC TAC GAG AAC CCC TTC CTG CAC GCC ATC AAC
 AAC GGC GGC TAC ACC AAC ACC **CAC**
 ATCGAGAAGTACGAGGACGGCGGGCGTGCTGCACGTGAGCTTCAGCTACCGCTACGAGGCCGGCCGCGTGA
 TCGGCGACTTCAAGGTGATGGGCACCGGCTTCCCCGAGGACAGCGTGATCTTCACCGACAAGATCATCCG
 CAGCAACGCCACCGTGGAGCACCTGCACCCCATGGGCGATAACGATCTGGATGGCAGCTTCACCCGCACC
 TTCAGCCTGCGCGACGGCGGCTACTACAGCTCCGTGGTGGACAGCCACATGCACTTCAAGAGCGCCATCC
 ACCCCAGCATCCTGCAGAACGGGGGCCCATGTTTCGCCTTCCGCCGCGTGG**AGGAGGATCACAGCAACAC**
GGAGCTGGGCATCGTGGAGTACCAGCACGCCTTCAAGACCCCG GAT GCA GAT GCC GGT GAA
 GAG
 ACGCGT
GAGGGCAGAGGAAGTCTGCTGACATGCGGTGACGTGGAGGAGAATCCAGGGctaGCACGCACGAAGCAAA
 CAGCTCGTAAGTCCACTGGCGGCAAAGCCCCGCGCAAGCAGCTGGCCACTAAGGCGGCTCGCAAAAGCGC
 GCCAGCCACCGGTGGCGTGAAGAAGCCCCACCGCTACAGGCCTGGTACTGTGCGCCCTCCGTGAAATCCGC
 CGCTATCAGAAATCGACTGAGCTACTGATTGCGAAG**CTACCATTCCAGCGTCTGGT**ACGTGAGATCGCGC
 AGGACTTCAAGACCGACCTGCGCTTCCAGAGCTCGGCTGTGATGGCGCTGCAGGAGGCCTGCGAGGCTTA
 CCTGGTGGG**GCTCTTTGAGGACACCAAC**TGTGTGCTATCCACGCCAAGCGAGTGACTATCATGCCCAAG
 GACATCCAGCTCGCTCGCCGCATTGCGGGAGAGAGGGGA
 GAATTC

Gcctcctccgaggacgtcatcaaggagttcatgcgcttcaaggtgcgcatggaggggtccgtgaacggcc
 acgagttcgagatcgagggcgagggcgagggcgcccccctacgagggcaccagaccgccaagctgaaggt
 gaccaagggcgggccccctgcccttcgcctgggacatcctgtccctcagttccagtacgggtccaagggc
 tacgtgaagcaccgccgacatccccgactacttgaagctgtccttccccgaggggttcaagtgggagc
 gcgtgatgaacttcgaggacggcggtggtgacctgacccaggactcctccctgcaggacggcgagtt
 catctacaaggtgaagctgcgcggcaccaacttccccctccgacggccccgtaatgcagaagaagaccatg
 ggctgggaggcctccaccgagcggatgtacccccgaggacggcgccctgaagggcgagatcaagatgaggc
 tgaagctgaaggacggcgggccactacgacgcccaggtcaagaccacctacatggccaagaagcccgtgca
 gctgccccggcgctacaagaccgacatcaagctggacatcacctcccacaacgaggactacaccatcgtg
 gaacagtacgagcgcgcgagggcgccactccaccggcgcc **taa**GGCGGCC
 ggatccgcatgcatctagggcgggccaattccgccccctccccccccccccctctccctcccccccccta
 acgttactggccgaagcgc **cttgggaataaggccgggtgt**
 gcgtttgtctatatgtgattttccaccatattgcgctcttttggcaatgtgagggcccgaaacctggcc
 ctgtcttcttgacgagcattcctaggggtcttccccctctcgccaaaggaatgcaaggtctgttgaatgt
 cgtgaaggaagcagttcctctggaagcttcttgaagacaaacaacgtctgtagcgacccttgcaggcag
 cggaacccccacctggcgacaggtgcctctgcggccaaaagccacgtgtataagatacacctgcaaagg
 cggcacaacccccagtgccacgttgtgagttggatagttgtggaaagagtcaaattggctctcctcaagcgt
 attcaacaaggggctgaaggatgccagaaggtacccattgtatgggatctgatctggggcctcgggtgc
 acatgctttacatgtgtttagtcgaggttaaaaaaacgtctaggccccccgaaccacggggacgtgggtt
 tccccctgaaaaacacgatgataagcttgcacacccacaaggagacgacctcc
 atgaccgagtacaagcccacgggtgcgctcgcaccccgcgacgacgtccccggggcggtacgcacctcg
 ccgcccgttcgcccactaccccgccacgcgcccacacgcgtcgaccggacccgacacatcgagcgggtcac
 cgagctgcaagaactcttccctcacgcgcgtcgggctcgacatcggcaaggtgtgggtcgcgacgacggc
 gccgcggtggcggtctggaccacgcggagagcgtcgaagcggggcggtgttcgcccagatcgggccgc
 gcatggccgagttgagcgggtcccggtggccgcgcagcaacagatggaaggcctcctggcgccgcaccg
 gcccaaggagcccgcgtgggtccctggccaccgtcggcgtctcgcccgaccaccagggcaagggctcgggc
 agcgccgtcgtgctccccggagtgaggcgggcgagcgcgcgggggtgccgccttccctggagacctccg
 cgccccgcaacctcccccttctacgagcgggtcgggttcaccgtcacccgcgacgtcgagtgccgaagga
 ccgcgcgacctgggtgcatgaccgcgaagcccgggtgcctga
 taataggcgggcgctcgagacctagaaaaacatggagcaatcacaagtagcaatacagcagctaccaatg
 ctgattgtgcctggctagaagcacaagaggaggaggaggtgggtttccagtcacacctcaggtaccttt
 aagaccaatgacttacaaggcagctgtagatcttagccactttttaaagaaaaggggggactggaaggg
 ctaattcactcccaacgaagacaagatctgcttttctgtactgggtctctctgggttagaccagatct
 gagcctgggagctctctggctaactaggaacccactgcttaagcctcaataaagcttgcccttgagtgt
 tcaagtagtggtgcccgtctgttgtgtgactctggtaactagagatccctcagaccttttagtcagt
 tggaaaatctctagcagtagtagttcatgtcatcttattattcagttattataacttgcaaagaaatgaa
 tatcagagagtgagaggccttgacattataatagatttagcaggaattgaaactaggagtgagcacacag
 gcaaagttctagagctcgtgatcagcctcgactgtgccttctagtgtccagccatctgttgtttgccc
 tcccccgctgccttccctgacctggaaggtgccactcccactgtccttccctaataaaatgaggaaattg
 catcgcatgtctgagtaggtgtcattctattctgggggggtgggggtggggcaggacagcaagggggagga
 ttgggaagacaatagcaggcatgctggggatgcgggtgggctctatggcttctgaggcggaaagaaccagc
 tgggggcgcgccccctcgaggccgcatggtcatagctgtttgacgtcaggtggcacttttcggggaaatg
 tgcgcggaacccctatattgtttatatttctaaatacattcaaataatgtatccgctcatgagacaataacc
 ctgataaatgcttcaataatattgaaaaaggaagagtatgagtattcaacatttccgtgtgcgcccttatt
 ccccttttttgccgcatatttgcccttccctgtttttgtcaccagaaaacgctgggtgaaagtaaaagatgctg
 aagatcagttgggtgcacgagtggtttacatcgaaactggatctcaacagcggtaagatccttgagagttt
 tcgccccgaagaacgttttccaatgatgagcacttttaaagttctgctatgtggcgcggtattatcccgt
 attgacgcggggcaagagcaactcggctcgccgcatacactattctcagaatgacttgggtgagtagctcac
 cagtcacagaaaagcatcttacggatggcatgacagtaagagaattatgcagtgctgccataacctgag
 tgataaacactgcggccaacttacttctgacaacgatcggaggacccaaggagctaaccgcttttttgac
 aacatgggggatcatgtaactcgcccttgatcgttgggaacccggagctgaatgaagccatacacaacgacg
 agcgtgacaccacgatgcctgtagcaatggcaacaacgttgcgcaaacatttaactggcgaactacttac
 tctagcttccccggcaacaattaatagactggatggaggcggataaagttgcaggaccacttctgcgctcg
 gcccttccggctgggtgtttattgtgataaatctggagccgggtgagcgtgggtctcgcggtatcattg
 cagcactggggccagatggtaagccctcccgatcgtagttatctacacgacggggagtcaggcaactat
 ggatgaacgaaatagacagatcgctgagataggtgcctcactgattaagcattggtaactgtcagaccaa
 gtttactcatatatacttttagattgatttaaaacttcatttttaatttaaaggatctaggtgaagatcc

```

tttttgataatctcatgaccaaaatcccttaacgtgagttttcggtccactgagcgtcagaccccgtaga
aaagatcaaaggatcttcttgagatccttttttctgcgcgtaatctgctgcttgcaaacaaaaaacca
ccgctaccagcgggtggtttgtttgccggatcaagagctaccaactctttttccgaaggtaactggcttca
gcagagcgcagataccaaatactgtccttctagtgtagccgtagttaggccaccacttcaagaactctgt
agcaccgcctacatacctcgtctctgctaatacctgttaccagtggctgctgccagtggcgataagtcgtgt
cttaccgggttgactcaagacgatagttaccggataaggcgcagcggtcgggctgaacggggggttcgt
gcacacagcccagcttgagcgaacgacctacaccgaactgagatacctacagcgtgagcattgagaaag
cgccacgcttcccgaaggagaaaaggcggacaggtatccggttaagcggcagggctcggaacaggagagcgc
acgagggagcttccagggggaaacgcctggtatctttatagtcctgtcgggtttcgccacctctgacttg
agcgtcgatttttgtgatgctcgtcagggggcgaggcctatggaaaaacgccagcaacgcggccttttt
acggttctctggccttttgc

```

Table 5.1. Final sequence of pSin-EF2-LA-tGFP-T2A-Histone3B-mRFP-IRES-Puro plasmid. Red highlights indicate pSin-F and IRES-R primers.

5.2.2 Lentivirus Production and Harvest

The production of lentivirus stock was achieved using the Human embryonic kidney (HEK) 293FT packaging cell line (Life Technologies), which stably expresses the SV40 large T antigen from the pCMVSPORT6Tag.neo plasmid. Approximately 9×10^6 HEK293FT cells were seeded into 150 mm tissue culture treated dishes and grown in high glucose DMEM (Life Technologies) supplemented with 1X MEM non-essential amino acids (Life Technologies) and 10% fetal bovine serum (Life Technologies) at 37°C, 5% CO₂ in a humidified incubator.

Approximately 24 hours post-seeding, media was removed and dishes were washed with warm OptiMEM (Life Technologies) to remove any residual serum and antibiotics, after which they were replenished with fresh Opti MEM with no serum nor antibiotics. 24 µg of the H3B-Lifeact plasmid was combined with 16 µg of the lentiviral packaging plasmid psPAX2 and 8 µg of the envelope vector VSV-G into 1.4 ml of Opti MEM in a DNA-LoBind tube (Eppendorf), lightly vortexed and briefly centrifuged. 168 µl of Polyethylenimine (PEI) [305] was added to this tube (pre-calibrated to 168 µl per 48 ug

DNA), vortexed for 10 seconds, centrifuged briefly and then incubated at room temperature for 15 minutes. This mixture was then added to the culture dish of HEK293FT cells dropwise while swirling the media for optimal distribution. After 6 hours of incubation at 37°C, 5% CO₂ in a humidified incubator, a final concentration of 10% serum was added to the dish and returned to the incubator to incubate overnight. The following day, the media was changed to serum containing high glucose DMEM supplemented with non-essential amino acids and 4 mM of caffeine (from 25X stock) to boost titer of the virus.

After 24 hours, media was collected, filtered with a surfactant free cellulose acetate 0.45 µm pore size filter (Millipore), and subsequently stored at 4°C. The dish was replaced with fresh high glucose DMEM, and 24 hours later, media was collected in the same fashion. The lentivirus was subsequently concentrated via ultra-centrifugation at 50,000 x G for 2 hours at 4°C. After spinning, virus was resuspended in 500 µl of sterile PBS, incubated for several hours, then aliquoted and stored at -80°C.

5.2.3 hMSC Transduction and Selection

hMSCs were seeded at a density of 5000 cells/cm² in a 24-well plate to prepare for lentiviral transduction. 24 hours post-seeding, media was replaced with alpha MEM supplemented with 10% heat inactivated fetal bovine serum and 8 µg/ml polybrene (Sigma-Aldrich) free of antibiotics. After 1 hour, lentivirus was added to the wells in a 1:200 virus to media volume ratio. hMSCs were allowed to incubate with lentivirus for 24 hours, after which puromycin (Life Technologies) was added to select for successfully

transduced cells. After 24 hours of incubation in puromycin, media was replaced with phenol-red free alpha MEM media, and the cells were imaged shortly after.

5.2.4 Live-Cell Real-Time Microscopy

Living hMSCs were imaged using a Leica TCS SP2 confocal laser scanning microscope equipped with a stage incubator (Life Imaging Services, Basel, Switzerland) set to 37°C and 5% CO₂. Lifeact-TurboGFP was visualized using an Argon-Krypton laser with 488 nanometer excitation and emission was detected using a photomultiplier tube set to a range of 505 to 550 nanometers. Histone H3B-RFP was visualized with Helium-Neon 594 nanometer wavelength excitation laser, and emission was detected with a photomultiplier tube set to a range of 600 to 670 nanometers. All images were acquired using a 40X dry objective with a numerical aperture of 0.6 (Leica Microsystems). Resolution format was set to 1024x1024 pixels, pinhole was constant at 1 Airy Unit, and laser power was maintained at 8% of total power to prevent laser induced cytotoxicity over time. Images were acquired at 10-30 minute intervals for various total periods of time, from 12 hours to 72 hours. The final image dataset that was analyzed via quantitative descriptor analysis was acquired over a total of 36 hours at 20 minute intervals, for a total of 108 images for each of 9 conditions.

5.2.5 Quantitative Assessment of Cell Body and Nucleus Relationship

hMSCs were cultured in the presence of differentiation inducing soluble growth factors or on different discrete stiffness PEGDM hydrogels in combination with the KMTi's

DZNep and MTA, as described in sections 2.2.1 and 2.2.2. After two weeks, hMSCs were fixed and immunolabeled for H3K4me3, H3K27me3 and Integrin β -1 (cat. no. ab30394, Abcam), as described in section 2.2.4. Cells' cytoskeletal actin was subsequently fluorescently labeled with Rhodamine Phalloidin (Life Technologies) according to the manufacturer's instructions. Images were processed for analysis using Image Pro 7.0 (Media Cybernetics), as described in section 2.2.7. A total of 29 morphometric descriptors characterizing geometrical features of actin expression, as well as the total area of Integrin β -1 expression, were extracted using Image Pro 7.0, and a total of 13 mean value Haralick texture descriptors characterizing intranuclear H3K4K27me3 organization were extracted using MATLAB (Mathworks).

All descriptors were normalized according to their global averages and standard deviations using Excel, and these values were averaged per treatment condition. Heatmaps describing the relationship between morphometric descriptors of the cell body and texture descriptors of the nucleus were generated by averaging the normalized values of each descriptor type, using MATLAB (Mathworks).

5.3 Results

5.3.1 Texture Image Analysis of Actin, Integrin β -1 and PTMs as a Response to Chemical Cues

hMSCs were cultured in the presence of adipogenic and osteogenic soluble growth factors, or maintained in media without growth factors to prevent their differentiation, as well as simultaneously treated with two lysine methyltransferase inhibitors (DZNep and MTA) to probe their cytoskeletal and intranuclear organizational response to these chemical cues. After two weeks of differentiation, hMSCs were immunolabeled for four marks (H3K4me3, H3K27me3, Actin, Integrin β 1) to potentially detect quantitative correlations between geometrical aspects of the cell body, the expression of integrins, and the intranuclear organization of H3K4K27me3 (Figure 5.3). Quantitative characterizations of the cell body were obtained by extracting descriptors that describe geometrical features of actin expression (i.e. area, aspect ratio, intensity, diameter, perimeter, roundness, margination etc.). The expression of integrin was quantified as the total area in pixels that integrins occupied, and these cell body descriptors were then related to Haralick texture descriptors describing the intranuclear organization of H3K4K27me3.

A particularly interesting observation across virtually every condition are the consistencies in trends for certain groups of texture descriptors. The values of entropy, inertia, correlation, information measure 2, sum average, sum variance, sum entropy,

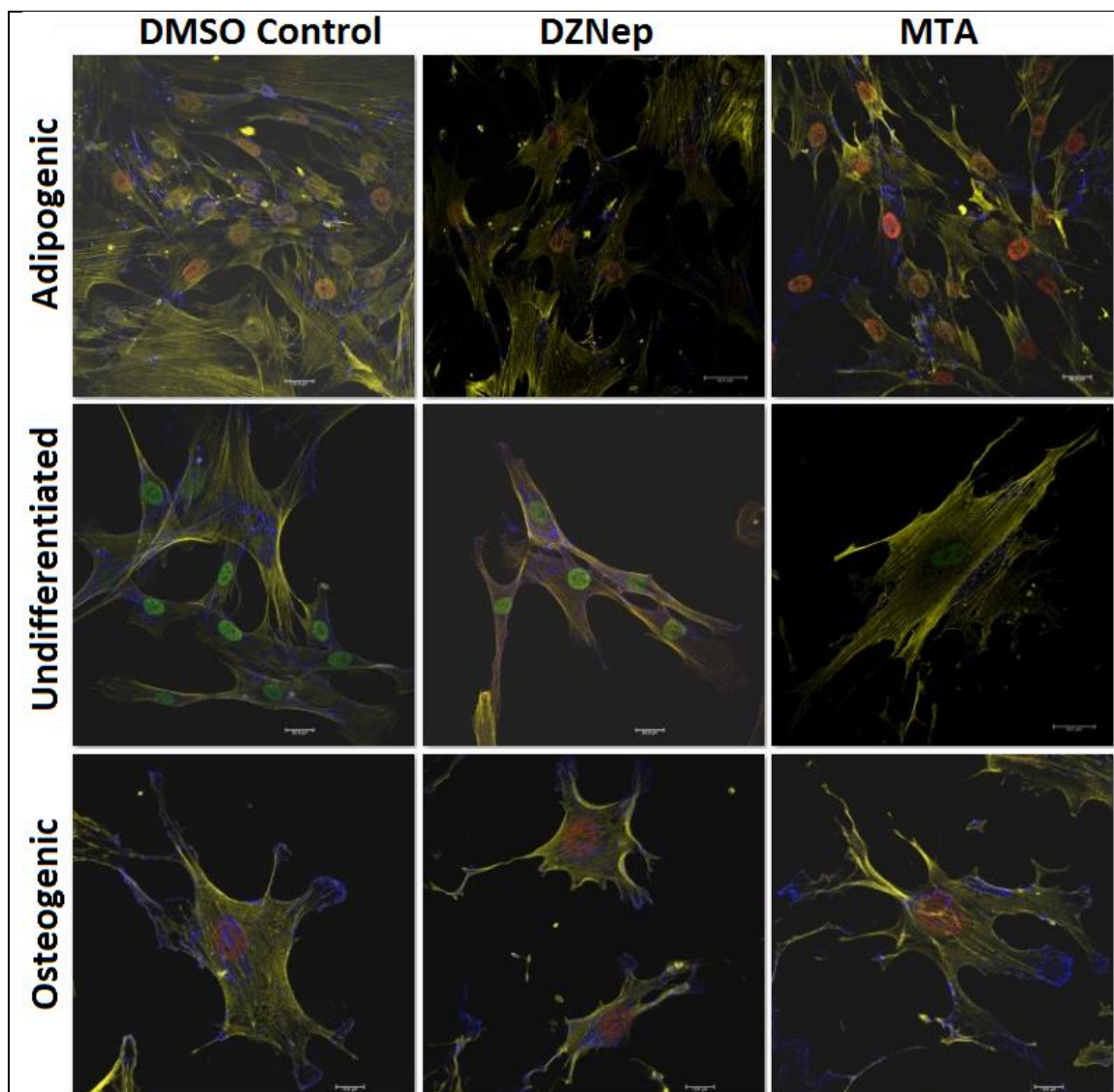
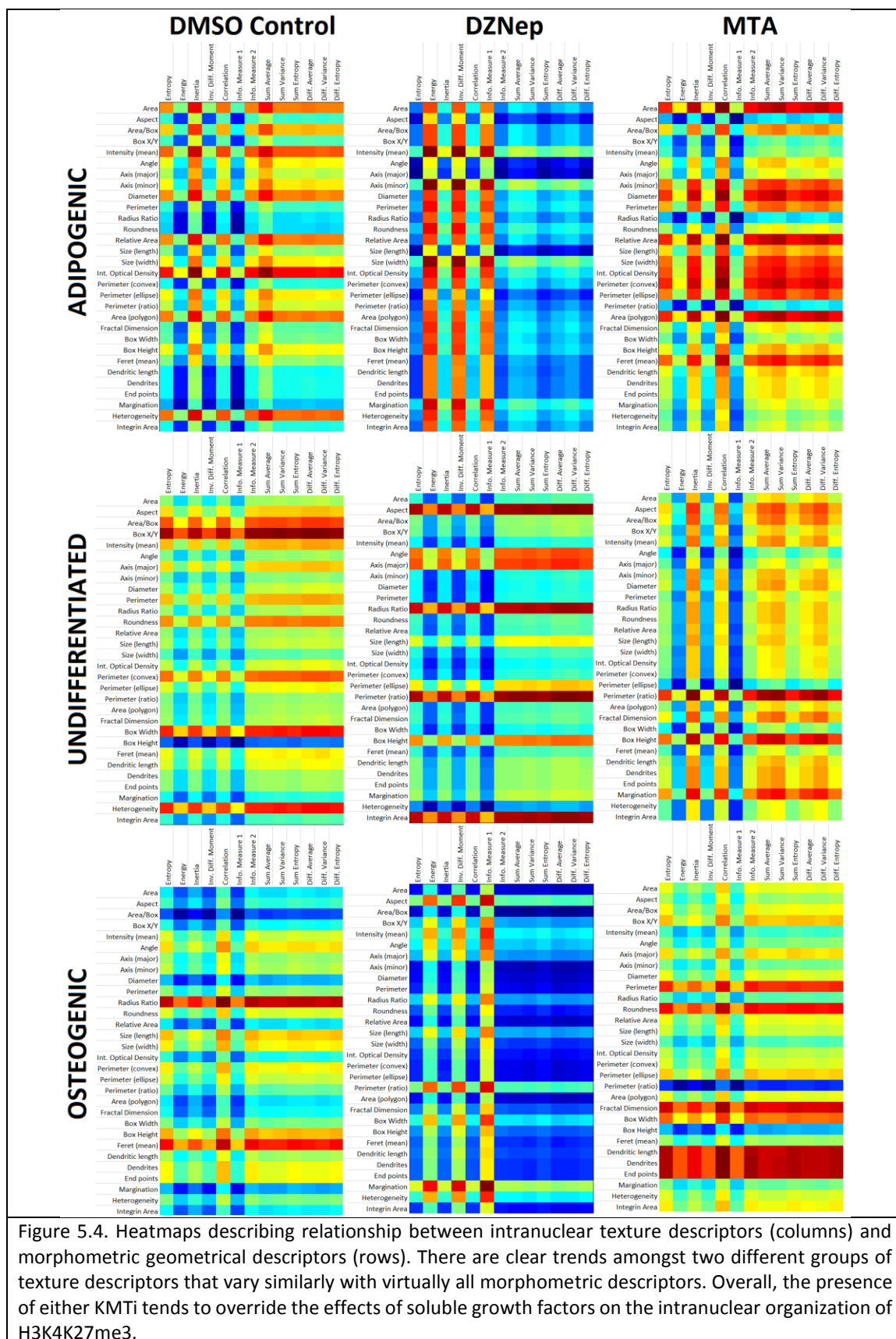


Figure 5.3. Quad-immunolabeling of hMSCs exposed to different combinations of chemical cues. hMSCs were treated with the KMTi's DZNep and MTA and induced to differentiate towards adipogenic or osteogenic lineages, or maintained as undifferentiated hMSCs. After two weeks of growth, hMSCs were fixed and labeled for H3K4me3 (green), H3K27me3 (red), Actin (yellow) and integrin β 1 (blue).



difference average, difference variance and difference entropy (herein referred to as “texture group 1”) tend to increase or decrease with each other in relation to the geometric descriptors characterizing cell body features. The values of energy, inverse difference moment and information measure 1 (herein referred to as “texture group 2”) tend to exhibit values that inversely correlate with the previously mentioned group of descriptors, also in relation to all geometric descriptors (**Figure 5.4**).

For differentiating hMSCs not treated with KMTi’s, we begin to notice some notable trends. Texture group 1 is highest in adipogenic hMSCs, lowest for osteogenic hMSCs, and maintains intermediate values for undifferentiated hMSCs, whereas texture group 2 exhibits the opposite trends (i.e. lowest in adipogenic, highest in osteogenic) in relation to the geometric descriptors. This is likely due to a combination of general increase in cell body size from adipogenic to undifferentiated to osteogenic hMSCs, but may also be reflective of increasing disorder of H3K4K27me3 organization in osteogenic hMSCs, as compared to both undifferentiated and adipogenic hMSCs. Another intriguing observation is that the total area of integrin expression seems to be rather consistent in all three cell phenotypes, suggesting that the overall presence of integrins may not be significantly affected as hMSCs are exposed to different differentiation inducing chemical soluble growth factors. Thus, this suggests that the total amount of integrin expression is minimally reflective of the downstream changes in gene transcription programs occurring as a response to exposure to different growth factors.

When hMSCs are exposed to KMTi’s in combination with different groups of growth factors, these previously noted trends tend to change. From a general, global

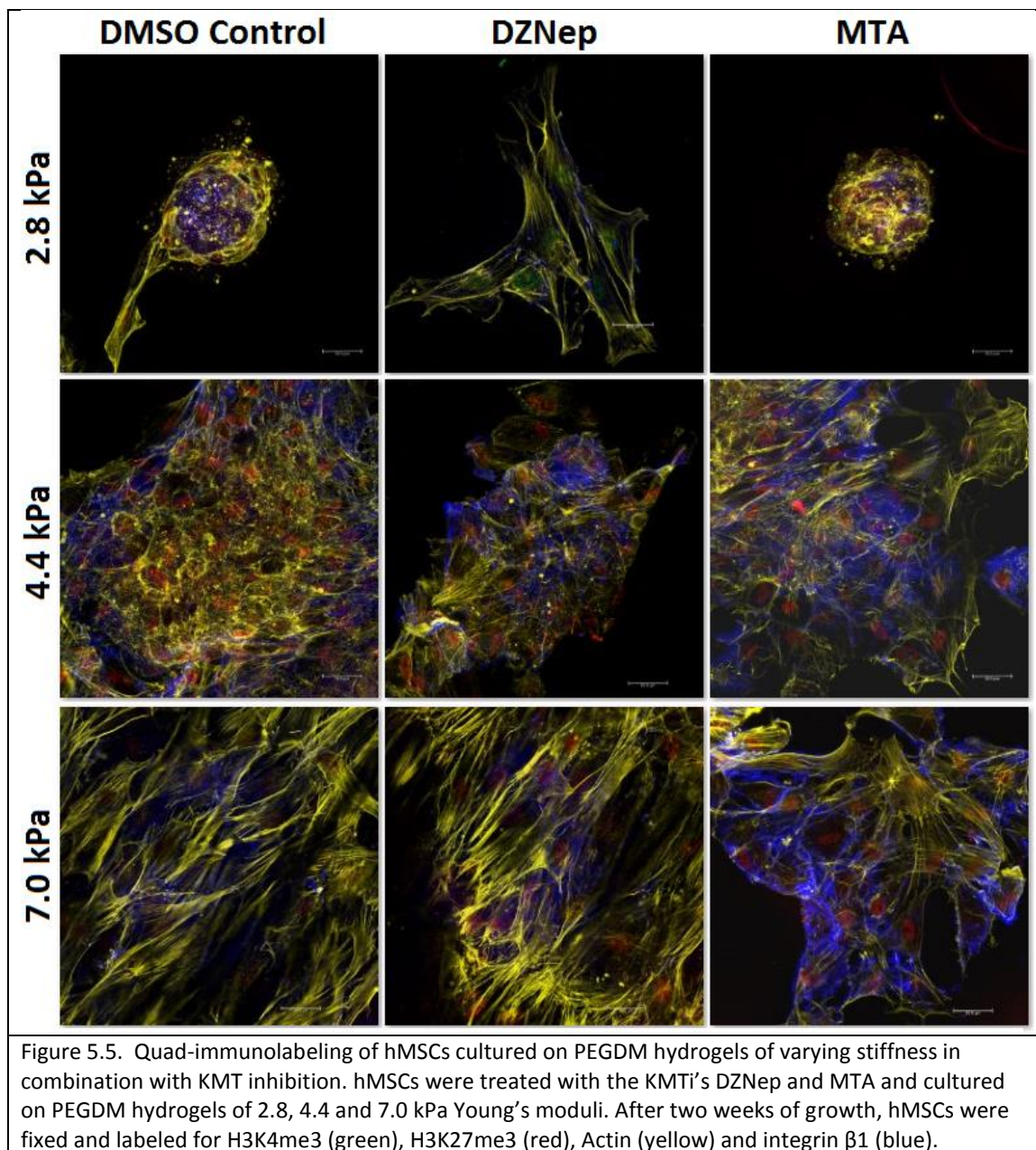
perspective, DZNep tends to cause an overall decrease in the values of texture group 1, whereas MTA tends to cause an overall increase in these values. The opposite effect is observed for texture group 2, with DZNep tending to increase these values and MTA tending to cause a decrease. The relative similarity in trends of intranuclear texture descriptors in relation to cytoskeletal geometric descriptors in hMSCs exposed to either KMTi and adipogenic and osteogenic growth factors is intriguing. This may suggest that KMTi's override the effects of growth factors on the intranuclear organization of H3K4K27me3, which is consistent with previous observations from the texture descriptor calibration and parsing index formulation studies. Finally, the integrin area does not seem to exhibit any blatantly consistent trends; integrin expression area does tend to be higher in MTA treated hMSCs, as compared to DZNep treated hMSCs, however the highest values are found in undifferentiated hMSCs exposed to DZNep. Thus, these observations of the lack of correlative changes in integrin area in response to exposure to different chemical cues may suggest that the total presence of integrins may not play a significant role in gene transcription navigation. Since integrins are vital to the transduction of extracellular cues into the cell, one may speculate that their organization may be more important, and more insightful, to the manipulation of protein signaling cascades that cause robust changes to gene transcription programs.

5.3.2 Texture Image Analysis of Actin, Integrin β -1 and PTMs as a Response to Mechanical Cues

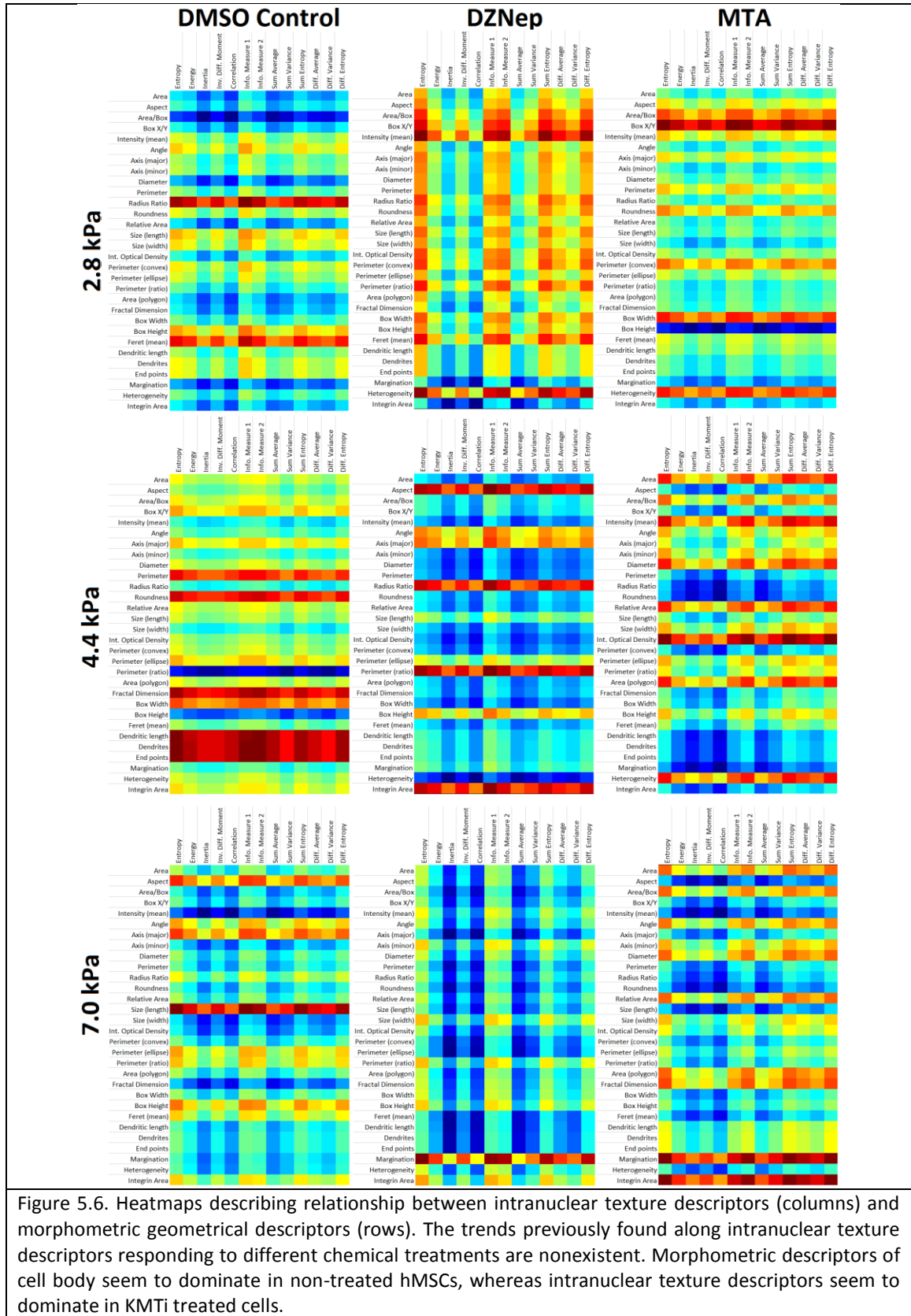
hMSCs were cultured on three PEGDM hydrogels with different values of discrete stiffness (2.8, 4.4 and 7.0 kPa) in the presence or absence of the two KMTi's, DZNep and MTA. Similar to the previous section, hMSCs were fluorescently labeled with four biomarkers, and were subsequently imaged, processed and quantitative morphometric and texture descriptors were extracted from these processed images (**Figure 5.5**).

When hMSCs are cultured on different degrees of stiffness without KMTi's, morphometric descriptors describing cell shape seem to be more responsive to different young's moduli when compared to nuclear texture descriptors. The overall area of the cell body and the total area of integrin expression seem to increase with increasing stiffness. Also, the trends between the two groups of texture descriptors described in the previous section do not seem to vary the same way, as when exposed to soluble growth factors.

On the other hand, when KMTi's are introduced, many of these trends in texture groups seem to reappear, which may suggest that texture descriptors describing the intranuclear organization of H3K4K27me3 are much more sensitive to KMT inhibition. The morphometric descriptors characterizing cell shape seem to be less responsive to these KMTi's, which is not surprising, since the KMTi's directly target specific nuclear enzymes. Moreover, the integrin area in KMTi treated hMSCs seem to vary more with the intranuclear texture descriptors, which further suggests that although there are some clear differences in integrin expression of hMSCs grown on different degrees of



stiffness, the effect of KMT inhibition cause even larger detectable differences (**Figure 5.6**).

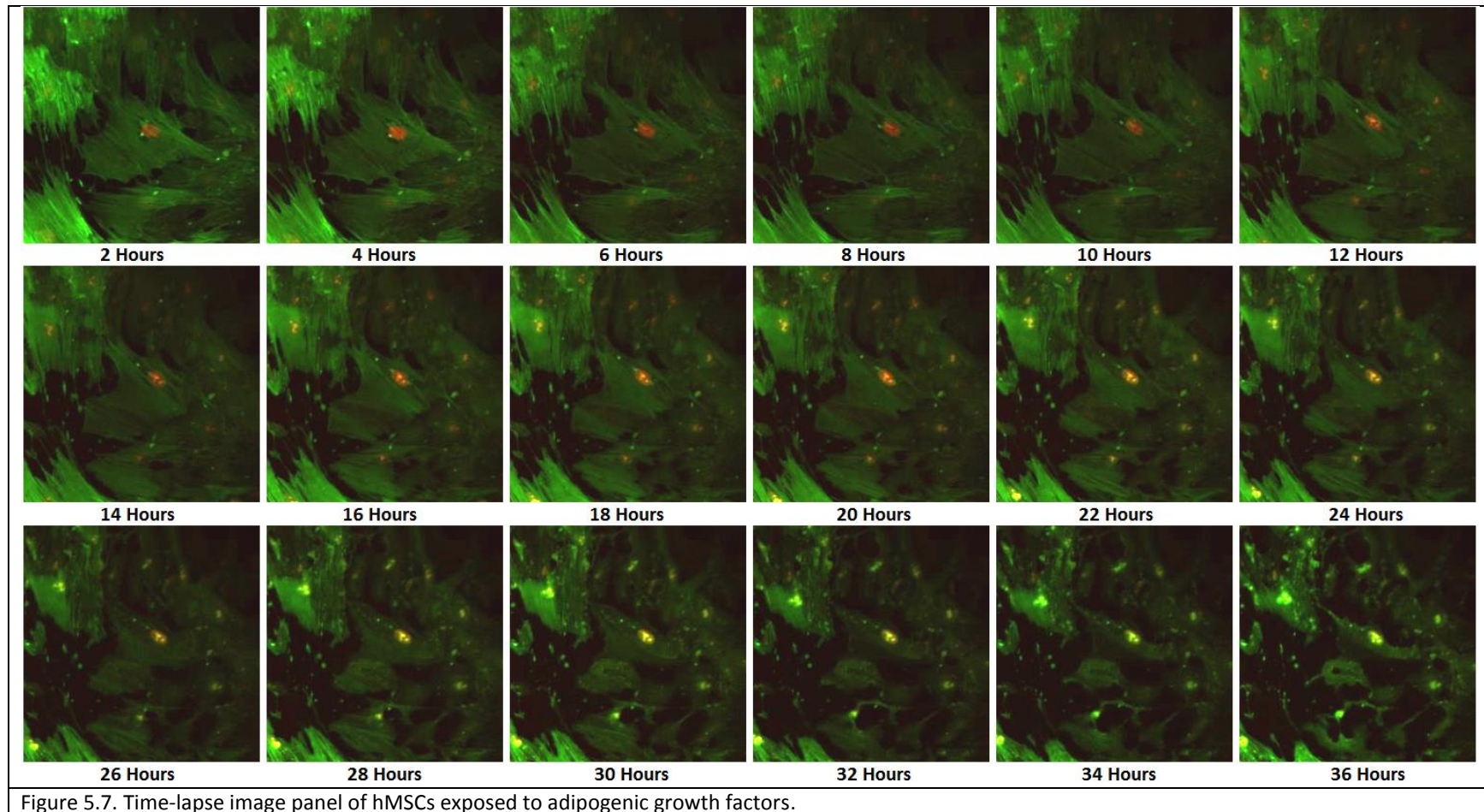


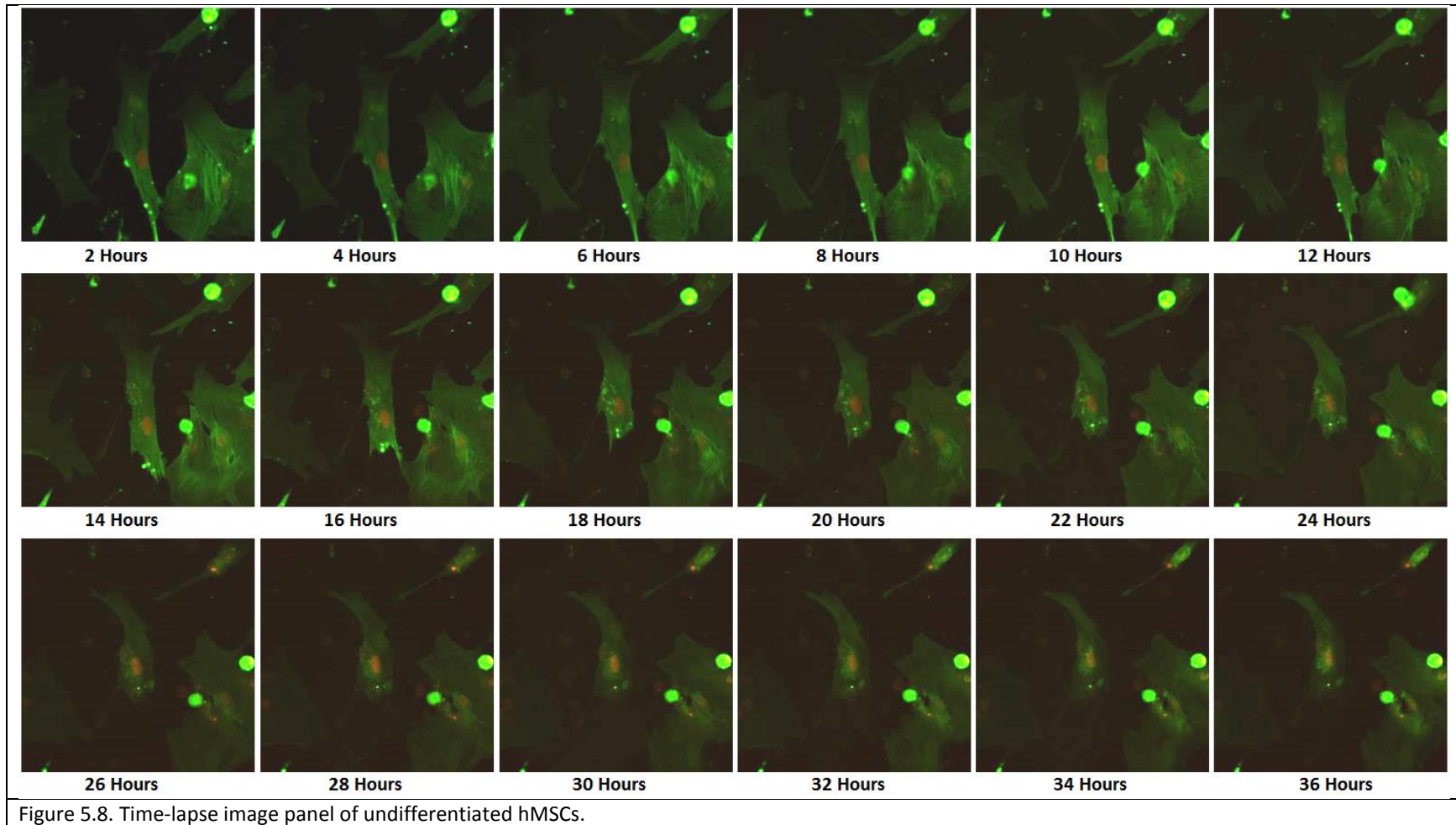
5.3.3 Live Image Analysis of H3B and Actin in Response to Chemical Cues in Living Human Mesenchymal Stem Cells

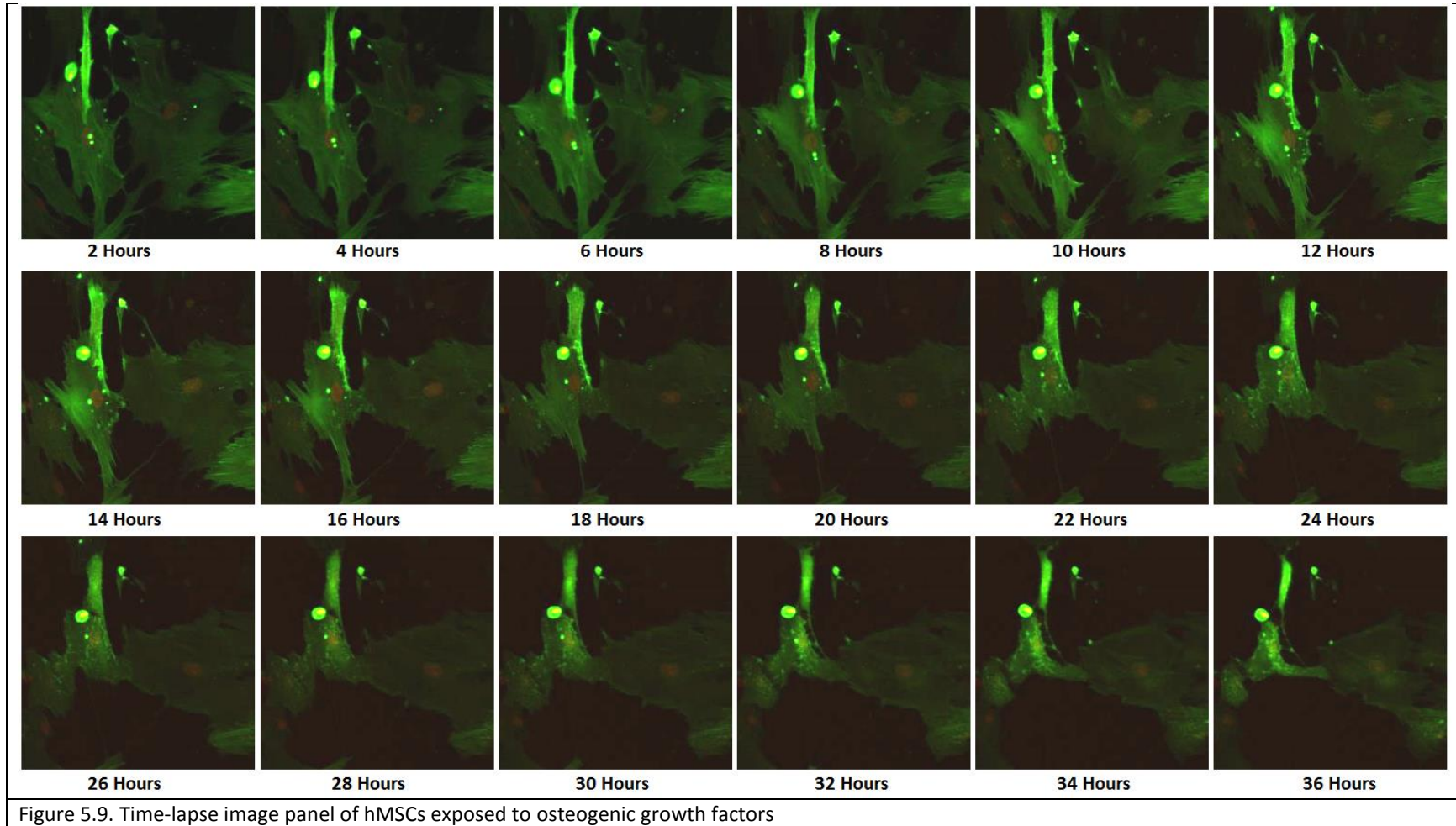
All image analysis conducted in this dissertation was performed on cells that have been chemically fixated using paraformaldehyde, prior to immunocytochemical labeling of proteins of interest. However, as mentioned throughout this document, cellular behavior is highly dynamic, and this approach to fixing and labeling cells is analogous to investigating a developmental process by taking “snapshots” through development. Moreover, the fixation effectively kills the cells, limiting this image analytical tool to a static cellular assay. Thus, to address these shortcomings, we designed a plasmid fluororeporter to monitor the expression of the core histone fraction H3.1 in combination with cytoskeletal actin. This allows for the real-time monitoring of H3.1 and actin dynamics, for investigating the live dynamics of intranuclear organization in relation to cytoskeletal structural changes, and using this quantitative information to characterize cell state with the goal of sorting cells based on this data.

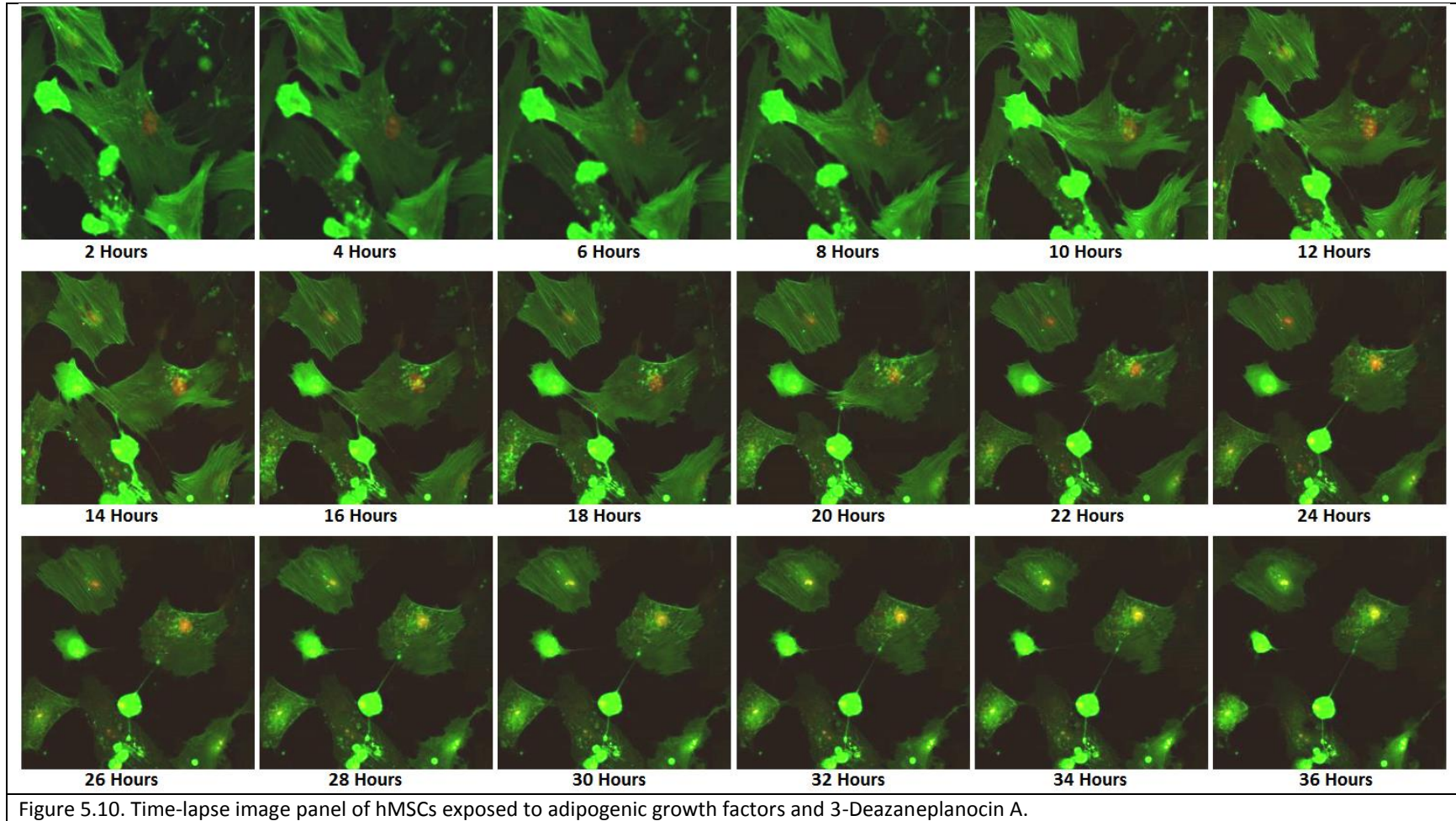
We began these investigations by monitoring the organizational dynamics of H3.1 and actin in response to lineage specific growth factor cocktails in combination with KMTi's. Different conditions were monitored in parallel for a total of 36 hours, and texture descriptors of intranuclear organization were obtained at 6 hour intervals. Descriptors were plotted using PCA, as previously described.

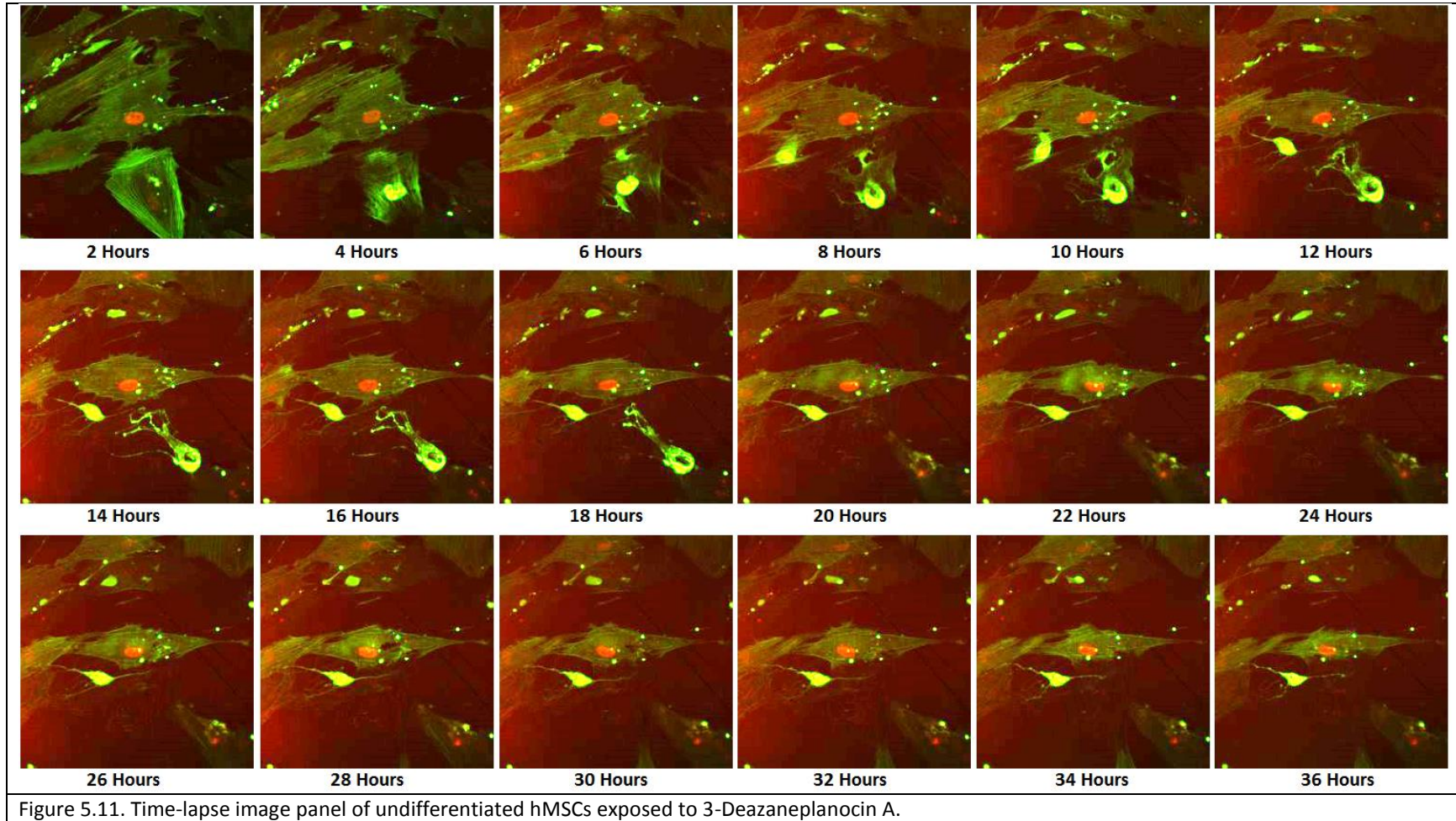
Time-Lapse Image Panels of H3B and Actin in Response to Chemical Cues in Living Human Mesenchymal Stem Cells

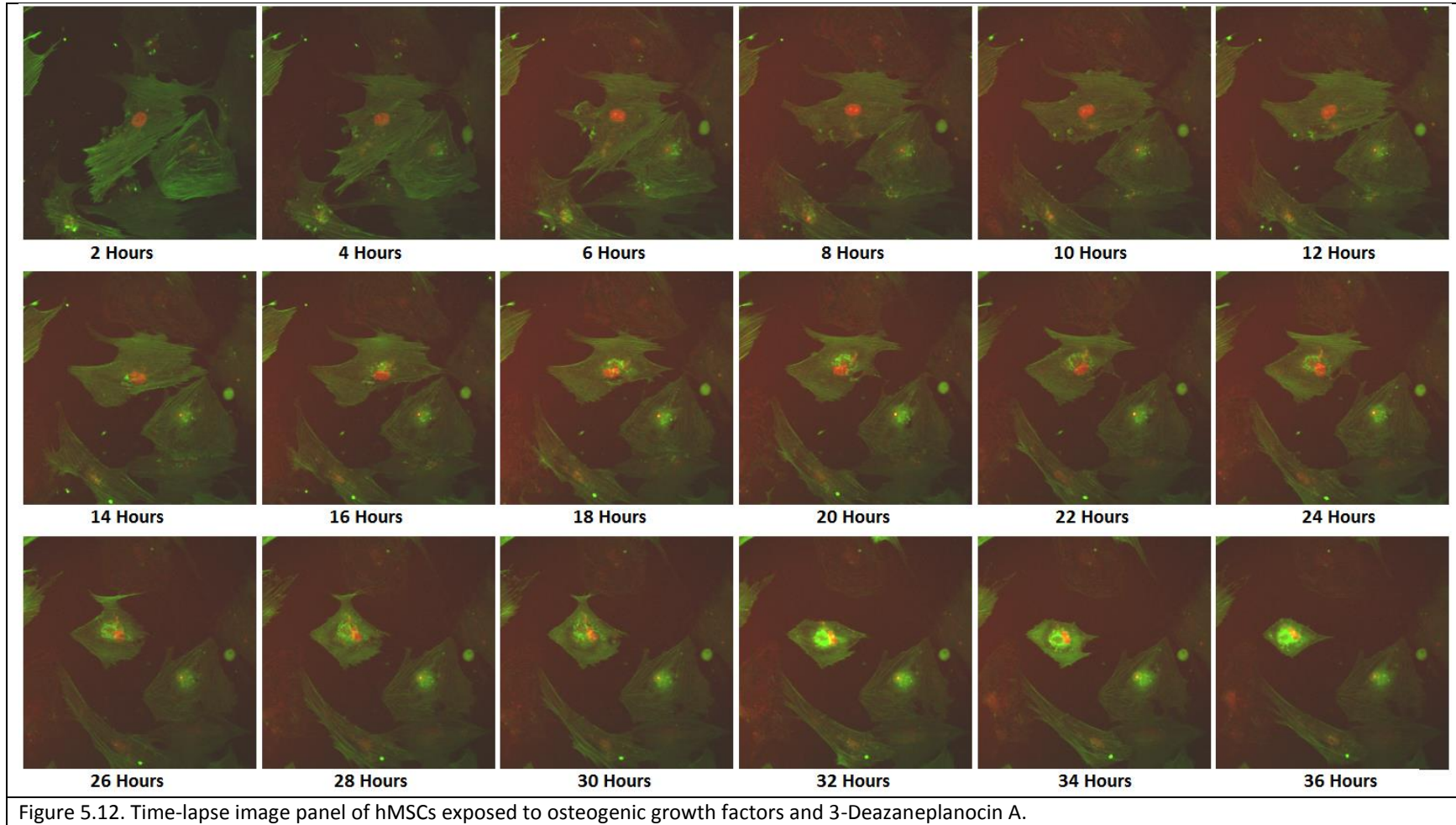


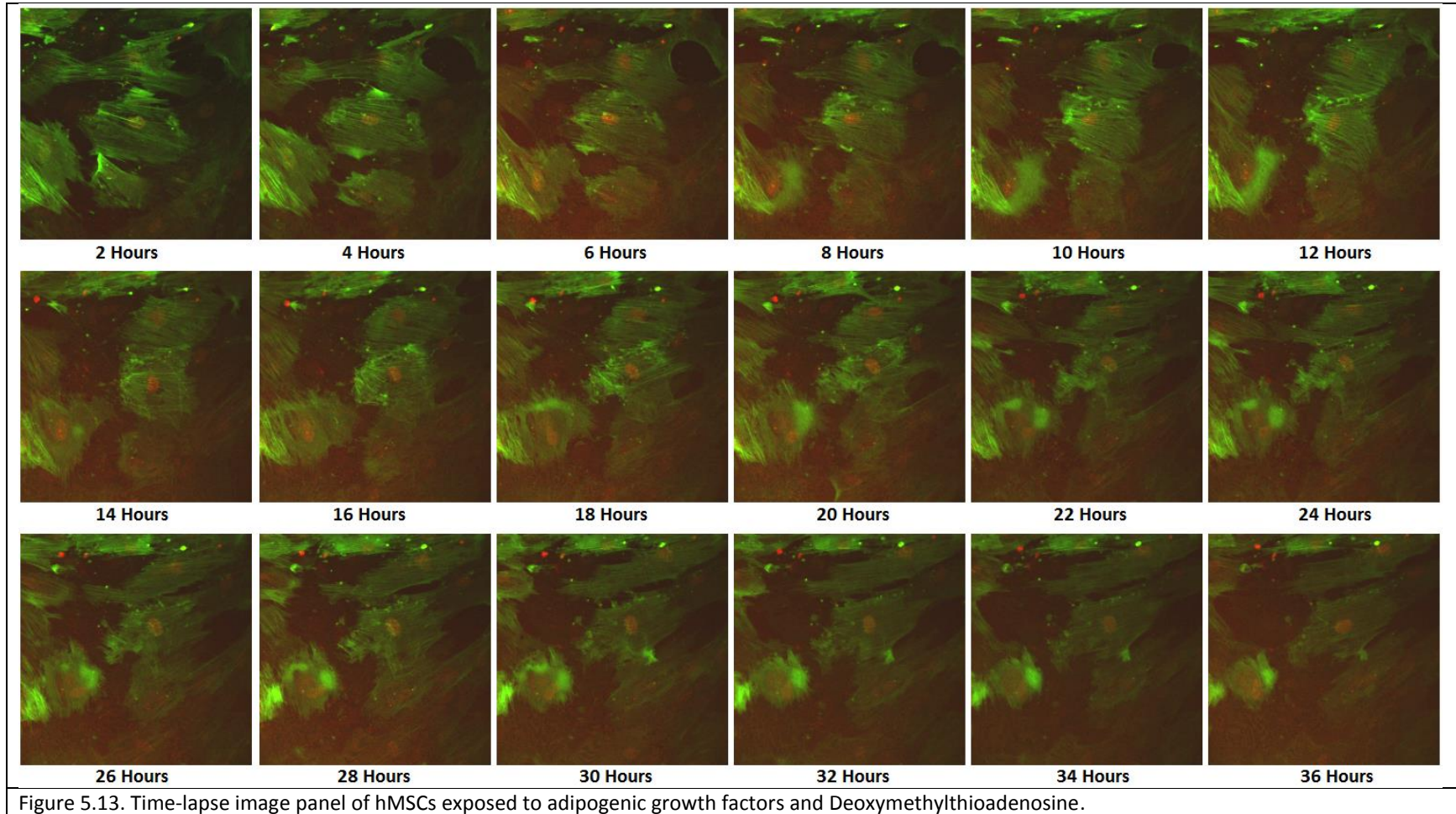












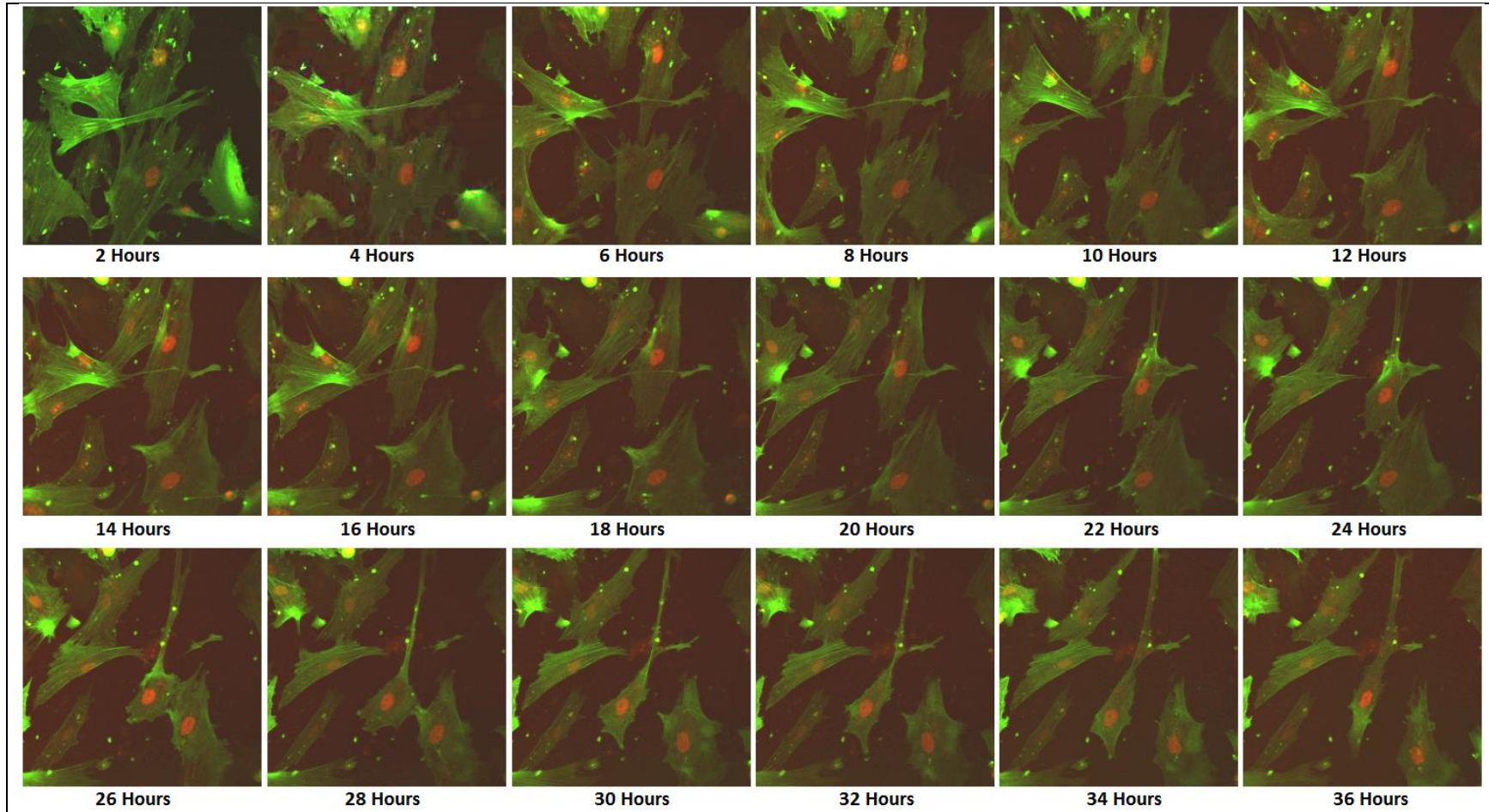
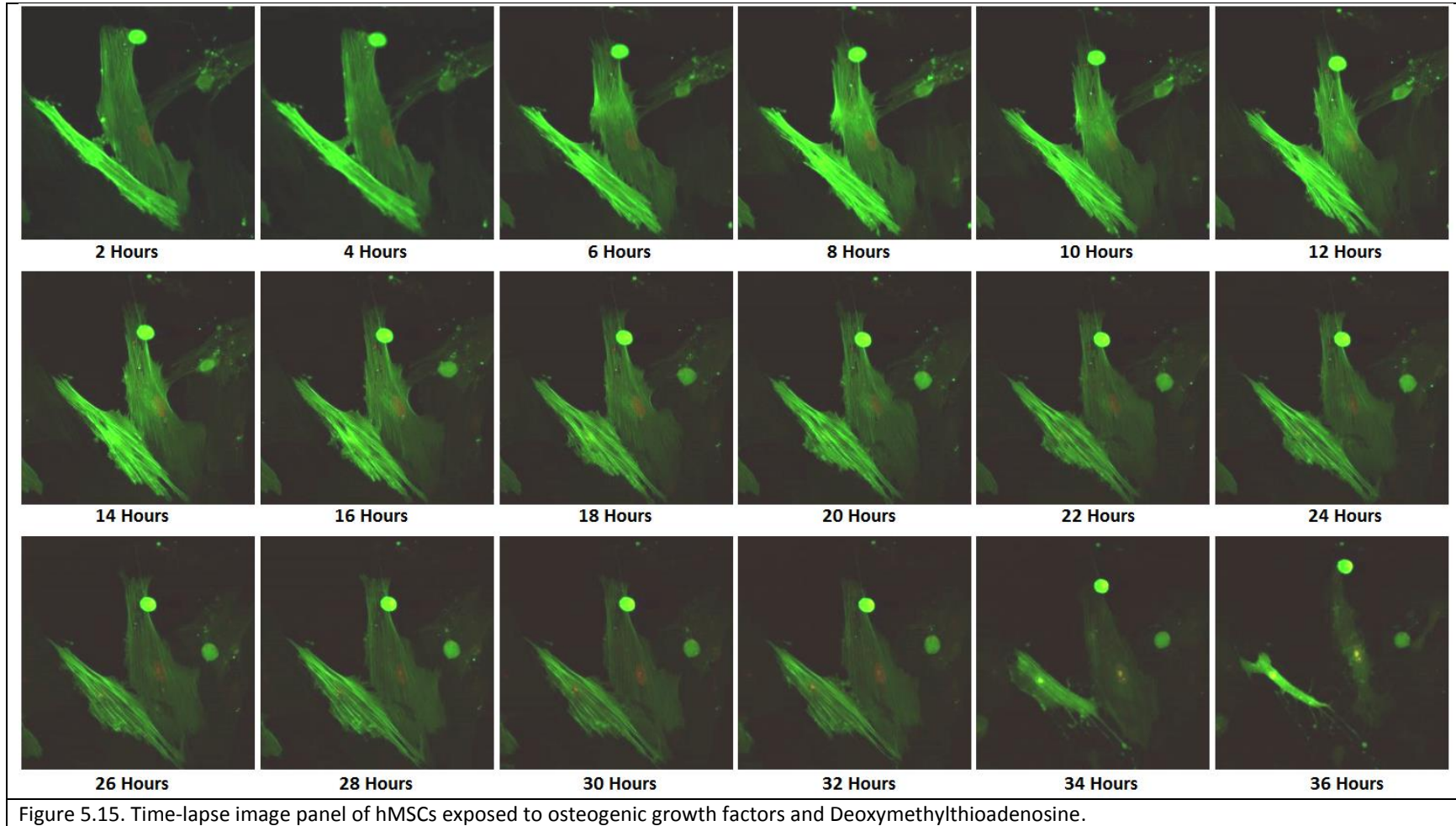
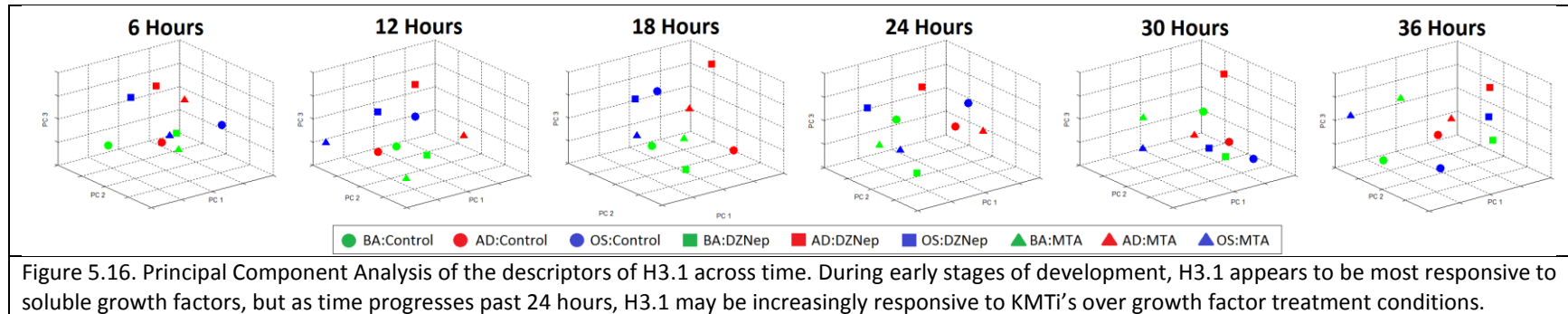


Figure 5.14. Time-lapse image panel of undifferentiated hMSCs exposed to Deoxymethylthioadenosine.





At earlier time points (i.e. 6-18 hours), the texture descriptors of H3.1 seem most responsive to lineage inducing growth factors (or lack thereof), as the spatial coordinates of dimensionally reduced descriptors of cells exposed to common growth factor conditions begin to aggregate towards each other. However, for the later time points (i.e. 24-36 hours), the effects of the KMTi's seem to overpower the growth factors, as the descriptor coordinates start to migrate and aggregate toward common KMTi conditions. Thus, these results may indicate two points: 1) Texture descriptors of H3.1 seem to be dynamically responsive to different chemical cocktail conditions, and 2) the effects of both KMTi's used in this study appear to take have a strong effect post 24 hours administration, which is seemingly enough to negate (or at least overcome) the effects of different growth factor administration conditions. However, it is important to note that the nature of data analysis was essentially still conducted on rather static images, and more rigorous data analysis that takes dynamics into paramount account (i.e. delta expressional organizations and fluorescence correlation spectroscopy) would be most appropriate to analyze this kind of bioimage information.

5.4 Discussion

The results summarized in this chapter are the first direct investigations quantitatively relating intranuclear epigenetic organizational activity and cytoskeletal morphological dynamics, to date. Despite the numerous studies detailing the biochemical pathways and seemingly infinite number of genes and proteins involved in specific biological phenomena involved in the communication between the nucleus and cell body, there has been little progress made on understanding this relationship from a structure/function perspective. As clearly evidenced *in vivo*, the functional diversity of the many different cell phenotypes that make up an organism is reflected in their morphological diversity. To a lesser extent, the nuclei of different cell types exhibit minute differences in their structure, but when considering the fact that all of the instructions that drive a cell's skeletal structure originate from the nucleus, one must acknowledge the fact that the spatiotemporal dynamics within the nucleus plays a large role in determining a cell's structure and function, especially when considering the fact that all of the different cells comprising a single organism share a common DNA sequence.

Thus, we sought to exploit such previously unexplored information by quantitatively characterizing cellular phenotypes from a structural perspective. Specifically, this involved employing optical imaging techniques to capture the expressional organization of nuclear and cytoskeletal proteins relevant to gene transcription dynamics. Previous studies in the Moghe laboratory investigated how cytoskeletal actin differentially responds to chemical cues and provides early clues on how naïve mesenchymal stem cells will develop later on [191]. Based on the success of

these investigations, we also monitored cytoskeletal actin in response to defined chemical cues, but we quantitatively related this to intranuclear organizational changes that simultaneously occur. Furthermore, as integrins are one of the major mediators between a cell and its immediate environment, we also investigated how the relative amount of integrin expression relates to intranuclear organization. For most conditions, the total area of integrin expression did not vary with intranuclear texture descriptors, suggesting that integrin expression was relatively independent of intranuclear organization. Furthermore, there were no noticeable trends in integrin expression that varied with different soluble growth factor chemical cues. However, when hMSCs were cultured on hydrogels of varying stiffness, there were detectable differences between different Young's modulus values, as well as chemical KMTi treatment. Thus, the mechanotransduction that is mediated by integrins is clearly evidenced in substrates of varying mechanical properties, whereas trends are less apparent (and perhaps non-existent) when cells are grown on glass and exposed to different growth factor cocktails.

Finally, real-time H3.1 dynamics were monitored by obtaining intranuclear texture descriptors at fixed time intervals over a 36 hour period. The PCA plots of these descriptors indicate that these dynamics are initially most responsive to soluble growth factor cocktail differences, but as time progresses past 24 hours, these descriptors become increasingly responsive to KMT inhibitors. This suggests that the KMT inhibitors may be overwhelming the differential effects of exposure to different growth factors, but this only begins to happen (or at least is able to be quantitatively detected) after a sufficient amount of time exposure to the KMT inhibitor has passed.

5.5 Conclusion

In summary, there were three main conclusions from the results of the studies in this chapter. First, when quantitatively relating the cell body and nucleus, the intranuclear organization was quantitatively more responsive to different chemical cues than the morphometrics of the cell body when hMSCs were cultured on glass and exposed to different cocktails of soluble growth factors. Conversely, when hMSCs were cultured on PEGDM hydrogels of different stiffness, the cytoskeletal morphology was more responsive than the intranuclear organization, which is perhaps not surprising considering the fact that varying mechanical properties directly alter the mechanotransduced signaling pathways in a cell, leading to drastic alterations in morphology. Finally, when monitoring H3.1 dynamics in real-time, the intranuclear organization is initially most responsive to different growth factor combinations, but as time progresses past 24 hours, KMT inhibitor treatment seems to overwhelm this effect.

CHAPTER 6: DISSERTATION SUMMARY AND FUTURE DIRECTIONS

6.1 Dissertation Summary

It is becoming increasingly clear that regenerative medicine using stem cells will radically revolutionize the future of medicine. This potential is rooted in the fact that, collectively, undifferentiated stem cells have the capacity to differentiate into every cell type in the human body. Aside from the obvious implications this has for tissue engineering and cell replacement therapy in the clinic, stem cells will continue to alter the very approach to investigating biological questions and discovering new drugs and materials in the laboratory. Thus, an immensely high level of comprehension for culturing and controlling the behavior of stem cells is vital to its safe and seamless incorporation into medical practice.

As mentioned throughout this dissertation, the bulk of scientific studies investigating stem cell behavior have been focused on “downstream” gene transcription changes, and subsequent protein translation changes, that occur in response to the presentation of specific environmental cues. While these studies have collectively served to increase our understanding of the somewhat delayed response of stem cells to defined stimuli, they have minimally addressed many of the dynamic epigenetic mechanisms that orchestrate these downstream responses. Thus, the work in this dissertation was concentrated on how some aspects of the spatial organizational expression of the epigenome change in response to environmental cues to navigate stem cell differentiation or maintain self-renewal.

Out of the many interacting posttranslational modifications to core histone N-terminal tails that influence chromatin structural dynamics and gene transcription

regulation, we initially focused on the two bivalent marks H3K4me3 and H3K27me3. These two marks have been reported to substantially influence the balance between differentiation and self-renewal in pluripotent stem cells by co-occurring on many of the same genes and regulating their activation or silencing [209, 210]. Since the bulk of investigations into these marks, and most other PTMs to histones, have been population based, we investigated the potential to characterize the organizational manifestation of these marks on a single-cell basis. This was particularly motivated by frequently heterogeneous nature of stem cell populations in general, due to their pliable nature.

We began by investigating the dynamic nature of H3K4me3 and H3K27me3 in human mesenchymal stem cells using established scientific methodologies. Forster Resonance Energy Transfer (FRET) analysis confirmed the higher presence of bivalency of these two marks in undifferentiated hMSCs, and a gradual loss of this bivalency after exposure to soluble chemical differentiation inducing growth factors. Chromatin immunoprecipitation (ChIP) analysis revealed the general activation role of H3K4me3 for genes important for the proper development of different phenotypes, and the silencing role of H3K27me3 for undesired genes in each respective cell type. Immunoelectron microscopy (IEM) of isolated nuclei labeled with gold-nanoparticles conjugated to H3K4me3 and H3K27me3 antibodies revealed the change in presence of these marks in different cell phenotypes with respect to their localization in euchromatic vs. heterochromatic areas. These results (i.e. FRET, ChIP & IEM) considered together indicate an organizational dynamic expression of H3K4K27me3 in response to, and perhaps directing, differentiation.

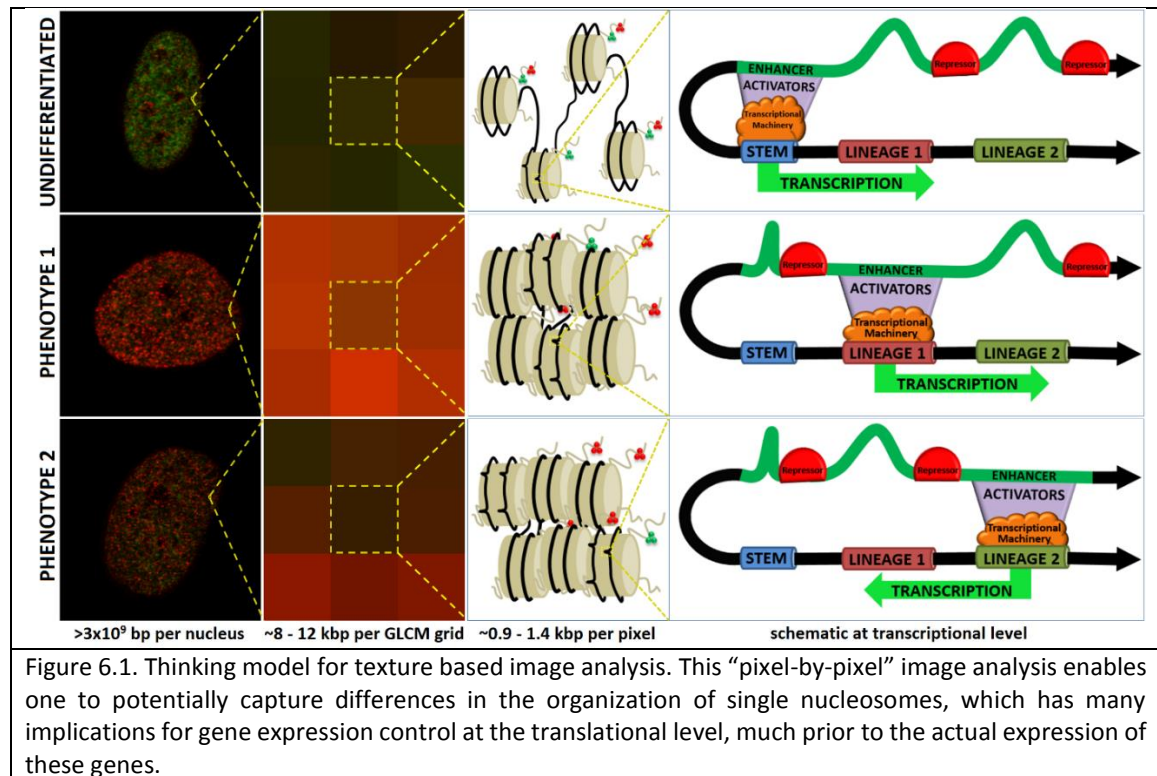
After confirming the dynamic nature of H3K4K27me3 in cellular development, we began to explore strategies to capture and characterize these dynamics in single cells using image analysis. After the exploration of several quantitative image analytical approaches (i.e. Gabor filters, Haar wavelets, nucleoli features, fluorophore intensity, geometric descriptors), we discovered that Haralick texture descriptors were able to capture these organizational dynamics. We calibrated and trained support vector machines (SVM) to distinguish between large shifts in the balance between H3K4me3 and H3K27me3 using selective lysine methyltransferase inhibitors (i.e. 3-Deazaneplanocin A and Deoxymethylthioadenosine). We subsequently applied this trained, calibrated SVM to distinguish H3K4K27me3 expression in differentiating hMSCs and iPSCs. After establishing the efficacy and accuracy of this tool post-differentiation, we investigated the organizational dynamics of H3K4K27me3 throughout development, starting from as early as 24 hours post differentiation induction. This study revealed that we were able to identify and distinguish hMSC differentiation after just 72 hours post differentiation induction, which is prior to the onset of classical lineage markers.

The success of this tool in characterizing H3K4K27me3 expression in 2D motivated us to investigate the potential to use this tool to screen biomaterial properties of hMSCs cultured in 3D. The two substrates we investigated were focused on varying mechanical properties (i.e. Young's modulus) and nanotopography. When we compared the H3K4K27me3 textures of hMSCs cultured on these substrates to those of pre-differentiated hMSCs cultured in 2D, we found that hMSCs cultured on soft PEGDM hydrogels exhibited H3K4K27me3 expression similar to that of adipogenic hMSCs. When

hMSCs were cultured on PUA nanogrooves, they exhibited H3K4K27me3 expression similar to those of pre-differentiated osteogenic cells. Histological evaluation of osteogenic and adipogenic lineage markers on these two materials confirmed that these cells were in fact differentiating toward lineages that resembled their H3K4K27me3 expression. These results suggest that this approach could be potentially used to screen other material properties for the purpose of facilitating the achievement of desired cellular phenotypes.

Important points to consider, which rationalize and somewhat validate this image analysis approach, are the size-scale equivalents at the biochemical-structural level and the chronological order of events taking place at the transcriptional level. Human cells contain slightly over three billion base pairs of DNA in the nuclei of every diploid cell in the body. Based on the approximate average of pixel area of the nuclei that were imaged throughout this thesis, this equates to roughly 0.9 – 1.4 kilobase pairs of DNA contained per pixel. The GLCM, on which Haralick texture features are computed, depends on the neighboring 8 pixels around every pixel, which essentially means the final value attributed to any given single pixel depends on a minimum 3x3 grid of pixels that surround it. This is the equivalent of roughly 8-12 kilobase pairs of DNA that could influence the quantitative value of any one pixel at any given time. From the perspective of nucleosomes, this would equate to approximately 7 nucleosomes per pixel, on average, and up to 63 nucleosomes per 3x3 grid, which inevitably, either slightly or largely, influence the value of the center pixel (Figure 5.17). Thus, the organizational patterns of PTMs manifested on these

nucleosomes can be quite accurately reflective of what is occurring at the local chromatin structural level.



The temporal aspect of these epigenetic events is also quite important, especially when considering the potential of this type of analysis for predictive purposes. The dynamic organization that occurs at the PTM level highly influences downstream gene transcriptional changes. To date, these downstream gene transcription changes have been mainly measured via the amplification of the resultant gene levels via PCR, much after these early PTM organizational signatures have previously been already established, or perhaps even disappeared,. Even further downstream of this are protein quantifications that monitor changes made at the post-translational level. We present experimental data that indicates that certain “epimark” organizational footprints

correspond to downstream gene transcription changes that drive the differentiation of specific lineage directions, which can be captured prior to alternative assays for gene and protein quantification. Thus, this has many implications for how to more effectively and efficiently approach and probe cellular responses to controlled environmental conditions.

6.2 Future Directions

This thoroughly characterized image textural analytical approach provides a unique perspective on chromatin structural dynamics and their influence on gene transcription regulation. Since it is relatively easy to perform and substantially reduces the time and costs required for more comprehensive methods of interrogating the epigenome, along with allowing cells to stay intact, they are good places to begin investigations, as well as supplement data, on the structural dynamics of chromatin as a response to epigenetic modifications. As we continue to decipher the mysteries underlying how the dynamic epigenome regulates gene transcription and controls cellular behavior, we can begin to investigate different ways to exploit this information for the precise control of cellular behavior. Developing methods that enable us to have increasingly precise spatiotemporal control over the epigenome will allow us to gain more precise control over directing cellular behavior, and could open the door to currently abstruse possibilities such as bioactive epigenetic biomaterials and iPSC generation from integration-free, epigenetic reprogramming.

6.2.1 Fabrication of Bioactive Scaffolds for Directed Cell Differentiation

A major general challenge to regenerative medicine is the efficient generation of purified, homogenous populations of desired cellular phenotypes. Although there has been tremendous progress made in the generation of mature somatic cell types from the directed differentiation of stem cells, the innate heterogeneity of undifferentiated stem cell populations inevitably pollutes these resultant differentiated cell populations. Currently, the majority of techniques for directing cellular differentiation involve targeting the activation or silencing of specific sets of developmental genes using soluble growth factors [306], siRNA [307], pharmaceutical agents [308] and viral transfection [244]. However, mechanobiology also plays a large role in directing stem cell differentiation, as many environmental factors such as substrate mechanical properties, extracellular matrix composition and other physicochemical properties of a microenvironment contribute to the ultimate behavior of cells [309]. There have been several studies investigating the correlations between physical substrate properties and gene transcription regulation, but the root of most gene transcription changes stem from epigenetic modifications. Thus, it is advantageous to focus on directing desired epigenetic states that produce defined patterns of gene transcription. This will enable an increased control over the subsequent cellular differentiation, which would be advantageous for designing transplantable biomaterials that promote the development of homogenous and purified cell phenotypes of interest.

6.2.2 Epigenetic Drug Development for Cancer Therapy

The influence of pharmaceutical agents on specific aspects of epigenetic behavior is a field of active interest. Among the many different debilitating diseases that have been linked with an aberrant epigenome, the epigenetic regulation of cancer transformation has received the most attention. In particular, the global hypoacetylation of histones observed in cancer cells [310, 311] has inspired efforts for investigating the efficacy of HDAC inhibitors as potential anticancer agents [312-315]. Several candidate HDAC inhibitors are currently undergoing clinical trials [316-324], and a few have already been approved by the FDA for the treatment of cutaneous T-cell lymphoma [325-327].

Thus, the development of image based techniques which characterize dynamic epigenetic signatures during cellular differentiation can also be applied to profiling aberrant epigenetic signatures which accompany cancer transformation. This has the potential to greatly facilitate high throughput cancer drug screening and discovery.

6.2.3 Epigenetic Modifications to Induce Pluripotent Stem States

A reliable and readily available source of cells is critical for the development of cell-therapies for use in regenerative medicine. Pluripotent human stem cells have the potential for use in the widest range of applications, as they have an inherent ability to form almost every cell type in the human body. iPSCs are particularly attractive as they can be generated from any patient and scaled up to provide a seemingly infinite amount of pluripotent cells for directed differentiation. However, their clinical translatability is compromised due to the fact that current methods of their generation involve transfection with a viral vector, which can ultimately result in the creation of mutations

and other genomic aberrations. Therefore, recently there has been much attention paid toward the development of integration-free methods for cellular reprogramming. One of the earlier reports used non-integrating episomal vectors that can be removed after reprogramming for generation of iPSCs that are free of vector and transgene sequences [328]. Another group derived iPSCs from mouse embryonic fibroblasts by exposing them to recombinant cell-penetrating proteins [329]. Still others have explored reprogramming using synthetic mRNA [330], and miRNA [331] approaches. However, all of these approaches exhibit extremely low efficiency rates, albeit successful at ultimately reverting some cells to pluripotency, and are thus currently impractical for consistently robust and efficient iPSC generation.

An inevitably imperative and vital task for the alteration of any cell phenotype is the induction of precise changes to gene transcription programs. As repeatedly emphasized throughout this thesis, this is largely accomplished via epigenetic mechanisms. Thus, one potential way to revert somatic cells to pluripotency is by systematically identifying the epigenetic modification patterns (i.e. histone codes, DNA methylation locations and chromatin remodeling protein activity) that are linked to the activation of the key developmental genes (i.e. OCT4, SOX2, KLF-4, c-MYC). Subsequently, through the use of pharmaceutical agents and/or siRNA, those epigenetic modifications can either be forcibly upregulated or downregulated to promote gene transcription patterns reminiscent of iPSC generation via viral transfection. This discovery has the potential to greatly facilitate the clinical translation of iPSCs in regenerative medicine, and expedite the developmental progress of truly personalized medicine.

6.2.4 Mapping Material-Responsive PTM Landscapes Using Mass Spectrometry

Proteomic interrogation using Mass Spectrometry is a powerful technique to resolve the variety of PTMs that occur on isolated histone fractions. [161, 162, 165]. By employing MS to resolve and compare the PTM landscapes that occur on histones in different, well-defined materials, we can begin to establish correlations between epigenetic changes as a response to material properties. Aside from the traditional approach to separating peptides based on their m/z ratio, we can also distinguish peptides based on their retention time on a high-performance liquid chromatography (HPLC) column. This is especially useful for distinguishing between PTMs that share a nearly identical m/z value. When m/z values and retention times are both nearly identical between two PTMs, tandem MS (MS/MS) can be employed to further separate and identify them [218, 332].

Once PTMs are separated and identified, we can quantify their relative presence by computing the area under each peak in a mass chromatogram, and subsequently dividing this by the sum of all areas of all peaks to obtain a relative percentage quantity. The ultimate goal is to compare the mass chromatograms of histones isolated from cells cultured in different microenvironments. For substrate variation studies, it is important to expose cells to well defined physical/chemical parameters, and have defined variations between different conditions in order to attribute the PTM responses to specific physical/chemical attributes. Also, since there are often variations that occur between different runs in HPLC and MS, it is vital to analyze samples to be compared

simultaneously by labeling them with different stable isotopes. It is also crucial to load equal weight amounts of histone peptides from different samples to control for artifacts that may arise from comparing samples of unequal amounts.

6.2.5 Quantitative Analysis of Chromatin Structural Dynamics Using Fluorescence Correlation Spectroscopy

The continuous rapid local chromatin structural dynamics that drive DNA accessibility and proper gene transcription patterns can be captured and analyzed in living cells in real time using an optical technique called fluorescence correlation spectroscopy (FCS) [333, 334]. Commonly employed on confocal microscopes, FCS is capable of detecting single molecules and monitoring their mobility and diffusion by recording and correlating the fluctuations in measurements of their fluorescence intensities [335]. These fluctuations are caused by the movement of fluorophores between a defined illuminated volume and its surroundings, as a result of thermal energy. As an illustration, say dynamic fluorescence intensities in a defined volume is recorded over a defined time period, and this fluorescence intensity trace continues to either increase or decrease in response to the changing number of fluorophores in the defined volume. Spatiotemporal information of these fluorescence fluctuations is determined by auto-correlating, or cross-correlating, those recorded fluorescence intensity traces, from which insightful physical parameters, such as diffusion rate and molecular size, can be computed [335]. Diffusion coefficients can then be determined, which reflect how far molecules can move in a specified period of time, and can additionally be related to structural and size changes

[336], as well as dynamic molecular interactions [337, 338] (**Figure 6.2**). In the context of dynamic chromatin, determining these parameters can provide a wealth of information detailing the local structural dynamics of the nucleosome as a response to specific epigenetic modifications. This has been investigated for general histone marks in living cells to illustrate the rapid nature of structural dynamics in chromatin [304], but can be further applied to monitor the nature of these local dynamics in response to specific environmental stimuli.

Since chromatin structural dynamics occur constantly and are highly influenced by the environmental signals that are transduced to the nucleus after traveling through the cytoplasm, there may be a correlation between a cell's single nucleosome movements and defined stimuli from its microenvironment. In addition, there are correlations between the organizational dynamics of the cell body and nucleus which occur in response to environmental stimuli, and these correlations can potentially be identified via quantitative high-content image analysis in living cells, and ultimately coupled with microfluidic devices for effective cell sorting.

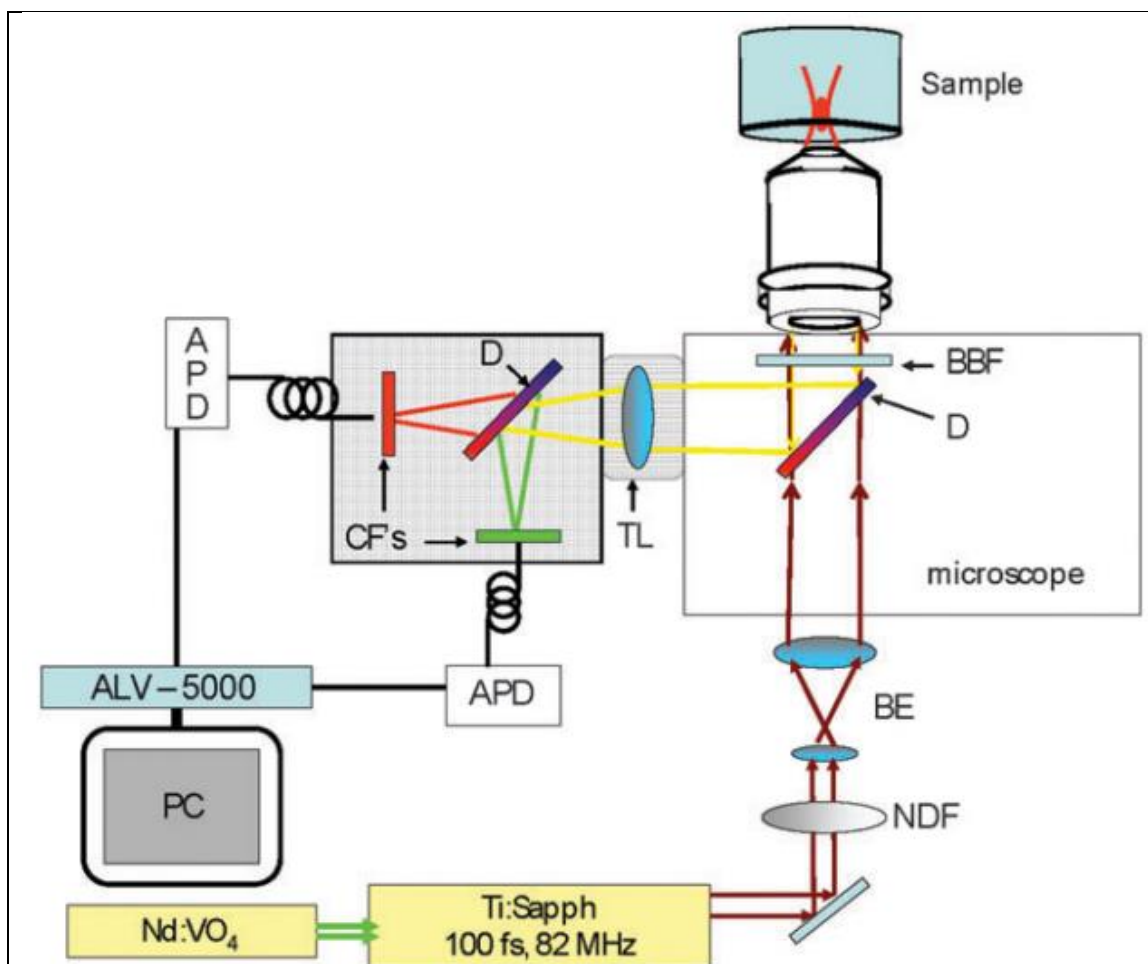


Figure 6.2. Schematic of a typical fluorescence correlation spectroscopy imaging set-up. A laser excitation source's power is attenuated by a neutral density filter (NDF), and this beam is expanded to a higher numerical aperture lens via beam expanders (BE). The beam is directed via a dichroic mirror (D) through a broad band filter (BBF), which separates excited and emitted light. A tube lens (TL) directs the emitted light to another dichroic mirror, which separates signals from different fluorophores in the sample. Figure modified from [339].

6.3 Closing Remarks

The directional power of the intricately dynamic epigenome from a small group of posttranslational modifications to histones is analogous to the creational power of the diverse cast of proteins in the human body from a small group of four base nucleotides. The scientific community has been quite successful in boiling down the combinatorial complexity of this language of cells to these much simpler root foundations; however, when considering the temporal dimension, this language becomes impossibly complex. The efficacy of future regenerative medicine relies on improving our ability to decipher this language and subsequently exploit desired cellular behaviors. This inevitably entails using the best of our resources to develop and execute cellular assays that optimally facilitate experimental discoveries. The paramount aim of this dissertation is to do just that, and contribute to the ongoing effort of unraveling how the epigenome regulates the genome.

CHAPTER 7: REFERENCES

1. Thomson, J.A., et al., *Embryonic stem cell lines derived from human blastocysts*. Science, 1998. **282**(5391): p. 1145-7.
2. Shambloott, M.J., et al., *Derivation of pluripotent stem cells from cultured human primordial germ cells*. Proceedings of the National Academy of Sciences of the United States of America, 1998. **95**(23): p. 13726-31.
3. Marshall, C., et al., *The New York Stem Cell Foundation: Fifth Annual Translational Stem Cell Research Conference*. Annals of the New York Academy of Sciences, 2011. **1226**: p. 1-13.
4. Rao, M.S. and F.S. Collins, *Steering a new course for stem cell research: NIH's intramural Center for Regenerative Medicine*. Stem cells translational medicine, 2012. **1**(1): p. 15-7.
5. Corona, B.T., et al., *Regenerative medicine: basic concepts, current status, and future applications*. Journal of investigative medicine : the official publication of the American Federation for Clinical Research, 2010. **58**(7): p. 849-58.
6. Langer, R. and J.P. Vacanti, *Tissue engineering*. Science, 1993. **260**(5110): p. 920-6.
7. Trounson, A., et al., *Clinical trials for stem cell therapies*. BMC medicine, 2011. **9**: p. 52.
8. Schwartz, S.D., et al., *Embryonic stem cell trials for macular degeneration: a preliminary report*. Lancet, 2012. **379**(9817): p. 713-20.
9. *World's first clinical trial of human embryonic stem cell therapy cleared*. Regenerative medicine, 2009. **4**(2): p. 161.
10. Takahashi, K. and S. Yamanaka, *Induction of pluripotent stem cells from mouse embryonic and adult fibroblast cultures by defined factors*. Cell, 2006. **126**(4): p. 663-76.
11. Van Damme, A., et al., *Bone marrow stromal cells as targets for gene therapy*. Current gene therapy, 2002. **2**(2): p. 195-209.
12. Mendelson, A. and P.S. Frenette, *Hematopoietic stem cell niche maintenance during homeostasis and regeneration*. Nature medicine, 2014. **20**(8): p. 833-46.
13. Kim, S. and H. von Recum, *Endothelial stem cells and precursors for tissue engineering: cell source, differentiation, selection, and application*. Tissue engineering. Part B, Reviews, 2008. **14**(1): p. 133-47.
14. Krabbe, C., J. Zimmer, and M. Meyer, *Neural transdifferentiation of mesenchymal stem cells--a critical review*. APMIS : acta pathologica, microbiologica, et immunologica Scandinavica, 2005. **113**(11-12): p. 831-44.
15. Heo, J.S., et al., *Neural transdifferentiation of human bone marrow mesenchymal stem cells on hydrophobic polymer-modified surface and therapeutic effects in an animal model of ischemic stroke*. Neuroscience, 2013.
16. Ayatollahi, M., et al., *Hepatogenic differentiation of mesenchymal stem cells induced by insulin like growth factor-I*. World journal of stem cells, 2011. **3**(12): p. 113-21.
17. Kazemnejad, S., et al., *Biochemical and molecular characterization of hepatocyte-like cells derived from human bone marrow mesenchymal stem cells on a novel three-dimensional biocompatible nanofibrous scaffold*. Journal of gastroenterology and hepatology, 2009. **24**(2): p. 278-87.
18. Bruder, S.P., D.J. Fink, and A.I. Caplan, *Mesenchymal stem cells in bone development, bone repair, and skeletal regeneration therapy*. Journal of cellular biochemistry, 1994. **56**(3): p. 283-94.

19. Franchini, M., *[Mesenchymal stem cells: from biology to clinical applications]*. Recenti progressi in medicina, 2003. **94**(11): p. 478-83.
20. Wang, L., et al., *MCP-1, MIP-1, IL-8 and ischemic cerebral tissue enhance human bone marrow stromal cell migration in interface culture*. Hematology, 2002. **7**(2): p. 113-7.
21. Horwitz, E.M., et al., *Isolated allogeneic bone marrow-derived mesenchymal cells engraft and stimulate growth in children with osteogenesis imperfecta: Implications for cell therapy of bone*. Proc Natl Acad Sci U S A, 2002. **99**(13): p. 8932-7.
22. Jager, M., et al., *Bone marrow concentrate: a novel strategy for bone defect treatment*. Curr Stem Cell Res Ther, 2009. **4**(1): p. 34-43.
23. Kitoh, H., et al., *Differential effects of culture-expanded bone marrow cells on the regeneration of bone between the femoral and the tibial lengthenings*. J Pediatr Orthop, 2009. **29**(6): p. 643-9.
24. Ringden, O., et al., *Tissue repair using allogeneic mesenchymal stem cells for hemorrhagic cystitis, pneumomediastinum and perforated colon*. Leukemia, 2007. **21**(11): p. 2271-6.
25. Richardson, S.M. and J.A. Hoyland, *Stem cell regeneration of degenerated intervertebral discs: current status*. Curr Pain Headache Rep, 2008. **12**(2): p. 83-8.
26. Wakitani, S., et al., *Autologous bone marrow stromal cell transplantation for repair of full-thickness articular cartilage defects in human patellae: two case reports*. Cell Transplant, 2004. **13**(5): p. 595-600.
27. Horwitz, E.M., et al., *Transplantability and therapeutic effects of bone marrow-derived mesenchymal cells in children with osteogenesis imperfecta*. Nat Med, 1999. **5**(3): p. 309-13.
28. Mohamadnejad, M., et al., *Phase 1 human trial of autologous bone marrow-hematopoietic stem cell transplantation in patients with decompensated cirrhosis*. World J Gastroenterol, 2007. **13**(24): p. 3359-63.
29. Terai, S., et al., *Improved liver function in patients with liver cirrhosis after autologous bone marrow cell infusion therapy*. Stem Cells, 2006. **24**(10): p. 2292-8.
30. Koc, O.N., et al., *Allogeneic mesenchymal stem cell infusion for treatment of metachromatic leukodystrophy (MLD) and Hurler syndrome (MPS-IH)*. Bone Marrow Transplant, 2002. **30**(4): p. 215-22.
31. Schmitt, A., et al., *Application of stem cells in orthopedics*. Stem cells international, 2012. **2012**: p. 394962.
32. Watanabe, F.D., et al., *Clinical experience with a bioartificial liver in the treatment of severe liver failure. A phase I clinical trial*. Annals of surgery, 1997. **225**(5): p. 484-91; discussion 491-4.
33. Humes, H.D., et al., *Replacement of renal function in uremic animals with a tissue-engineered kidney*. Nature biotechnology, 1999. **17**(5): p. 451-5.
34. Sullivan, S.J., et al., *Biohybrid artificial pancreas: long-term implantation studies in diabetic, pancreatectomized dogs*. Science, 1991. **252**(5006): p. 718-21.
35. Kobayashi, H., et al., *Collagen-immobilized hydrogel as a material for lamellar keratoplasty*. Journal of applied biomaterials : an official journal of the Society for Biomaterials, 1991. **2**(4): p. 261-7.
36. Shinoka, T., et al., *Tissue-engineered heart valves. Autologous valve leaflet replacement study in a lamb model*. Circulation, 1996. **94**(9 Suppl): p. II164-8.
37. Dvir, T., et al., *Nanowired three-dimensional cardiac patches*. Nature nanotechnology, 2011. **6**(11): p. 720-5.

38. Zund, G., et al., *The in vitro construction of a tissue engineered bioprosthetic heart valve*. European journal of cardio-thoracic surgery : official journal of the European Association for Cardio-thoracic Surgery, 1997. **11**(3): p. 493-7.
39. Carrier, R.L., et al., *Cardiac tissue engineering: cell seeding, cultivation parameters, and tissue construct characterization*. Biotechnology and bioengineering, 1999. **64**(5): p. 580-9.
40. Niklason, L.E., et al., *Functional arteries grown in vitro*. Science, 1999. **284**(5413): p. 489-93.
41. Shinoka, T. and C. Breuer, *Tissue-engineered blood vessels in pediatric cardiac surgery*. The Yale journal of biology and medicine, 2008. **81**(4): p. 161-6.
42. Vacanti, C.A., et al., *Tissue-engineered growth of bone and cartilage*. Transplantation proceedings, 1993. **25**(1 Pt 2): p. 1019-21.
43. Amini, A.R., C.T. Laurencin, and S.P. Nukavarapu, *Bone tissue engineering: recent advances and challenges*. Critical reviews in biomedical engineering, 2012. **40**(5): p. 363-408.
44. Vacanti, C.A., et al., *Synthetic polymers seeded with chondrocytes provide a template for new cartilage formation*. Plastic and reconstructive surgery, 1991. **88**(5): p. 753-9.
45. Cao, Y., et al., *Generation of neo-tendon using synthetic polymers seeded with tenocytes*. Transplantation proceedings, 1994. **26**(6): p. 3390-2.
46. Karlsson, C., et al., *Human embryonic stem cell-derived mesenchymal progenitors--potential in regenerative medicine*. Stem cell research, 2009. **3**(1): p. 39-50.
47. Simaria, A.S., et al., *Allogeneic cell therapy bioprocess economics and optimization: single-use cell expansion technologies*. Biotechnology and bioengineering, 2014. **111**(1): p. 69-83.
48. Atoui, R. and R.C. Chiu, *Mesenchymal stromal cells as universal donor cells*. Expert opinion on biological therapy, 2012. **12**(10): p. 1293-7.
49. Faustman, D. and C. Coe, *Prevention of xenograft rejection by masking donor HLA class I antigens*. Science, 1991. **252**(5013): p. 1700-2.
50. Boland, M.J., K.L. Nazor, and J.F. Loring, *Epigenetic Regulation of Pluripotency and Differentiation*. Circulation research, 2014. **115**(2): p. 311-324.
51. Hsieh, T.F. and R.L. Fischer, *Biology of chromatin dynamics*. Annual review of plant biology, 2005. **56**: p. 327-51.
52. Chakalova, L., et al., *Replication and transcription: shaping the landscape of the genome*. Nature reviews. Genetics, 2005. **6**(9): p. 669-77.
53. Benayahu, D., G. Shefer, and I. Shur, *Insights into chromatin remodelers in mesenchymal stem cells and differentiation*. Frontiers in bioscience, 2009. **14**: p. 398-409.
54. Callinan, P.A. and A.P. Feinberg, *The emerging science of epigenomics*. Human molecular genetics, 2006. **15 Spec No 1**: p. R95-101.
55. Crews, D., et al., *Nature, nurture and epigenetics*. Molecular and cellular endocrinology, 2014.
56. Harp, J.M., et al., *Asymmetries in the nucleosome core particle at 2.5 Å resolution*. Acta crystallographica. Section D, Biological crystallography, 2000. **56**(Pt 12): p. 1513-34.
57. Luger, K., et al., *Crystal structure of the nucleosome core particle at 2.8 Å resolution*. Nature, 1997. **389**(6648): p. 251-60.
58. Camerini-Otero, R.D., B. Sollner-Webb, and G. Felsenfeld, *The organization of histones and DNA in chromatin: evidence for an arginine-rich histone kernel*. Cell, 1976. **8**(3): p. 333-47.

59. Bohr, J. and K. Olsen, *Twist neutrality and the diameter of the nucleosome core particle*. Physical review letters, 2012. **108**(9): p. 098101.
60. Fenley, A.T., D.A. Adams, and A.V. Onufriev, *Charge state of the globular histone core controls stability of the nucleosome*. Biophysical journal, 2010. **99**(5): p. 1577-85.
61. Bjorklund, C.C. and W.B. Davis, *Attenuation of DNA charge transport by compaction into a nucleosome core particle*. Nucleic acids research, 2006. **34**(6): p. 1836-46.
62. Zheng, C. and J.J. Hayes, *Structures and interactions of the core histone tail domains*. Biopolymers, 2003. **68**(4): p. 539-46.
63. Jaenisch, R. and A. Bird, *Epigenetic regulation of gene expression: how the genome integrates intrinsic and environmental signals*. Nat Genet, 2003. **33** Suppl: p. 245-54.
64. Bird, A.P., *CpG-rich islands and the function of DNA methylation*. Nature, 1986. **321**(6067): p. 209-13.
65. Feinberg, A.P. and B. Tycko, *The history of cancer epigenetics*. Nat Rev Cancer, 2004. **4**(2): p. 143-53.
66. Mello, M.L., *Cytochemical properties of euchromatin and heterochromatin*. The Histochemical journal, 1983. **15**(8): p. 739-51.
67. Herman, J.G. and S.B. Baylin, *Gene silencing in cancer in association with promoter hypermethylation*. N Engl J Med, 2003. **349**(21): p. 2042-54.
68. Prendergast, J.G., et al., *Chromatin structure and evolution in the human genome*. BMC evolutionary biology, 2007. **7**: p. 72.
69. Lee, J.Y. and T.H. Lee, *Effects of histone acetylation and CpG methylation on the structure of nucleosomes*. Biochimica et biophysica acta, 2012. **1824**(8): p. 974-82.
70. Choy, J.S., et al., *DNA methylation increases nucleosome compaction and rigidity*. Journal of the American Chemical Society, 2010. **132**(6): p. 1782-3.
71. Vidali, G., N. Ferrari, and U. Pfeffer, *Histone acetylation: a step in gene activation*. Advances in experimental medicine and biology, 1988. **231**: p. 583-96.
72. Nowak, S.J. and V.G. Corces, *Phosphorylation of histone H3 correlates with transcriptionally active loci*. Genes & development, 2000. **14**(23): p. 3003-13.
73. Fleming, A.B., et al., *H2B ubiquitylation plays a role in nucleosome dynamics during transcription elongation*. Molecular cell, 2008. **31**(1): p. 57-66.
74. Tiefenbach, J., et al., *SUMOylation of the corepressor N-CoR modulates its capacity to repress transcription*. Molecular biology of the cell, 2006. **17**(4): p. 1643-51.
75. Chew, Y.C., et al., *Lysine residues in N-terminal and C-terminal regions of human histone H2A are targets for biotinylation by biotinidase*. The Journal of nutritional biochemistry, 2006. **17**(4): p. 225-33.
76. Filenko, N.A., et al., *The role of histone H4 biotinylation in the structure of nucleosomes*. PloS one, 2011. **6**(1): p. e16299.
77. Jensen, O.N., *Interpreting the protein language using proteomics*. Nature reviews. Molecular cell biology, 2006. **7**(6): p. 391-403.
78. Yang, X.J., *Multisite protein modification and intramolecular signaling*. Oncogene, 2005. **24**(10): p. 1653-62.
79. Prabakaran, S., et al., *Post-translational modification: nature's escape from genetic imprisonment and the basis for dynamic information encoding*. Wiley interdisciplinary reviews. Systems biology and medicine, 2012. **4**(6): p. 565-83.
80. Jenuwein, T. and C.D. Allis, *Translating the histone code*. Science, 2001. **293**(5532): p. 1074-80.
81. Dillon, N., *Heterochromatin structure and function*. Biol Cell, 2004. **96**(8): p. 631-7.

82. Latham, J.A. and S.Y. Dent, *Cross-regulation of histone modifications*. Nature structural & molecular biology, 2007. **14**(11): p. 1017-24.
83. Owen-Hughes, T., *Colworth memorial lecture. Pathways for remodelling chromatin*. Biochemical Society transactions, 2003. **31**(Pt 5): p. 893-905.
84. Muchardt, C. and M. Yaniv, *ATP-dependent chromatin remodelling: SWI/SNF and Co. are on the job*. Journal of molecular biology, 1999. **293**(2): p. 187-98.
85. Caserta, M., L. Verdona, and E. Di Mauro, *Aspects of nucleosomal positional flexibility and fluidity*. Chembiochem : a European journal of chemical biology, 2002. **3**(12): p. 1172-82.
86. Saha, A., J. Wittmeyer, and B.R. Cairns, *Chromatin remodelling: the industrial revolution of DNA around histones*. Nature reviews. Molecular cell biology, 2006. **7**(6): p. 437-47.
87. Phelan, M.L., et al., *Reconstitution of a core chromatin remodeling complex from SWI/SNF subunits*. Molecular cell, 1999. **3**(2): p. 247-53.
88. Tsukiyama, T., et al., *ISWI, a member of the SWI2/SNF2 ATPase family, encodes the 140 kDa subunit of the nucleosome remodeling factor*. Cell, 1995. **83**(6): p. 1021-6.
89. Corona, D.F., et al., *ISWI is an ATP-dependent nucleosome remodeling factor*. Molecular cell, 1999. **3**(2): p. 239-45.
90. Xue, Y., et al., *NURD, a novel complex with both ATP-dependent chromatin-remodeling and histone deacetylase activities*. Molecular cell, 1998. **2**(6): p. 851-61.
91. Bakshi, R., et al., *In silico characterization of the INO80 subfamily of SWI2/SNF2 chromatin remodeling proteins*. Biochemical and biophysical research communications, 2004. **320**(1): p. 197-204.
92. Kato, S., K. Inoue, and M.-Y. Youn, *Emergence of the osteo-epigenome in bone biology*. IBMS BoneKEy, 2010. **7**(9): p. 314-324.
93. Davie, J.K. and C.M. Kane, *Genetic interactions between TFIIS and the Swi-Snf chromatin-remodeling complex*. Molecular and cellular biology, 2000. **20**(16): p. 5960-73.
94. Chai, B., et al., *Distinct roles for the RSC and Swi/Snf ATP-dependent chromatin remodelers in DNA double-strand break repair*. Genes & development, 2005. **19**(14): p. 1656-61.
95. de la Serna, I.L., K.A. Carlson, and A.N. Imbalzano, *Mammalian SWI/SNF complexes promote MyoD-mediated muscle differentiation*. Nat Genet, 2001. **27**(2): p. 187-90.
96. Badenhorst, P., et al., *Biological functions of the ISWI chromatin remodeling complex NURF*. Genes & development, 2002. **16**(24): p. 3186-98.
97. Hendricks, K.B., F. Shanahan, and E. Lees, *Role for BRG1 in cell cycle control and tumor suppression*. Molecular and cellular biology, 2004. **24**(1): p. 362-76.
98. Yaniv, M., *Chromatin remodeling: from transcription to cancer*. Cancer genetics, 2014.
99. Narlikar, G.J., R. Sundaramoorthy, and T. Owen-Hughes, *Mechanisms and functions of ATP-dependent chromatin-remodeling enzymes*. Cell, 2013. **154**(3): p. 490-503.
100. Henriques, R. and P. Mas, *Chromatin remodeling and alternative splicing: pre- and post-transcriptional regulation of the Arabidopsis circadian clock*. Seminars in cell & developmental biology, 2013. **24**(5): p. 399-406.
101. Bi, X., *Functions of chromatin remodeling factors in heterochromatin formation and maintenance*. Science China. Life sciences, 2012. **55**(1): p. 89-96.
102. Yao, Y. and W. Dai, *Mitotic checkpoint control and chromatin remodeling*. Frontiers in bioscience, 2012. **17**: p. 976-83.
103. Wu, J.L., *Diverse functions of ATP-dependent chromatin remodeling complexes in development and cancer*. Acta biochimica et biophysica Sinica, 2012. **44**(1): p. 54-69.

104. Muller, C. and A. Leutz, *Chromatin remodeling in development and differentiation*. Curr Opin Genet Dev, 2001. **11**(2): p. 167-74.
105. Kim, K., et al., *Epigenetic memory in induced pluripotent stem cells*. Nature, 2010. **467**(7313): p. 285-90.
106. Lister, R., et al., *Hotspots of aberrant epigenomic reprogramming in human induced pluripotent stem cells*. Nature, 2011. **471**(7336): p. 68-73.
107. Apostolou, E. and K. Hochedlinger, *Chromatin dynamics during cellular reprogramming*. Nature, 2013. **502**(7472): p. 462-71.
108. Harikumar, A. and E. Meshorer, *Measuring the dynamics of chromatin proteins during differentiation*. Methods in molecular biology, 2013. **1042**: p. 173-80.
109. Hinde, E., et al., *Tracking the mechanical dynamics of human embryonic stem cell chromatin*. Epigenetics & chromatin, 2012. **5**(1): p. 20.
110. Paige, S.L., et al., *A temporal chromatin signature in human embryonic stem cells identifies regulators of cardiac development*. Cell, 2012. **151**(1): p. 221-32.
111. Watanabe, T.M., et al., *Chromatin plasticity as a differentiation index during muscle differentiation of C2C12 myoblasts*. Biochemical and biophysical research communications, 2012. **418**(4): p. 742-7.
112. Shafa, M., R. Krawetz, and D.E. Rancourt, *Returning to the stem state: epigenetics of recapitulating pre-differentiation chromatin structure*. BioEssays : news and reviews in molecular, cellular and developmental biology, 2010. **32**(9): p. 791-9.
113. Lee, J.H., S.R. Hart, and D.G. Skalnik, *Histone deacetylase activity is required for embryonic stem cell differentiation*. Genesis, 2004. **38**(1): p. 32-8.
114. Perry, P., et al., *A dynamic switch in the replication timing of key regulator genes in embryonic stem cells upon neural induction*. Cell cycle, 2004. **3**(12): p. 1645-50.
115. Shen, S., J. Li, and P. Casaccia-Bonnel, *Histone modifications affect timing of oligodendrocyte progenitor differentiation in the developing rat brain*. The Journal of cell biology, 2005. **169**(4): p. 577-89.
116. Ezhkova, E., et al., *Ezh2 orchestrates gene expression for the stepwise differentiation of tissue-specific stem cells*. Cell, 2009. **136**(6): p. 1122-35.
117. Bottardi, S., et al., *Developmental stage-specific epigenetic control of human beta-globin gene expression is potentiated in hematopoietic progenitor cells prior to their transcriptional activation*. Blood, 2003. **102**(12): p. 3989-97.
118. Wamstad, J.A., et al., *Dynamic and coordinated epigenetic regulation of developmental transitions in the cardiac lineage*. Cell, 2012. **151**(1): p. 206-20.
119. Kubicek, S., et al., *The role of histone modifications in epigenetic transitions during normal and perturbed development*. Ernst Schering Research Foundation workshop, 2006(57): p. 1-27.
120. Kaji, K., et al., *The NuRD component Mbd3 is required for pluripotency of embryonic stem cells*. Nature cell biology, 2006. **8**(3): p. 285-92.
121. Jamaladdin, S., et al., *Histone deacetylase (HDAC) 1 and 2 are essential for accurate cell division and the pluripotency of embryonic stem cells*. Proceedings of the National Academy of Sciences of the United States of America, 2014. **111**(27): p. 9840-5.
122. Wan, M., et al., *The trithorax group protein Ash2l is essential for pluripotency and maintaining open chromatin in embryonic stem cells*. The Journal of biological chemistry, 2013. **288**(7): p. 5039-48.
123. Adamo, A., et al., *LSD1 regulates the balance between self-renewal and differentiation in human embryonic stem cells*. Nature cell biology, 2011. **13**(6): p. 652-9.

124. Whyte, W.A., et al., *Enhancer decommissioning by LSD1 during embryonic stem cell differentiation*. Nature, 2012. **482**(7384): p. 221-5.
125. Ding, J., et al., *Oct4 links multiple epigenetic pathways to the pluripotency network*. Cell research, 2012. **22**(1): p. 155-67.
126. Serrano, L., B.N. Vazquez, and J. Tischfield, *Chromatin structure, pluripotency and differentiation*. Experimental biology and medicine, 2013. **238**(3): p. 259-70.
127. Liang, G. and Y. Zhang, *Embryonic stem cell and induced pluripotent stem cell: an epigenetic perspective*. Cell research, 2013. **23**(1): p. 49-69.
128. Leung, K.S., et al., *The involvement of DNA methylation and histone modification on the epigenetic regulation of embryonic stem cells and induced pluripotent stem cells*. Current stem cell research & therapy, 2014. **9**(5): p. 388-95.
129. Tan, Y., S. Ooi, and L. Wang, *Immunogenicity and tumorigenicity of pluripotent stem cells and their derivatives: genetic and epigenetic perspectives*. Current stem cell research & therapy, 2014. **9**(1): p. 63-72.
130. Suva, M.L., N. Riggi, and B.E. Bernstein, *Epigenetic reprogramming in cancer*. Science, 2013. **339**(6127): p. 1567-70.
131. Li, M., G.H. Liu, and J.C. Izpisua Belmonte, *Navigating the epigenetic landscape of pluripotent stem cells*. Nature reviews. Molecular cell biology, 2012. **13**(8): p. 524-35.
132. Lee, J. and T. Shinohara, *Epigenetic modifications and self-renewal regulation of mouse germline stem cells*. Cell research, 2011. **21**(8): p. 1164-71.
133. Christophersen, N.S. and K. Helin, *Epigenetic control of embryonic stem cell fate*. The Journal of experimental medicine, 2010. **207**(11): p. 2287-95.
134. Meissner, A., *Epigenetic modifications in pluripotent and differentiated cells*. Nature biotechnology, 2010. **28**(10): p. 1079-88.
135. Hochedlinger, K. and K. Plath, *Epigenetic reprogramming and induced pluripotency*. Development, 2009. **136**(4): p. 509-23.
136. Chen, J.C. and C.R. Jacobs, *Mechanically induced osteogenic lineage commitment of stem cells*. Stem cell research & therapy, 2013. **4**(5): p. 107.
137. Alliston, T., *Biological Regulation of Bone Quality*. Current osteoporosis reports, 2014.
138. Engler, A.J., et al., *Matrix elasticity directs stem cell lineage specification*. Cell, 2006. **126**(4): p. 677-689.
139. Her, G.J., et al., *Control of three-dimensional substrate stiffness to manipulate mesenchymal stem cell fate toward neuronal or glial lineages*. Acta biomaterialia, 2013. **9**(2): p. 5170-80.
140. Banerjee, A., et al., *The influence of hydrogel modulus on the proliferation and differentiation of encapsulated neural stem cells*. Biomaterials, 2009. **30**(27): p. 4695-9.
141. Discher, D.E., P. Janmey, and Y.L. Wang, *Tissue cells feel and respond to the stiffness of their substrate*. Science, 2005. **310**(5751): p. 1139-43.
142. Saha, K., et al., *Substrate modulus directs neural stem cell behavior*. Biophysical journal, 2008. **95**(9): p. 4426-38.
143. Mammoto, A., et al., *A mechanosensitive transcriptional mechanism that controls angiogenesis*. Nature, 2009. **457**(7233): p. 1103-8.
144. Majkut, S., P.C. Dingal, and D.E. Discher, *Stress sensitivity and mechanotransduction during heart development*. Current biology : CB, 2014. **24**(10): p. R495-501.
145. Holle, A.W., et al., *In situ mechanotransduction via vinculin regulates stem cell differentiation*. Stem cells, 2013. **31**(11): p. 2467-77.
146. Wen, J.H., et al., *Interplay of matrix stiffness and protein tethering in stem cell differentiation*. Nature materials, 2014.

147. Banks, J.M., et al., *The combined effects of matrix stiffness and growth factor immobilization on the bioactivity and differentiation capabilities of adipose-derived stem cells*. Biomaterials, 2014.
148. Zhao, W., et al., *Effects of substrate stiffness on adipogenic and osteogenic differentiation of human mesenchymal stem cells*. Materials science & engineering. C, Materials for biological applications, 2014. **40**: p. 316-23.
149. Wang, T., et al., *Chondrogenic Differentiation of Adipose-Derived Stromal Cells in Combinatorial Hydrogels Containing Cartilage Matrix Proteins with Decoupled Mechanical Stiffness*. Tissue engineering. Part A, 2014.
150. Chaterji, S., et al., *Synergistic Effects of Matrix Nanotopography and Stiffness on Vascular Smooth Muscle Cell Function*. Tissue engineering. Part A, 2014.
151. Swift, J., et al., *Nuclear lamin-A scales with tissue stiffness and enhances matrix-directed differentiation*. Science, 2013. **341**(6149): p. 1240104.
152. Eroshenko, N., et al., *Effect of substrate stiffness on early human embryonic stem cell differentiation*. Journal of biological engineering, 2013. **7**(1): p. 7.
153. Witkowska-Zimny, M., et al., *Effect of substrate stiffness on the osteogenic differentiation of bone marrow stem cells and bone-derived cells*. Cell biology international, 2013. **37**(6): p. 608-16.
154. Sniadecki, N.J., et al., *Magnetic microposts as an approach to apply forces to living cells*. Proc Natl Acad Sci U S A, 2007. **104**(37): p. 14553-8.
155. McNamara, L.E., et al., *Skeletal stem cell physiology on functionally distinct titania nanotopographies*. Biomaterials, 2011. **32**(30): p. 7403-10.
156. Kilian, K.A., et al., *Geometric cues for directing the differentiation of mesenchymal stem cells*. Proceedings of the National Academy of Sciences of the United States of America, 2010. **107**(11): p. 4872-4877.
157. Unadkat, H.V., et al., *An algorithm-based topographical biomaterials library to instruct cell fate*. Proc Natl Acad Sci U S A, 2011. **108**(40): p. 16565-70.
158. Jackson, V., *Studies on histone organization in the nucleosome using formaldehyde as a reversible cross-linking agent*. Cell, 1978. **15**(3): p. 945-54.
159. Garcia, B.A., J. Shabanowitz, and D.F. Hunt, *Characterization of histones and their post-translational modifications by mass spectrometry*. Current opinion in chemical biology, 2007. **11**(1): p. 66-73.
160. Collas, P. and J.A. Dahl, *Chop it, ChIP it, check it: the current status of chromatin immunoprecipitation*. Frontiers in bioscience : a journal and virtual library, 2008. **13**: p. 929-43.
161. Garcia, B.A., J. Shabanowitz, and D.F. Hunt, *Characterization of histones and their post-translational modifications by mass spectrometry*. Curr Opin Chem Biol, 2007. **11**(1): p. 66-73.
162. Britton, L.M., et al., *Breaking the histone code with quantitative mass spectrometry*. Expert Rev Proteomics, 2011. **8**(5): p. 631-43.
163. Peach, S.E., et al., *Quantitative assessment of chromatin immunoprecipitation grade antibodies directed against histone modifications reveals patterns of co-occurring marks on histone protein molecules*. Molecular & cellular proteomics : MCP, 2012. **11**(5): p. 128-37.
164. Bernstein, B.E., et al., *Genomic maps and comparative analysis of histone modifications in human and mouse*. Cell, 2005. **120**(2): p. 169-81.
165. Garcia, B.A., et al., *Chemical derivatization of histones for facilitated analysis by mass spectrometry*. Nature protocols, 2007. **2**(4): p. 933-8.

166. Brumbaugh, J., et al., *Proteomics and pluripotency*. Crit Rev Biochem Mol Biol, 2011. **46**(6): p. 493-506.
167. Phanstiel, D., et al., *Mass spectrometry identifies and quantifies 74 unique histone H4 isoforms in differentiating human embryonic stem cells*. Proc Natl Acad Sci U S A, 2008. **105**(11): p. 4093-8.
168. Bonetta, L., *Epigenomics: Detailed analysis*. Nature, 2008. **454**(7205): p. 795-8.
169. Cramer, P., *A Tale of Chromatin and Transcription in 100 Structures*. Cell, 2014. **159**(5): p. 985-994.
170. Richmond, T.J., et al., *Structure of the nucleosome core particle at 7 Å resolution*. Nature, 1984. **311**(5986): p. 532-7.
171. Schalch, T., et al., *X-ray structure of a tetranucleosome and its implications for the chromatin fibre*. Nature, 2005. **436**(7047): p. 138-41.
172. Robinson, P.J., et al., *EM measurements define the dimensions of the "30-nm" chromatin fiber: evidence for a compact, interdigitated structure*. Proceedings of the National Academy of Sciences of the United States of America, 2006. **103**(17): p. 6506-11.
173. Scheffer, M.P., M. Eltsov, and A.S. Frangakis, *Evidence for short-range helical order in the 30-nm chromatin fibers of erythrocyte nuclei*. Proceedings of the National Academy of Sciences of the United States of America, 2011. **108**(41): p. 16992-7.
174. Bolzer, A., et al., *Three-dimensional maps of all chromosomes in human male fibroblast nuclei and prometaphase rosettes*. PLoS biology, 2005. **3**(5): p. e157.
175. Hell, S.W., *Toward fluorescence nanoscopy*. Nature biotechnology, 2003. **21**(11): p. 1347-55.
176. Vicidomini, G., et al., *STED nanoscopy with time-gated detection: theoretical and experimental aspects*. PLoS One, 2013. **8**(1): p. e54421.
177. Laevsky, G.S. and C.B. O'Connell, *Comparative and practical aspects of localization-based super-resolution imaging*. Current protocols in cytometry / editorial board, J. Paul Robinson, managing editor ... [et al.], 2013. **Chapter 2**: p. Unit2 20.
178. Shroff, H., et al., *Live-cell photoactivated localization microscopy of nanoscale adhesion dynamics*. Nat Methods, 2008. **5**(5): p. 417-23.
179. Swedlow, J.R., I.G. Goldberg, and K.W. Eliceiri, *Bioimage informatics for experimental biology*. Annual review of biophysics, 2009. **38**: p. 327-46.
180. Yang, G., *Bioimage informatics for understanding spatiotemporal dynamics of cellular processes*. Wiley interdisciplinary reviews. Systems biology and medicine, 2013.
181. Peng, H., *Bioimage informatics: a new area of engineering biology*. Bioinformatics, 2008. **24**(17): p. 1827-36.
182. Girish, V. and A. Vijayalakshmi, *Affordable image analysis using NIH Image/ImageJ*. Indian journal of cancer, 2004. **41**(1): p. 47.
183. Carpenter, A.E., et al., *CellProfiler: image analysis software for identifying and quantifying cell phenotypes*. Genome biology, 2006. **7**(10): p. R100.
184. Francisco, J.S., H.P. Moraes, and E.P. Dias, *Evaluation of the Image-Pro Plus 4.5 software for automatic counting of labeled nuclei by PCNA immunohistochemistry*. Brazilian oral research, 2004. **18**(2): p. 100-4.
185. Song, Y., et al., *Discriminative data transform for image feature extraction and classification*. Medical image computing and computer-assisted intervention : MICCAI ... International Conference on Medical Image Computing and Computer-Assisted Intervention, 2013. **16**(Pt 2): p. 452-9.

186. Borst, H., W. Abmayr, and P. Gais, *A thresholding method for automatic cell image segmentation*. The journal of histochemistry and cytochemistry : official journal of the Histochemistry Society, 1979. **27**(1): p. 180-7.
187. Alliney, S. and C. Morandi, *Digital image registration using projections*. IEEE transactions on pattern analysis and machine intelligence, 1986. **8**(2): p. 222-33.
188. He, S., D. Kirovski, and M. Wu, *High-fidelity data embedding for image annotation*. IEEE transactions on image processing : a publication of the IEEE Signal Processing Society, 2009. **18**(2): p. 429-35.
189. Hamilton, N.A. and R.D. Teasdale, *Visualizing and clustering high throughput sub-cellular localization imaging*. BMC bioinformatics, 2008. **9**: p. 81.
190. Eliceiri, K.W., et al., *Biological imaging software tools*. Nature methods, 2012. **9**(7): p. 697-710.
191. Treiser, M.D., et al., *Cytoskeleton-based forecasting of stem cell lineage fates*. Proceedings of the National Academy of Sciences of the United States of America, 2010. **107**(2): p. 610-5.
192. Vidi, P.A., et al., *Interconnected contribution of tissue morphogenesis and the nuclear protein NuMA to the DNA damage response*. Journal of cell science, 2012. **125**(Pt 2): p. 350-61.
193. Matsuoka, F., et al., *Morphology-based prediction of osteogenic differentiation potential of human mesenchymal stem cells*. PLoS One, 2013. **8**(2): p. e55082.
194. Liu, E., et al., *Parsing the early cytoskeletal and nuclear organizational cues that demarcate stem cell lineages*. Cell cycle, 2010. **9**(11): p. 2108-17.
195. Zhuang, X., *Nano-imaging with Storm*. Nature photonics, 2009. **3**(7): p. 365-367.
196. Haralick, R., K. Shanmugam, and I. Dinstein, *Textural Features for Image Classification*. Systems, Man and Cybernetics, 1973. **3**(6): p. 610-621.
197. Jolliffe, I.T., *Principal component analysis*. 2nd ed. Springer series in statistics 2002, New York: Springer. xxix, 487 p.
198. Jolliffe, I.T. and B.J. Morgan, *Principal component analysis and exploratory factor analysis*. Statistical methods in medical research, 1992. **1**(1): p. 69-95.
199. Semmlow, J.L., *Biosignal and medical image processing*. 2nd ed 2009, Boca Raton: CRC Press. xvii, 450 p.
200. Steinley, D., *K-means clustering: a half-century synthesis*. The British journal of mathematical and statistical psychology, 2006. **59**(Pt 1): p. 1-34.
201. Smellie, A., *Accelerated K-means clustering in metric spaces*. Journal of chemical information and computer sciences, 2004. **44**(6): p. 1929-35.
202. Frank, E., et al., *Data mining in bioinformatics using Weka*. Bioinformatics, 2004. **20**(15): p. 2479-81.
203. Hong, S.H., et al., *Cell fate potential of human pluripotent stem cells is encoded by histone modifications*. Cell Stem Cell, 2011. **9**(1): p. 24-36.
204. Lee, H.W., et al., *Histone deacetylase 1-mediated histone modification regulates osteoblast differentiation*. Molecular endocrinology, 2006. **20**(10): p. 2432-43.
205. Zhang, Q., et al., *Dynamic and distinct histone modifications modulate the expression of key adipogenesis regulatory genes*. Cell cycle, 2012. **11**(23): p. 4310-22.
206. Hata, K., et al., *Arid5b facilitates chondrogenesis by recruiting the histone demethylase Phf2 to Sox9-regulated genes*. Nature communications, 2013. **4**: p. 2850.
207. Ceballos-Chavez, M., et al., *Control of neuronal differentiation by sumoylation of BRAF35, a subunit of the LSD1-CoREST histone demethylase complex*. Proceedings of the

- National Academy of Sciences of the United States of America, 2012. **109**(21): p. 8085-90.
208. Gaspar-Maia, A., et al., *Open chromatin in pluripotency and reprogramming*. Nature reviews. Molecular cell biology, 2011. **12**(1): p. 36-47.
 209. Roh, T.Y., et al., *The genomic landscape of histone modifications in human T cells*. Proceedings of the National Academy of Sciences of the United States of America, 2006. **103**(43): p. 15782-7.
 210. Bernstein, B.E., et al., *A bivalent chromatin structure marks key developmental genes in embryonic stem cells*. Cell, 2006. **125**(2): p. 315-26.
 211. Anastassova-Kristeva, M., *The nucleolar cycle in man*. Journal of cell science, 1977. **25**: p. 103-10.
 212. Cao, R., et al., *Role of histone H3 lysine 27 methylation in Polycomb-group silencing*. Science, 2002. **298**(5595): p. 1039-43.
 213. Agger, K., et al., *UTX and JMJD3 are histone H3K27 demethylases involved in HOX gene regulation and development*. Nature, 2007. **449**(7163): p. 731-4.
 214. Seward, D.J., et al., *Demethylation of trimethylated histone H3 Lys4 in vivo by JARID1 JmjC proteins*. Nature structural & molecular biology, 2007. **14**(3): p. 240-2.
 215. Avan, A., et al., *Molecular mechanisms involved in the synergistic interaction of the EZH2 inhibitor 3-deazaneplanocin A with gemcitabine in pancreatic cancer cells*. Molecular cancer therapeutics, 2012. **11**(8): p. 1735-46.
 216. Chau, C.M. and P.M. Lieberman, *Dynamic chromatin boundaries delineate a latency control region of Epstein-Barr virus*. Journal of virology, 2004. **78**(22): p. 12308-19.
 217. El Mansouri, F.E., et al., *Contribution of H3K4 methylation by SET-1A to interleukin-1-induced cyclooxygenase 2 and inducible nitric oxide synthase expression in human osteoarthritis chondrocytes*. Arthritis and rheumatism, 2011. **63**(1): p. 168-79.
 218. Lin, S. and B.A. Garcia, *Examining histone posttranslational modification patterns by high-resolution mass spectrometry*. Methods in enzymology, 2012. **512**: p. 3-28.
 219. !!! INVALID CITATION !!!
 220. Richmond, T.J. and C.A. Davey, *The structure of DNA in the nucleosome core*. Nature, 2003. **423**(6936): p. 145-50.
 221. Vicidomini, G., et al., *Sharper low-power STED nanoscopy by time gating*. Nature methods, 2011. **8**(7): p. 571-3.
 222. De Gobbi, M., et al., *Generation of bivalent chromatin domains during cell fate decisions*. Epigenetics & chromatin, 2011. **4**(1): p. 9.
 223. Vastenhouw, N.L. and A.F. Schier, *Bivalent histone modifications in early embryogenesis*. Current opinion in cell biology, 2012. **24**(3): p. 374-86.
 224. Burney, M.J., et al., *An epigenetic signature of developmental potential in neural stem cells and early neurons*. Stem cells, 2013. **31**(9): p. 1868-80.
 225. Lesch, B.J., et al., *A set of genes critical to development is epigenetically poised in mouse germ cells from fetal stages through completion of meiosis*. Proceedings of the National Academy of Sciences of the United States of America, 2013. **110**(40): p. 16061-6.
 226. Yin, F., et al., *LSD1 regulates pluripotency of embryonic stem/carcinoma cells through histone deacetylase 1-mediated deacetylation of histone H4 at lysine 16*. Molecular and cellular biology, 2014. **34**(2): p. 158-79.
 227. Alberts, B., *Molecular biology of the cell*. 5th ed2008, New York: Garland Science.
 228. Ting, A.E., et al., *Therapeutic pathways of adult stem cell repair*. Critical reviews in oncology/hematology, 2008. **65**(1): p. 81-93.

229. Thirumala, S., W.S. Goebel, and E.J. Woods, *Clinical grade adult stem cell banking*. Organogenesis, 2009. **5**(3): p. 143-54.
230. Koc, O.N. and H.M. Lazarus, *Mesenchymal stem cells: heading into the clinic*. Bone marrow transplantation, 2001. **27**(3): p. 235-9.
231. Minguell, J.J., A. Erices, and P. Conget, *Mesenchymal stem cells*. Experimental biology and medicine, 2001. **226**(6): p. 507-20.
232. Lotfinegad, P., et al., *Immunomodulatory nature and site specific affinity of mesenchymal stem cells: a hope in cell therapy*. Advanced pharmaceutical bulletin, 2014. **4**(1): p. 5-13.
233. Stagg, J. and J. Galipeau, *Mechanisms of immune modulation by mesenchymal stromal cells and clinical translation*. Current molecular medicine, 2013. **13**(5): p. 856-67.
234. Deans, R.J. and A.B. Moseley, *Mesenchymal stem cells: biology and potential clinical uses*. Experimental hematology, 2000. **28**(8): p. 875-84.
235. Pascucci, L., et al., *Ultrastructural morphology of equine adipose-derived mesenchymal stem cells*. Histology and histopathology, 2010. **25**(10): p. 1277-85.
236. Zohar, R., J. Sodek, and C.A. McCulloch, *Characterization of stromal progenitor cells enriched by flow cytometry*. Blood, 1997. **90**(9): p. 3471-81.
237. Schellenberg, A., et al., *Matrix elasticity, replicative senescence and DNA methylation patterns of mesenchymal stem cells*. Biomaterials, 2014. **35**(24): p. 6351-8.
238. Hemming, S., et al., *EZH2 and KDM6A act as an epigenetic switch to regulate mesenchymal stem cell lineage specification*. Stem cells, 2014. **32**(3): p. 802-15.
239. Eslaminejad, M.B., N. Fani, and M. Shahhoseini, *Epigenetic regulation of osteogenic and chondrogenic differentiation of mesenchymal stem cells in culture*. Cell journal, 2013. **15**(1): p. 1-10.
240. Carpenter, M.K. and L.A. Couture, *Regulatory considerations for the development of autologous induced pluripotent stem cell therapies*. Regenerative medicine, 2010. **5**(4): p. 569-79.
241. Cyranoski, D., *Stem-cell pioneer banks on future therapies*. Nature, 2012. **488**(7410): p. 139.
242. Cyranoski, D., *Stem cells cruise to clinic*. Nature, 2013. **494**(7438): p. 413.
243. Csobonyei, M., et al., *Induced pluripotent stem cells and their implication for regenerative medicine*. Cell and tissue banking, 2014.
244. Vierbuchen, T., et al., *Direct conversion of fibroblasts to functional neurons by defined factors*. Nature, 2010. **463**(7284): p. 1035-41.
245. Chen, H., et al., *Measurement of FRET efficiency and ratio of donor to acceptor concentration in living cells*. Biophysical journal, 2006. **91**(5): p. L39-41.
246. Varghese, S.S., et al., *FRET for lab-on-a-chip devices - current trends and future prospects*. Lab on a chip, 2010. **10**(11): p. 1355-64.
247. Machleidt, T., et al., *TR-FRET cellular assays for interrogating posttranslational modifications of histone H3*. Journal of biomolecular screening, 2011. **16**(10): p. 1236-46.
248. Lomberk, G., L. Wallrath, and R. Urrutia, *The Heterochromatin Protein 1 family*. Genome biology, 2006. **7**(7): p. 228.
249. Azzaz, A.M., et al., *Human heterochromatin protein 1alpha promotes nucleosome associations that drive chromatin condensation*. The Journal of biological chemistry, 2014. **289**(10): p. 6850-61.
250. Mosch, K., et al., *HP1 recruits activity-dependent neuroprotective protein to H3K9me3 marked pericentromeric heterochromatin for silencing of major satellite repeats*. PloS one, 2011. **6**(1): p. e15894.

251. Lu, Z., J. Lai, and Y. Zhang, *Importance of charge independent effects in readout of the trimethyllysine mark by HP1 chromodomain*. Journal of the American Chemical Society, 2009. **131**(41): p. 14928-31.
252. Kim, H.N., et al., *Nanotopography-guided tissue engineering and regenerative medicine*. Advanced drug delivery reviews, 2013. **65**(4): p. 536-58.
253. Ling, L., V. Nurcombe, and S.M. Cool, *Wnt signaling controls the fate of mesenchymal stem cells*. Gene, 2009. **433**(1-2): p. 1-7.
254. Beildeck, M.E., E.P. Gelmann, and S.W. Byers, *Cross-regulation of signaling pathways: an example of nuclear hormone receptors and the canonical Wnt pathway*. Experimental cell research, 2010. **316**(11): p. 1763-72.
255. Sun, Y., C.S. Chen, and J. Fu, *Forcing stem cells to behave: a biophysical perspective of the cellular microenvironment*. Annual review of biophysics, 2012. **41**: p. 519-42.
256. Nohe, A. and N.O. Petersen, *Analyzing for co-localization of proteins at a cell membrane*. Current pharmaceutical biotechnology, 2004. **5**(2): p. 213-20.
257. Kim, S.H., J. Turnbull, and S. Guimond, *Extracellular matrix and cell signalling: the dynamic cooperation of integrin, proteoglycan and growth factor receptor*. The Journal of endocrinology, 2011. **209**(2): p. 139-51.
258. Rhee, S. and F. Grinnell, *Fibroblast mechanics in 3D collagen matrices*. Advanced drug delivery reviews, 2007. **59**(13): p. 1299-305.
259. Larsen, M., et al., *The matrix reorganized: extracellular matrix remodeling and integrin signaling*. Current opinion in cell biology, 2006. **18**(5): p. 463-71.
260. Meredith, J.E., Jr., B. Fazeli, and M.A. Schwartz, *The extracellular matrix as a cell survival factor*. Molecular biology of the cell, 1993. **4**(9): p. 953-61.
261. Kim, T.J., et al., *Substrate rigidity regulates Ca²⁺ oscillation via RhoA pathway in stem cells*. Journal of cellular physiology, 2009. **218**(2): p. 285-93.
262. Yang, M.T., et al., *Assaying stem cell mechanobiology on microfabricated elastomeric substrates with geometrically modulated rigidity*. Nature protocols, 2011. **6**(2): p. 187-213.
263. Sun, Y., et al., *Hippo/YAP-mediated rigidity-dependent motor neuron differentiation of human pluripotent stem cells*. Nature materials, 2014. **13**(6): p. 599-604.
264. Dalby, M.J., et al., *Osteoprogenitor response to semi-ordered and random nanotopographies*. Biomaterials, 2006. **27**(15): p. 2980-7.
265. Yang, K., et al., *Multiscale, Hierarchically Patterned Topography for Directing Human Neural Stem Cells into Functional Neurons*. ACS nano, 2014.
266. Downing, T.L., et al., *Biophysical regulation of epigenetic state and cell reprogramming*. Nature materials, 2013. **12**(12): p. 1154-62.
267. Lee, J., et al., *Controlling cell geometry on substrates of variable stiffness can tune the degree of osteogenesis in human mesenchymal stem cells*. Journal of the mechanical behavior of biomedical materials, 2014. **38**: p. 209-18.
268. Carlson, A.L., et al., *Microfibrous substrate geometry as a critical trigger for organization, self-renewal, and differentiation of human embryonic stem cells within synthetic 3-dimensional microenvironments*. FASEB journal : official publication of the Federation of American Societies for Experimental Biology, 2012. **26**(8): p. 3240-51.
269. Kuo, Y.C. and M.J. Huang, *Material-driven differentiation of induced pluripotent stem cells in neuron growth factor-grafted poly(epsilon-caprolactone)-poly(beta-hydroxybutyrate) scaffolds*. Biomaterials, 2012. **33**(23): p. 5672-82.
270. Leipzig, N.D., et al., *Differentiation of neural stem cells in three-dimensional growth factor-immobilized chitosan hydrogel scaffolds*. Biomaterials, 2011. **32**(1): p. 57-64.

271. Arany, P.R. and D.J. Mooney, *At the edge of translation - materials to program cells for directed differentiation*. Oral diseases, 2011. **17**(3): p. 241-51.
272. Tang, M., et al., *Enhancement of electrical signaling in neural networks on graphene films*. Biomaterials, 2013. **34**(27): p. 6402-11.
273. Colazzo, F., et al., *Shear stress and VEGF enhance endothelial differentiation of human adipose-derived stem cells*. Growth factors, 2014: p. 1-11.
274. Ghezzi, C.E., et al., *The role of physiological mechanical cues on mesenchymal stem cell differentiation in an airway tract-like dense collagen-silk fibroin construct*. Biomaterials, 2014. **35**(24): p. 6236-47.
275. Kim, K.M., et al., *Shear stress induced by an interstitial level of slow flow increases the osteogenic differentiation of mesenchymal stem cells through TAZ activation*. PloS one, 2014. **9**(3): p. e92427.
276. Yao, X., R. Peng, and J. Ding, *Cell-material interactions revealed via material techniques of surface patterning*. Advanced materials, 2013. **25**(37): p. 5257-86.
277. Fisher, O.Z., et al., *Bioinspired materials for controlling stem cell fate*. Accounts of chemical research, 2010. **43**(3): p. 419-28.
278. Detzel, C.J., A.L. Larkin, and P. Rajagopalan, *Polyelectrolyte multilayers in tissue engineering*. Tissue engineering. Part B, Reviews, 2011. **17**(2): p. 101-13.
279. Armentano, I., et al., *Biodegradable composite scaffolds: a strategy to modulate stem cell behaviour*. Recent patents on drug delivery & formulation, 2013. **7**(1): p. 9-17.
280. Callahan, L.A., et al., *Primary human chondrocyte extracellular matrix formation and phenotype maintenance using RGD-derivatized PEGDM hydrogels possessing a continuous Young's modulus gradient*. Acta biomaterialia, 2013. **9**(4): p. 6095-104.
281. Teo, B.K., et al., *Nanotopography modulates mechanotransduction of stem cells and induces differentiation through focal adhesion kinase*. ACS nano, 2013. **7**(6): p. 4785-98.
282. Willert, K. and K.A. Jones, *Wnt signaling: is the party in the nucleus?* Genes & development, 2006. **20**(11): p. 1394-404.
283. Wend, P., et al., *Wnt/beta-catenin signalling induces MLL to create epigenetic changes in salivary gland tumours*. The EMBO journal, 2013. **32**(14): p. 1977-89.
284. McMurray, R.J., et al., *Surface topography regulates wnt signaling through control of primary cilia structure in mesenchymal stem cells*. Scientific reports, 2013. **3**: p. 3545.
285. Lelievre, S.A., *Contributions of extracellular matrix signaling and tissue architecture to nuclear mechanisms and spatial organization of gene expression control*. Biochimica et biophysica acta, 2009. **1790**(9): p. 925-35.
286. Flouriot, G., et al., *The actin/MKL1 signalling pathway influences cell growth and gene expression through large-scale chromatin reorganization and histone post-translational modifications*. The Biochemical journal, 2014. **461**(2): p. 257-68.
287. Buck, C.A. and A.F. Horwitz, *Integrin, a transmembrane glycoprotein complex mediating cell-substratum adhesion*. Journal of cell science. Supplement, 1987. **8**: p. 231-50.
288. Hynes, R.O., *Integrins: bidirectional, allosteric signaling machines*. Cell, 2002. **110**(6): p. 673-87.
289. Iqbal, J. and M. Zaidi, *Molecular regulation of mechanotransduction*. Biochemical and biophysical research communications, 2005. **328**(3): p. 751-5.
290. Sachs, F., *Stretch-activated ion channels: what are they?* Physiology, 2010. **25**(1): p. 50-6.
291. Storch, U., M. Mederos y Schnitzler, and T. Gudermann, *G protein-mediated stretch reception*. American journal of physiology. Heart and circulatory physiology, 2012. **302**(6): p. H1241-9.

292. Ingber, D.E., *Cellular mechanotransduction: putting all the pieces together again*. FASEB journal : official publication of the Federation of American Societies for Experimental Biology, 2006. **20**(7): p. 811-27.
293. Rajgor, D. and C.M. Shanahan, *Nesprins: from the nuclear envelope and beyond*. Expert reviews in molecular medicine, 2013. **15**: p. e5.
294. Tapley, E.C. and D.A. Starr, *Connecting the nucleus to the cytoskeleton by SUN-KASH bridges across the nuclear envelope*. Current opinion in cell biology, 2013. **25**(1): p. 57-62.
295. Rothballer, A., T.U. Schwartz, and U. Kutay, *LINCing complex functions at the nuclear envelope: what the molecular architecture of the LINC complex can reveal about its function*. Nucleus, 2013. **4**(1): p. 29-36.
296. Dahl, K.N. and A. Kalinowski, *Nucleoskeleton mechanics at a glance*. Journal of cell science, 2011. **124**(Pt 5): p. 675-8.
297. Shumaker, D.K., E.R. Kuczmarski, and R.D. Goldman, *The nucleoskeleton: lamins and actin are major players in essential nuclear functions*. Current opinion in cell biology, 2003. **15**(3): p. 358-66.
298. Kornberg, R.D., *Chromatin structure: a repeating unit of histones and DNA*. Science, 1974. **184**(4139): p. 868-71.
299. Yabuki, H., N. Dattagupta, and D.M. Crothers, *Orientation of nucleosomes in the thirty-nanometer chromatin fiber*. Biochemistry, 1982. **21**(20): p. 5015-20.
300. Li, H.J., *A model for chromatin structure*. Nucleic acids research, 1975. **2**(8): p. 1275-89.
301. Eltsov, M., et al., *Analysis of cryo-electron microscopy images does not support the existence of 30-nm chromatin fibers in mitotic chromosomes in situ*. Proceedings of the National Academy of Sciences of the United States of America, 2008. **105**(50): p. 19732-7.
302. Maeshima, K., S. Hihara, and M. Eltsov, *Chromatin structure: does the 30-nm fibre exist in vivo?* Current opinion in cell biology, 2010. **22**(3): p. 291-7.
303. Nishino, Y., et al., *Human mitotic chromosomes consist predominantly of irregularly folded nucleosome fibres without a 30-nm chromatin structure*. The EMBO journal, 2012. **31**(7): p. 1644-53.
304. Hihara, S., et al., *Local nucleosome dynamics facilitate chromatin accessibility in living mammalian cells*. Cell reports, 2012. **2**(6): p. 1645-56.
305. Baker, A., et al., *Polyethylenimine (PEI) is a simple, inexpensive and effective reagent for condensing and linking plasmid DNA to adenovirus for gene delivery*. Gene therapy, 1997. **4**(8): p. 773-82.
306. Barthelery, M., U. Salli, and K.E. Vrana, *Nuclear proteomics and directed differentiation of embryonic stem cells*. Stem cells and development, 2007. **16**(6): p. 905-19.
307. Ma, Y., et al., *High-efficiency siRNA-based gene knockdown in human embryonic stem cells*. RNA, 2010. **16**(12): p. 2564-9.
308. Yoshikawa, T., et al., *Systemic administration of valproic acid and zonisamide promotes differentiation of induced pluripotent stem cell-derived dopaminergic neurons*. Frontiers in cellular neuroscience, 2013. **7**: p. 11.
309. Jonathan, E., S. Jin, and K. Ye, *Mechanobiology of Human Pluripotent Stem Cells*. Tissue engineering. Part B, Reviews, 2013.
310. Archer, S.Y. and R.A. Hodin, *Histone acetylation and cancer*. Curr Opin Genet Dev, 1999. **9**(2): p. 171-4.
311. Xiao, L., et al., *Deficient histone acetylation in acute leukemia and the correction by an isothiocyanate*. Acta Haematol, 2010. **123**(2): p. 71-6.

312. Shabason, J.E., P.J. Tofilon, and K. Camphausen, *HDAC inhibitors in cancer care*. Oncology (Williston Park), 2010. **24**(2): p. 180-5.
313. Smith, K.T. and J.L. Workman, *Histone deacetylase inhibitors: anticancer compounds*. Int J Biochem Cell Biol, 2009. **41**(1): p. 21-5.
314. Kim, T.Y., Y.J. Bang, and K.D. Robertson, *Histone deacetylase inhibitors for cancer therapy*. Epigenetics, 2006. **1**(1): p. 14-23.
315. Marks, P.A. and W.S. Xu, *Histone deacetylase inhibitors: Potential in cancer therapy*. J Cell Biochem, 2009. **107**(4): p. 600-8.
316. Tan, J., et al., *Novel histone deacetylase inhibitors in clinical trials as anti-cancer agents*. J Hematol Oncol, 2010. **3**: p. 5.
317. Glaser, K.B., *HDAC inhibitors: clinical update and mechanism-based potential*. Biochem Pharmacol, 2007. **74**(5): p. 659-71.
318. Kell, J., *Drug evaluation: MGCD-0103, a histone deacetylase inhibitor for the treatment of cancer*. Curr Opin Investig Drugs, 2007. **8**(6): p. 485-92.
319. Atmaca, A., et al., *Valproic acid (VPA) in patients with refractory advanced cancer: a dose escalating phase I clinical trial*. Br J Cancer, 2007. **97**(2): p. 177-82.
320. Ellis, L., et al., *Histone deacetylase inhibitor panobinostat induces clinical responses with associated alterations in gene expression profiles in cutaneous T-cell lymphoma*. Clin Cancer Res, 2008. **14**(14): p. 4500-10.
321. Dizon, D.S., et al., *A phase II evaluation of belinostat and carboplatin in the treatment of recurrent or persistent platinum-resistant ovarian, fallopian tube, or primary peritoneal carcinoma: a Gynecologic Oncology Group study*. Gynecol Oncol, 2012. **125**(2): p. 367-71.
322. Younes, A., et al., *Mocetinostat for relapsed classical Hodgkin's lymphoma: an open-label, single-arm, phase 2 trial*. Lancet Oncol, 2011. **12**(13): p. 1222-8.
323. Pili, R., et al., *Phase I study of the histone deacetylase inhibitor entinostat in combination with 13-cis retinoic acid in patients with solid tumours*. Br J Cancer, 2012. **106**(1): p. 77-84.
324. Mandl-Weber, S., et al., *The novel inhibitor of histone deacetylase resminostat (RAS2410) inhibits proliferation and induces apoptosis in multiple myeloma (MM) cells*. Br J Haematol, 2010. **149**(4): p. 518-28.
325. Prince, H.M. and M. Dickinson, *Romidepsin for cutaneous T-cell lymphoma*. Clin Cancer Res, 2012.
326. Rangwala, S., C. Zhang, and M. Duvic, *HDAC inhibitors for the treatment of cutaneous T-cell lymphomas*. Future Med Chem, 2012. **4**(4): p. 471-86.
327. Duvic, M. and J. Vu, *Vorinostat: a new oral histone deacetylase inhibitor approved for cutaneous T-cell lymphoma*. Expert Opin Investig Drugs, 2007. **16**(7): p. 1111-20.
328. Yu, J., et al., *Human induced pluripotent stem cells free of vector and transgene sequences*. Science, 2009. **324**(5928): p. 797-801.
329. Zhou, H., et al., *Generation of induced pluripotent stem cells using recombinant proteins*. Cell stem cell, 2009. **4**(5): p. 381-4.
330. Warren, L., et al., *Highly efficient reprogramming to pluripotency and directed differentiation of human cells with synthetic modified mRNA*. Cell stem cell, 2010. **7**(5): p. 618-30.
331. Miyoshi, N., et al., *Reprogramming of mouse and human cells to pluripotency using mature microRNAs*. Cell stem cell, 2011. **8**(6): p. 633-8.

332. Baliban, R.C., et al., *A novel approach for untargeted post-translational modification identification using integer linear optimization and tandem mass spectrometry*. Molecular & cellular proteomics : MCP, 2010. **9**(5): p. 764-79.
333. Ehrenberg, M. and R. Rigler, *Fluorescence correlation spectroscopy applied to rotational diffusion of macromolecules*. Quarterly reviews of biophysics, 1976. **9**(1): p. 69-81.
334. Magde, D., E.L. Elson, and W.W. Webb, *Fluorescence correlation spectroscopy. II. An experimental realization*. Biopolymers, 1974. **13**(1): p. 29-61.
335. Fitzpatrick, J.A. and B.F. Lillemeier, *Fluorescence correlation spectroscopy: linking molecular dynamics to biological function in vitro and in situ*. Current opinion in structural biology, 2011. **21**(5): p. 650-60.
336. Schwille, P., F. Oehlenschläger, and N.G. Walter, *Quantitative hybridization kinetics of DNA probes to RNA in solution followed by diffusional fluorescence correlation analysis*. Biochemistry, 1996. **35**(31): p. 10182-93.
337. Lieto, A.M., R.C. Cush, and N.L. Thompson, *Ligand-receptor kinetics measured by total internal reflection with fluorescence correlation spectroscopy*. Biophysical journal, 2003. **85**(5): p. 3294-302.
338. Slaughter, B.D., J.W. Schwartz, and R. Li, *Mapping dynamic protein interactions in MAP kinase signaling using live-cell fluorescence fluctuation spectroscopy and imaging*. Proc Natl Acad Sci U S A, 2007. **104**(51): p. 20320-5.
339. Heuff, R.F., J.L. Swift, and D.T. Cramb, *Fluorescence correlation spectroscopy using quantum dots: advances, challenges and opportunities*. Physical chemistry chemical physics : PCCP, 2007. **9**(16): p. 1870-80.